

Studies of the secondary electron
emission
from diamond films

Raquel Maria Amaro Vaz



**A dissertation submitted to the University of Bristol in accordance with the
requirements of the degree of Doctor of Philosophy in the Faculty of Science,
School of Chemistry**

Abstract

The aim of the present research was the development of an optimised secondary electron emission (SEE) diamond film to use as a dynode material. The project was a partnership between the School of Chemistry in the University of Bristol, the Space Research Centre (SRC) at the University of Leicester and Photek, a company specialized in the manufacture of systems for photon detection. The role of Bristol in this project consisted in the preparation of CVD diamond films and their characterization, before supply to the other collaborators. SEE characterisation of the samples was performed at SRC and Photek would proceed to further testing in actual tubes. Besides its participation in the project, Bristol went further and developed the means to do its own SEE measurements.

This thesis describes the work undertaken at Bristol using the facilities at the Diamond CVD group. Diamond films were prepared by hot-filament (HF) CVD covering a range of crystallinities, thicknesses and levels of boron (B) doping, on different substrate materials.

A new home-built apparatus has been developed for the acquisition of SEE data from diamond films, both in reflection and transmission configurations. The setup consists of a system of phosphor screens acting as detectors and associated to PMTs for the acquisition of signal measured from the diamond samples.

A comprehensive study evaluating the effects of B-doping, crystallinity, surface termination, thickness and substrate material of diamond films on yield and yield degradation in the SEE reflection yields has been performed.

In addition, SEE yields from commercial CVD diamond samples were analysed, after surface functionalization by hydrogenation, caesiation and lithiation.

Moreover, the present study allowed for an improvement in the growth of thin NCD films, essentially through the optimization of the seeding processes. Finally, the development of techniques to manufacture free standing diamond films on silicon substrates were investigated, and preliminary SEE measurements in transmission were undertaken.



I declare that the work in this dissertation was carried out in accordance with the Regulations of the University of Bristol. The work is original, except where indicated by special reference in the text, and no part of the dissertation has been submitted for any other academic award. Any views expressed in the dissertation are those of the author.

SIGNED: DATE:.....



Acknowledgements

I would like to express my gratitude to all the people who made this work possible; my supervisor Professor Paul May, co-supervisor Dr. Neil Fox, Dr. James Smith for their support and guidance. A special acknowledge to the Dr. John Lapington for funding through the Dynode Project funds and also to EPSRC.

Big special thanks go to my colleagues at the Diamond group for all the good times.

Thanks to my family and friends.



Contents

List of Tables	xiii
List of Figures	xv
<i>Chapter 1. Introduction</i>	1
1.1. <i>Structure, Properties and Applications of Diamond</i>	1
1.2. <i>Deposition techniques of synthetic diamond</i>	3
1.2.1. <i>High Temperature High Pressure</i>	4
1.2.2. <i>Chemical vapour deposition of diamond</i>	5
1.2.2.1. <i>Hot-Filament CVD</i>	5
1.2.2.2. <i>Microwave plasma CVD</i>	6
1.3. <i>CVD diamond materials</i>	7
1.3.1. <i>Single-crystal diamond</i>	8
1.3.2. <i>Microcrystalline diamond</i>	8
1.3.3. <i>Nanocrystalline diamond</i>	8
1.4. <i>Mechanisms of diamond growth: gas-phase and surface chemistry</i>	9
1.4.1. <i>Chemical reactions in CVD reactors</i>	10
1.4.2. <i>Importance of Atomic hydrogen</i>	13
1.5. <i>Defects and doping of diamond</i>	14
1.5.1. <i>n-type doping</i>	14
1.5.2. <i>p-type doping</i>	14
1.5.3. <i>Boron incorporation into diamond</i>	15
1.6. <i>The substrate material</i>	16
1.6.1. <i>Homoeptaxial growth</i>	16
1.6.2. <i>Heteroepitaxial growth</i>	17
1.7. <i>Nucleation methods: substrate pre-treatment</i>	18
1.7.1. <i>Manual scratching</i>	18
1.7.2. <i>Ultrasonic seeding</i>	18
1.7.3. <i>Electrospray deposition seeding</i>	19
1.7.4. <i>Bias-enhanced nucleation (BEN)</i>	19
1.8. <i>Electron emission from solids</i>	19
1.8.1. <i>The Secondary Electron Emission process</i>	21
1.8.2. <i>The Secondary Electron Emission Yield</i>	23
1.8.3. <i>Theoretical models</i>	25
1.8.4. <i>Surface Electron Affinity</i>	29
1.8.5. <i>SEE from metals</i>	30

1.8.6.	<i>SEE from insulators</i>	30
1.8.7.	<i>SEE from semiconductors</i>	31
1.8.8.	<i>SEE from diamond</i>	31
1.8.8.1.	<i>The Effect of Negative Electron Affinity</i>	32
1.8.8.2.	<i>The effect of dopant and dopant concentration</i>	35
1.8.8.3.	<i>The effect of surface roughness</i>	36
1.8.8.4.	<i>The effect of film thickness</i>	36
1.8.8.5.	<i>The effect of crystallinity</i>	37
1.8.8.6.	<i>The effect of substrate</i>	37
1.8.8.7.	<i>The energy distribution of secondary electrons emitted from diamond</i>	37
1.8.8.8.	<i>Angular distribution of secondary electrons</i>	38
1.8.9.	<i>SEE from diamond: A state-of-the-art review</i>	39
1.8.9.1.	<i>Reflection yield studies</i>	39
1.8.9.2.	<i>Transmission yield studies</i>	41
1.9.	<i>Measurement methods</i>	43
1.9.1.1.	<i>Measurement of the total electron yield</i>	43
1.9.1.2.	<i>The effect of the angle of incidence</i>	46
1.9.1.3.	<i>The effect of temperature</i>	46
1.9.1.4.	<i>The effect of beam current</i>	48
1.9.1.5.	<i>Measurement of the energy distribution of the emitted electrons</i>	48
1.10.	<i>Potential Device Applications</i>	49
1.11.	<i>Thesis overview</i>	51
1.12.	<i>References</i>	52
<i>Chapter 2</i>		67
<i>Experimental methods and characterization techniques</i>		67
2.1.	<i>Hot-Filament CVD</i>	67
2.2.	<i>Substrate pre-treatment methods</i>	70
2.2.1.	<i>Seeding by electrospray deposition</i>	70
2.3.	<i>Laser Alpha 532-XYZ-A-U system</i>	71
2.4.	<i>Raman Spectroscopy</i>	72
2.5.	<i>Scanning electron microscopy</i>	74
2.6.	<i>Atomic force microscopy</i>	74
2.7.	<i>Secondary electron emission equipment</i>	75
2.7.1.	<i>Bristol setup</i>	75
2.7.2.	<i>Leicester setup</i>	75
2.8.	<i>References</i>	76
<i>Chapter 3. HFCVD deposition of diamond films</i>		79
3.1.	<i>Introduction</i>	79

3.2.	<i>Experimental</i>	80
3.3.	<i>Results and Discussion</i>	81
3.3.1.	<i>MCD versus NCD films</i>	82
3.3.1.1.	<i>Comparison between resistance values</i>	83
3.3.1.2.	<i>Microstructure Characterization</i>	84
3.3.1.3.	<i>Raman spectra and B-doping level</i>	88
3.4.	<i>Conclusions</i>	90
3.5.	<i>References</i>	91
<i>Chapter 4.</i>		93
<i>Development of a new apparatus for secondary electron emission measurements</i>		93
4.1.	<i>Initial assumptions and testing</i>	93
4.1.1.	<i>System calibration</i>	100
4.1.1.1.	<i>Electron Beam output monitoring</i>	102
4.1.1.2.	<i>Measurement method</i>	106
4.2.	<i>Conclusions</i>	110
4.3.	<i>References</i>	111
<i>Chapter 5.</i>		113
<i>Studies of the SEE from HFCVD diamond films</i>		113
5.1.	<i>Introduction</i>	113
5.2.	<i>Experimental</i>	114
5.3.	<i>Results and discussion</i>	117
5.3.1.	<i>Measurement of the SEE yield from MCD films on Si and Mo</i>	118
5.3.2.	<i>Measurement of the SEE yield from NC diamond on Si and Mo</i>	120
5.3.3.	<i>Variation of yield with surface termination</i>	124
5.3.4.	<i>Variation of the SEE yield across the hydrogenated surfaces</i>	126
5.3.5.	<i>Variation of the yield with beam exposure</i>	127
5.4.	<i>Conclusions</i>	128
5.5.	<i>References</i>	130
<i>Chapter 6.</i>		133
<i>Study of the influence of the surface termination in the yield of commercial PCCVD diamond</i>		133
6.1.	<i>Introduction</i>	133
6.2.	<i>Experimental</i>	134
6.3.	<i>Results and discussion</i>	136
6.3.1.	<i>Yield measurements from oxygenated-caesiated surfaces: (C/O/Cs)</i>	136
6.3.2.	<i>Lithiated surfaces (LiO/C)</i>	139
6.4.	<i>Conclusions</i>	143
6.5.	<i>References</i>	145
<i>Chapter 7.</i>		147

<i>Growth and characterisation of thin diamond membranes</i>	147
7.1. <i>Introduction</i>	147
7.2. <i>Experimental</i>	148
7.3. <i>Results and discussion</i>	150
7.3.1. <i>HFCVD diamond deposition and seeding methods</i>	150
7.3.2. <i>Preparation of free standing diamond membranes</i>	160
7.3.2.1. <i>Laser machining</i>	160
7.3.3. <i>Transmission yield measurements</i>	165
7.3.4. <i>Monte Carlo simulation</i>	167
7.4. <i>Conclusions</i>	169
7.5. <i>References</i>	169
<i>Chapter 8. Conclusions</i>	171
8.1. <i>Future work</i>	173
8.1.1. <i>SEE apparatus</i>	174
8.1.2. <i>SEE yield measurements</i>	174
8.2. <i>Growth and characterisation of thin diamond membranes</i>	174
<i>Appendix A. Scientific communications and collaborations</i>	176

List of Tables

Table 1.1- Some of the outstanding properties of diamond. ^[3]	2
Table 1.2- A few examples of the wide range of diamond applications.	3
Table 1.3- Range of typical operating parameters for diamond deposition using hot-filament CVD. ^[27]	6
Table 1.4- Summary of research studies found in the literature of SEE from diamond, sample characteristics and reflection yield values. (PCD = polycrystalline diamond, SCD = single-crystal diamond, MCD = microcrystalline diamond, f-NCD = faceted nanocrystalline diamond).....	40
Table 1.4 (cont.)- Summary of research studies found in the literature of SEE from diamond, sample characteristics and reflection yield values.	41
Table 1.5- Summary of research studies of secondary electron emission from diamond, sample characteristics and transmission yield values found in the literature. (PCD = polycrystalline diamond, SCD = single-crystal diamond, MCD = microcrystalline diamond, f-NCD = faceted nanocrystalline diamond).....	42
Table 2.1- Standard deposition conditions employed in a hot filament CVD reactor.	67
Table 2.2- Specifications of the laser system according to the Oxford Lasers manual.	72
Table 3.1- Deposition parameters for the MCD films grown at a ratio of 1% CH ₄ /H ₂ with different B-doping levels (at concentrations between 0 and 10000 ppm) and thicknesses ~ 3.5 μm, and the resistance values measured from the samples. R.D. = residual doping (see above).....	82
Table 3.2- Deposition parameters for NCD films grown at 2.5-5% CH ₄ /H ₂ with different B-doping levels (at concentrations between 0 and 10000 ppm) and thickness ~ 3.5 μm, plus the resistance values measured from the samples. R.D. = residual doping (see above).....	82
Table 4.1- Power supply controllable outputs.....	103
Table 5.1- HFCVD diamond deposition conditions for the samples used in the present study, divided into different sets according to the substrate material (Si <i>versus</i> Mo), crystallinity (MCD <i>versus</i> NCD), thickness (constant or variable) and resistance (in decreasing order for each set).....	115
Table 5.2- Summary of the maximum yield values from samples S10 to S13 (3.5 μm-thick MCD films on Mo substrates), with different surface terminations.	125

Table 6.1- Different surface treatments applied to the CVD samples before SEE measurements.....	135
Table 6.2- Summary of the SEE yield values measured for the PCD CVD and SCD CVD samples with different surface functionalization.	143
Table 7.1- Parameters used in the preparation of a series of thin NCD films. The diamond films were grown in a B-free undoped atmosphere, varying the cycle duration, C content and seeding methods. The samples are presented in order of decreasing deposition time.....	150
Table 7.2- Particle sizing DLS of 5 nm diamond suspension in methanol, prepared in equivalent conditions to the seeding suspension. The values indicate that the average diameter of the diamond particles in the suspension varied from ~ 78 nm to ~ 59 nm, before and after centrifugation. The difference between ultrasonication and centrifugation was found to be insignificant.....	154
Table 7.3- Parameters used in the preparation of a series of thin NCD films, varying the deposition time, C content and seeding methods. The samples are presented in order of decreasing deposition time. The diamond films were grown using a B-doping chamber although no B was added to the gas phase.....	156
Table 7.4-Experimental parameters for the laser milling shown in figure 7.9.	161

List of Figures

Figure 1.1- The unit cell of diamond showing a tetrahedral structure. The diamond structure can be defined as two interpenetrating face-centered-cubic lattices shifted along the body diagonal by $(1/4, 1/4, 1/4) a_0$. ^[2]	2
Figure 1.2- Pressure and temperature phase and reaction diagram for elemental carbon. ^[18]	4
Figure 1.3- Schematics of a linear antenna-type MW-plasma CVD reactor.	7
Figure 1.4- Original C-H-O ternary phase diagram (Bachmann diagram) for CVD diamond based on the gas phase compositions, resulting from the summary of 70 experiments using different gas mixtures. ^[37]	10
Figure 1.5- Schematic diagram of the reactions occurring during CVD diamond growth. The activation source represented is a hot-filament. ^[39]	10
Figure 1.6- Illustration of the main gas-phase reactions occurring during the CVD diamond deposition process. The reactions correspond to the fast hydrogen transfer reactions with the interconversion between C_1 and C_2 hydrocarbon species. ^[38]	11
Figure 1.7- A simplified schematic diagram of the standard growth model occurring at a (100) diamond surface. Adapted from references. ^[43, 39]	12
Figure 1.8- Schematics of the energy-band diagrams showing (a) the overlap between the valence band (VB) and the conduction band (CB) in metals, (b) the large energy gap (E_g) in insulators, (c) the smaller gap in intrinsic semiconductor materials, (d) an extrinsic p-type semiconductor, with an additional acceptor level (E_a) lying just above VB and (e) an n-type semiconductor with its donor level (E_d) lying just below the CB.....	21
Figure 1.9- Schematic illustration of the spectrum of emitted electrons from a surface generated by a primary electron beam of energy E_0 . ^[89]	22
Figure 1.10- Schematic illustration for the variation of SEE yield with primary electron beam of energy E_0 . ^[85]	24
Figure 1.11- Plot showing the relation between the penetration depth (R) of the primary electrons through the solid and the production rate of secondaries (Nx). The escape depth of the internal secondary electrons is normally described by an exponential decay law. ^[103]	27

Figure 1.12- Illustration of the energy band diagrams of a semiconductor showing (a) positive electron affinity and (b) effective negative electron affinity, and (c) true negative electron affinity. ^[109]	29
Figure 1.13- Schematic models for the surface dipoles of an oxygen-chemisorbed diamond (left), and of a hydrogenated diamond surface (right). The sign of the electric dipoles differ, resulting in a negative and a positive electron affinity, respectively. The higher electronegative O atoms in relation to C, creates the PEA. The dipole due to the larger electron negativity of C in relation to H is the origin of the NEA. ^[130]	33
Figure 1.14- SEE yield δ obtained from an N-doped diamond film in comparison with a B-doped film with resistivity in the range of 50-170 k Ω cm, both H-terminated. ^[123]	35
Figure 1.15- EDC curves illustrating the emitted electron intensity as a function of the emitted electron energy for a hydrogen terminated B-doped diamond sample (curve A) and the same sample after heating to 1000°C (curve B). ^[104]	38
Figure 1.16- Schematic diagrams of the angular distribution of (a) secondary electrons, and (b) backscattered electrons, emitted from a polycrystalline surface. ^[105]	39
Figure 1.17- Energy distribution curves measured from an 8.3 μ m diamond film in reflection and transmission with normalized peak intensities. ^[17]	43
Figure 1.18- Arrangement for measuring the SEE. All emitted electrons independent of their emission direction are collected. It is possible to separate the slow secondary electrons from the energetic backscattered electrons by using a retarding field. ^[80]	44
Figure 1.19-Illustration of a typical UHV chamber used for SEE measurements both in reflection and transmission configurations (top view), with a 4-grid energy analyser (low-energy electron diffraction (LEED) system) for determination of the EDC curves, adapted from reference. ^[119]	45
Figure 1.20- Variation of the maximum yield values measured after heating a PC diamond grown on Mo at various temperatures: 1) 500°C, 2) 600°C, 3) 700°C, 4) 750°C, 5) 850°C and 6) 975 °C. ^[161]	47
Figure 1.21- Schematic diagram of the principal elements of a photomultiplier (adapted from Photonis PMT Handbook ^[179]).....	50
Figure 1.22- SEE yields of three common dynode materials. (Inset from Photonis PMT Handbook ^[179]).....	50

Figure 2.1- Sketch of the hot-filament reactor used to grow the diamond CVD films in the experiments presented across this thesis. This reactor is used to produce B-doped diamond films but presents the exact same setup of the one used for non-doped films.	68
Figure 2.2- Schematic diagrams of the system for mounting the filaments, showing a coil (in a) and the new version using up to three filaments connected in parallel (in b).	69
Figure 2.3- Sketch of electrospray deposition equipment, showing the different components: a) sample holder connection to ground, b) sample holder which is adjustable vertically and horizontally, c) rotating component of the sample holder where the substrates are mounted with a 40 ° to the vertical axis, d) capillary nozzle and e) motor control.	70
Figure 2.4- Apparatus for secondary electron emission measurements located at the University of Leicester. ^[11]	76
Figure 3.1- Plot of the variation of 4-point resistance against 2-point resistance for MC and NCD films (logarithmic plot), and linear best fits showing the increase in the gradient as crystallite size decreases.	83
Figure 3.2- SEM images of the surfaces of the MCD films (see Table 3.1) with thickness ~ 3.5 μm, showing predominantly randomly-oriented crystallites with grain sizes around 0.5 - 1 μm. The increasing B content has not has a significant effect upon the film morphology.	85
Figure 3.3- SEM images of the cross-section of sample SMC5, showing a thickness ~ 3.5 μm as predicted for a 7 hour deposition run with 1% CH ₄ /H ₂ . This shows that the growth rate was also not significantly affected by B content.	86
Figure 3.4- SEM images of the surface of the NCD films, showing a decrease in crystallite size with increasing methane concentration (samples SNC1 - SNC7), and a cauliflower or amorphous appearance for the highest methane concentrations (SNC8 and SNC9).	87
Figure 3.5- Raman spectra obtained with UV (325 nm) excitation wavelength from MCD films with different B-doping levels and thickness ~ 3.5 μm (Table 3.1). The films decrease in resistance from the top to the bottom. The spectra of samples SMC7 and SMC8 are inset for better detail.	88
Figure 3.6- Raman spectra obtained with UV (325 nm) excitation from NCD films with different B-doping levels and thickness ~ 3.5 μm. The B content increases from the top to the bottom of the graph.	90
Figure 4.1- Sketch of the configuration for measurements in reflection (a), and transmission (b) configurations, respectively.	93

Figure 4.2- Schematic diagram of the electron transmission and reflection testing rig used for preliminary tests.....	95
Figure 4.3- Pictures of the sample holder with nine apertures to allow evaluation of the transmission of electrons through the diamond membranes, showing the PS positioned at 45° to the sample surface for reflection (in a)) and the PS fixed on the glass window by means of silver tag, placed behind the thin diamond membrane (in b)).	96
Figure 4.4- Pictures taken during one of the experiments made at 5 keV, using a P15 PS facing of the emitting surface of a 140 nm thick diamond membrane, showing a strong transmission through the diamond film with the electron gun pointing toward the observer (in a)). In b) a fibre-optic cable taking the light to a monochromator in order to quantify the transmitted signal through the diamond membrane in comparison with a the primary signal detected by the PS in the absence of the membrane.	97
Figure 4.5- Graphs showing the emission spectrum obtained from the PS at different primary electron energies impinging a 140 nm diamond membrane (a), and the emission curves with and without the diamond membrane acquired at 5 keV (b).....	97
Figure 4.6- Picture of the setup developed for the acquisition of SEE yields, prepared to work in both reflection and transmission configurations (front view). From the image are identifiable the main components which compose the external parts of the equipment: (a) electron gun, (b) view port for visual control (fully covered during the measurements), (c) feedthroughs for biasing and current reading, (d) camera for beam observation under calibration, (e) loading port and (f) electron gun control box.....	98
Figure 4.7- Picture of the setup developed for the acquisition of SEE yields (side views), showing: (a) electron gun, (b) support arm for the PMT during reflection measurements, and associated view-port (c) (covered during the measurements, except for the PMT area), (d) support arm for the PMT for transmission measurements, (e) front view port for visual control and (f) turbo pump connected to the back of the vacuum chamber.	99
Figure 4.8- Schematic diagram of the setup adopted for reflection and transmission measurements, using a system with PSs and PMTs.	100
Figure 4.9- Standard EGL-2022 electron gun block diagram (from Kimball Physics EGL-2022 electron gun manual).....	101
Figure 4.10- Images showing the method adopted for the electron beam calibration, with visual control of the spot by means of a phosphor screen (a) and control of the beam current using a SFC placed side-by-side with the phosphor screen on the sample holder.	102

Figure 4.11- Graph with the variation of the beam current with the emission current E_c for beam energies up to 5 keV, showing an increased reduction of the beam current with increasing E_c . For $E_0 < 1.3$ keV the difference between both values is even more remarkable, possibly because a percentage of the electrons do not have enough energy to reach the SFC.	104
Figure 4.12- Graph of the variation of the beam current with the beam energy for five different values of emission current E_c , showing a decrease in the ratio of the beam current to E_c (a) and the linearity between E_c and the beam current (b).....	104
Figure 4.13- Graphs representing the variation of the signal acquired by the PMT, showing a linear relation and the increase of gradient with beam energy.....	105
Figure 4.14- Measurement of $S_{background}$ taken with the electron beam centred with a 1 cm square hole made on a metal plate similar to the ones used for the measurements mounted in the sample holder (a). The graph in (b) shows the measurement of the background current by comparing the currents measured at the grid placed in front of the view-port where the PMT is associated, the current at the sample holder and the current generated in the sample holder with the beam facing a graphite sample.	108
Figure 4.15- Graphs showing the SEE yields measured from two different samples in both setups. The graphs in blue (a_1 and b_1) were obtained from the new setup and the ones in red (a_2 and b_2) at SRC. The samples were ~ 2.3 μm medium B-doped diamond films on Si (5 and 170k Ω , respectively, in a) and b)).	110
Figure 5.1- Schematic diagram of the setup used for measurements in a reflection configuration.	117
Figure 5.2- Relative SEE yields measured from the samples belonging to the sets 1 and 3 (table 5.1), corresponding to ~ 3.5 μm thick MCD films, grown with different B_2H_6 additions to the gas phase. The substrate materials were Si (green) and Mo (red). The 2-point resistances of the diamond films are shown for each sample.	118
Figure 5.3- SEE yields measured from the samples from sets 1 and 3 (table 5.1) <i>versus</i> the resistance measured from the different ~ 3.5 - μm -thick MCD films, grown with different B contents. The substrate materials were Si (green) and Mo (red).....	119
Figure 5.4- Variation of the SEE yield with the film thickness measured from the samples S6-S9 from set 2 (table 5.1), corresponding to MCD films grown on Si with similar B contents. The thicknesses vary from 0.5 μm - 4 μm . Sample S3 with 13 k Ω cm (from set 1) was included as a matter of comparison.....	119

Figure 5.5- Comparison of the SEE yields measured from the samples S15 – S23 belonging to the sets 4 and 5 (table 5.1), corresponding to ~ 3.5 μm thick NCD films, grown with different B contents. Substrate materials were Si (green) and Mo (red).	120
Figure 5.6- SEE yields measured from the samples S15 – S23 from sets 4 and 5 (table 5.1), corresponding to different ~ 3.5- μm -thick NCD films, grown with different B contents <i>versus</i> the resistance values. As substrate materials were used Si (in green) and Mo (in red).	121
Figure 5.7- Comparison of the SEE yields measured from the MCD samples (S1-S5) from set 1 and the NCD samples (S15 –S20) from set 4 in relation to the resistance.	121
Figure 5.8- Comparison of the SEE yields measured from the MCD samples (S1-S5) from set 1 and the NCD samples (S15 –S20) from set 4, all corresponding to Si substrates.	122
Figure 5.9- Comparison of the SEE yields measured from the MCD samples (S10-S14) from set3 and the NCD samples (S21 –S23) from set 5, all corresponding to ~ 3.5 μm -thick films on Mo substrates.	122
Figure 5.10- Comparison of the of all the SEE yields measured from the samples with ~ 3.5 μm thickness, both MCD and NCD on Si and Mo, according to the colours displayed in the legend.....	123
Figure 5.11- The graphs represent the SEE yields as a function of the primary beam energy measured from as-grown surfaces by comparison with further surface treatments of hydrogenation (in a) and b) for samples S11 and S12) and oxygenation plus lithiation (in c) and d) samples S10 and S13).	124
Figure 5.12- Comparison of the maximum SEE yields measured from samples S10 - S13 with distinct surface treatments: as grown, H-, LiO- and CsO- terminated.....	125
Figure 5.13- Variation of yield across the surface of sample S11 measured after hydrogenation treatment.	126
Figure 5.14- Variation of yield across the surface of sample S12 measured after hydrogenation treatment.	126
Figure 5.15- Comparison of the yield variation under continuous exposure of the same area in the sample surfaces to a 1.5 keV electron beam. The measurements correspond to the C/H, C/O/Li and C/O/Cs surfaces of sample S12, S13 and S11, respectively.	127
Figure 5.16- Comparison of the yield variation as a function of the beam energy for the C/H surface of sample S12, in measurements performed before and after continuous exposure to a 1.5 keV electron beam. This is an indication of a variation in the emission properties, which may be associated with H-desorption.	128

Figure 6.1- SEM image taken from a PC sample where the left side has a CsO-termination and the right side only an O- termination. The CsO-terminated side appears brighter, indicating a larger intensity of secondary electron emission.	137
Figure 6.2- Graph showing the SEE yield values corresponding to the surface displayed in the SEM picture in figure 6.1. Position 1 is on the right-hand half of the film (CsO- terminated), Position 3 is on the left-hand side of the sample (O-terminated), and Position 2 in between those.	137
Figure 6.3- Graph presenting the SEE yield values measured from two PCD unpolished surfaces, showing a maximum yield value of 9 at 2.9 keV (in b)), despite the fluctuation that can be observed across the surface in both samples which may be related with a non-uniform surface termination. The measurements were performed with the beam impinging three different areas (positions 1-4). In figure c), a graph taken from the literature ^[3] shows a similar shape up to 3 keV but with much higher yield coefficients.	138
Figure 6.4- SEE yield values measured from a Li-O terminated PCD unpolished surface, showing a maximum yield value of 8.9 at 1.5 keV but a maximum of ~ 7 if averaged across the surface. The variation of SEE values across the surface which may be related with a non-uniform termination.	140
Figure 6.5- The SEE yield values measured from the front (growth) surface of a PCD sample (in a) and from the back side (nucleation surface) of the sample (in b) after lithiation of one side at a time. As observable from the graphs, the back surface displayed a reduction in the yield of about 50% in relation to the top surface.	140
Figure 6.6- UV-Raman spectra taken from both sides of one of the Element Six samples after cleaning for 3 hours, showing that besides the sharp diamond peak at 1332 cm ⁻¹ the back side of the sample still contains a small amount of sp ² carbon (G-band at 1550 cm ⁻¹) probably present at the grain boundaries.	141
Figure 6.7- SEM image comparing two identical PCD samples, one with oxygen termination (left) and the other with Li-O termination (right), showing a considerably larger intensity of secondary electron emission from the lithiated surface.	141
Figure 6.8- The SEE yield values measured from a SCD sample prepared with H-termination after being coated with a 500 nm residual B-doped layer, showing a maximum yield value of ~ 10 at 2.6 keV.	142
Figure 7.1- SEM images of the NCD films grown under the conditions described in table 7.1.	152

Figure 7.2- AFM images of two different samples showing the surfaces after seeding by ESD using 1ml of colloidal suspension (a), and (b) after undergoing 30 min of CVD diamond growth at 1.25% and 1.5% CH ₄ /H ₂ , respectively. The grey scale relates to a depth profile, measured from the deeper areas (in black) to the highest level at the top of the surface (in white).	153
Figure 7.3- AFM images of two different surface areas of a manually abraded sample after a CVD diamond cycle of 45 min using 2.5% CH ₄ /H ₂ , showing areas of reduced growth after a reasonably long cycle.....	155
Figure 7.4- SEM images of the NC diamond films grown under the conditions described in table 7.3.....	157
Figure 7.5- SEM images of five diamond films seeded by ESD with 0.8 ml of seeding suspension immediately after ultrasonication for 20 min. All the films were grown for 50 min at 1.25% CH ₄ /H ₂ except the sample in for a ₄) at 2.5%. The films presented good uniformity and the cross-section images show a similar thickness of ~ 1 μm and ~ 1.3 μm for the sample in b ₄).	158
Figure 7.6- SEM images from a continuous thin diamond film (a), and b) a cross-section image where a film thickness under 220 nm can be measured. The seeding method was ESD with ~ 0.6 ml of diamond suspension and it was grown at 1% CH ₄ /H ₂ for 40 min.	159
Figure 7.7- SEM images of Si seeded via the LBL process, showing evidence of the polymer layer drying and cracking.....	159
Figure 7.8- Sketch of the method that has been used in the production of free-standing diamond membranes.	160
Figure 7.9- Optical microscope pictures of the milling experiments performed on Si samples, showing the removal of material in depth with increasing the number of scans, in the conditions summarized in table 7.4.	161
Figure 7.10- SEM image taken from the back side of a diamond film (~ 10 μm thick) undergoing the etching process. In a) can be seen a diamond surface with clear evidence of the holes created during the laser milling. Image b) has been taken from the top side, showing evidence of diamond film cracking during the chemical etching (left), induced by the presence of holes and the stresses created in the film during the chemical etching. Image c) (sample front and back side, respectively), shows a case successfully fabricated membrane using a ~ 140-nm-thick diamond film, kindly supplied by Dr. Oliver Williams (Fraunhofer Institute).	162

Figure 7.11- SEM image taken from a cross-section after undergoing the milling process. The picture illustrates the feasible limit of ~ 80% for the milled depth without compromising the diamond film integrity.....	163
Figure 7.12- SEM image taken from the back side of a diamond membrane (~ 10 μm thick) after completing the etching process with success.....	163
Figure 7.13- Schematic diagrams of the setup mounted for the chemical etching of thin diamond films, consisting of two metal plates firmly clamped together and sandwiching the sample to etch. The top metal plate has an aperture that exposes the substrate and defines the area to etch. Small drops of etchant are poured into the hole and left to react.	164
Figure 7.14- Schematic diagrams of the apparatus for the transmission measurements, detailed in chapter 3.	165
Figure 7.15- Photograph of the sample holder illustrating the method of mounting the samples for transmission measurements.	166
Figure 7.16- SEE yields measured from samples 1 - 3. The value increases from ~ 0.6 for the diamond films with 3.5 μm and 10 μm, to ~ 0.9 for 0.4 μm thick diamond.....	166
Figure 7.17- Yield curves obtained for sample 2 with H-terminated surface by comparison with the acid cleaned O-terminated surface.	167
Figure 7.18- Monte Carlo simulation for the distribution of backscattered electrons in diamond at $E_0 = 5$ keV. The colours represent the electron energy.	168



Astronomical observations suggested that 10 to 20% of interstellar carbon exists in the form of diamond powders.^[1]

Chapter 1. Introduction

Natural diamond has been known since it was first mined *circa* 4000 BC in India. Its natural resources have been exploited since then as a gemstone material. In 2000 BC, the Chinese started to employ diamond as an industrial material owing to its extreme hardness. However, the use of natural diamond in science or engineering was limited due its scarcity and high cost, despite its unique properties. This was the driving force for the development of techniques to produce synthetic diamond.

1.1. Structure, Properties and Applications of Diamond

Diamond is one of the elemental forms of carbon, along with graphite, another carbon allotrope which can be found in nature. At room temperature and pressure, graphite is the thermodynamically stable allotrope of carbon (see section 1.2). Despite having the same elemental composition, graphite and diamond exhibit very different physical and mechanical properties. This is due to their different lattice arrangements. In graphite each carbon is covalently bonded to three nearest neighbours (sp^2 hybridized) forming a structure of layers weakly bonded by van der Waals forces. Conversely, the carbon atoms in diamond are arranged in a tetrahedral configuration (sp^3 hybridized) where each carbon atom in the lattice shares one of its outer four electrons with one from another carbon atom. Figure 1.1 shows the relative positions of carbon atoms in the diamond unit cell, consisting of a face-centred cubic lattice structure with a lattice constant $a_0 = 0.357$ nm.^[2] The minimum distance between neighbour atoms is $\sqrt{3/4} a_0$, although this value can vary slightly depending on the temperature and level of impurities. The diamond interatomic space is small when compared

with that in silicon and other semiconductor materials, which makes doping of diamond difficult to achieve.

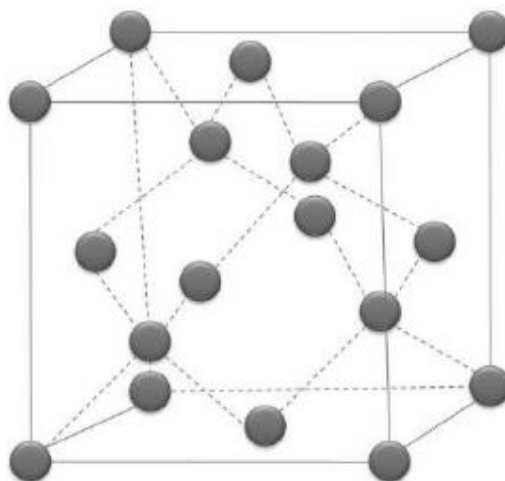


Figure 1.1- The unit cell of diamond showing a tetrahedral structure. The diamond structure can be defined as two interpenetrating face-centered-cubic lattices shifted along the body diagonal by $(1/4, 1/4, 1/4) \mathbf{a}_0$.^[2]

The tetrahedral arrangement of strong carbon-carbon single bonds is responsible for the diamond extreme hardness along with other remarkable properties (see Table 1.1). Diamond can be doped to form a semiconductor material. Owing to its wide band-gap and low surface electron affinity, diamond possesses excellent electron emission characteristics. This particular characteristic will be discussed in detail in section 1.8.8.

Table 1.1- Some of the outstanding properties of diamond.^[3]

Hardness	$1.0 \times 10^4 \text{ kg/mm}^2$
Young's modulus	1.22 GPa
Thermal expansion coefficient	$1.1 \times 10^{-6} \text{ K}^{-1}$
Thermal conductivity	20 W/cm.K
Electron mobility	$2200 \text{ cm}^2/\text{V.s}$
Hole mobility	$1600 \text{ cm}^2/\text{V.s}$
Band-gap	5.45 eV
Resistivity	$10^{13} - 10^{16} \text{ } \Omega \text{ cm}$
Chemical inertness and corrosion resistance	

Diamond films can be designed to suit different technological applications. The diversity of current applications and potential for innovative ones is so large that a complete compilation becomes too extensive and out of the scope of this work. Nonetheless, as an indication of

such variety, in Table 1.2 are highlighted some of the uses of diamond and a reference to authors involved in the respective field of research.

Table1.2- A few examples of the wide range of diamond applications.

Application	Author	Year
Radiation sensors	P. Bergonzo <i>et al.</i> ^[4]	2001
Cold cathodes	P.K. Baumann <i>et al.</i> ^[5]	2000
Biosensing	C.E. Nebel <i>et al.</i> ^[6]	2007
Bionics	A.E. Hadjinicolaou <i>et al.</i> ^[7]	2012
Micro-electromechanical systems (MEMS)	O. Auciello <i>et al.</i> ^[8,9]	2012
Electron multiplication	D.M. Trucchi <i>et al.</i> ^[10]	2006
Optical windows	R.A. Campos <i>et al.</i> ^[11]	2013
Cutting tools	X. Ding <i>et al.</i> ^[12]	2012
Electrodes	Y. Zhang <i>et al.</i> ^[13]	2013
Transistors /superconductors	Y. Takano <i>et al.</i> ^[14]	2009
Room temperature quantum computing	M.L. Markham <i>et al.</i> ^[15]	2011

Yater and co-workers at the Naval Research Laboratory in Washington have undertaken a great amount of research in the development of diamond current amplifiers^[16] motivated by the secondary electron emission characteristics of diamond. Her work will often be taken as a literature reference in this dissertation.

1.2. Deposition techniques of synthetic diamond

In the beginning of the 20th century it was believed that natural diamond had been made from carbon under high temperature and great pressure, a story to capture the imagination, as it was described by Bundy *et al.*^[17] At room temperature and atmospheric pressure diamond exists as a metastable phase of carbon, with graphite being the thermodynamically stable form in these

conditions (see Figure 1.2). The inter-conversion between the two phases under ambient conditions is prevented by a large activation barrier. Therefore, these particular characteristics make diamond rare and created the necessity to develop artificial methods to synthesize it.

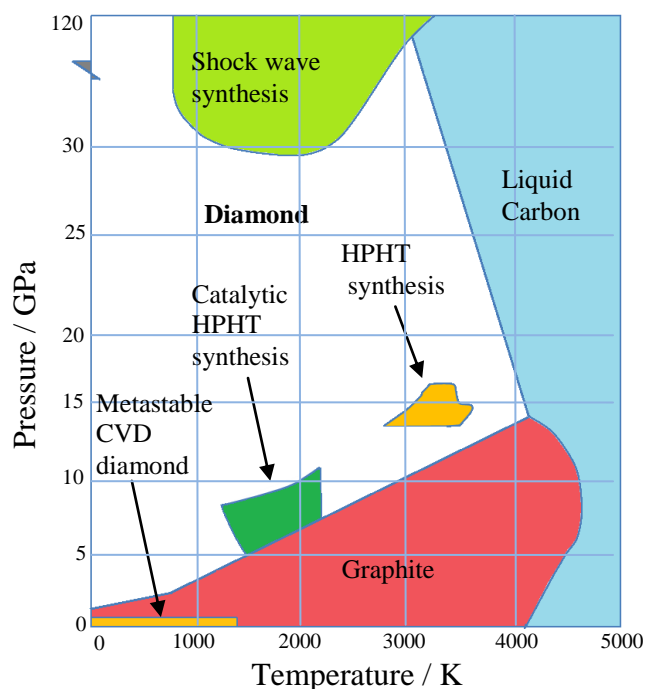


Figure 1.2- Pressure and temperature phase and reaction diagram for elemental carbon.^[18]

1.2.1. High Temperature High Pressure

The method for growth of artificial diamond called ‘high-pressure high-temperature’ (HPHT) was successfully developed by General Electric in the early 1950s, reproducing the conditions under which diamond is formed in nature. In this process, graphite and a catalyst transition-metal, usually Ni, Fe or Co powders, are mixed and then submitted to a high pressure in the range of 80 to 300 kbar and temperature in the order of 1900 to 3000 °C.^[17] HPHT diamond is produced in the form of solid crystals usually a few mm in size. They are often coloured yellow due to nitrogen impurities incorporated during growth. This generally makes them unsuitable for use as gemstones, but they are still used as abrasives and in cutting tools. The HPHT process presents a number of constraints, for instance, the growth rate limits the size of HPHT crystals to about 1 cm³.^[19]

To expand the use of diamond in terms of technological applications it was crucial to develop techniques which allowed the creation of diamond in functional forms such as thin films and produced at lower costs.

1.2.2. Chemical vapour deposition of diamond

The diamond synthesis by means of chemical vapour deposition (CVD) processes was discovered and initially reported in 1958 by Eversole^[20]. He used the thermal decomposition of carbon-containing gases under low pressures to grow diamond on top of natural diamond crystals heated at 900 °C. Those studies were followed by Deryagin *et al.*^[21] a decade later who achieved a substantial improvement in the growth rate. Soon after, Angus^[22] and his team made a decisive contribution in the field when they verified the preferential etching effect of graphite rather than diamond by the atomic-hydrogen present in the gas phase during the growth process.^[23] This was the crucial discovery that made growth of diamond by CVD a commercial possibility.

CVD involves a complex series of chemical reactions occurring in the gas phase above a sample surface, ultimately causing deposition of diamond onto that surface. Such reactions need an activation source of the carbon-containing precursor present in the gas phase, which can be achieved by thermal processes as in the case of hot-filament CVD (HFCVD) systems.^[24] Other reactors are based on microwave (MW) activated plasmas. MW-plasma CVD reactors work in similar conditions to the ones of HFCVD, although presenting a number of advantages namely in terms of growth rate. However, they are significantly more expensive than HFCVD reactors.

In addition to these methods there are other forms of plasma generation, such as direct current (DC) electrical discharge arc and radio-frequency (RF). Alternatively, some CVD reactors use combustion flames such as an oxyacetylene torch.^[25]

1.2.2.1. Hot-Filament CVD

In 1982 Matsumoto *et al.*^[26] in the National Institute of Research in Inorganic Materials (NIRIM) in Japan, introduced the concept of hot-filament (HF) activated CVD for diamond deposition. Presently, HF-activation of diluted hydrocarbon/H₂ gas mixture is a well established CVD process,^[27, 28] consisting of a simple and cost effective method to grow diamond at low pressures. A range of typical operating parameters for diamond deposition using HFCVD are listed in Table 1.3. In this process the filament imposes the maximum operation temperature. Hence, HFCVD runs at considerably lower gas activation

temperatures in comparison with plasma processes. Depending on the deposition conditions, the growth rates are generally low ($\sim 1\text{-}10 \mu\text{m h}^{-1}$) relative to those obtained with plasma activation. One of the advantages of HFCVD is the possibility to scale-up to larger deposition areas and complex shapes, limited by the reactor chamber dimensions.^[29]

Table 1.3- Range of typical operating parameters for diamond deposition using hot-filament CVD.^[27]

Parameter	Typical Range
Pressure	1 - 80 Torr
Substrate temperature	600 - 1200 °C
Filament temperature	2000 - 2600 °C
Filament distance to the surface	1 - 20 mm
Carbon sources	CH ₄ , C ₂ H _(x = 2,4,6) , CH ₃ OH and other alcohols, H ₂ CO

The filaments are normally made of tungsten, tantalum or rhenium. The first two metals have the advantage of being low cost materials. However, their life-time is limited due to their reaction with the carbon present in the CVD deposition atmosphere to form brittle carbide layers. Thus, the stability of HFCVD relies enormously on the filament performance. Another disadvantage is related to the diamond film contamination by metal impurities from the filament.^[30]

As the HFCVD system was used as the deposition apparatus for the diamond films studied in the aim of the present research, it will be discussed in greater detail in section 2.1.

1.2.2.2. Microwave plasma CVD

The first successful growth of diamond from MW-plasma discharge in CH₄/H₂ atmospheres was reported in 1983 by Kamo et al. at NIRIM in Japan.^[31] A common type of MW-plasma CVD reactor is the linear antenna type (see Figure 1.3), with excitation frequency usually of 2.45 GHz.^[32] These used to be called ASTEX-type reactors after the US company that originally designed and produced them, but they have since been taken over by the Japanese company Seki Technotron.

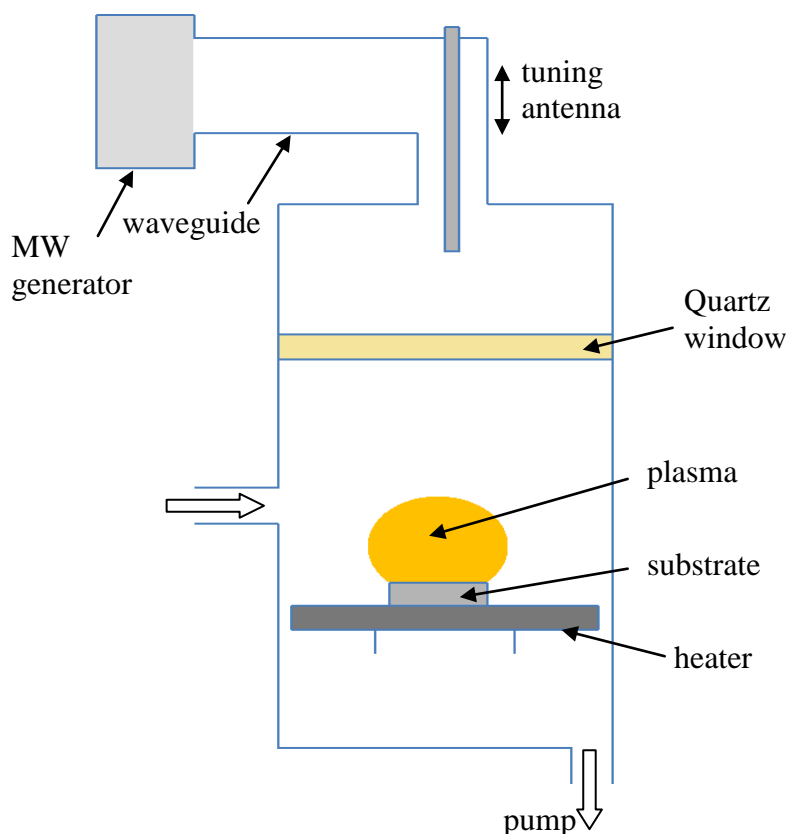


Figure 1.3- Schematics of a linear antenna-type MW-plasma CVD reactor.

Microwaves enter the chamber by means of an antenna and couple into the reactor chamber through a quartz window, transferring energy to the gas atmosphere igniting the plasma. High ionization fractions are generated by the collision from the electrons in the plasma and the atoms and molecules in the gas mixture. The gas temperature produced of 2000-3000K is a function of gas pressure and microwave power. MW-plasma CVD reactors can grow diamond at rates of up to several hundred μm per hour, depending upon growth conditions.

1.3. CVD diamond materials

CVD diamond films of different qualities, such as single crystal (SC) or monocrystalline, microcrystalline (MC), nanocrystalline (NC) and ultrananocrystalline (UNC) can be found commercially both as coatings on various substrate materials and as freestanding diamond layers. Depending on the nature of the application it is possible to select among those diamond film according to the desired functionalities, such as surface morphology, roughness

or surface conductivity, amongst others. A description of the main characteristics of the different diamond types is presented in the following sections.

1.3.1. Single-crystal diamond

Commercial SC diamond films can be purchased from a few suppliers although they are generally available as undoped diamond and have typically small areas $< 5 \times 5 \text{ mm}^2$. When compared with other diamond morphologies SC diamond contains the lowest sp^2 content making it suitable for electrochemical applications.^[33] Additionally, it can be obtained with very low surface roughness. The absence of grain boundaries in SC diamond samples promotes a minimum of structural defects.

1.3.2. Microcrystalline diamond

The morphology of CVD diamond films depends crucially on the different process parameters, especially the gas phase mixture. In the case of methane/hydrogen CVD atmospheres, for mixing ratios up to 2%, diamond films with a microcrystalline morphology are formed. One of the characteristics of this category of polycrystalline diamond films is that the surface roughness depends on the film thickness, which may be in the order of a few μm making it useless for applications where surface patterning at nanoscale is important. MC diamond films contain relatively low carbon sp^2 content which is mainly located at the grain boundaries.

1.3.3. Nanocrystalline diamond

Nanocrystalline diamond (NC) films grow in the presence of gas mixing ratios generally greater than 3% of methane/hydrogen. These films contain a higher content of carbon sp^2 than MC films, exhibiting a larger concentration of grain boundaries and lower surface roughness generally around 10-20 nm rms¹. The grain sizes of NC diamond films are typically between

¹ The root mean square (r.m.s) roughness is the root mean square average of the roughness profile coordinates.

10-500 nm. Grain sizes and film thicknesses as small as 30 nm and consequently, high boundary content films were reported by Williams *et al.*^[34]

Under the classification of NC films, are included two different categories: faceted-NC and non-faceted NC or “cauliflower” diamond, sometimes called ballas-like diamond. The differences in the microstructure have to do with the percentage of methane in the gas mixture. Cauliflower diamond tends to give rise to smoother films (r.m.s. a few nm) as the methane/hydrogen ratio increases. NC diamond can be effectively doped with boron.

Another class of diamond films characterized by grain sizes below 10 nm are the so-called UNC diamond films. These films have the largest sp^2 carbon content of all the diamond morphologies described in the sections above. CVD pure-phase UNCD films with grain sizes of 2 to 5 nm were successfully developed at Argonne National Laboratory in the United States in the late 1990s^[35] and commercialized by Advanced Diamond Technology, Inc. UNCD films are grown under argon-rich plasmas and have the advantage that they can be deposited at temperatures as low as 400 °C.^[36] They are also very smooth, but their high sp^2 carbon content means that their physical properties are often very inferior to that of other types of diamond film.

1.4. Mechanisms of diamond growth: gas-phase and surface chemistry

A large amount of research has been performed in the study of the gas-phase chemistry that occurs during the diamond CVD process. The vast majority of results are in accordance with the C-H-O diagram of CVD diamond, known as the Bachmann diagram^[37] (see figure 1.4). From studying many different types of diamond deposition conditions in different reactors, Bachmann concluded that diamond growth takes place in a well defined region regardless of deposition system or hydrocarbon precursor.

Once the gas phases mix inside the reactor chamber, they diffuse in the direction of the substrate surface. In their trajectory they cross the activation region, which can be originated by an electrically heated filament as in the case of HFCVD represented in Figure 1.5. This activation heats the gas to a high temperature of the order of a few thousand degrees Celsius, causing the molecules to dissociate into reactive radical species and generating atoms, ions and electrons. These reactive species continue mixing and experience a complex chain of chemical reactions (see figure 1.6) until they eventually hit the surface of the substrate.

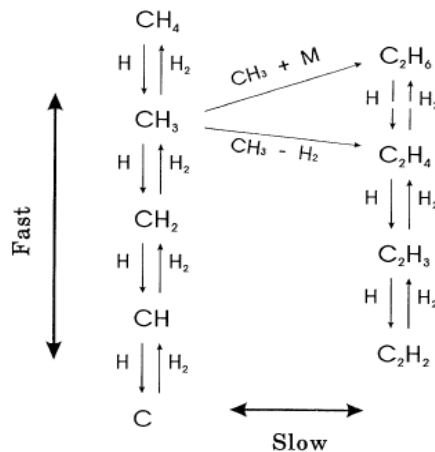


Figure 1.6- Illustration of the main gas-phase reactions occurring during the CVD diamond deposition process. The reactions correspond to the fast hydrogen transfer reactions with the interconversion between C₁ and C₂ hydrocarbon species.^[38]

On the diamond surface, atomic hydrogen abstracts an H from a surface C-H bond to form H₂, leaving behind surface radical sites. These sites are reactive and gas-phase species can adsorb onto these sites. Models of diamond growth try to describe the effects of addition of hydrocarbon radicals, namely CH₃, CH₂, CH and C atoms to both monoradical and biradical surface sites.^[40] Under typical CVD diamond growth conditions, the addition of CH₃ radicals to monoradical sites is the main growth mechanism, although it can also take place via CH₃ radicals addition to biradical sites.^[41]

A simplified version of the surface chemistry of CVD diamond growth is schematically represented in Figure 1.7. The mechanism of a series of reactions begins with the abstraction of a surface hydrogen (equation 1.1) atom creating thereby a reactive surface site:



where C_d symbolizes a surface radical.^[38]

This reaction may be followed by the addition of a hydrocarbon active radical as CH_3 (equation 1.2) or other species.



If the same process occurs at an adjacent lattice site, another CH_3 radical is then added.

A very frequent reaction is the recombination of the active site with a hydrogen atom (equation 1.3):



This competition between surface activation and hydrogen recombination defines the number of active sites for nucleation at the surface for determined reaction conditions.^[42]

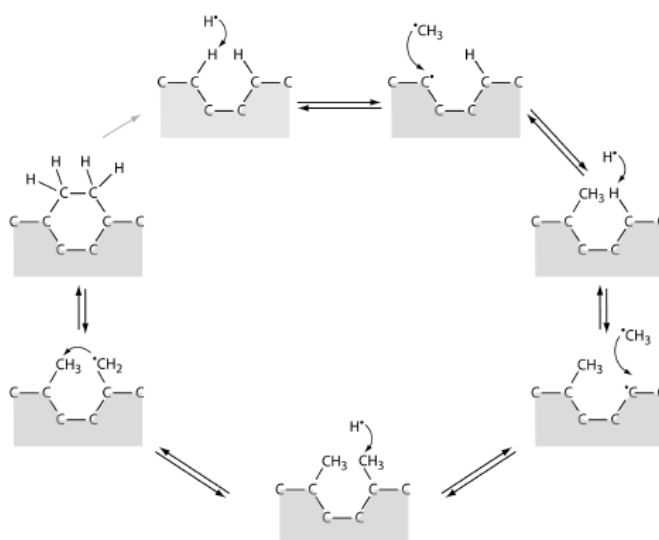


Figure 1.7- A simplified schematic diagram of the standard growth model occurring at a (100) diamond surface. Adapted from references.^[43, 39]

The model is rather simplistic thus introducing a number of errors when ignoring for instance, surface migration or addition to different lattice sites, although it represents well the standard growth mechanism occurring at a (100) diamond surface.

As the isolated crystallites resulting from the nucleation process start to grow, they start to develop facets. The growth of a specific texture may be explained as a evolutionary selection of crystallite orientations, according to Van der Drift modulations.^[44] Under typical growing CVD parameters, the morphology can be estimated from the growth parameter α defined as:

$$\alpha = \sqrt{3} \frac{V_{100}}{V_{111}} \quad (1.4)$$

where V_{100} and V_{111} are the growth rates of the (100) and (111) surfaces, respectively.^[45] The parameter α determines the crystal orientation and twinning in polycrystalline films.

1.4.2. Importance of Atomic hydrogen

The role played by atomic hydrogen in the gas-phase mixture is important for diamond film quality and growth rate. Diamond growth is due to sufficient production of atomic hydrogen as an etchant of non-diamond carbon phase at the growing surface. Atomic hydrogen etches graphite around 20 to 30 times faster than diamond, which results in a fast removal of the non-diamond phases from the growing surface. Hence, only the diamond clusters are able to survive to the etching process and grow.^[46] If the substrate temperature is below 400 °C the etching rate becomes insufficient for the same carbon precursor concentration and as such, the growth rate needs to be reduced. Several methods have been attempted to this end, such as reducing carbon source concentration.^[47] Another technique, has been the incorporation of oxygen in the gas-phase mixture for diamond growth at low temperatures.^[48] Common oxygen containing gas sources are CO, CO₂ and CH₃OH.^[49-51]

1.5. Defects and doping of diamond

Pure diamond is a good insulator material having a wide band gap of 5.45 eV but when doped with boron becomes a p-type semiconductor, and depending on the doping level, can present electrical conductivity ranging from insulating to near metallic values.^[52]

The extremely compact diamond lattice makes the process of doping difficult, because the space for substitutional impurities is reduced. Therefore just a few dopant species can be incorporated in as-grown diamond, namely B, N, Si, P, Ni, Li, Na and S.^[53, 54] In most cases problems arise from the low solubility of the dopant atom or the position of the donor or acceptor energy levels, which are often too deep or too shallow to make effective semiconductor devices. B is the most common impurity added to CVD gas mixtures during the diamond growth to produce p-type diamond films.

1.5.1. n-type doping

Donor doping is still a matter of much research. Nitrogen and phosphorus have been the source of numerous investigations as dopants for diamond. Nitrogen forms a deep donor level in diamond at 1.7 eV^[55] with an ionisation energy too large to be electrically active.^[56] In addition, nitrogen has a maximum solubility of 10^{18} cm^{-3} which is too low for effective doping and cannot be activated at room temperature.

Phosphorus forms a donor level between 0.57 eV and 0.62 eV^[42, 57, 58] and presents a maximum solubility around $5 \times 10^{19} \text{ cm}^{-3}$.^[59] Again, this solubility is too low and the donor level too deep for effective semiconductor performance. N-type diamond is an insulator at room temperature. Nevertheless some simple p-n devices have been fabricated in diamond in this way.

1.5.2. p-type doping

The addition of boron to the diamond lattice leads to the creation of an extrinsic p-type semiconductor material. Because boron has one fewer electrons than carbon, one boron atom incorporated into the diamond lattice corresponds to one free hole carrier, creating an acceptor level with an activation energy at 0.37 eV above the valence band. This is verified

when boron is present at low concentrations in the region of $\sim 10^{17} \text{ cm}^{-3}$. The activation energy corresponds to the energy necessary for the dopant ionisation. At higher boron contents in the range of 10^{19} - 10^{21} cm^{-3} , boron centres interact and form an impurity band that moves towards the valence band as the boron content increases. The solubility of boron into the diamond lattice is above 10^{21} cm^{-3} .^[60]

The resistivity of pure diamond can be over $10^{16} \Omega \text{ cm}$ at room temperature. Such high insulating characteristics are related with the very low concentration of intrinsic carriers at room temperature, due to its wide band gap. For sufficiently high boron contents the activation energy is virtually zero and the diamond acquires metallic type conductivity. At boron concentrations above 10^{21} cm^{-3} diamond can exhibit a resistivity in the region of $10^{-3} \Omega \text{ cm}$ at room temperature.^[59]

Despite its effectiveness for diamond doping the incorporation of boron into the diamond lattice presents a mismatch that can cause significant stresses and lattice distortion especially for high doping levels. This is due to the difference in radius between carbon and boron atoms.^[61, 62]

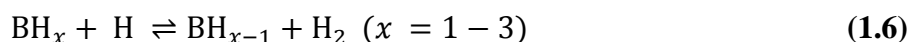
1.5.3. Boron incorporation into diamond

In section 1.4.1 a description of the main reactions taking place in a CH_4/H_2 gas phase mixture under CVD diamond deposition conditions was given. Given the relevance of B-doping in this research, a brief discussion follows, of the chemistry associated with a $\text{CH}_4/\text{H}_2/\text{B}_2\text{H}_6$ deposition atmosphere. B_2H_6 is the most commonly used gas source of B for the growth of B-doped diamond films. For safety reasons, considering that it is a poisonous and highly explosive gas, diborane is used in diluted solutions in H_2 of a few hundred ppm at most.

When this $\text{B}_2\text{H}_6/\text{H}_2$ mixture is added to the system during CVD diamond deposition, the thermal decomposition of B_2H_6 proceeds according to equation 1.5, where M is a third-body such as B_2H_6 , C_2H_2 , H_2 and CH_4 .^[63] From here, there is formation of a series of BH_x ($x = 1 - 3$) active radicals (equation 1.6), which undergo fast H-shifting reactions, defined according to equations 1.7 to 1.9.^[64] This process is followed by the addition of BH_x species to surface radical sites. It was found that B and BH_3 are the most abundant BH_x species near the growing diamond surface.^[65]



Thus, some of these species will be incorporated into the growing surface through a complex series of reactions. As in the case of carbon, boron incorporation occurs by a similar ring expansion mechanism, and by direct insertion of surface-bound B species into the C–C bond on the diamond surface.^[64]



As-grown diamond films revealed up to one order of magnitude higher preference for B incorporation in (111) facets rather than in (100).^[56, 62] Moreover, the B atoms in CVD diamond, will preferentially occupy substitutional sites in the diamond lattice.

1.6. The substrate material

1.6.1. Homoepitaxial growth

According to the mechanism of diamond growth detailed in section 1.4, diamond starts to grow on a surface when a carbon atom is added to the surface in a configuration suitable for the construction of a sp^3 tetrahedral lattice. When growing diamond on top of a diamond substrate, the process is simply the extension of the substrate diamond lattice atom-by-atom.^[25]

1.6.2. Heteroepitaxial growth

A material frequently used as a substrate for diamond growth is silicon (Si), due to its low cost, availability and properties, although a variety of other materials are also used. The substrate material characteristics are crucial for the success of diamond growth with a number of requirements to satisfy.

Despite recent studies on diamond deposition at low temperatures^[66], the melting point of the substrate material remains a limiting factor in the use of CVD diamond coatings in some microelectronic applications, where the substrate materials are essentially polymeric. Although, recent studies have shown the growth of UNCD films at temperatures as low as 350 °C.^[9,67-69] Additionally, a mismatch in thermal expansion coefficients between diamond and substrate may lead to the film cracking and further delamination during the cooling down process due to the compressive stresses created in the film. Thus, substrates with high thermal expansion coefficient are not ideally suited for diamond growth. Nevertheless, the use of an interlayer material between substrate and diamond has proved to improve the adhesion.^[70] An additional aspect to take into consideration in matters of adhesion of the grown diamond films is how the substrate reacts with carbon from the CVD gas-phase, especially during the first stages of the deposition cycle.

Substrates for diamond coating can be divided in three main categories: highly soluble, with little solubility and carbide forming materials.^[39] There are some substrates into which carbon has a high solubility, such as iron (Fe), titanium (Ti), nickel (Ni), platinum (Pt) and palladium (Pd). The high carbon incorporation into the substrate has two negative effects: it hampers the formation of a nucleation layer for diamond at the surface and by absorbing all the carbon striking the surface to form a thick carbide material, and the intrinsic properties of the substrate are modified. Certain materials present a very limited reactivity with carbon such as copper (Cu), iridium (Ir), silver (Ag), tin (Sn), sapphire or alumina. Therefore, in the absence of a carbide layer any grown diamond layer will have a poor adhesion to the substrate and will ultimately delaminate. Hence, such materials can successfully be used as substrates to produce free-standing diamond films. Materials like Si, molybdenum (Mo), and tantalum (Ta), tungsten (W), chromium (Cr), cobalt (Co) niobium (Nb) and quartz are carbide forming. Thus, during the first stages of diamond growth they form only a thin carbide interfacial layer between the substrate surface and the growing diamond film, enhancing the nucleation and the adhesion of the diamond films.

1.7. Nucleation methods: substrate pre-treatment

Without any substrate pre-treatment prior to diamond growth, the nucleation density achieved on a substrate is very low. For instance, on a clean Si surface it is less than 10^5 cm^{-2} . The techniques to enhance the diamond nucleation for heteroepitaxial growth are diverse.

Abrasive treatments have been widely used due to their simplicity, effectiveness and low cost. Nevertheless, for some applications such as in electronics the scratching can contaminate or damage the substrate which makes the method inappropriate.

1.7.1. Manual scratching

Manual abrasion or scratching is a simple abrasive method by which the substrate material is scratched with diamond powder or paste prior to the deposition process. The nucleation of diamond crystallites will be favourable on the surface defects created.^[38] In addition, any remaining residual diamond particles from the abrasive will contribute positively to the nucleation process. Although diamond powders are most commonly used, other particles have been used for pre-treatment of non-diamond substrates with relative success, namely silicon carbide (SiC), cubic boron nitride (CBN), stainless steel (SS) and non-diamond carbon powders.^[48,71-73] The nucleation density was verified to increase with the decrease in abrasive grain size.^[74]

1.7.2. Ultrasonic seeding

This is a highly reproducible abrasive method, where the samples to be seeded are immersed in a suspension of diamond particles in an appropriate liquid medium and are submitted to ultrasonic agitation in an ultrasonic bath or by means of a sonicator. After removal from the bath, the diamond seeds stick to the surface by electrostatic or van der Waals forces. If it is done carefully using nanodiamond of size 3-5 nm, a near monolayer of diamond seeds can be produced giving extremely high nucleation densities.

1.7.3. Electrospray deposition seeding

The method involves the electrostatic-spraying of highly ionized droplets of a suspension containing diamond nanoparticles onto a substrate creating a dispersion of diamond seeds at the surface. This electrospray deposition (ESD) seeding method was developed in the Diamond group at the University of Bristol^[75] and will be presented in further detail in section 2.2.1.

1.7.4. Bias-enhanced nucleation (BEN)

The so-called bias-enhanced nucleation (BEN)^[76] is a pre-treatment method which consists of negatively biasing the substrate relatively to the ground. In general terms, a negative DC-bias around 100 to 250 V is applied to the substrate at the same time that the methane concentration in the CVD gas mixture is increased, normally to 4-10% in hydrogen.^[76, 77]

Typical pressures are in the range of 30-100 Torr. Obviously, the exact parameters used depend on the specific plasma conditions and apparatus. The negative biasing of the substrate promotes a high flux of hydrocarbon ions towards the substrate surface, which implant just below the surface and form a saturated carbon solid solution. The implanted carbon atoms receive a thermal energy spike from new incoming ions, and this enables them to register with the underlying Si lattice into an ordered layer. Subsequent growth on this layer produces films which are epitaxially registered to the Si lattice allowing near single-crystal diamond to be grown over areas of nearly a centimetre.

One of the advantages of this method is the reduced damage to the substrate surface when compared to scratching techniques. With BEN, nucleation densities of 10^9 - 10^{11} cm⁻² have been obtained on silicon substrates with good reproducibility.

1.8. Electron emission from solids

Electron emission is a fundamental phenomenon associated with most interactions of energetic particles with solid surfaces, extremely important in areas such as radiation biology^[78], particle detectors^[4], microscopy and surface analysis.^[79]

The electron emission mechanism can be induced by a diversity of physical processes, depending on the source of kinetic energy supplied to the electrons.^[80] When the emission of electrons from a sample surface into the vacuum is made under the action of a high

electrostatic field, the process is called field emission, also known as the Fowler-Nordheim tunnelling effect.^[81] If the surface is irradiated with light in the visible or ultraviolet (UV) region, the phenomenon is defined as photoelectric emission.^[82] If the emission is promoted by heat applied to the solid, is a thermionic emission process.^[83] When the electron emission is induced by accelerated particles as ions or electrons, the process is called electron-induced (EIEE) or ion-induced electron emission (IIEE).^[84]

To contextualize this section, the energy of the electrons within the solid, usually represented by a potential or band diagram, will be described. The solid can be considered to act as a potential ‘well’^[85] from which the electrons are prevented from escaping. This is because, in the absence of an external energy supply, they do not possess enough energy to overcome the potential barrier between the solid surface and the vacuum.

As well as the surface barrier, it is necessary to distinguish between the energy of electrons in metals, semiconductors and insulators. The conductivity of a solid depends upon the distribution of electrons in the allowed energy bands. Figures 1.8a-c illustrate the characteristic band structures for metals, insulators and intrinsic semiconductors. In metals, valence electrons can move freely through the lattice and form a ‘cloud’ of electrons responsible for the conduction in the presence of an electric field. In contrast, in insulators all the electrons are contained in filled bands thus there are no free electrons for conduction. The band-gap (E_g) in these materials may be as large as 12 eV.^[86] Semiconductor materials present intermediate characteristics, with a small number of free electrons for conduction. With $E_g \sim 1$ eV, the electrons can jump across the band-gap due to thermal activation, and the conduction occurs due to holes and electrons. Figures 1.8d) and e) represent the band structures for extrinsic p-type and n-type semiconductors, respectively, which are produced as the result of the addition of trace impurities through a doping process. Example of this includes p-type and n-type semiconducting diamond, as introduced in section 1.5. Adding trivalent impurities like B or other Group III elements to a carbon lattice creates holes due to the deficiency of valence electrons, forming an acceptor level (E_a) of holes and promoting the conduction.

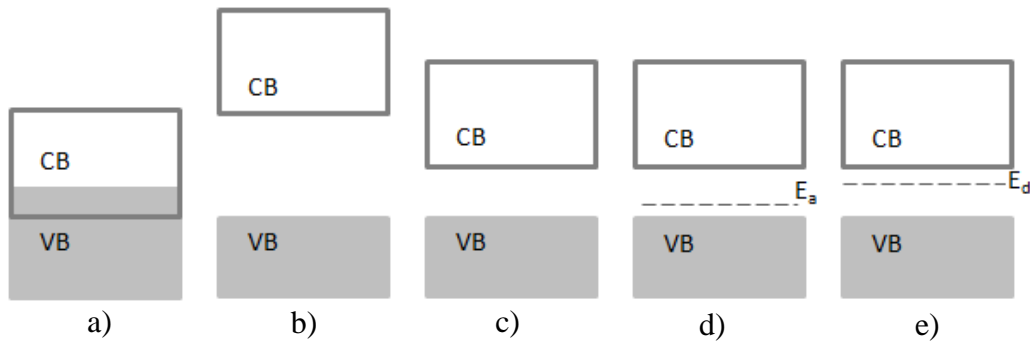


Figure 1.8- Schematics of the energy-band diagrams showing (a) the overlap between the valence band (VB) and the conduction band (CB) in metals, (b) the large energy gap (E_g) in insulators, (c) the smaller gap in intrinsic semiconductor materials, (d) an extrinsic p-type semiconductor, with an additional acceptor level (E_a) lying just above VB and (e) an n-type semiconductor with its donor level (E_d) lying just below the CB.

Alternatively, the addition of pentavalent elements such as N, P or other Group V elements, introduces extra electrons for conduction and a donor level (E_d) is formed, reducing the effective band-gap and allowing conductivity.

1.8.1. The Secondary Electron Emission process

Electron emission has attracted the attention of scientists for more than a century. In 1902 Austin and Starke^[87] observed that under certain conditions more electrons were emitted from a metal surface than the incident number, indicating the liberation of electrons from the solid when bombarded with primary electrons. This marked the discovery of the secondary electron emission (SEE) phenomenon.

The phenomenon of emission of slow electrons induced by electron bombardment is still not quantitatively well understood. Various aspects make the quantitative interpretation of secondary electron spectra rather complex. Even if in practice, the true secondary electrons are defined as the electrons emitted from the sample having energy below 50 eV, in reality there are no experiments capable of distinguishing between a true secondary electron and a backscattered primary electron. Despite some secondary electrons leaving the sample with energies higher than 50 eV and a number of backscattered electrons exiting with less than this energy, those numbers are considered to be small. Thus, 50 eV was defined as a reasonable threshold to classify the true secondary electrons emitted from a sample.^[88]

There is a large variety of mechanisms by which incident electrons of energy E_0 , may lose their energy when interacting with a solid. Although being common to use the designation “secondary electrons” to refer to all electrons emitted by the surface and collected by a positively biased collector, a distinction between them has to be made. Hence, secondary electrons can be categorized into three groups, according to the loss of energy they suffer during the scattering process:

- Elastically reflected
- Inelastically reflected
- “True” secondary electrons

Elastically and inelastically reflected electrons are defined as backscattered electrons. The true secondary electrons have, as defined above, energy less than 50 eV and are the result of a cascade process of electron interactions in the solid.

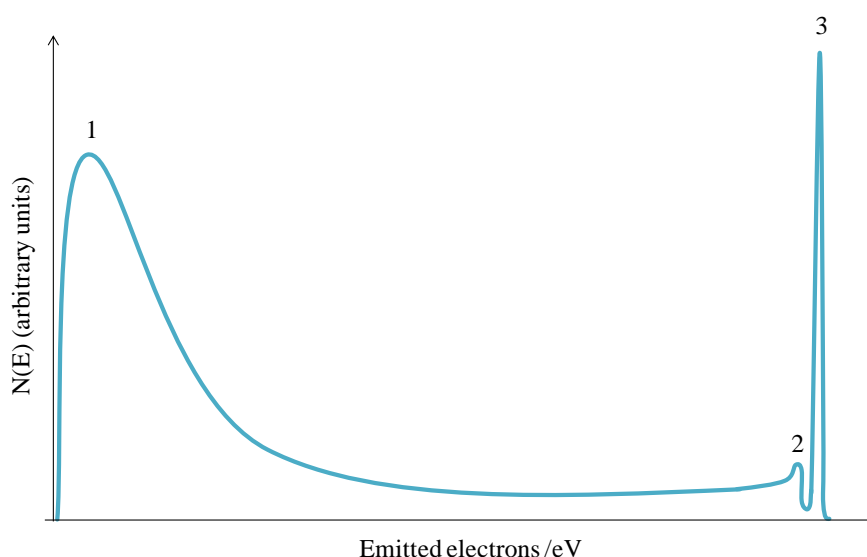


Figure 1.9- Schematic illustration of the spectrum of emitted electrons from a surface generated by a primary electron beam of energy E_0 .^[89]

The spectrum of electrons emerging from a solid surface as a function the emitted electron energy is schematically illustrated in figure 1.9. Peak 1 represents the true secondary electron emission cascade maximum, the intensity of which increases with E_0 but the position of which is nearly independent of E_0 . For instance, experiments on diamond have shown that while the peak intensity increases with E_0 , the position and width remain practically invariable. This feature was verified experimentally for primary energies ranging from 50 eV to 3 kV.^[90] The flat region in the chart consists of a mixture of the contribution of true secondaries and

inelastically backscattered electrons. Peak 2 represents the inelastically backscattered electrons, which correspond to the primaries that penetrate the solid and lose some of their energy by a process of excitation of the lattice electrons into higher energy levels. Inelastically reflected electrons are predominant at high primary energies. Peak 3 correspond to the fraction of primaries that are elastically scattered by the surface, undergoing a single collision and therefore with $E = E_0$. This type of reflection is predominant at primary energies below 200 eV once the primary electrons energy is insufficient to penetrate the surface. The ratio between inelastically and elastically backscattered electrons is independent of the primary energy.^[89] The proportion of backscattered electrons is typically around 20%, although it depends on the material.^[91]

1.8.2. The Secondary Electron Emission Yield

The process of secondary electron emission is generally interpreted as a three-step phenomenon, with different contributions:^[82]

- the generation of secondary electrons;
- transport or diffusion of secondaries through the solid;
- emission of the secondary electrons into the vacuum.

To understand the process of generation of the secondary electrons it is necessary to consider the mechanisms by which the primary electron beam interacts with the solid and transfers the energy required to create a secondary electron. Such mechanisms comprise single-particle excitations by electron-electron scattering and ionization of core levels, amongst others. The material band structure also influences the excitation mechanisms.

During their trajectory towards the target surface, electrons undergo a series of collisions with other electrons in the solid in a process of multi-scattering events. Thus, the energy that is transferred to an electron in a primary event is shared by other electrons. Each primary electron can originate more than one secondary and providing they are sufficiently energetic, these secondaries can excite other electrons by means of a cascade generation process. Seah and Dench^[92] estimated that for metals and semiconductors the mean free path would be between 5 Å and 20 Å for electrons with energies up to a few hundred eV, and significantly larger for insulators. After diffusing through the solid, the electrons thermalize to the bottom of the conduction band. At this stage, the emission of electrons depends only on the ability of the low energy electrons to overcome the energy barrier present at the surface.

The whole process can be simply described as the transformation of a high-voltage, low-current electron beam into a low-voltage, high-current secondary beam. Therefore, the secondary electron emission (SEE) yield δ , is generally defined as the ratio of the number of emitted electrons or total emitted secondary electron current I_t , to the number of incident electrons or primary electron current I_0 , as:

$$\delta = \frac{I_t}{I_0} \quad (1.10)$$

According to the definition above, δ includes all the categories of emitted electrons described in section 1.8.1. Consequently, the expression describes the total yield because all backscattered electrons are included in I_t .

The most frequent way to analyse the SEE process from a solid under the action of a primary electron beam is by representing the variation of δ with the beam energy. This relation presents a typical bell-shaped curve, as presented in figure 1.10, with three characteristic parameters: two cross-over energies E_I and E_{II} at which δ equals unity, and a maximum yield δ_m at an energy E_m .

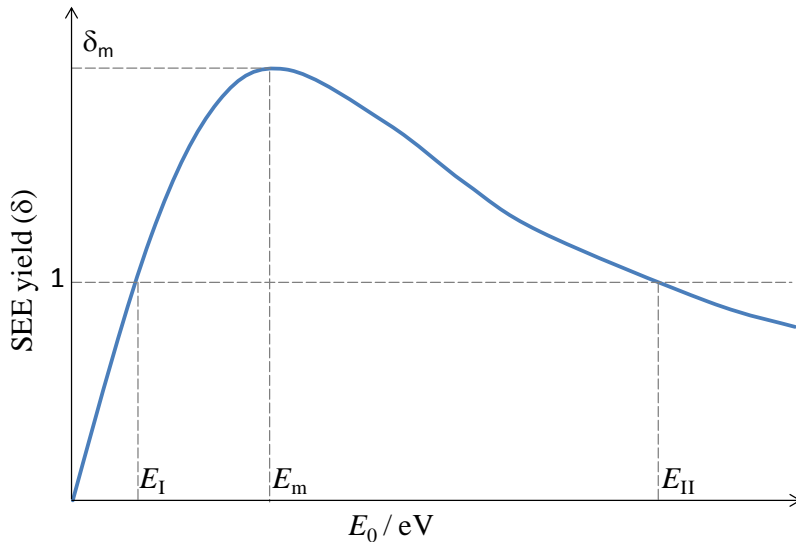


Figure 1.10- Schematic illustration for the variation of SEE yield with primary electron beam of energy E_0 .^[85]

The yield curves contain fundamental information on the electron transport characteristics of the material under measurement. The shape of the curve reflects the relation between the penetration depth of the primary electrons and the escape depth of the internal secondary electrons. The net current of a solid being bombarded by energetic electrons can be zero if the

number of incident electrons and the electrons being emitted is the same in which case $\delta = 1$. At E_I and E_{II} the net current is zero.^[93] The location of E_I and E_{II} depends on the material, angle of incidence of the primary beam and surface roughness.

As the primary energy increases, the number of secondary electrons generated increases. For $E < E_I$ the primaries are not energetic enough to penetrate the surface and simply reflect back. For $E_I < E < E_m$ the increase of δ is justified by the fact that the penetration depth of the primary electrons is shorter than the escape depth of the secondaries. The penetration depth of the primary electrons and therefore the depth at which the secondary electrons are generated increases proportionally to the primary energy. At $E = E_m$ the penetration depth becomes equivalent to the escape depth. When $E > E_m$ the secondaries are generated so deep in the material that many lose their energy by absorption before reaching the surface. Hence, just a few electrons arrive at the surface with energy enough to overcome the surface barrier. Thus, for $E < E_m$ the penetration depth of the primaries is the controlling factor whereas for $E > E_m$ the escape depth of the generated electrons prevails.

1.8.3. Theoretical models

A number of theories have been developed to explain the SEE mechanism from solids. The proposed early models (1948-1991) were subject of review, namely by McKay^[94], Dekker^[95], Devooght^[96], Schou^[97] and M. Rösler.^[98] Overall, the theories were able to give a good prediction of the secondary emission yield as a function of beam energy and the energy distribution of the secondary electrons emitted, in good agreement with experimental observations. However, some of the simplifications in the earlier models were not completely justified.^[96]

Some of the researchers who contributed importantly to the evolution of the classical theories were Bruining (1954)^[89], Lye and Dekker (1957)^[95] and Dionne (1973,75).^[99, 100] A detailed explanation of the theories, their assumptions and simplifications would be excessively extensive and out of the scope of this study. For that reason, in this section only a brief overview of the theory developed by Lye and Dekker will be given, which illustrates the fundamental principles of SEE process. The authors developed an elementary theory for the secondary electron emission phenomena. Their model is an extension of the universal law derived by Bruining^[89] and is the basis of most of the recent numerical treatments.

As detailed in section 1.8.1, the secondary electron emission is generally understood as a three-step process: the impact of primary electrons and generation of internal secondaries, the transport of the secondaries towards the surface and finally, their escape through the vacuum barrier and emission into vacuum. The SEE yield, δ is proportional to the number of secondaries generated as a function of the generation depth. With this principle in mind, Lye and Dekker calculated the secondary electron emission yield as follows:

$$\delta = \int_0^{\infty} N(x, E) f(x) dx \quad (1.11)$$

where $N(x, E)dx$ represents the generation process occurring in a layer of thickness dx , *i.e.*, the number of internal secondaries produced by a primary electron with energy E at a depth x . The term $f(x)$ symbolizes the escape probability of the secondaries and is an exponential function of x , according to the following expression:

$$f(x) = B e^{-x/\lambda} \quad (1.12)$$

with λ equal to the mean escape depth and B a constant < 1 . In their diffusion through the solid, electrons are assumed to follow straight paths, transferring energy and therefore slowing down by a process of collisions with electrons and ions with the generation of internal secondaries. This process of energy loss is then described by the power law (stopping power) represented by equation 1.13,

$$-\frac{dE}{dx} = \frac{A}{E^n(x)} \quad (1.13)$$

where E is the energy of a primary electron at a depth x , A is an arbitrary constant proportional to the density of the material and n is a fitting parameter determined through the reduced yield curves (described below). A was found to be material independent and equal to $0.35^{[95, 102]}$ over a range of experimental primary energies between 300 eV and 7 keV.^[103]

The number of generated secondaries $N(x)$, created in the layer dx is considered to be equivalent to the energy loss dE , in the layer, divided by the average excitation energy ϵ required to produce a secondary electron. Thus,

$$N(x)dx = -\frac{dE}{\epsilon} \quad (1.14)$$

Jenkins and Trodden^[85] transformed equation 1.14 into equation 1.15, where R corresponds to the maximum penetration depth as defined in equation 1.16 and is directly proportional to the initial energy of the primary electrons E_0 .

$$N(x) = \left(\frac{A}{2}\right)^{\frac{1}{n+1}} \frac{1}{\epsilon(R-x)^{\frac{n}{n+1}}} \quad (1.15)$$

$$R = \frac{E_0^{n+1}}{(n+1)A} \quad (1.16)$$

This proportionality can be observed by sketching the variation of the production rate of internal secondaries as a function of the straight line distance along the primary electron trajectory, as mentioned above (see figure 1.11). The shape of the curve indicates that at high primary energies, electrons have a short interaction time with the lattice electrons and $N(x)$ is small. As the primaries lose their energy, the interaction time increases and so does $N(x)$, but the internal secondaries are generated deeper into the solid.

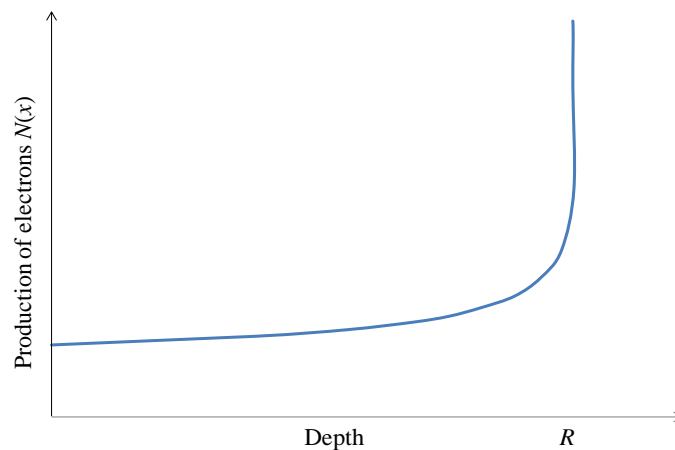


Figure 1.11- Plot showing the relation between the penetration depth (R) of the primary electrons through the solid and the production rate of secondaries ($N(x)$). The escape depth of the internal secondary electrons is normally described by an exponential decay law.^[103]

As mentioned in section 1.8.1, the penetration depth of the primaries increases with E_0 , whereas the escape depth of the internal secondaries generated is independent of E_0 , depending only on the sample properties, such as crystal structure, impurities or concentration of defects. The secondary electrons are scattered and a fraction is lost by absorption within the material before they reach the surface.

In 1948, McKay^[94] observed that the maximum yield δ_m was proportional to the work function ϕ , which seemed rather surprising since this would correspond to an increased surface barrier for emission. However, in 1950, Barroody^[101] showed that the proportionality of δ_m with $\phi^{1/2}$ arose as result of the generation process of the secondary electrons. Nevertheless, Jenkins and Trodden neglected the effect of the surface barrier on the emission of secondaries and the impact on the yield.^[85] Surface effects moderate the intensity of the yield curve but not the variation of δ with primary energy.^[88]

Barroody^[101] and Jonker^[104] were the first to indicate based on theoretical considerations, that it would be possible to determine a reduced yield curve for δ/δ_m versus E/E_m independent of the material under analysis. Several other authors have observed the same effect, *i.e.* the similarity in the shape of yield curves for arbitrary materials.^[79, 82, 95, 100-105] Lin and Joy^[106] presented an analytical expression (“The universal curve”) which describes the phenomenon of SEE through the following relation:

$$\frac{\delta}{\delta_m} = 1.28 \left(\frac{E_0}{E_m}\right)^{-0.67} \left[1 - \exp \left\{ -1.614 \left(\frac{E_0}{E_m}\right)^{1.67} \right\} \right] \quad (1.17)$$

where δ_m and E_m represent the material dependent parameters.

Normally there are significant variations reported in the literature for the yields measured at a given primary energy, due to differences in the sample preparation methods, experimental setups or other factors. Thus, equation 1.17 can be useful to fit all those values and extract the best estimate for δ versus E_0 .

1.8.4. Surface Electron Affinity

The electron affinity (χ) is defined as the difference in energies between the vacuum level and the conduction band minimum.^[5] In other words, χ is equivalent to the energy barrier that an electron at the bottom of the conduction band has to overcome in order to be emitted into vacuum. Figure 1.12a shows a typical scheme of a semiconductor surface, where the vacuum level lies above the conduction band minimum and therefore $\chi > 0$ preventing the escape of low-energy electrons. Such a condition is generally identified as a positive electron affinity (PEA) surface. In contrast, a negative electron affinity (NEA) surface condition is established when the bulk of the conduction band lies above the vacuum level, as seen figure 1.12c, so-called *true* NEA.^[107]

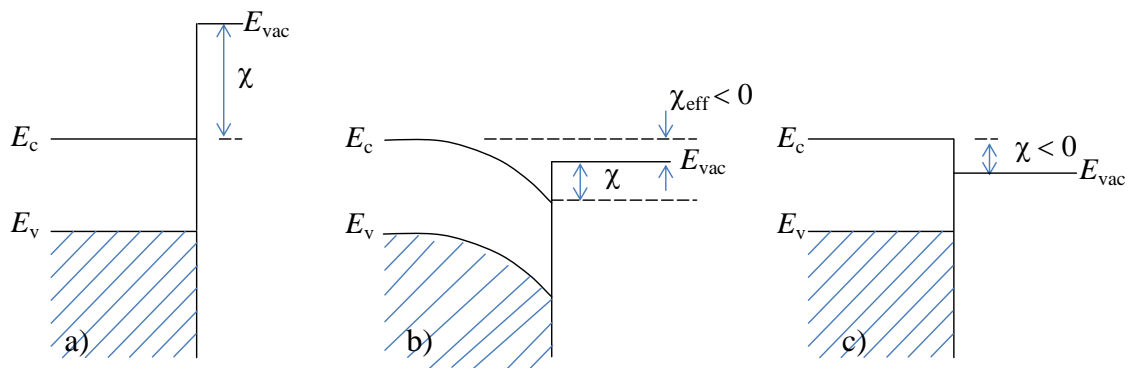


Figure 1.12- Illustration of the energy band diagrams of a semiconductor showing (a) positive electron affinity and (b) effective negative electron affinity, and (c) true negative electron affinity.^[109]

In NEA conditions, electrons thermalized to the conduction band minimum of a semiconductor can simply diffuse through the surface region and into the vacuum. When conduction band electrons encounter the surface, they can be emitted into vacuum, acquiring an energy equivalent to the difference between the energy of their final conduction band state and the vacuum level.^[110] In practice, the criterion for NEA is that the work function (ϕ) is smaller than the bandgap, where ϕ is then defined as the energy needed to move an electron from the Fermi level to the vacuum energy level.^[111] Generally for insulators and semiconductors the electron affinity is used, whereas for metals the work function is used.^[112] *True* NEA is not found for conventional semiconductors. However, it may be achieved after heavy p-doping together with surface functionalization by a highly polarising adsorbed layer, such as caesium or caesium oxide.^[108] Such adsorbed species are deposited as ions to form a monolayer, creating a surface dipole which reduces χ . At the same time, the heavy p-doping

promotes a short (~ 10 nm) characteristic band-bending at the surface. Those two conditions together create a so-called *effective* NEA surface (see figure 1.12b).

Both types of NEA surfaces create the right conditions for the emission of the low-energy electrons by removing the vacuum barrier. Therefore, in the following sections of this study whether the surface has true or effective NEA will not be specified explicitly, and it will be generally referred to as simply NEA.

Studies of caesium on oxygen-terminated and hydrogen-terminated diamond have shown *true* NEA surfaces.^[108, 113-115] The impact of NEA on the electron emission properties of diamond and the conditions in which such surface conditions are achieved will be discussed in section 1.8.8.1.

1.8.5. SEE from metals

The energy loss mechanism for the internal secondary electrons in metals is governed by their interaction with conduction electrons, lattice vibrations and defects. In metals, the work function produces a large minimum escape energy (~ 10 eV)^[103] which prevents electrons from being emitted from the surface into the vacuum. In addition, there is a high collision probability arising from the large number of conduction electrons in metals, leading to the secondary electrons having small escape depths of approximately 1 nm.^[79] Thus, metallic materials present small SEE yields generally close to unity, although the values of E_m and δ_m depend on the metal.

1.8.6. SEE from insulators

When an insulator material is bombarded with an electron beam there is a dynamic competition between two effects: an induced negative charge due to the trapping of a fraction of the incident electrons, and conversely, an induced positive charging caused by the emission of secondary electrons. These competing effects can produce a surface potential. Several authors have suggested that electron-hole recombination processes may also significantly affect electron emission leading to a significant decrease of the yield values.^[116] Despite these effects, insulator materials generally exhibit high secondary electron yields.^[95] This can be linked to their characteristic large band-gap, which prevents the secondary electrons from

losing energy through electron-electron collisions, resulting in a large escape depth for the low-energy secondary electrons. The internal secondary electrons lose energy by the excitation of valence electrons into the conduction band.^[103]

The mean free path of secondary electrons in metals is smaller than that in insulators. Thus, the escape depth and the SEE yield will be smaller for metals.^[117] Conversely, metals have a larger work function than insulators, which translates into a greater number of low energy electrons being able to overcome the surface barrier ~ 1 eV for insulators. These effects increase the total yield, shifting the curve maximum to lower energies.^[84]

To overcome some of the negative effects that can be induced in a sample under irradiation, a few precautions can be taken when performing the yield measurements. The sample charging effect can be reduced or prevented by the use of low incidence electron fluence and pulsed beams^[89], and by the use of a source of electrical conductivity to refill the electrons emitted in the SEE process.

1.8.7. SEE from semiconductors

In the case of semiconductor materials the emission of electrons is more complex than for metals. Here, electrons have to be supplied to the material and then extracted by means of an electric field at the surface, as in field emission. In addition, the electron emission characteristics depend fundamentally on the surface functionalization. Wide band-gap semiconductors are known for displaying high SEE yields owing to the good electron transport characteristics offering a large escape depth for the electrons. The prevailing energy-loss mechanism for the energetic electrons is impact ionization, by which valence electrons are excited into the conduction band.^[118]

1.8.8. SEE from diamond

CVD diamond films have, among other extraordinary properties, excellent electron emission characteristics, presenting higher yields than metals and many insulator materials.^[9, 119-121]

This is attributed to the combination of good transport characteristics from the region where the secondary electrons are generated to the surface resulting in a high mean escape depth

(around tens of nm for $E_0 \sim 1$ keV) for polycrystalline diamond films and a NEA surface favourable for the emission.^[9]

In the SEE process, when a primary electron beam impacts a diamond surface, it produces secondary electrons by exciting valence band electrons into the conduction band. Each incident electron generates several secondaries creating a current amplification proportional to the primary energy E_0 . For diamond, the internal gain can be estimated as being proportional to the band-gap energy E_g (5.47 eV) according to the relation: $E_0 / 2.5 E_g$.^[165, 167]

Then, the generated secondary electrons diffuse through the solid and thermalize to the bottom of the conduction band. The wide-band gap allows the secondary electrons to have a long mean free path.^[122] Thus, when electrons reach the surface they present a characteristic narrow low energy distribution.^[16] Finally, the emission of electrons depends only on the energy barrier present at the surface.

The high SEE yields observed in hydrogen-terminated diamond are attributed to a combination of large escape depth, arising from the efficient transport to the surface plus the absence of a vacuum barrier for electron emission due to the NEA surface.^[103]

Properties such as surface termination, doping level, surface roughness, crystal morphology, *etc.*, and their combination will determine the SEE values measured from diamond. The following sections give an overview of the effects of such properties on the SEE, with reference to relevant numerical values found in the literature.

1.8.8.1. The Effect of Negative Electron Affinity

In microelectronic applications, surface conductivity and electrochemistry, the surface termination of diamond plays a determining role.^[122] One of the extraordinary properties of diamond is its ability to present a NEA surface. The first evidence of this fact was published in 1979 by Himpsel *et al.*^[113] as a result from their experiments with photoelectron emission from (111) diamond surfaces. The electron affinity depends essentially on the dipoles formed at the surface by the surface termination groups. The surface dipole results from the surface charge redistribution and the rearrangement of the surface ions from their lattice positions. The as-grown CVD diamond films present mostly a surface terminated with chemisorbed hydrogen but this layer can be modified by deposition of different species.

The dipole generated by hydrogen on the diamond surface leads to experimentally measured electron affinities of ~ -1 eV for the different crystallographic configurations.^[123, 124] An OH-terminated C(100) surface was found to present a similar (-1.1 eV) value of NEA, whilst the bare diamond surface has a value of 0.35 to 0.5 eV.^[125, 126] The more negative NEA value for the OH-terminated surface was associated with the fact that the OH bond produces a dipole opposing the CO bond, enhancing the NEA more than a simple CH bond.^[107] In contrast, exposure of the diamond surface to oxygen or argon plasmas causes an increase in the surface electron affinity to 2.6 to 3.6 eV.^[126-128] The dipoles are attributed to the bond C^-H^+ and C^+-O^- (see figure 1.13), resulting from the difference in electronegativities between the two bonded atoms. H is expected to be positive when bonded to C, lowering the surface barrier, whereas oxygen should be negative when bonded to C, increasing the surface barrier. The interchange between those surface terminations is a reversible process. For example, after exposure to hydrogen the NEA surface is established, but it was found that when the diamond samples are heated up to 1000 °C in vacuum the electron affinity becomes positive, due to the H desorption leaving a bare diamond surface.^[129] However, further exposure to hydrogen may re-establish the NEA surface.

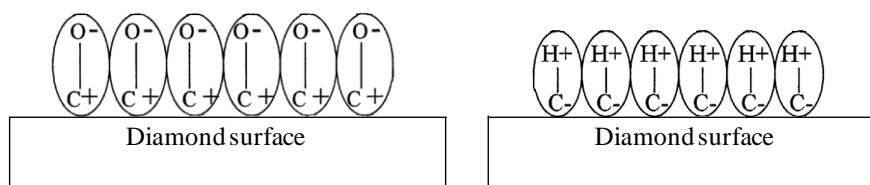


Figure 1.13- Schematic models for the surface dipoles of an oxygen-chemisorbed diamond (left), and of a hydrogenated diamond surface (right). The sign of the electric dipoles differ, resulting in a positive and a negative electron affinity, respectively. The higher electronegative O atoms in relation to C, creates the PEA. The dipole due to the larger electron negativity of C in relation to H is the origin of the NEA.^[130]

The effectiveness of a Cs layer in terms of lowering the electron affinity, was suggested by Langmuir and Kingdon^[131] in studying the effect of adsorbed layers on tungsten surfaces. The adsorption was stronger on surfaces partially covered with oxygen than on clean surfaces. These Cs-O surfaces must be chemically bonded to the surface by a short heat treatment at a few hundred degrees. During this activation process, part of the oxygen desorbs and then the remaining oxygen ions and Cs ions and atoms, will configure their positions on the surface to find their most favourable positions. The result is a mixture of Cs and Cs-O bonds at the

surface, where the Cs-O is much stronger.^[132] In addition, the C-O-Cs termination is thought to be chemically stable.^[133] Several researchers have shown that CVD diamond surfaces modified with Cs displayed NEA.^[122, 134-136] The addition of a caesium submonolayer adsorbed on an oxygenated diamond surface was found to produce an effective NEA of - 0.85 eV induced by the large Cs-O dipole.^[116]

The PEA/NEA characteristics of the surface directly affect the measured SEE values. For example, SEE yields ~ 45 at 2.4 keV were obtained for B-doped diamond films with hydrogen termination.^[137] However, the initially high yield was not stable and tended to decrease rapidly. Such effects have been associated with a decrease in the NEA of the film surface and by structural defects produced by the irradiation process.^[138] Under continuous electron-irradiation, electron stimulated desorption of hydrogen and charge trapping are decisive factors controlling the electron emission process.^[139]

CVD diamond surfaces terminated with Cs display yields as high as 83 at 2.9 keV from Cs/CVD diamond surfaces.^[140] These surfaces seem to suffer a similar process of electron induced desorption, although the desorption in caesiated diamond surfaces proved to be extended to the whole surface whereas in hydrogenated this phenomena is localised in the areas irradiated by the electron spot.^[141]

Besides H and Cs, many electropositive metals such as alkaline earth metals^[142] and metals like Ti, Ni, Co or Cu^[143] are expected to create NEA surfaces when put onto diamond. For instance, a submonolayer of titanium deposited after argon plasma treatment or onto an oxygen-terminated surfaces produced NEA in (111) diamond surfaces.^[143, 144] The effect of adsorption of other alkali metals as well as barium (Ba) and thorium (Th) is the same as of Cs, each one considerably lowering the surface work function.^[133] They all form a dipole layer at the surface with its positive side pointing out of the surface. Recent studies using Li on oxygen-terminated diamond surfaces have shown NEA values of - 3.9 eV and even higher bonding energy than Cs oxide coatings.^[145, 146] However, no SEE yield values have yet been published in the literature for these cases.

1.8.8.2. The effect of dopant and dopant concentration

Previous studies demonstrated that higher electron emission can be obtained from boron-doped diamond films with hydrogen termination.^[113, 147] Research has shown low SEE yields for lightly B-doped, which increased with the B concentration to a certain level and then falling again for heavily doped diamond. This was associated with an increasing downward band bending at the surface, increasing electron emission from the surface for a certain level of boron doping. But after a certain boron concentration, a decrease in the SEE yield can be associated with a reduction of electron mobility and an increase of electron-hole recombination sites.^[110, 122] Therefore, the B-doping levels in the diamond films seem to have an important role in their electron emission characteristics.

Shih *et al.*^[122] investigated the effect of dopant type and doping content on the transport efficiency within the diamond bulk and the role of surface conductivity (see figure 1.14). As detailed in section 1.5.1.1, N is a deep donor in diamond and at room temperature N-doped diamond samples are insulators, showing very low SEE yields.

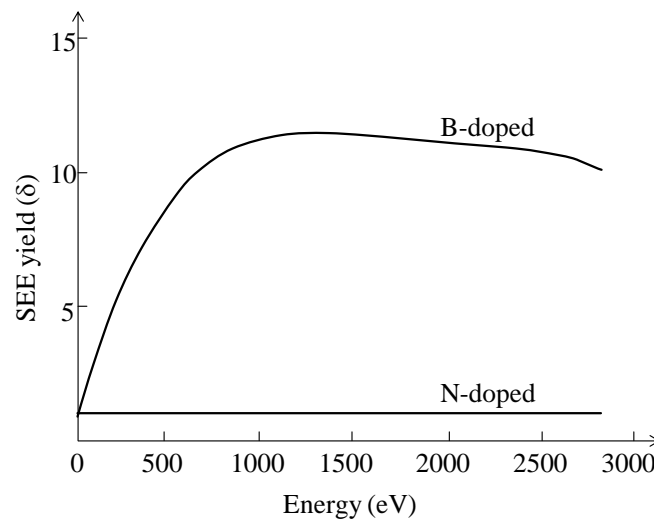


Figure 1.14- SEE yield δ obtained from an N-doped diamond film in comparison with a B-doped film with resistivity in the range of 50-170 k Ω cm, both H-terminated.^[122]

The differences observed can be related to the downward band bending combined with the reduced electron affinity in B-doped diamond, whereas in the case of N-doped diamond the emission would be hindered by the high upward band bending.^[125]

1.8.8.3. The effect of surface roughness

The surface roughness is also a factor that determines the maximum SEE yield measured from a certain material. When secondary electrons are emitted from a rough surface they are likely to be intercepted by neighbouring crystals or other surface irregularities, which may deflect them back to the surface. Electrons emitted from a smooth surface face no further obstacles in their trajectory, and can easily be detected.^[89] It is reasonable to do a similar association when comparing between microcrystalline and nanocrystalline diamond films, or different thicknesses amongst microcrystalline films. However, nanocrystalline films are associated with a higher number of grain boundaries and have increased graphite content present in those grain boundaries. A series of microcrystalline films grown for the same thickness but under different CH₄/H₂ ratios were found to show a decrease in the SEE with increase of the CH₄ content and therefore smaller grain size. This behaviour was associated with a decrease in the mean escape depth.^[120]

1.8.8.4. The effect of film thickness

Considering the transport mechanisms in polycrystalline diamond films^[134], a small decrease in SEE yield is expected for larger thicknesses, which can be explained assuming an accumulation of positive charge within the thicker films which hinders the escape of electrons through the surface.^[148, 149] Trucchi *et al.*^[10] observed the variation of the yield from microcrystalline diamond films grown from 2 to 21.7 μm, under the similar CVD conditions. The yield increased up to a maximum value corresponding to a film thickness around 15 μm, which was associated with the maximum escape depth calculated to be around 10 nm, subsequently decreasing for thicker films. The authors explain those results assuming a combined effect between the improvement of the film quality with growth time and the evolution of intrinsic stresses. Those effects should happen relatively fast at the beginning and slow down considerably with deposition time and the increase of film thickness. For thin films (100 nm up to 4.7 μm) a decrease in the yield with the increase in thickness was associated with a substrate effect.^[149]

1.8.8.5. The effect of crystallinity

From all diamond crystallinities, measurements confirm the excellent transport and emission characteristics of single-crystal diamond as compared with polycrystalline diamond.^[90, 16] The yield curves suggested escape distances over 5 μm for diamond (100) and (111), and above 1 μm for polycrystalline CVD.^[90, 150]

Crystal orientation has influence upon the surface properties, namely in the surface adsorption properties, but no effect on the transport characteristics in the bulk.

1.8.8.6. The effect of substrate

Besides Si and Mo, other materials have been considered as potential substrates for diamond in electron multiplication studies with good results. Palladium, titanium and aluminium nitride are examples of such materials, although in the case of Ti the lack of adhesion of the diamond film caused yield instability.^[151] Other characteristics to have in consideration will be the material conductivity for an effective back contact.

1.8.8.7. The energy distribution of secondary electrons emitted from diamond

The energy distribution of the emitted electron from a generalised surface was introduced in section 1.8 and the whole spectrum of electrons sketched in figure 1.9. In this section a few brief considerations are made in terms of the energy distribution curve (EDC) of the *true* secondary electrons, though this analysis is not part of the present experimental work.

Most of the early theoretical studies did not treat the escape of the secondary electrons through the vacuum barrier in an explicit way. Some brought out the dependence of the shape of the EDC on the surface-vacuum barrier for emission but ignored its influence on the yield value.^[85, 152] However, the high yields obtained from diamond NEA surfaces proved the opposite.

The EDC obtained from diamond films generally displays a narrow energy spread and sharply peaked distribution of the emitted electrons (see figure 1.15, curve A).^[16] The intensity of the emission peak increases with primary energy but its position and width is essentially constant over the interval $50 \leq E_0 \leq 3000 \text{ eV}$.^[90] This is an indication of the near

independence of the EDC with the transport distance and consequently with penetration depth, which changes from ~ 10 to ~ 1000 Å within this E_0 interval.^[153]

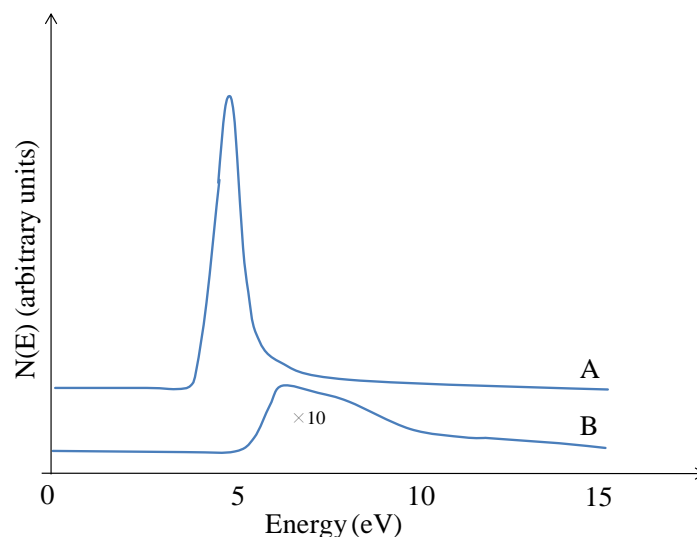


Figure 1.15- EDC curves illustrating the emitted electron intensity as a function of the emitted electron energy for a hydrogen terminated B-doped diamond sample (curve A) and the same sample after heating to 1000°C (curve B).^[103]

The graph in figure 1.15 shows that when the energy barrier at the surface is removed at the hydrogenated surface, a narrow energy distribution is obtained from the samples with the presence of a sharp peak in the EDC curve indicative of the existence of a NEA surface and the emission of electrons from the bottom of the conduction band. When the sample is heated or after prolonged electron beam exposure, the NEA surface disappears and so does the characteristic narrow peak.^[103, 154] The energy distribution of the emitted electrons is now broader, with low intensity and shifted to higher energies (curve B).

1.8.8.8. Angular distribution of secondary electrons

The angular distribution of the secondary electrons is approximately a cosine distribution and is nearly independent of the incidence angle of the primary electrons. For the backscattered electrons, the distribution shows a slightly preferential direction for emission (see in figures 1.16a and b).

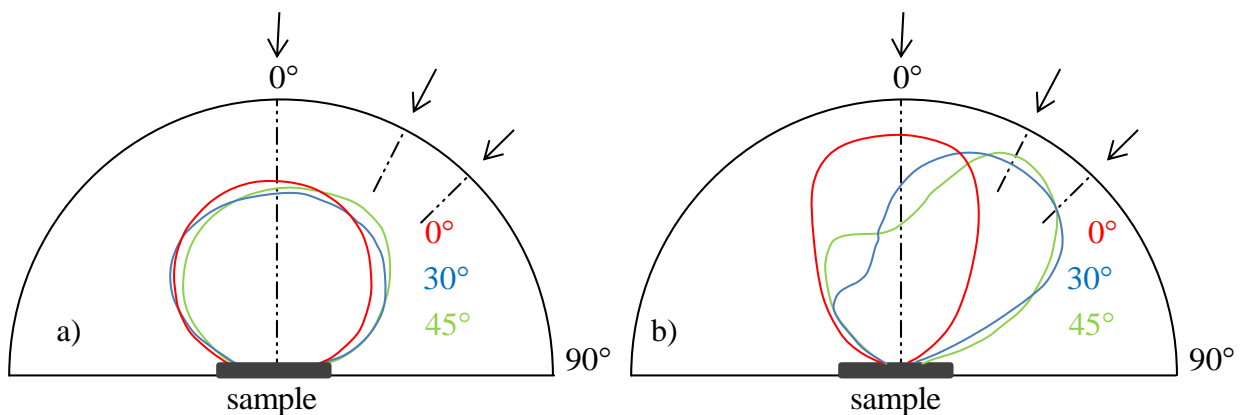


Figure 1.16- Schematic diagrams of the angular distribution of (a) secondary electrons, and (b) backscattered electrons, emitted from a polycrystalline surface.^[104]

The angular distribution of secondary electrons emitted from a single-crystal sample surface was found to display anisotropy.^[79]

1.8.9. SEE from diamond: A state-of-the-art review

The first studies on SEE from diamond specimens were made almost simultaneously with the development of the techniques for deposition of synthetic diamond. Several values of SEE yield from diamond are reported in the literature, with a wide variation depending on the surface treatment, microstructure, doping level, thermal history, crystal orientation and measurement setup, among others. The next sections present a compilation of those values in the most complete manner possible, since in many cases the experimental details available are not completely clear.

1.8.9.1. Reflection yield studies

The reflection yield measurements refer to a configuration where a primary electron beam strikes a surface and secondary electrons are emitted from the same surface. This is the reference mode for all the values presented, except when otherwise stated. A summary of the studies found in the literature of SEE measured in reflection from diamond is presented in Table 1.4. A detailed explanation of the configuration modes generally used for yield measurements is given in section 1.9.1.1.

Table 1.4- Summary of research studies found in the literature of SEE from diamond, sample characteristics and reflection yield values. (PCD = polycrystalline diamond, SCD = single-crystal diamond, MCD = microcrystalline diamond, f-NCD = faceted nanocrystalline diamond).

Sample	Surface	Doping	Yield	E_0 (eV)	Author	Year				
PCD on Mo	H	-	14 27	1 k	Bekker <i>et al.</i> ^[155]	1992				
SCD(100) type IIb	H	$B < 1.5 \times 10^{17} \text{ cm}^{-3}$	37.7	3 k	Malta <i>et al.</i> ^[156]	1994				
PCD on AlN	H	-	14	1.3 k	Mearini <i>et al.</i> ^[151,157]	1994/5				
PCD on Pd	H	-	5-18	1.5 k						
PCD on Ti	H	-	12	800						
PCD on Mo	H Cs	-	6-12 25-50	1 k 3 k	Mearini <i>et al.</i> ^[158]	1994				
PCD on Si (10-20 μm)	H	Medium B	84	3 k	Shih <i>et al.</i> ^[122]	1997				
PCD on Mo (10-20 μm)	H	$B \sim 10^{20} \text{ cm}^{-3}$	35	3 k	Krainsky <i>et al.</i> ^[154]	1997				
SCD (100) type IIb	Bare	$B < 1.5 \times 10^{17} \text{ cm}^{-3}$	3	~ 650	Yater <i>et al.</i> ^[150, 159]	1998				
	H		60	$\sim 2.9 \text{ k}$						
	Cs		132	$\sim 2.9 \text{ k}$						
PCD on Si	Bare	B (50-170 $\text{k}\Omega \text{ cm}$)	3	~ 650						
	H		25	$\sim 2.9 \text{ k}$						
	Cs		77	$\sim 2.9 \text{ k}$						
PCD on Si	Bare	B (155 $\text{k}\Omega \text{ cm}$)	3	~ 650						
	H		43	$\sim 2.9 \text{ k}$						
	Cs		83	$\sim 2.9 \text{ k}$						
PCD on Mo (10-20 μm)	H	$B (10^{18} - 10^{19} \text{ cm}^{-3})$	50	3 k	Krainsky <i>et al.</i> ^[160]	1998				
SCD (100) type IIb	Bare/H Cs	$B < 1.5 \times 10^{17} \text{ cm}^{-3}$	3/60 132	$\sim 650 / \sim 2.9 \text{ k}$ $\sim 2.9 \text{ k}$	Yater <i>et al.</i> ^[90]	2000				
SCD (111) type IIb			3.8/1 13 58	$\sim 800 / \sim 2.9 \text{ k}$ $\sim 2.9 \text{ k}$ $\sim 2.9 \text{ k}$						
PCD on Si			$\sim 3/43$ 83	~ 900 $\sim 2.9 \text{ k}$						
PCD on Si (0.2 μm)			H-Cs O-Cs	Low B			76 63	1.8 k	Hopman <i>et al.</i> ^[141]	2000
PCD on Si (2-5 μm)			H	-			10	1 k	Ascarelli <i>et al.</i> ^[120]	2001
PCD (2 μm) PCD (5 μm)	H	B ($\sim 2 \text{ k}\Omega \text{ cm}$) B ($\sim 6 \Omega \text{ cm}$)	12 22	1.6 k 3 k	Yater <i>et al.</i> ^[118]	2002				
f-NCD on Si (0.15 μm)	Bare H	$B \sim 10^{20} \text{ cm}^{-3}$	16 -	1 k	Yater <i>et al.</i> ^[161]	2003				
f-NCD on Si (2.5 μm)	Bare H	-	12 20	1 k						

Table 1.4 (cont.)- Summary of research studies found in the literature of SEE from diamond, sample characteristics and reflection yield values.

Sample	Surface	Doping	Yield	E_0 (eV)	Author	Year
PCD on Si (2-5 μm)	H Cs	B $\sim 10^{18} \text{ cm}^{-3}$	18 ~ 38	950 $\sim 1.5 \text{ k}$	Dvorkin <i>et al.</i> ^[162]	2004
MCD (2.2 μm)	H Cs	B $\sim 10^{21} \text{ cm}^{-3}$	19 70	1.65 k 2.65 k	Yater <i>et al.</i> ^[134]	2004
PCD on Si (2~22 μm)	H	-	~ 9	$\sim 1 \text{ k}$	Trucchi <i>et al.</i> ^[10]	2006
PCD on Si (0.1- 4.7 μm)	H	-	10- 5.8	$\sim 1 \text{ k}$	Ternyak <i>et al.</i> ^[149]	2006
PCD on Si (21 μm)	H	-	6-8	1 k	Belhaj <i>et al.</i> ^[163]	2010
SCD (100) (8.3 μm)	H	B $\sim 1 \times 10^{15} \text{ cm}^{-3}$	6-18	1 k	Yater <i>et al.</i> ^[16]	2011

In such a reflection configuration mode electron impact and emission takes place at the same surface, which means fairly small transport distances of 0.1 μm or less, for E_0 up to 3 keV.^[161]

When E_0 is increased the primary electrons penetrate deeper into the material and consequently the secondary electrons are generated at greater distances from the emitting surface. However, the increase in E_0 usually has serious implications in terms of electron-induced surface modifications, such as changes in the surface termination, for example, the hydrogen desorption. These are common issues related with measurements of SEE yields in reflection configurations. One possible method to overcome these problems is using a transmission configuration.

1.8.9.2. Transmission yield studies

In transmission mode, the yield measurements are made with the high-energy primary electrons being injected into the back surface of the sample. The sample has to be thin enough so that the low-energy secondary electrons can travel through it to be ejected out of the front surface, which possesses NEA characteristics. For diamond films, the substrate has to be etched away completely or in a small area, to expose a diamond membrane.

In fact, the transmission configuration is the appropriate approach in order to evaluate the escape depths of electrons in solids and therefore their transport properties. Previous research in the transmission of electrons from polycrystalline diamond samples have shown low yields

≤ 5 , which were attributed to increased electron scattering at grain boundaries and longer transport distances, with low transport efficiency.^[16, 164] Electron transmission was detected for penetration depths for the generation of secondaries within $\approx 1.3 \mu\text{m}$ from the emitting surface, thus providing a direct indication of the escape depth for polycrystalline diamond films. SC diamond samples proved to have more efficient transport and emission properties when compared with PC diamond films.^[161] Diffusion lengths of $8.1 \mu\text{m}$ were determined for SC diamond samples in comparison with the $1.3 \mu\text{m}$ detected for PC diamond.^[16] The transport properties are limited by the diffusion length within the film, which may be shortened through the application of a bias to the sample. A summary of the studies found in the literature of SEE yield from diamond measured in transmission is presented in Table 1.5.

Table 1.5- Summary of research studies of secondary electron emission from diamond, sample characteristics and transmission yield values found in the literature. (PCD = polycrystalline diamond, SCD = single-crystal diamond, MCD = microcrystalline diamond, f-NCD = faceted nanocrystalline diamond).

Sample	Surface	Doping	Yield	E_0 (eV)	Author	Year
PCD (2 μm)	H	B ($\sim 2 \text{ k}\Omega \text{ cm}$)	4	5 k	Yater <i>et al.</i> ^[118]	2002
PCD (5 μm)	H	B ($\sim 6 \Omega \text{ cm}$)	2.5	20 k		
f-NCD (0.15 μm)	H	B $\sim 10^{20} \text{ cm}^{-3}$	1	4 k	Yater <i>et al.</i> ^[161]	2003
f-NCD (2.5 μm)	H		5	7 k		
			1	15 k		
		3	18 k			
PCD (2-5 μm)	H	B $\sim 10^{18} \text{ cm}^{-3}$	~ 4	25 k	Dvorkin <i>et al.</i> ^[162]	2004
MCD (4.2 μm)	H Cs	B $\sim 10^{21} \text{ cm}^{-3}$	≤ 0.1	$0 \leq E \leq 20 \text{ k}$	Yater <i>et al.</i> ^[134]	2004
SC CVD (100) (8.3 μm)	H	-	$\sim 3-4$	20 k	Yater <i>et al.</i> ^[16]	2010
PCD (2.5 μm)	H		$\sim 3-4$			

One of the disadvantages of this configuration is that transmission measurements are generally made with much higher beam energies ($\sim 0-20 \text{ keV}$) than in reflection configuration ($\sim 0-5 \text{ keV}$), and the same applies to the beam currents, although the NEA surface is preserved. Additionally, is necessary to take in consideration the existence of the diamond nucleation layer, which affects the diffusion of the electrons.^[118] Figure 1.17 shows the EDC from a $8.3 \mu\text{m}$ thick diamond film obtained by homoepitaxial growth on a SC (100) diamond substrate, obtained both in reflection and transmission.

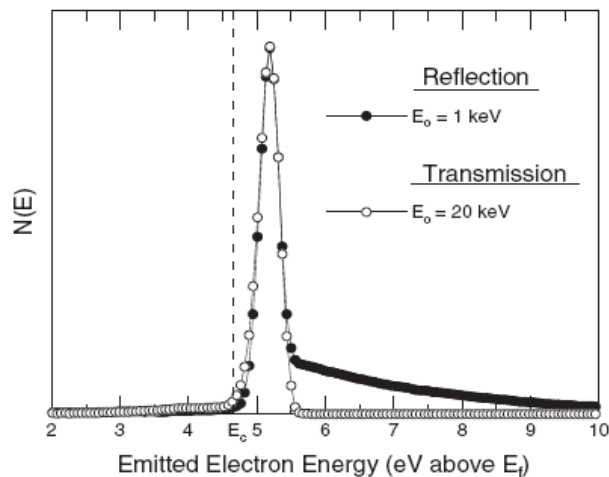


Figure 1.17- Energy distribution curves measured from an 8.3 μm diamond film in reflection and transmission with normalized peak intensities. ^[16]

The graph confirms the emission of electrons from just above the bottom of the conduction band, indicating the presence of NEA in both cases. Moreover, it gives important information on the superiority of a transmission configuration. With similar peak positions and widths, the narrowness of the curve for the transmitted electrons indicates the full thermalization of the electrons before arriving at the surface, due to the longer transport distances. ^[16]

1.9. Measurement methods

This section presents a description of the type of setup generally employed in electron emission measurements from solid surfaces under electron bombardment, with regard to reflection and transmission yields and energy distribution of secondary electrons. In addition, it discusses how the values obtained may be affected by the measurement parameters, such as angle of incidence, beam current and temperature.

1.9.1.1. Measurement of the total electron yield

A number of methods have been developed to measure the SEE yield. The most commonly used method for the determination of total electron yields refers to the quotient of the total number of emitted electrons to the number of incident primary electrons, using a Faraday cup (FC) as a collector. Figure 1.18 shows the type of arrangement generally used for the

reflection configuration. The measurements are performed in UHV chambers, with base pressures of $\sim 10^{-10}$ Torr. The sample under measurement is bombarded with primary electrons produced by an electron gun facing the sample. All the emitted electrons are collected independently of the direction in which they are emitted. The grid is kept to a negative potential in relation to the collector, to avoid any secondaries formed at the collector itself influencing the measurements.

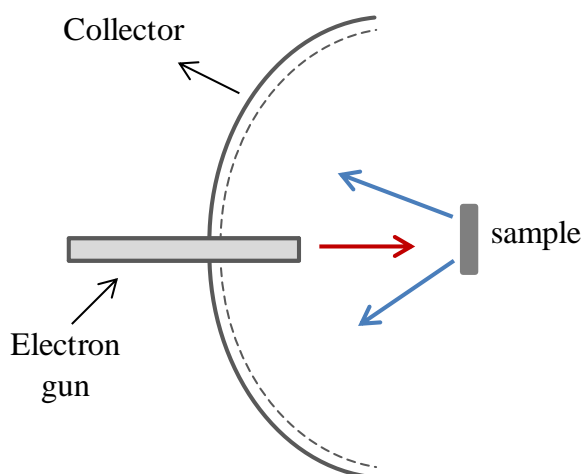


Figure 1.18- Arrangement for measuring the SEE. All emitted electrons independent of their emission direction are collected. It is possible to separate the slow secondary electrons from the energetic backscattered electrons by using a retarding field.^[79]

The emitted electrons are collected by a separate collector electrode consisting generally of a cylinder or a half-sphere positioned in front of the target. A frequent setting is having the collector positively biased and the target kept at ground potential. The currents generated at the target and the collector can be measured simultaneously. Such detail is of special importance in the case of unstable primary beams or if fast changes of the electron yield are to be measured. A variable positive bias V can also be applied to the target acting as a retarding field and $\delta(V)$ can then be measured.

The current in the sample is measured at two stages: with a positive and with a negative bias on the target. When the sample is negatively biased, the secondary electrons are repelled from it and the value measured for the current (I_-) corresponds to the primary current (I_0) minus the secondary electron current (I_{sec}) and the reflected electrons (I_b). With a positive bias

applied to the sample the current measured is (I_+) and equals to I_0 minus I_b . Thus the SEE yield is achieved by the expression^[170]:

$$\delta(E) = \frac{I_+ - I_-}{I_+} = \frac{I_{\text{sec}}}{(I_0 - I_b)} \quad (1.18)$$

The yield calculated using this method does not include the backscattered electrons.

Yater *et al.*^[161] described a slightly less sophisticated measurement method using the setup illustrated in figure 1.19. The target is biased alternatively by a sufficiently high positive and negative bias. When a positive bias is applied (+90 V), electrons are prevented from leaving the target and the charge accumulated equals that of the primary current, I_0 . Whereas if the applied bias is negative (-72 V) the secondary electrons generated at the target are repelled from it and the current measured at the target is the generated secondary current I_{sec} , minus I_0 . Finally, the ratio between those two measurements gives δ , as defined previously in equation 1.10 (see section 1.8.2).

Accordingly, the primary current I_0 can be measured by means of a FC at the target position or, alternatively, it may be determined from the current at the target with an applied bias of +90 V.^[141]

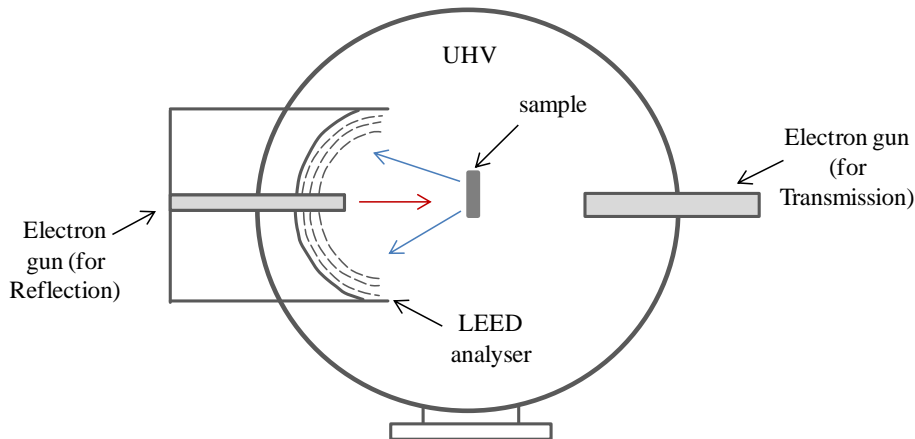


Figure 1.19- Illustration of a typical UHV chamber used for SEE measurements both in reflection and transmission configurations (top view), with a 4-grid energy analyser (low-energy electron diffraction (LEED) system) for determination of the EDC curves, adapted from reference.^[118]

The measurement of the total yield from insulators can present some issues due to the charging of the target during electron bombardment. This effect can be minimized with the use of low beam currents or by application of short pulse beams (\sim few μ s) or charge dissipation by target heating.^[176] In the case of thin insulating films on conducting substrates the charging effect is substantially reduced.

Some systems are equipped with a hot filament, to allow for *in situ* measurements under atomic hydrogen atmosphere. The hot filament at a temperature of \sim 1900 °C activates the molecular hydrogen introduced into the chamber.^[160] In addition, some systems have an option for resistive heating in order to anneal the samples, during or after measurement.

In the case of transmission measurements, the SEE yield δ is defined as the ratio of the total transmitted current I_T to the primary current I_0 , where I_T represents the total transmitted current measured at the collector without retarding grid biasing.

1.9.1.2. The effect of the angle of incidence

The relation between the penetration depth of the primary electrons and the escape depth of the internal secondary electrons explains the dependence of yield on the angle of incidence of the primaries. Usually, reflection yield measurements are taken at normal incidence to the surface. When the primary electron beam has an angle of incidence θ with respect to the surface normal, then the total yield can be calculated from the equation:

$$\delta(\theta) = \delta(0) \cos^{-1} \theta \quad (1.19)$$

where $\delta(0)$ is the total yield at normal incidence. Thus, with the incidence positioned at an angle θ , the maximum penetration depth is reduced by a factor $\cos \theta$, with higher yields obtained at more oblique angles. Shih and Hor^[174] used this argument to analyse the results obtained for the yields measured from Mo samples at different incidence angles.

1.9.1.3. The effect of temperature

Stacey *et al.*^[139] demonstrated that a moderate heating may effectively reduce the decay of yield verified in CVD diamond hydrogenated surfaces under continuous electron

bombardment due to the hydrogen desorption. Such a decrease was linked to a decrease in the surface NEA due to electron-stimulated hydrogen desorption, but the initial values could be restored or even enhanced with exposure to a hydrogen plasma or by annealing the surface in vacuum.^[141, 155] Belhaj *et al.*^[163] showed a similar trend using a pulsed electron beam.

Heating in vacuum to 700 K (~427 °C) proved to contribute to an increase in the maximum yield (from 12 to 15), measured from Mo-coated diamond with hydrogen termination.^[151] The authors attributed this effect to the desorption of surface hydrocarbons promoted by the heating. Figure 1.20 aims to illustrate the effect of temperature on the yield curves obtained from polycrystalline diamond films.

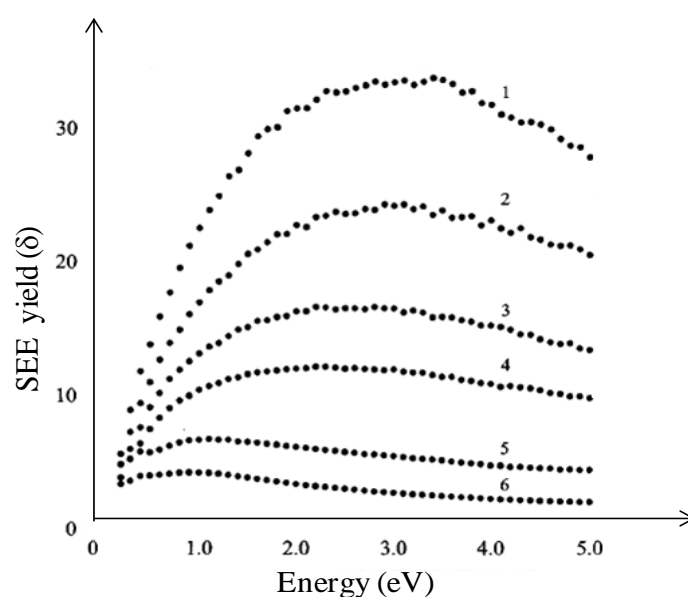


Figure 1.20- Variation of the maximum yield values measured after heating a PC diamond grown on Mo at various temperatures: 1) 500°C, 2) 600°C, 3) 700°C, 4) 750°C, 5) 850°C and 6) 975 °C.^[160]

Thus, from the figure above, the maximum yield decreases when the sample is heated from 600 to 950 °C. The effect was associated with a gradual hydrogen desorption from the diamond surface^[160] although, other authors report that following a heating to 900 °C there were no significant changes in the yields measured from PC CVD diamond films, i.e. after all the H has desorbed there is no further decrease. In contrast, a clear decrease in the yield of similar CVD samples was observed for caesiated surfaces, after heating to temperatures of 500 °C and over^[90], suggesting that desorption is still incomplete until higher temperatures.

1.9.1.4. The effect of beam current

Typical beam currents of ~10 nA (for spots around 1 mm) are used in reflection measurements, and values of ~100 nA in transmission (for spots ~0.3 mm). The total yield measured from polycrystalline diamond films increases with temperature and decreases with the current density. This would be the result of a dynamic competition between an accumulation of holes which reduces the internal secondary electron emission and the reduction of space charge formation by a thermally activated conductivity.^[121]

Mearini *et al.*^[151] showed that the yield under continuous electron bombardment may be stabilized upon operation in a molecular hydrogen environment. Another approach in the attempt to provide surface stabilization has been the application of caesium layers to diamond^[158] as mentioned above. Such surfaces presented relative stability when exposed to air or heated in vacuum to temperatures below 120°C. In addition they were stable under continuous electron beam exposure. However, the electron-stimulated desorption from caesiated diamond surfaces proved to be extended across the whole surface whereas in hydrogenated samples this phenomenon is localised to the areas irradiated by the electron spot.^[141]

1.9.1.5. Measurement of the energy distribution of the emitted electrons

As described in section 1.8.8.7, the study of the energy distribution of secondary electrons is a valuable tool to understand the transport and emission properties of diamond.

Various aspects of the emission process have been reported in studies using photoemission spectroscopy^[113, 124] and secondary electron emission spectroscopy (SEES).^[90, 110, 160] Those techniques are particularly useful for investigating the effect of crystal orientation and surface adsorbed species on the emission characteristics of diamond.

SEES provides useful information on both electron transport and emission processes in the material, through energy distribution curves and electron intensity measurements, allowing an insight into the surface electronic properties and their impact both in the energy spread and intensity of the emitted secondary electrons.^[90] Those measurements are a function of the beam energy, thus, providing the opportunity to get additional information on the transport distance variation for different values of E_0 .

The energy distribution of the emitted electrons can be determined by the single yield differential $d\delta/dE$, integrated over all angles of emission as a function of the electron energy E . Hence, $d\delta/dE$ or $N(E)$, gives the number of electrons of energy E per energy interval of 1 eV and per incident primary electron, which are emitted in all directions from the target surface.^[117] Thus, by definition:

$$\delta = \int \left(\frac{d\delta}{dE} \right) dE \quad (1.20)$$

The equipment for measuring the energy distribution curves for $E \leq 500$ eV, normally uses retarding field analysis, in which a retarding field applied in front of the emitting surface only allows the escape of electrons with energy higher than $e.V$, e being the elementary charge and V the retarding potential.^[117] Concentric sphere analysers (CSA) and concentric hemispherical analysers, such as those used in low energy electron diffraction (LEED) are generally applied. The LEED analyser consists of a hemispherical collector with three or four grids and is usually operated by a modulated retarding field (see figure 1.19).

1.10. Potential Device Applications

Dynodes are electrodes used for electron multiplication in detectors such as photomultiplier tubes (PMT). A PMT is the detector used when a high sensitivity in the region of visible light or UV is necessary. It basically comprises a photocathode, a system of electron multiplier electrodes called dynodes which amplify the electron current to measurable levels, and an anode to collect and measure the current. These are all kept at increasingly positive potentials to attract the electrons from one electrode to the following (see figure 1.21).

When a photon strikes the photocathode this emits a photoelectron which is accelerated towards the first dynode where it collides, and as a result of the collision secondary electrons are generated and emitted.

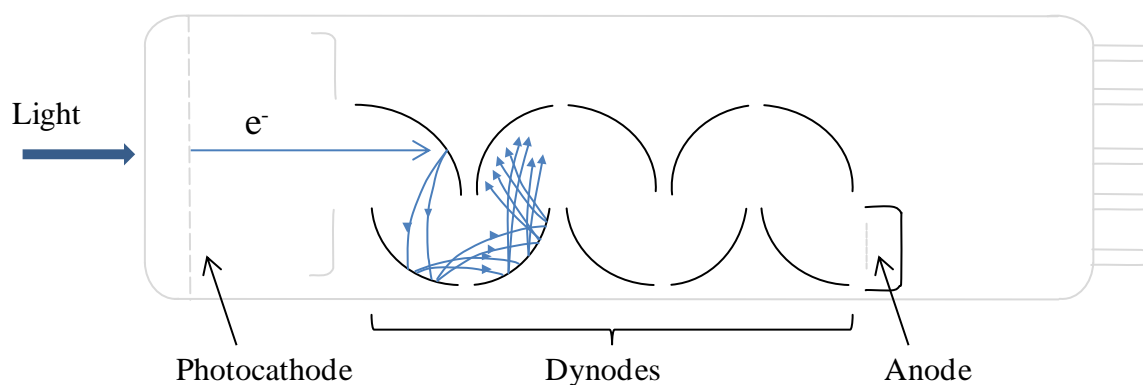


Figure 1.21- Schematic diagram of the principal elements of a photomultiplier (adapted from Photonis PMT Handbook^[178]).

The emitted electrons are then accelerated from this dynode to the next, where more secondary electrons are emitted. This process continues from dynode to dynode until they are finally collected by the anode and the signal processed by means of appropriate electronics. The chain of dynodes, (generally up to 19) can be arranged in different forms and the dynodes themselves may have a range of different geometries.^[91]

Materials such as beryllium oxide (BeO), gallium phosphide (GaP) and gallium arsenide phosphide (GaAsP), aluminium oxide (Al₂O₃) and magnesium oxide (MgO) are used in commercial dynodes. Figure 1.22 presents yield values obtained for some of those materials. They are normally coated onto a substrate electrode made of nickel, stainless steel, or beryllium copper (CuBe).

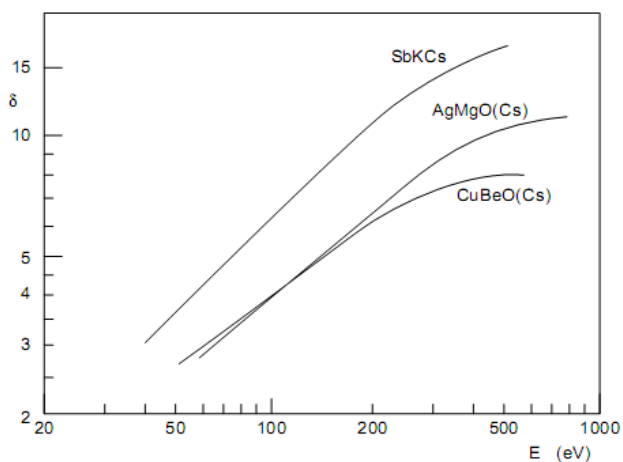


Figure 1.22- SEE yields of three common dynode materials. (Inset from Photonis PMT Handbook^[178]).

Common dynode materials emit roughly three secondary electrons per incident electron.^[166] Hence, at the end of the dynode chain, the initial photoelectron will have been multiplied to 10^5 to 10^6 electrons. Ideally, the gain of a PMT with n dynode stages and average SEE yield per stage δ will correspond to δ^n .^[178]

1.11. Thesis overview

The aim of the research undertaken within this thesis was the investigation of the secondary electron emission from diamond films for the development of an optimised diamond film to use as a dynode material.

The outline of this thesis consists of eight chapters. Chapter 1 presents a general overview of the diamond structure, properties and applications of CVD diamond, including a description of the technologies associated with the production of synthetic diamond. The last topics within this chapter describe the main electron emission mechanisms from solids, focusing on the basic principles involved in the secondary electron emission from diamond and the theoretical models which predict its behaviour under high-energy electron bombardment. Finally, the chapter includes a brief introduction on the measurement methods used for secondary electron emission and the potential device applications.

Chapter 2 comprises a description of the experimental methods employed during this research from the preparation of the diamond films to the techniques employed for their characterization.

Chapter 3 describes the experimental studies done in the characterization and comparison of hot-filament CVD diamond films grown under a range of deposition conditions, namely in terms of microstructure, crystallinity and boron-doping level.

Chapter 4 describes how an entirely new system for the measurement of the total secondary electron emission yield was designed, built and calibrated.

Chapter 5 presents a comparative study of the total yield measured from a selection of the diamond films grown on Mo and Si under different HF CVD deposition conditions. The influence of morphology, doping level, surface termination and substrate material on the secondary electron emission from diamond are considered. The surfaces of a number of films were functionalized by means of hydrogenation, oxygenation, caesiation and lithiation

treatments and the effect upon the SEE yields was investigated using the setup described in chapter 4.

Chapter 6 describes the investigation of the effect of surface termination upon the yields measured from commercial polycrystalline CVD diamond samples. In the experiments described in the chapters above, all the measurements were done using reflection of secondaries from the diamond growth surface.

In contrast, Chapter 7 describes the method of measuring transmission of electrons through a diamond free-standing membrane. Moreover, it also includes a detailed presentation of the development of preparation procedures required to fabricate thin diamond membranes.

Finally, Chapter 8 brings together the main results obtained in this thesis, summarizing the principal conclusions from these studies and reveals potential opportunities for improvement and future work. At the end of the chapter are included a series of appendices containing descriptions of other activities undertaken during the PhD, communications and publications.

1.12. References

1. A.G.G.M. Tielens, C.G. Seab, D.J. Hollenbach and C.F. Mckee, Shock processing of interstellar dust: Diamonds in the sky, *The Astrophysical Journal* **319** (1987) L109-L113.
2. B.S. Mitchell, in *An introduction to materials engineering and science: for chemical and materials engineers*, John Wiley & Sons, Inc., Hoboken, New Jersey, chapter 1 (2004) 59.
3. K.E. Spear and J.P. Dismukes, in *Synthetic Diamond: Emerging CVD Science and Technology*, John Wiley & Sons, Chichester, UK (1994).
4. P. Bergonzo, D. Tromson, C. Mer, B. Guizard, F. Foulon and A. Brambilla, Particle and radiation detectors based on diamond, *Physica Status Solidi A* **185** (2001)167.
5. P.K. Baumann and R.J. Nemanich, Electron emission from CVD diamond cold cathodes, in *Low-Pressure Synthetic Diamond: manufacturing and applications*, edited by B. Dischler and C. Wild, Springer-Verlag Berlin Heidelberg, chapter 15 (2000) 281-303.
6. C.E. Nebel, B. Rezek, D. Shin, H. Uetsuka and N. Yang, Diamond for bio-sensor applications, *Journal of Physics D - Applied Physics* **40** (2007) 6443.
7. A.E. Hadjinicolaou, R.T. Leung, D. J. Garrett, K. Ganesan, K. Fox, D.A.X. Nayagam, M.N. Shivdasani, H. Meffin, M.R. Ibbotson, Steven Praver and B.J. O'Brien, Electrical stimulation of retinal ganglion cells with diamond and the development of an all diamond retinal prosthesis, *Biomaterials* **33** (2012) 5812-5820.

8. O. Auciello and D.M. Gruen Science and Technology of Ultrananocrystalline Diamond (UNCD™) Film-Based MEMS and NEMS Devices and Systems, in *Ultrananocrystalline Diamond: Synthesis, Properties and Applications*, Second Edition, edited by O. Shenderova and D. Gruen, Micro & Nano Technologies Series, Elsevier 2012, chapter 12 (2012) 383–420.
9. O. Auciello, S. Pacheco, A.V. Sumant, C. Gudeman, S. Sampath, A. Datta, R.W. Carpick, V.P. Adiga, P. Zurcher, Z. Ma ; H-C. Yuan, J.A. Carlisle, B. Kabius, J. Hiller and S. Srinivasan, Are Diamonds a MEMS' Best Friend?, *IEEE Microwave Magazine* Dec. (2007) 61-75.
10. D.M. Trucchi, C. Scilletta, E. Cappelli, P.G. Merli, S. Zoffoli, G. Mattei and P. Ascarelli, Optimization of the performance of CVD diamond electron multipliers, *Diamond and Related Materials* **15** (2006) 827-832.
11. R.A. Campos, V.J. Trava-Airoldi, O.R. Bagnato, J.R. Moro and E.J. Corat, Development of nanocrystalline diamond windows for application in synchrotron beamlines, *Vacuum* **89** (2013) 21-25.
12. X. Ding and M. Rahman, A study of the performance of cutting polycrystalline Al 6061 T6 with single crystalline diamond micro-tools, *Precision Engineering* **36** (2012) 593-603.
13. Y. Zhang, N. Yang, M. Muruganathan and S. Yoshihara, Electrochemical degradation of PNP at boron-doped diamond and platinum electrodes, *Journal of Hazardous Materials* **244-245** (2013) 295-302.
14. Y. Takano, Superconductivity in Diamond, in *CVD Diamond for Electronic Devices and Sensors*, edited by R.S. Sussmann, John Wiley & Sons (2009) chapter 19, 549-562.
15. M.L. Markham, J.M. Dodson, G.A. Scarsbrook, D.J. Twitchen, G. Balasubramanian, F. Jelezko and J. Wrachtrup, CVD diamond for spintronics, *Diamond and Related Materials* **20** (2011) 134-139.
16. J.E. Yater, J.L. Shaw, K.L. Jensen, T. Feygelson, R.E. Myers, B.B. Pate and J.E. Butler, Secondary electron amplification using single crystal CVD diamond film, *Diamond and Related Materials* **20** (2011) 798-802.
17. F.P. Bundy, H.T. Hall, H.M. Strong and R.H. Wentorf, Man-made diamonds, *Nature* **51** (1955) 176.
18. F.P. Bundy, The P,T Phase and Reaction diagram for elemental Carbon, 1979, *Journal of Geophysical Research* **85** (1980) 6930-6936.

19. R. Abbaschian, H. Zhu, C. Clarke, High pressure–high temperature growth of diamond crystals using split sphere apparatus, *Diamond and Related Materials* **14** (2005) 1916–1919.
20. W.G. Eversole, Synthesis of Diamond, *US Patent* No. 3030187 and 3030188 (1958).
21. B.V. Derjaguin, D.V. Fedoseev, V.M. Lukyanovich, B.V. Spitzin, V.A. Ryabov and A.V. Lavrentyev, Filamentary diamond crystals, *Journal of Crystal Growth* **2** (1968) 380-384.
22. J.C. Angus, H.A. Will and W.S. Stanko, Growth of Diamond Seed Crystals by Vapor Deposition, *Journal of Applied Physics* **39** (1968) 2915.
23. D.J. Poferl, N.C. Gardner and J.C. Angus, Growth of boron-doped diamond seed crystals by vapor deposition, *Journal of Applied Physics* **44** (1973) 1428.
24. A. Argoitia, C.S. Kovach and J.C. Angus, Hot-filament CVD deposition, in *Handbook of Industrial Diamonds and Diamond Films*, chapter 20 (1998) 797-819.
25. M.N.R. Ashfold, P.W. May, C.A. Rego and N.M. Everitt, Thin Film Diamond by Chemical Vapour Deposition Methods, *Chemical Society Reviews* **23** (1994) 21-30.
26. S. Matsumoto, S.Y. Sato, M. Kamo and N. Setaka, Vapor deposition of diamond particles from methane, *Japanese Journal of Applied Physics* **21** (1982) L183-L185.
27. F.G. Celii and J.E. Butler, Diamond Chemical Vapor Deposition, *Annual Review of Physical Chemistry* **42** (1991) 643-684.
28. M.N.R. Ashfold, P.W. May, J.R. Petherbridge, K.N. Rosser, J.A. Smith, Yu.A. Mankelevich and N.V. Suetin, Unravelling aspects of the gas phase chemistry involved in diamond chemical vapour deposition, *Physical Chemistry Chemistry Physics* **3** (2001) 3471-3485.
29. J. Zimmer and K.V. Ravi, Aspects of scaling CVD diamond reactors, *Diamond and Related Materials* **15** (2006) 229-233.
30. J. Cifre, F. Lopez, J.L. Morenza and J. Esteve, Analysis of contamination in diamond films by secondary ion mass spectroscopy, *Diamond and Related Materials* **1** (1992) 500-503.
31. M. Kamo, Y. Sato, S. Matsumoto and N. Setaka, Diamond synthesis from gas phase in microwave plasma, *Journal of Crystal Growth* **62** (1983) 642-644.
32. V.V.S.S. Srikanth and X. Jiang, Synthesis of diamond films, in *Synthetic diamond films: preparation, electrochemistry, characterization and applications*, edited by E.

-
- Brillas and C.A. Martínez-Huitle, John Wiley & Sons, Hoboken, NJ, USA, chapter 2 (2011) 21-55.
33. H.B. Martin, A. Argoitia, J.C. Angus and U. Landau, Voltammetry Studies of Single-Crystal and Polycrystalline Diamond Electrodes, *Journal of the Electrochemical Society* **146** (1999) 2959.
 34. O.A. Williams, M. Daenen, J. D'Haen, K. Haenen, J. Maes, V.V. Moshchalkov, M. Nesládek, D.M. Gruen, Comparison of the growth and properties of ultrananocrystalline diamond and nanocrystalline diamond, *Diamond and Related Materials* **15** (2006) 654-658.
 35. D.M. Gruen, Nanocrystalline Diamond Films, *Annual Review of Materials Science* **29** (1999) 211-259.
 36. X. Xiao, J. Birrell, J.E. Gerbi, O. Auciello and J.A. Carlisle, Low temperature growth of ultrananocrystalline diamond, *Journal of Applied Physics* **96** (2004) 2232.
 37. P.K. Bachmann, D. Leers and H. Lydtin, Towards a general concept of diamond chemical vapour deposition, *Diamond and Related Materials* **1** (1991) 1-12.
 38. J.E. Butler, R.L. Woodin, L.M. Brown and P. Fallon, Thin Film Diamond Growth Mechanisms, *Philosophical Transactions of The Royal Society A* **342** (1993) 209-224.
 39. P.W. May, Diamond Thin Films: A 21st Century Material, *Philosophical Transactions of Royal Society London. A* **358** (2000) 474-494.
 40. P.W. May and Y.A. Mankelevich, From Ultrananocrystalline Diamond to Single Crystal Diamond Growth in Hot Filament and Microwave Plasma-Enhanced CVD Reactors: a Unified Model for Growth Rates and Grain Sizes, *Journal of Physical Chemistry C* **112** (2008) 12432-12441.
 41. S. Skokov, C.S. Carmer, B. Weiner and M. Frenklach, Reconstruction of (100) diamond surfaces using molecular dynamics with combined quantum and empirical forces, *Physical Review B* **49** (1994) 5662-5671.
 42. S. Koizumi, M. Kamo, Y. Sato, H. Ozaki and T. Inuzuka, Growth and characterization of phosphorous doped {111} homoepitaxial diamond thin films, *Applied Physics Letters* **71** 8 (1997) 1065-1074.
 43. S.J. Harris, Mechanism for diamond growth from methyl radicals, *Applied Physics Letters* **56** (1990) 2298-2301.
 44. V. der Drift, A Evolutionary selection: a principle governing growth orientation in vapour deposited layers, *Philips Research Reports* **22** (1967) 267-288.

45. C. Wild, R. Kohl, N. Herres, W. Müller-Sebert and P. Koidl, Oriented CVD diamond films: twin formation, structure and morphology, *Diamond and Related Materials* **3** (1994) 373-381.
46. B. Sun, X. Zhang and Z. Lin, Growth mechanism and the order of appearance of diamond (111) and (100) facets, *Physical Review B* **47** 15 (1993) 9816-9824.
47. X. Jiang, W.J. Zhang, M. Paul and C.P. Klages, Diamond film orientation by ion bombardment during deposition, *Applied Physics Letters* **68** 14 (1996) 1927-1929.
48. C.P Chang, D. L. Flamm, D. E. Ibbotson, and J. A. Mucha, Diamond crystal growth by plasma chemical vapor deposition, *Journal of Applied Physics* **63** (1988) 1744-1748.
49. Y. Muranaka, H. Yamashita and H. Miyadera, Characterization of diamond films synthesized in the microwave plasmas of CO/H₂ and CO/O₂/H₂ systems at low temperatures (403-1023 K), *Journal of Applied Physics* **69** (1991) 8145-8153.
50. J. Wei, H. Kawarada, J. Suzuki, A. Hiraki, Growth of diamond films at low pressure using magneto-microwave plasma CVD, *Journal of Crystal Growth* **99** (1990) 1201-1205.
51. M. Yuasa, O. Arakaki, J.S. Ma, A. Hiraki and H. Kawarada, Low temperature diamond film fabrication using magneto-active plasma CVD, *Diamond and Related Materials* **1** (1992) 168-174.
52. R. Kalish, Doping of Diamond, *Carbon* **37** (1999) 781.
53. J.P. Goss, R.J. Eyre and P.R. Briddon, Theoretical models for doping diamond for semiconductor applications, in *Physics and Applications of CVD Diamond*, Wiley-VCH, Weinheim (2008).
54. T.H. Borst and O. Weis, Electrical characterization of homoepitaxial diamond films doped with B, P, Li and Na during crystal growth, *Diamond and Related Materials* **4** (1995) 948-953.
55. S. Kajihara, A. Antonelli, J. Bernholc, R. Car, Nitrogen and potential n-type dopants in diamond, *Physical Review Letters* **66** (1991) 2010–2013.
56. R. Samlenski, Characterisation and lattice location of nitrogen and boron in homoepitaxial CVD diamond, *Diamond and Related Materials* **5** (1996) 947-951.
57. S. Koizumi, K. Watanabe, M. Hasegawa and H. Kanda, Ultraviolet Emission from a Diamond p-n Junction, *Science* **292**, (2001) 1899.
58. S. Koizumi, M. Kamo, Y. Sato, S. Mita, A. Sawabe, A. Reznik, C. Uzan-Saguy and R. Kalish, Growth and characterization of phosphorous doped n-type diamond thin films, *Diamond and Related Materials* **7** (1998) 540-544.

59. T. Makino, H. Kato, S.G. Ri, Y. Chen and H. Okushi, Electrical characterization of homoepitaxial diamond p-n⁺ junction, *Diamond and Related Materials* **14** (2005) 1995 – 1998.
60. A.T Collins and A.W.S. Williams, The nature of the acceptor centre in semiconducting diamond, *Journal of Physics C: Solid State Physics* **4** (1971) 1789-1800.
61. W.L. Wang, M. Polo, G. Sanchez, J. Cifre and J. Esteve, Internal stress and strain in heavily boron-doped diamond films grown by microwave plasma and hot filament chemical vapor deposition, *Journal of Applied Physics* **80** (1996) 1846- 1851.
62. P. Wurzinger, P. Pongratz, P. Hartmann, R. Haubner and B. Lux, Investigation of the boron incorporation in polycrystalline CVD diamond films by TEM, EELS and Raman spectroscopy, *Diamond and Related Materials* **6** (1997) 763-768.
63. J. Ma, J.C. Richley, D.R.W. Davies, M.N.R. Ashfold, Y.A. Mankelevich, Spectroscopic and Modelling Investigations of the Gas Phase Chemistry and Composition in Microwave Plasma Activated B₂H₆/CH₄/Ar/H₂ Mixtures, *Journal of Physical Chemistry A* **114** (2010) 10076-10089.
64. A. Cheesman, J.N. Harvey and M.N.R. Ashfold, Computational studies of elementary steps relating to boron doping during diamond chemical vapour deposition, *Physical Chemistry Chemical Physics* **7** (2005) 1121-1126.
65. D.W. Comerford, A. Cheesman, T.P.F. Carpenter, D.M.E. Davies, N. A. Fox, R.S. Sage, J.A. Smith, M.N.R. Ashfold, and Yu. A. Mankelevich, Experimental and Modelling Studies of B Atom Number Density Distributions in Hot Filament Activated B₂H₆/H₂ and B₂H₆/CH₄/H₂ Gas Mixtures, *Journal of Physical Chemistry A* **110** (2006) 2868-2875.
66. Y. Muranaka, H. Yamashita and H. Miyadera, Worldwide status of low temperature growth of diamond, *Diamond and Related Materials* **3** 4 (1994) 313-318.
67. A. Hatta, K. Kadota, Y. Mori, T. Ito, T. Sasaki, A. Hiraki and S. Okada, Pulse modulated electron cyclotron resonance plasma for chemical vapor deposition of diamond films, *Applied Physics Letters* **66** 13 (1995) 1602-1605.
68. M. Ihara, H. Maeno, K. Miyamoto, and H. Komiyama, Diamond deposition on silicon surfaces heated to temperature as low as 135 °C, *Applied Physics Letters* **59** (1991) 1473-1475.
69. Y. Muranaka, H. Yamashita and H. Miyadera, Low temperature (~400 °C) growth of polycrystalline diamond films in the microwave plasma of CO/H₂ and CO/H₂/Ar systems, *Journal of Vacuum Science and Technology A* **9** (1991) 76-84.

70. V.F. Neto, R. Vaz, N. Ali, M.S.A. Oliveira and J. Grácio, Diamond coatings on 3D structured steel, *Diamond and Related Materials* **17** (2008) 1424-1428.
71. K.V. Ravi, C.A. Koch, H.S. Hu, and A. Joshi, The nucleation and morphology of diamond crystals and films synthesized by the combustion flame technique, *Journal of Materials Research* **5** 11 (1990) 2356-2366.
72. P.C. Yang, W. Zhu, and J.T. Glass, Diamond nucleation on nickel substrates seeded with non-diamond carbon, *Journal of Materials Research* **9** 5 (1994) 1063-1066.
73. K. Suzuki, A. Sawabe, H. Yasuda and T. Inuzuka, Growth of diamond thin films by dc plasma chemical vapor deposition, *Applied Physics Letters* **50** 12 (1987) 728-730.
74. P. Ascarelli, S. Fontana, Dissimilar grit-size dependence of the diamond nucleation density on substrate surface pretreatments, *Applied Surface Science* **64** 4 (1993) 307-311.
75. O.J.L. Fox, J.O.P. Holloway, G.M. Fuge, P.W. May and M.N.R. Ashfold, Electrospray deposition of diamond nanoparticle nucleation layers for subsequent CVD diamond growth, *Materials Research Society Symposium Proceedings* **1203** (2010) J17-27.
76. S. Yugo, T. Kimura and T. Muto, Effects of electric field on the growth of diamond by microwave plasma CVD, *Vacuum* **41** 4 (1990) 1364-1367.
77. B.R. Stoner, G.-H.M. Ma, S.D. Wolter, and J.T. Glass, Characterization of bias-enhanced nucleation of diamond on silicon by in-vacuo surface analysis and transmission electron microscopy, *Physical Review B* **45** (1992) 11067-11084.
78. N. Getoff, M. Gerschpacher, J. Hartmann, J.C. Huber, H. Schittl and R.M. Quint, The 4-hydroxyestrone: Electron emission, formation of secondary metabolites and mechanisms of carcinogenesis, *Journal of Photochemistry and Photobiology B: Biology* **98** (2010) 20-24.
79. H Seiler, Secondary electron emission in the scanning electron microscope, *Journal of Applied Physics* **54** (1983) R1-R18.
80. J.H. De Boer, in *Electron Emission and Adsorption Phenomena*, Cambridge University Press, chapter 1, 9 (1935)1-25, 228-229.
81. R. Gomer, in *Field emission and field ionization*, edited by American Vacuum Society Classics, New York, chapter 1 (1993) 1-31.
82. W.S.M. Werner, Photon and electron induced emission from solid surfaces, , in *Slow Heavy-Particle Induced Electron Emission from Solid Surfaces*, edited by H. Winter and J. Burgdörfer, Springer Tracts in Modern Physics, Vol. 225, chapter 2 (2007) 39-77.

83. V.W. Hughes and H.L. Schultz, in *Methods of Experimental Physics, Atomic and Electron Physics, Atomic Sources and Detectors*, Vol. 4-Part A, Academic Press New York and London, (1967).
84. D. Hasselkamp, Kinetic electron emission from solids under ion bombardment, in *Particle Induced Electron Emission II*, edited by Springer Tracts in Modern Physics, Vol. 123, (1992) 1-81.
85. R.O. Jenkins and W.G. Trodden, in *Electron and Ion Emission from Solids*, edited by L. Jacob, Routledge and Kegan Paul, London, chapter 6 (1965) 54-67.
86. W.H. Strehlow and E.L. Cook, Compilation of Energy Band Gaps in Elemental and Binary Compound Semiconductors and Insulators, *Journal of Physical Chemistry* **2** (1973) 163-199.
87. L. Austin and H. Starke, *Ueber die Reflexion der Kathodenstrahlen und eine damit verbundene neue Erscheinung sekundärer Emission*, *Annalen der Physik* **9** (1902) 271.
88. C.G.H. Walker, M.M. El Gomati, A. Assa'd, M. Zadrazil, The secondary electron emission yield for 24 solid elements excited by primary electrons in the range 250-5000eV: a theory / experiment comparison, *Scanning* **30** (2008) 365-380.
89. H. Bruining, in *Physics and Applications of Secondary electron Emission*, McGraw-Hill, New York (1954) 1.
90. J.E. Yater and A. Shih, Secondary electron emission characteristics of single-crystal and polycrystalline diamond, *Journal of Applied Physics* **87** (2000) 8103-8112.
91. B. H. Candy, Photomultiplier characteristics and practice relevant to photon counting, *Review of Scientific Instruments* **56** (1985) 183-193.
92. M.P. Seah and W.A. Dench, Quantitative electron spectroscopy of surfaces: A standard data base for electron inelastic mean free paths in solids, *Surface and Interface Analysis* **1** (1979) 2-11.
93. J.R.M. Vaughan, A new formula for secondary emission yield, *IEEE Transactions on Electron Devices* **36** **9** (1989) 1963-1967.
94. K. McKay, *Advances in Electronics and Electron Physics* **1** (1948) 65-130.
95. A.J. Dekker, in *Solid State Physics*, London Macmillan & Co Ltd, chap. 6 (1958) 314-320.
96. J. Devooght, A. Dubus and J.C. Dehaes, Improved age-diffusion model for low-energy electron transport in solids. I. Theory, *Physical. Review B* **36** (1987) 5093-5109.
97. J. Schou, Secondary electron emission from solids by electron and proton bombardment, *Scanning Microscopy* **2** (1988) 607-632.

98. M. Rösler and W. Brauer, Theory of electron emission from nearly-free-electron metals by proton and electron bombardment, in *Particle Induced Electron Emission I*, edited by Springer Tracts in Modern Physics, Vol. 122, (1991) 1-65.
99. G.F. Dionne, Origin of secondary-electron-emission yield-curve parameters, *Journal of Applied Physics* **46** (1975) 3347.
100. G.F. Dionne, Secondary emission yield curves, *Journal of Applied Physics* **44** (1973) 5361.
101. E.M. Baroody, A theory of secondary electron emission from metals, *Physical Review* **78** (1950) 780-787.
102. J.R. Young, Penetration of Electrons in Aluminium Oxide Films, *Physical Review* **103**, (1956) 292–293.
103. A. Shih, J. Yater, C. Hor and R. Abrams, Secondary electron emission studies, *Applied Surface Science* **111** (1997) 251-258.
104. J.H. Jonker, On the theory of secondary electron emission, *Philips Research Reports*, **7** (1952) 1-20.
105. D.C. Joy, A Database on Electron-Solid Interactions, *Scanning* **17** (1995) 270–275.
106. Y. Lin and D.C. Joy, A new examination of secondary electron yield data, *Surface and Interface Analysis* **37** (2005) 895-900.
107. M.J. Rutter and J. Robertson, *Ab initio* calculation of electron affinities of diamond surfaces, *Physical Review B* **57** 15 (1998) 9241-9245.
108. R.U. Martinelli and D.G. Fisher, The Application of Semiconductors with Negative Electron Affinity Surfaces to Electron Emission Devices, *Proceedings of the IEEE* **62** (1974) 1339-1360.
109. C. Bandis and B.B Pate, Photoelectric emission from negative-electron-affinity diamond (111) surfaces exciton breakup versus conduction-band emission, *Physical Review B* **52** (1995) 12056-12071.
110. J.B. Miller and G.R. Brandes, Effects of dopant concentration, crystallographic orientation, and crystal morphology on secondary electron emission from diamond, *Journal of Applied Physics* **82** 9 (1997) 4538-4545.
111. J.D. Levine, Structural and electronic model of negative electron affinity on the Si/Cs/O surface, *Surface Science* **34** (1973) 90-107.
112. J. Schou, Transport theory for kinetic emission of secondary electrons from solids, *Physical Review B* **22** (1980) 2141–2174.

113. F.J. Himpsel, J.A. Knapp, J.A. VanVechten and D.E. Eastman, Quantum photoyield of diamond (111) - A stable negative-affinity emitter, *Physical Review B* **20** (1979) 624-627.
114. J.E. Yater, A. Shih and R. Abrams, Electron transport and emission properties of C (100), *Physical Review B* **56** (1997) R4410–R4416.
115. W. E. Pickett, Negative Electron Affinity and Low Work Function Surface: Cesium on Oxygenated Diamond (100), *Physical Review Letters* **73** (1994) 1664.
116. M. Belhaj, T. Tondu and V. Inguibert, Experimental investigation of the effect of the internal space charge accumulation on the electron emission yield of insulators submitted to e-irradiation: application to polycrystalline MgO, *Journal of Physics D: Applied Physics* **42** (2009) 145306.
117. The Bethe, On the theory of secondary emission, Proceedings of the American Physical Society, *Physical Review* **59** 136 (1941) 940.
118. J.E. Yater, A. Shih, J.E. Butler and P.E. Pehrsson, Electron transmission studies of diamond films, *Applied Surface Science* **191** (2002) 52-60.
119. W.S. Kim, W. Yi, S. Yu, J. Heo, T. Jeong, J. Lee, C.S. Lee, J.M. Kim, H.J. Jeong, Y.M. Shin and Y.H. Lee, Secondary electron emission from magnesium oxide on multiwalled carbon nanotubes, *Applied Physics Letters* **81** (2002) 1098-1100.
120. P. Ascarelli, E. Cappelli, F. Pinzari, M. C. Rossi, S. Salvatori, P. G. Merli and A. Migliori, Secondary electron emission from diamond: Physical modelling and application to scanning electron microscopy, *Journal of Applied Physics* **89** (2001) 689.
121. J. Cazaux, Some considerations on the secondary electron emission, δ , from e⁻ irradiated insulators, *Journal of Applied Physics* **85** (1999) 1137.
122. A. Shih, J. Yater, P. Pehrsson, J. Butler, C. Hor and R. Abrams, Secondary electron emission from diamond surfaces, *Journal of Applied Physics* **82** **4** (1997) 1860-1866.
123. F. Maier, M. Riedel, B. Mantel, J. Ristein and L. Ley, Origin of Surface Conductivity in Diamond, *Physical Review Letters* **B** 64 (2001) 165411.
124. L. Diederich, P. Aebi, O. Küttel and L. Schlapbach, NEA peak of the differently terminated and oriented diamond surfaces, *Surface Sciences* **424** (1999) 314-320.
125. L. Diederich, O.M. Küttel, P. Aebi and L. Schlapbach, Electron emission and NEA from differently terminated, doped and oriented diamond surfaces, *Diamond and Related Materials* **8** (1999) 743-747.
126. J. Robertson and M.J. Rutter, Band diagram of diamond and diamond-like carbon surfaces, *Diamond and Related Materials* **7** (1998) 620-625.

127. J. van der Weide and R.J. Nemanich, Argon and hydrogen plasma interactions on diamond (111) surfaces: Electronic states and structure, *Applied Physics Letters* **62** 16 (1993) 1878-1880.
128. N. Eimori, Y. Mori, A. Hatta, T. Ito, A. Hiraki, Photoyield measurements of CVD diamond, *Diamond and Related Materials* **4** (1995) 806-808.
129. B.B. Pate, The diamond surface atomic and electronic structure, *Surface Science* **165** (1986) 83-142.
130. M. Yokoyama and T. Ito, Dependence of the electron affinity of homoepitaxially grown CVD diamond on the amount of surface oxygen, *Applied Surface Science* **162-163** (2000) 457-463.
131. I. Langmuir and K.H. Kingdon, Thermionic effects caused by alkali vapors in vacuum tubes, *Science* **57** (1923) 58-60.
132. J.B. Taylor and I. Langmuir, The Evaporation of Atoms, Ions and Electrons from Caesium Films on Tungsten, *Physical Review* **44** (1933) 423-458.
133. M. W. Geis, J.C. Twichell, J. Macaulay and K. Okano, Electron field emission from diamond and other carbon materials after H₂, O₂, and Cs treatment, *Applied Physics Letters* **67** (1995) 1328-1331.
134. J.E. Yater, A. Shih, J.E. Butler and P.E. Pehrsson, Electron transport mechanisms in thin boron-doped diamond films, *Journal of Applied Physics* **96** 1 (2004) 446-453.
135. K.P. Loh, J.S. Foord, R.G. Egde and R.B. Jackman, Tuning the electron affinity of CVD diamond with adsorbed caesium and oxygen layers, *Diamond and Related Materials* **6** (1997) 874-878.
136. K.P. Loh, X.N. Xie, S.W. Yang, J.S. Pan and P. Wu, A spectroscopic study of the negative electron affinity of caesium oxide-coated diamond (111) and theoretical calculation of the surface density-of-states on oxygenated diamond (111), *Diamond and Related Materials* **11** (2002) 1379-1384.
137. J.S. Lapington, D.P. Thompson, P.W. May, N.A. Fox, J. Howorth, J.A. Milnes and V. Taillandier, Investigation of the secondary emission characteristics of CVD diamond films for electron amplification, *Nuclear Instruments and Methods in Physics Research A* **610** (2009) 253-257.
138. E. Cheifetz, V. Richter, A. Zalman and R. Kalish, Ion-induced electron emission from boron-doped diamond: effect of surface hydrogenation and sample temperature, *Diamond and Related Materials* **10** (2001) 824-828.

139. A. Stacey, S. Praver, S. Rubanov, R. Akhvledian, Sh. Michaelson and A. Hoffman, Temperature enhancement of secondary electron emission from hydrogenated diamond films, *Journal of Applied Physics* **106** (2009) 063715.
140. J.E. Yater, A. Shih and R. Abrams, Cold emission characterization using secondary electron emission, *Applied Surface Science* **146** (1999) 341–346.
141. H.J. Hopman, J. Verhoeven and P.K. Bachmann, Electron stimulated desorption from oxygenated and hydrogenated synthetic diamond films, *Diamond and Related Materials* **9** (2000) 1238.
142. H.J. Hopman, J. Verhoeven, P.K. Bachmann, H. Wilson and R. Kroon, Secondary electron emission measurements on synthetic diamond films, *Diamond and Related Materials* **8** (1999) 1033–1038.
143. J. van der Weide and R.J. Nemanich, Schottky barrier height and negative electron affinity of titanium on (111) diamond, *Journal of Vacuum Science and Technology* **B** 10 (1992) 1940-1943.
144. C. Bandis, D. Haggerty, B.B. Pate, Electron emission properties of the negative electron affinity (111)2x1 diamond-TiO interface, *Materials Research Society Symposium Proceedings* **339** (1994) 75-80.
145. K.M. O'Donnell, T.L. Martin, N.A. Fox and D. Cherns, *Ab initio* investigation of lithium on the diamond C(100) surface, *Physical Review B* **82** (2010) 115-303.
146. K.M. O'Donnell, T.L. Martin, N.A. Fox and D. Cherns, The Li-adsorbed C(100)-(1x1):O diamond surface, *MRS Proceedings* **1282** (2011) 163-168.
147. G. Piantanida, G. Breskin, A. Chechik, R. Katz, O. Laikhtman, A. Hoffman and A. Coluzza, Effect of moderate heating on the negative electron affinity and photoyield of air-exposed hydrogen-terminated chemical vapor deposited diamond, *Journal of Applied Physics* **89** 12 (2001) 8259-8264.
148. Sh. Michaelson, V. Richter, R. Kalish, A. Hoffman, E. Cheifetz and R. Akhvlediani, Ion-induced electron emission from undoped sub-micron thick diamond films, *Thin Solid Films* **420-421** (2002) 185-189.
149. O. Ternyak, Sh. Michaelson, R. Akhvlediani, A. Hoffman, Enhancement of electron emission from near-coalescent nanometer thick continuous diamond films, *Diamond and Related Materials* **15** (2006) 850.
150. J.E. Yater, A. Shih and R. Abrams, Electronic properties of diamond for high-power device applications, *Solid-State Electronics* **42** 12 (1998) 2225-2232.

151. G.T. Mearini, I.L. Krainsky, Y.X. Wang, J.A. Dayton, Jr., R. Ramesham and M.F. Rose, Fabrication of an electron multiplier utilizing diamond films, *Thin Solid Films*, **253** (1994) 151.
152. C. Bouchard and J.D. Carette, The surface potential barrier in secondary emission from semiconductors, *Surface Science* **100** (1980) 251-268.
153. C. Feldman, Range of 1-10 keV Electrons in Solids, *Physical Review* **117** (1960) 455.
154. I.L. Krainsky, V.M. Asnin and J.A. Dayton Jr., Secondary electron emission from chemical vapor deposited diamond films with negative electron affinity, *Applied Surface Science* **111** (1997) 265-269.
155. T.L. Bekker, J.A. Dayton, Jr., A. S. Gilmour, Jr., I.L. Krainsky, M.F. Rose, R. Rameshan, D. File and G. Mearini, Observations of secondary electron emission from diamond films, *Physical Review* **92** (1992) 949-952.
156. D.P. Malta, J.B. Posthill, T.P. Humphreys, R.E. Thomas, G.G. Fountain, R.A. Rudder, G.C. Hudson, M.J. Mantini, and R.J. Markunas, Secondary electron emission enhancement and defect contrast from diamond following exposure to atomic hydrogen, *Applied Physics Letters* **64** (1994) 1929.
157. G.T. Mearini, I.L. Krainsky and J.A. Dayton, Jr., Investigation of Diamond Films for Electronic Devices, *Surface and Interface Analysis* **21** (1994) 138-143.
158. G.T. Mearini, I.L. Krainsky, J.A. Dayton, Y. Wang, C.A. Zorman, J.C. Angus, R.W. Hoffman and D.F. Anderson, Stable secondary electron emission from chemical vapor deposited diamond films coated with alkali-halides, *Applied Physics Letters* **66** 2 (1995) 242-244.
159. J.E. Yater, A. Shih and R. Abrams, Electron transport and emission properties of diamond, *Journal of Vacuum Science and Technology A* **16** 3 (1998) 913-918.
160. I.L. Krainsky and V.M. Asnin, Negative electron affinity mechanism for diamond surfaces, *Applied Physics Letters* **72** (1998) 2574-2576.
161. J.E. Yater, A. Shih, J.E. Butler and P.E. Pehrsson, Transmission of low-energy electrons in boron-doped nanocrystalline diamond films, *Journal of Applied Physics* **93** (2003) 3082-3090.
162. V.V. Dvorkin, N.N. Dzbanovsky, N.V. Suetina, E.A. Poltoratsky, G.S. Rychkov, E.A. Il'ichev and S.A. Gavrilov, Secondary electron emission from CVD diamond films, *Diamond and Related Materials* **12** (2003) 2208-2218.

-
163. M. Belhaj, T. Tondu, V. Inguibert, P. Barroy, F. Silva and A. Gicquel, The effects of incident electron current density and temperature on the total electron emission yield of polycrystalline CVD diamond, *Journal of Physics D: Applied Physics* **43** (2010) 135303.
164. J.E. Yater, A. Shih, J.E. Butler and P.E. Pehrsson, Effect of material properties on low-energy electron transmission in thin chemical-vapour deposited diamond films, *Journal of Applied Physics* **97** (2005) 093717.
165. C.A. Klein, Bandgap Dependence and Related Features of Radiation Ionization Energies in Semiconductors, *Journal of Applied Physics* **39** (1968) 2029-2038.
166. G.R. Brades, Diamond vacuum electronics, in *Handbook of Industrial Diamonds and Diamond Films*, chapter 31 (1998) 1103-1127.
167. K.L. Jensen, J.E. Yater, J.L. Shaw, R.E. Myers, B.B. Pate, J.E. Butler, T. Feygelson, Bunch characteristics of an electron beam generated by a diamond secondary emitter amplifier, *Journal of Applied Physics* **108** 4 (2010) 044509-044521.
168. J.S. Foord and C.H. Goeting, Electrochemically controlled modification of CVD diamond surfaces, *Diamond and Related Materials* **13** (2004) 1054-1058.
169. J.E. Yater and A. Shih, Interpretation of low-energy feature in energy spectra measured from surfaces with low or negative electron affinity, *Applied Surface Science* **143** (1999) 219-222.
170. M.E. Woods, B.J. Hopkins, G.F. Matthews, G.M. McCracken, P.M. Sewell and H. Fahrang, An investigation of the secondary-electron emission of carbon samples exposed to a hydrogen plasma, *Journal of Physics D: Applied Physics* **20** (1987) 1136-1142.
171. T.H. Borst and O. Weis, Boron-Doped Homoepitaxial Diamond Layers: Fabrication, Characterization, and Electronic Applications, *Physica Status Solidi A* 154 (1996) 423-444.
172. J.C. Angus and C.C. Hayman, Low-pressure, metastable growth of diamond and 'diamond-like' phases, *Science*, **241** (1988) 913-921.
173. B.V. Spitsyn, L.L. Bouilov, B.V. Derjaguin, Vapor growth of diamond on diamond and other surfaces, *Journal of Crystal Growth* **52** 1 (1981) 219-226.
174. A. Shih and C. Hor, Secondary emission properties as a function of the electron incidence angle, *IEEE Transactions on Electron Devices* **40** (1993) 824-829.
175. S. Iijima, Y. Aikawa and K. Baba, Early formation of chemical vapor deposition diamond films, *Applied Physics Letters* **57** (1990) 2646-2648.

176. Y. Chen, T. Kouno, K. Toyoda and M. Cho, Total electron emission yield measurement of insulator by a scanning small detector, *Applied Physics Letters* **99** (2011) 152101-152104.
177. A. Shih, J. Yater, C. Hor and R.H. Abrams, Secondary Electron Emission Properties of BeO CFA cathodes, *IEEE Transactions on Electron Devices* **41** (1994) 2448-2454.
178. www.photonis.com / http://psec.uchicago.edu/links/pmt_handbook_complete.pdf

Chapter 2.

Experimental methods and characterization techniques

2.1. Hot-Filament CVD

The hot-filament uses a metal coil resistively heated as a means of activation of the gas phase. The filament is made of tantalum or rhenium wire and is electrically heated to a temperature in excess of 2200 °C and calibrated by means of a pyrometer. The gas phase comprises a mixture of methane, the precursor carbon containing gas, diluted in hydrogen in a typical mixing ratio of 1-2% CH₄/H₂, although the exact dilution factor varies according to the specific type of diamond film grown. Table 2.1 summarizes the general conditions under which the HFCVD reactor operates.

Table 2.1- Standard deposition conditions employed in a hot filament CVD reactor.

Pressure (Torr)	20
Gases	CH ₄ /H ₂ , CH ₄ /H ₂ /B ₂ H ₆
Total gas flow rate (sccm ¹)	0 - 10 (CH ₄) / 0 - 200 (H ₂) / 0 - 1 (B ₂ H ₆)
Filament temperature (°C)	2300-2400
Substrate temperature (°C)	~ 900
Filament/substrate distance (mm)	5
Power (W)	~ 118
Growth rate (average value) (μmh ⁻¹)	0.5

¹ Unit for flow rate: standard cubic centimetres (cm³) per minute (sccm).

The flow rates of the gases are individually controlled by the respective mass flow controllers (MFCs) and the pressure is kept at approximately 20 Torr by manually throttling the pump using a needle valve. A rotary pump linked to the CVD chamber allows the exhaustion of the processing gases.

The substrate sample to coat is positioned underneath the filament at a distance of roughly 5 mm, measured from the sample surface to the filament. This results in substrate temperatures around 900 °C as previously measured using an *in situ* thermocouple. The deposition rates have been previously studied and for standard deposition conditions (1% CH₄/H₂) averaged ~ 0.5 μm h⁻¹. The CVD diamond group in the School of Chemistry at the University of Bristol has two similar HFCVD reactors, which are used for undoped and B-doped diamond films, respectively. The setups are similar except that the B-reactor has an extra MFC to control the flow of diborane gas (supplied as 5% B₂H₆/H₂). Figure 2.1 shows a schematic diagram of the reactor used for growing B-doped diamond films.

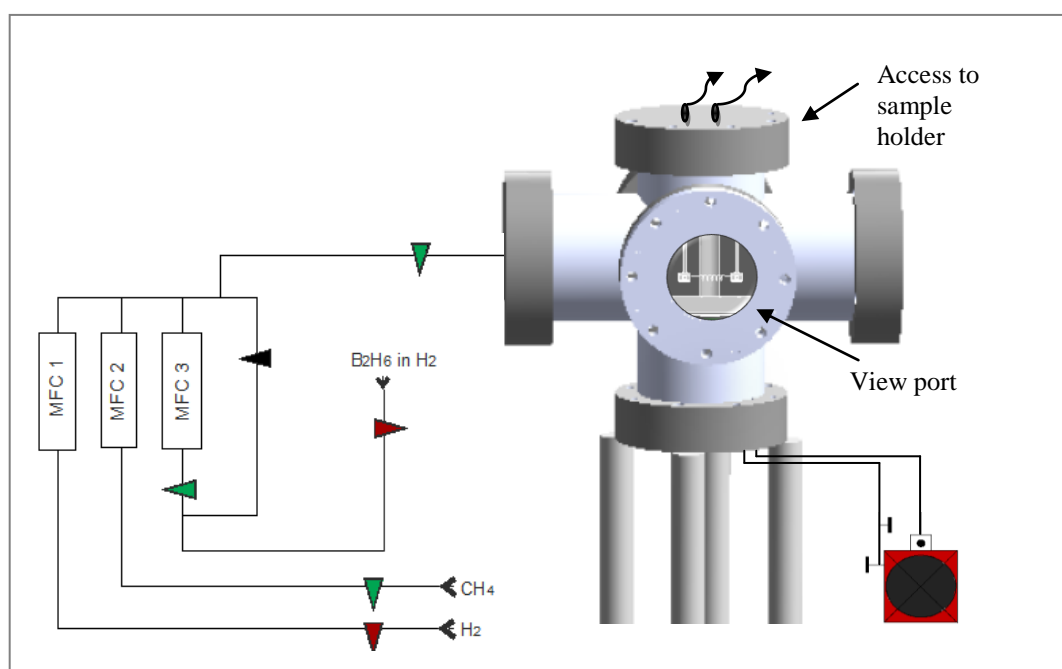


Figure 2.1- Sketch of the hot-filament reactor used to grow the diamond CVD films in the experiments presented across this thesis. This reactor is used to produce B-doped diamond films but presents the exact same setup of the one used for non-doped films.

The deposition chamber consists of a stainless steel six-way cross where one of the flanges incorporates a quartz window for viewing the substrate and filament and through which the filament temperature can be assessed by means of a pyrometer. The bottom flange connects to the vacuum pump, the top one connects the feedthroughs that lead to the power supply and

substrate heater, and the left-hand flange has feedthroughs for the gas inlet, vent valve and pressure gauge.

For the first stage of the experiments, all diamond deposition runs used 250 μm diameter wire made of Ta or Re with 7-coil turns, roughly 3 mm in diameter. Due to the need to increase the area of the diamond coated samples, the system was later modified from using a single coiled filament into a group of three straight wires, which were spring-loaded to kept them straight and tight during deposition. The remaining components were unchanged, except obviously for the clamping of the filaments and the conditions for the power supply input. The current normally used with the coil to obtain ~ 118 W was in the order of 6.75 A, whereas for the three filaments was 25 A. Figure 2.2 presents the schematic diagrams of the new setup of filaments.

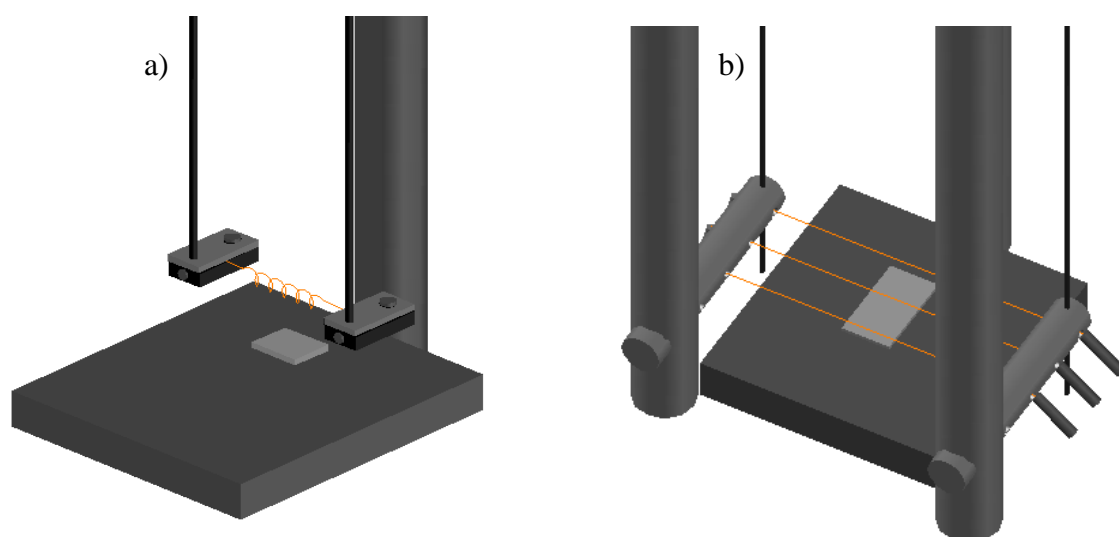


Figure 2.2- Schematic diagrams of the system for mounting the filaments, showing a coil (in a) and the new version using up to three filaments connected in parallel (in b).

The advantage of the new setup is the ability to coat several substrates simultaneously without compromising the continuity of the films at the edges of the sample as usually occurs with the coil, where the thickness varies from the middle of the sample to the edges. Nevertheless, both models can be used and the process of switching between them can be done easily. However, the new method has the disadvantage of consuming a large quantity of wire and therefore is not very convenient when using expensive Re filaments.

2.2. Substrate pre-treatment methods

The process of seeding can influence the adhesion of the diamond film to the substrate and reduce the nucleation time differently. They vary in reproducibility, complexity and adequacy depending on the shape, dimension and nature of the substrate to be seeded.

2.2.1. Seeding by electrospray deposition

The electrostatic spray or “electrospray” deposition (ESD) is a home-built system^[1] which consists of a non-abrasive pre-treatment method where a colloidal suspension containing diamond nanopowders is poured into a syringe directed into a metal nozzle located inside a sealed chamber at room pressure and temperature. A high voltage (35 kV) is applied to the nozzle ionising the diamond colloidal suspension which is sprayed towards the earthed substrate. Figure 2.3 shows the schematic diagram of the ESD setup.

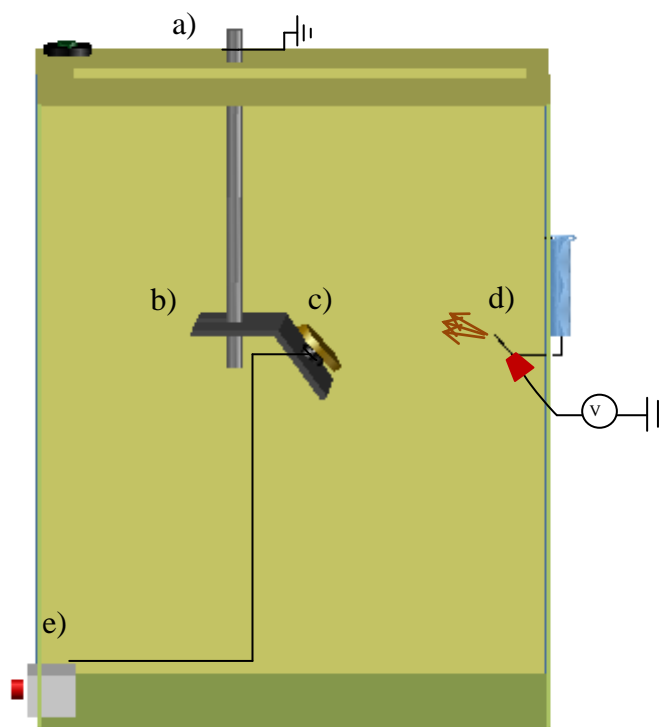


Figure 2.3- Sketch of electrospray deposition equipment, showing the different components: a) sample holder connection to ground, b) sample holder which is adjustable vertically and horizontally, c) rotating component of the sample holder where the substrates are mounted at 40 ° to the vertical axis, d) capillary nozzle and e) motor control.

The sample holder is adjustable in three axes and is equipped with a rotating plate where the samples to be seeded can be attached using sticky conductive carbon pads. The positioning determines the success of the seeding process and depends on the sample size. For a uniform seeding layer most of the liquid from the sprayed droplets must evaporate before reaching the sample surface. The rotation of the sample holder (~ 1500 r.p.m.) allows for easy drying any residual fluid although leaving marks from the droplets in the surface. The high voltage applied to the edge of the nozzle creates a strong electric field which promotes the disintegration of any agglomerates of nanoparticles present in the liquid dispersion, creating a finely dispersed colloid.^[2] Theoretical studies explained the phenomena by the formation of a cone of liquid at the edge of the metal nozzle, resulting from the hydrostatic balance between the electrostatic pressure inside and outside due to the surface tension.^[3] Furthermore, the viscosity and conductivity of the liquid that constitutes the suspension were found to play an important role in the dispersion of the droplets and for the success of the seeding process.^[4] Alcohols (such as methanol or ethanol) are normally good dispersion media due to their polarity and the ability to form hydrogen bonds to the nanodiamond particles in the suspension, decreasing the tendency of agglomeration of particles. In addition, the angle of the nozzle to the vertical (~ 90°) can be adjusted to optimize the substrate coverage. In the experiments undertaken in the context of this thesis, generally a 0.5 - 1 ml of colloidal suspension of diamond nanopowders (typically 5 nm, although other sizes have been tested) dispersed in methanol has been used to seed the substrates for CVD diamond deposition.

2.3. Laser Alpha 532-XYZ-A-U system

A commercial laser etching machine (Oxford lasers Alpha 532 –XYZ- A- U System) was used to cut and functionalize the substrates before diamond deposition, as well as to fabricate diamond membranes (chapter 7). This machine uses a 532 nm wavelength diode-pumped solid-state nanosecond laser capable of machining most types of common materials. The motion control is achieved with using servomotor driven *X-Y* axes with a *Z* axis for laser focusing (travel distance of 150×150×50 mm). The general system specifications are presented in table 2.2.

Table 2.2- Specifications of the laser system according to the Oxford Lasers manual.

Output: 2.5 W at 5 kHz
Pulse length: 15 ns (FWHM) nominal
Pulse frequency: 10 – 50.000 Hz
Max speed (mm/s): 200 (XY)
Focal length: 100 mm, corresponding to spot size of 20 μm

The laser machine used for cutting and etching creates rapid heating by a short-pulse focused laser causing a local sublimation of the material. For given laser parameters the material properties such as the optical absorption and thermal conductivity determine the etch rate.

The equipment has been used for the processing of Si, Mo SiC and other substrate materials, but processing diamond samples is also possible with this laser system. The use of Nd:YAG lasers is common in diamond cutting. Diamond is transparent at wavelengths above 227 nm, but the surface heating caused by the laser beam gives rise to a process of surface graphitization sufficient for the laser absorption.^[5]

2.4. Raman Spectroscopy

When monochromatic visible light illuminates a crystal a small fraction of light is scattered with a significant and well defined change in wavelength, giving rise to a series of emission lines when examined with a spectrometer. Elastic (Rayleigh) scattering dominates, but inelastic (Raman) scattering can be detected and analysed to provide information about the structure and phonon modes within the solid. In a typical spectrum a strong line corresponding to the Rayleigh scattering appears at the frequency of the exciting monochromatic light, and symmetrically placed on either side of it, a number of weaker Raman emission lines, which at the low frequency side are called the Stokes lines and on the high frequency side, the anti-Stokes lines.^[6] A filter is used to block off the Rayleigh line. In solid samples at room temperature, the Stokes lines dominate the spectrum and are used for diagnostics, giving information about the energy absorbed by the lattice.

Raman spectroscopy is a very useful, fast and non-destructive method to evaluate the quality of carbon films, revealing aspects of the vibrational properties of the material that can be related to atomic bonding configurations.^[7] Furthermore, the intensity of a specific Raman line is directly proportional to the amount of the species in the sampled area originating it, making Raman spectroscopy a valuable technique to quantitatively estimate the amounts of different compounds in a sample by measuring the relative peak intensities.

Pure diamond is revealed by a sharp characteristic line positioned at 1332 cm^{-1} , having a full-width at a half-maximum (FWHM) of about 2 cm^{-1} .^[8] CVD diamond films normally incorporate other carbon species, such as graphite and amorphous carbon. A single crystal of graphite produces a single peak at 1575 cm^{-1} ('G' peak), whilst other graphite species display a second peak feature at 1355 cm^{-1} ('D' peak) representing the presence of disordered graphite. The relative intensity of the peaks 'D' to 'G' is proportional to the presence of 'disordered' carbon and inversely proportional to graphite crystal size.^[9] Therefore, the quality of a CVD diamond film can be assessed in terms of the ratio of sp^2/sp^3 content determined from the corresponding Raman spectra, although it is also dependent on the excitation wavelength. This phenomenon was attributed to a resonance effect in which non-diamond carbon phases scatter much more effectively at higher excitation wavelengths. The sensitivity to the diamond component is maximised with UV excitation.^[10] Higher wavelengths are more sensitive to non-diamond species while shorter wavelengths produce Raman spectra with lower background, with a diamond peak relatively more intense, but the non-carbon phases are not revealed. Thus UV Raman is useful for studying small amounts of diamond present in a large sp^2 carbon matrix, while red or IR Raman is preferred for studying small sp^2 defects in otherwise pure diamond samples.

In the present study, a Renishaw 2000 instrument operating at room temperature has been used for the acquisition of the Raman spectra from the diamond films under study. The equipment offers the possibility of using three different laser excitation wavelengths: 325 nm (UV, He:Cd), 514 nm (green, Ar⁺) and 785 nm (red, diode laser).

2.5. Scanning electron microscopy

Scanning electron microscopy (SEM) is one of the most versatile techniques employed for the characterization of surface morphologies. In this study two scanning electron microscopes (SEM)s have been used: a JEOL JSM 5600LV and a JEOL JSM 6330F. In the 5600LV instrument the electron gun operates with a metal filament with the electrons being produced via thermionic emission, whereas the 6330F instrument operates with a field emission electron gun in ultra-high vacuum (UHV), being superior in terms of image resolution and magnification. With the latter microscope features down to the spot size (~10 nm) may be resolved.

Due to the charging effects promoted by the electron beam, insulating materials need special preparation before observation under SEM, as in the case of insulating diamond. To overcome this issue the samples are normally coated with a conductive metal layer or graphite about 10 - 15 nm thick.

2.6. Atomic force microscopy

Atomic force microscopy (AFM) works by scanning the surface of a specimen using a sharp tip (probe) at the end of a cantilever. The tip is slightly deflected according to Hooke's Law when in close proximity to the surface with the extent of the deflection being proportional to the topographic scale of the surface, relying on the forces between the probe and specimen.

In this study, a Bruker Multimode AFM instrument with 3D controller has been used to analyse diamond films and seeding layers using tapping mode. The equipment can operate in both contact and tapping mode. In tapping mode a stiff cantilever is oscillated close to the surface touching it intermittently and the changes to the resonant frequency or amplitude of the cantilever are measured. When operating in contact mode, the probe is deflected as it moves over the surface and the deflection is measured.

2.7. Secondary electron emission equipment

In this section two different setups are introduced which have been used for the secondary electron emission (SEE) measurements included in this work. One is a new setup built in the Diamond CVD group at the University of Bristol and the other is located at the Space Research Centre in the University of Leicester.

2.7.1. Bristol setup

The equipment used for the measurement of the SEE properties of the diamond films presented in this thesis is a home-built setup entirely developed in the aim of the present work. The equipment uses a Kimball Physics EGL-2022 electron gun, with beam energy capability from 50 eV to 5 keV, inserted in a stainless steel vacuum chamber operating at pressures $\sim 10^{-6}$ Torr. The setup consists of a system of phosphor screens acting as detectors and by viewing the light from these using photomultiplier tubes (PMTs) the signal equivalent to the electron emission from the samples was acquired and processed. The equipment has been designed to do measurements both in transmission and reflection configurations.

A detailed explanation of the working principles and equipment development is presented in chapter 4. The SEE yield results from this system will be presented in chapter 6.

2.7.2. Leicester setup

The group at Leicester University were partners in the original project to measure the SEE yield from diamond. Samples grown at Bristol were sent to Leicester for analysis, and their measured values compared to the values obtained in the Bristol apparatus.

The Leicester experimental setup is shown in figure 2.4. A vacuum chamber contains an insulated Large Faraday Cup (LFC) acting as the electron collector. The LFC contains a centrally-mounted, electrically insulated sample support which can be moved laterally and rotated around its axis. The sample holder and the collector can be independently biased to the desired voltage and the currents measured separately. The electron beam is generated by a ELS5000 electron gun (0.25 - 5 keV) to give a 50 μm spot size, and a beam current ranging from 10 nA to 10 μA , which is set normal to the sample surface. Keithley 6514 and 6517B electrometers and a 6485 Picoammeter operate as precision ammeters.

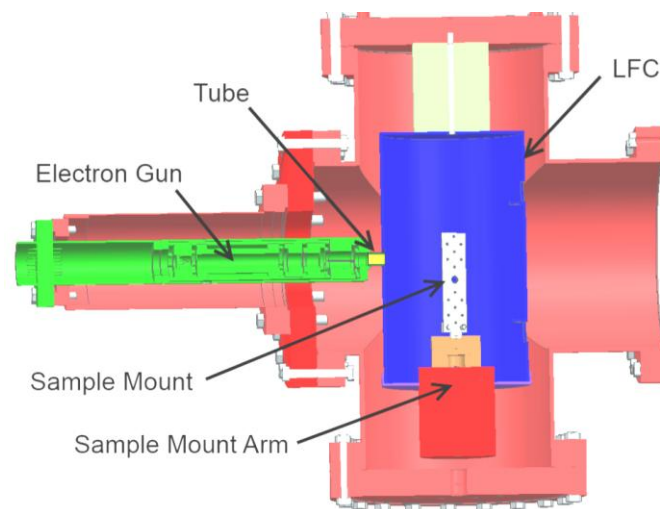


Figure 2.4- Apparatus for secondary electron emission measurements located at the University of Leicester.^[11]

Secondary electrons escaping from the sample surface, comprising low energy secondaries and elastic and inelastically scattered primaries, are collected by the LFC.

The total yield is calculated by the following relation:

$$\delta = \frac{I_{\text{LFC}}}{I_{\text{LFC}} + I_{\text{target}}} \quad (2.21)$$

where I_{LFC} is the LFC current and I_{target} is the sample or target current.

2.8. References

1. O.J.L. Fox, J.O.P. Holloway, G.M. Fuge, P.W. May and M.N.R. Ashfold, Electrospray deposition of diamond nanoparticle nucleation layers for subsequent CVD diamond growth, *Materials Research Society Symposium Proceedings* **1203** (2010) J17-27.
2. B. Vonnegut and R.L. Neubauer, Production of monodisperse liquid particles by electrical atomization, *Journal of Colloid Science* **7** (1952) 616.
3. G. Taylor, Disintegration of water drops in electric field, *Proceedings of the Royal Society of London Series A - Mathematical and Physical Sciences* **280** (1964) 383.

4. D.P.H. Smith, The electrohydrodynamic atomization of liquids, *IEEE Transactions on Industry Applications IA* **22** (1986) 527.
5. P. Ascarelli, S. Fontana, Dissimilar grit-size dependence of the diamond nucleation density on substrate surface pretreatments, *Applied Surface Science* **64** 4 (1993) 307-311.
6. J. Loader, in *Basic Laser Raman Spectroscopy*, edited by Heyden & Son Ltd., (1970).
7. R.J. Nemanich, J.T. Glass, G. Lucovsky, and R.E. Shroder, Raman scattering characterization of carbon bonding in diamond and diamondlike thin films, *Journal of Vacuum Science and Technology A* **6** (3) (1988) 1783-1787.
8. D.S. Knight and W.B. White, Characterization of diamond films by Raman spectroscopy, *Journal of Materials Research* **4** (1989) 385.
9. J. Filik, Raman Spectroscopy: a simple, non-destructive way to characterise diamond and diamond-like materials, *Spectroscopy Europe* **17** (5) (2005).
10. S. Praver and R.J. Nemanich, Raman spectroscopy of diamond and doped diamond, *Philosophical Transactions of the Research Society of London A* **362** (2004) 2537–2565.
11. J.S. Lapington, V. Taillandier, B.L. Cann, J. Howorth, J. Milnes, R. Vaz, P.W. May, N.A. Fox, R. Stevens and L. Wang, Investigation of the secondary electron emission characteristics of alternative dynode materials for imaging photomultipliers, *Journal of Instrumentation* **7** (2012) E04002.

Chapter 3. HFCVD deposition of diamond films

3.1. Introduction

As mentioned previously in section 1.5.2, diamond films are so versatile that they can easily be produced to exhibit p-type semiconducting properties when doped with boron. Their conductivity varies with the B-content and this can even reach metallic-like values for very high B levels ($\sim 10^{20} \text{ cm}^{-3}$).^[1] As seen in previous studies, the electrical properties of B-doped diamond films vary both with the B content and the crystallinity of the films. This is associated with the preferential B incorporation at the grain boundaries rather than in substitutional sites in the carbon matrix.^[2-4] Therefore when growing CVD diamond films under the same B percentage in the gas phase, the resistivity of the resulting films will be dependent upon the grain size, such that MC diamond films present normally lower resistivities than NC diamond films.

The aim of this section is to summarise a series of studies undertaken to understand the diamond growth under various growing conditions, and to verify the repeatability and reproducibility of the CVD reactors in use. Following that, a study on the effectiveness of the B-doping for MCD and NCD films, together with the analysis of the respective morphologies and Raman spectra is presented.

Different materials were used as substrates for the diamond growth, although not all will be included in the results section. This is due to the extensive amount of diamond samples prepared and also the fact that in many cases no relevant investigations were carried out on the samples, since they were grown to supply to external collaborators.

3.2. Experimental

All the diamond samples prepared for this thesis were deposited using the hot-filament (HF) CVD reactors in the Diamond CVD Group at the University of Bristol. To avoid any sample contamination by unwanted impurities, separate reactors were used for undoped and B-doped samples. The diamond films were grown on Si (100) p-doped to a resistivity of 1 - 40 Ω cm, except where otherwise stated. The substrates were cut to a size of 1 \times 1 cm² using a commercial laser milling machine from Oxford Laser micromachining systems as described in section 2.3. After being cut the samples were washed in methanol in an ultrasonic bath for 30 minutes cleaning each one before rinsing with deionised water (D.I.). The substrates were cleaned immediately before the application of any seeding layer.

Before deposition, the substrates were cleaned again with methanol followed by electrospray deposition (ESD) seeding with a 5 nm diamond colloidal suspension to ensure a high nucleation density. To understand the effectiveness of both processes some of the samples were manually abraded with diamond nanoparticles instead of being seeded by ESD. All the samples mentioned in this chapter have been seeded by ESD.

Diamond films were grown at a pressure of 20 Torr and substrate temperatures greater than 700 °C. For MC diamond films a ratio of 1% CH₄/H₂ was used, whereas for NC diamond films the methane concentration was increased to 2.5-5%. The source of B used was 5% diborane (B₂H₆) gas diluted in H₂, which was often diluted further to achieve lower doping levels. To ensure hydrogen termination after the growing process, the CH₄ and B₂H₆ flows were turned off, while maintaining the H₂ flow for an extra 5 min at the growth temperature. For a matter of duration and stability the filaments were made of tantalum or rhenium wire for the undoped and B-doped samples, respectively.

All the samples were analysed by Raman spectroscopy at room temperature by a Renishaw 2000 spectrometer, using UV 325 nm (HeCd laser) excitation wavelength. A JEOL JSM 5600LV SEM was used to analyse the surface morphology of the diamond films. Resistivity measurements were made using a digital voltmeter for two-point resistance measurements and a four-point probe method. This last method operates by pressing spring-loaded probes into contact with the sample surface, and measuring the resistance for a given applied voltage over a distance ~5 mm. This technique is expected to reduce considerably the effects of contact resistance, hence the results obtain from the equipment have shown Ohmic contacts.

3.3. Results and Discussion

The resistance measured from the diamond films in general did not have a linear variation with the amount of diborane added during the growth process. This fact was partially due to the B-adsorption by the materials within the reactor chamber, which desorbed back into the gas phase when the chamber became hot during the next deposition run. Thus, the results were dependent on the history of the chamber prior to a particular experiment. Therefore, the first experiments have been relative to testing the reactor in a series of consecutive cycles to evaluate the variation in the resistance of the diamond films without any B₂H₆ addition.

For a 'saturated' chamber (*i.e.*, that had been exposed to high concentrations for a long period and so had absorbed as much B as possible given its surface area and components) it was necessary to run the reactor in pure H₂ with no B₂H₆ added for approximately 24 hours before getting to a steady-state residual level of B in the films. An alternative method was to clean the chamber with isopropanol (IPA) after rubbing with fine sandpaper. It would still then take a few hours of operation in pure H₂ to bring the B concentration in the gas (and therefore in the film) to a steady state.

Given the importance in obtaining a predictable doping level in the samples, a preliminary study was conducted in order to evaluate the relation between the flow of B₂H₆ added to the gas mixture and the resistance measured from the resulting samples. To rapidly distinguish between the diamond films in terms of their resistances, four wide ranges were considered: non-doped (N.D.), residual doped (R.D.), medium-doped (M.D.) and heavily doped (H.D.). As mentioned previously, the N.D. diamond films ($\geq 10^6 \Omega$) were grown using a separate CVD reaction chamber free of impurities. Thus, films grown in this chamber have *zero* boron content. The R.D. range ($\sim 1 - 5 \text{ M}\Omega$), includes the films for which growth occurs using the residual B accumulated in the walls of the reaction chamber normally used to grow B-doped diamond, but without any additional B₂H₆ being added to the CVD gas mixture. The M.D. ($\sim 10 - 60 \text{ k}\Omega$) group corresponds to the films grown with flow rates of 0.1 - 0.2 sccm of B₂H₆, and the H.D. films ($\sim 100 - 900 \Omega$) are the films grown for higher B₂H₆ flow rates (> 0.2 sccm). In between these categories are included all the intermediate values.

3.3.1. MCD versus NCD films

After the preliminary tests, a first set of samples was produced using typical MCD growth conditions, a range of B-doping concentrations and constant thickness ($\sim 3.5 \mu\text{m}$). A second group of diamond samples has been prepared for the same thickness but under NCD deposition conditions, by increasing the flow of CH_4/H_2 . Tables 3.1 - 3.2 summarize the deposition parameters used for these samples.

Table 3.1 - Deposition parameters for the MCD films grown at a ratio of 1% CH_4/H_2 with different B-doping levels (at concentrations between 0 and 10000 ppm) and thicknesses $\sim 3.5 \mu\text{m}$, and the resistance values measured from the samples. R.D. = residual doping (see above).

Sample	H_2 (sccm) ¹	CH_4 (sccm)	B_2H_6 (sccm)	2-points resistance (Ω)	4-points resistance (Ω)
SMC1	200	2	0	5×10^6	3550
SMC2			R. D.	9×10^4	560
SMC3			0.1	1.8×10^4	400
SMC4			0.2	9000	350
SMC5			0.2	1800	230
SMC6			0.2	1600	180
SMC7			0.5	346	65
SMC8			0.5	123	48

Table 3.2- Deposition parameters for NCD films grown at 2.5-5% CH_4/H_2 with different B-doping levels (at concentrations between 0 and 10000 ppm) and thickness $\sim 3.5 \mu\text{m}$, plus the resistance values measured from the samples. R.D. = residual doping (see above).

Sample	H_2 (sccm)	CH_4 (sccm)	B_2H_6 (sccm)	2-point resistance (Ω)	4-points resistance (Ω)
SNC1	200	10	0	6×10^7	4.2×10^5
SNC2		10	R. D.	1.9×10^7	8×10^4
SNC3		10	0.1	1×10^4	1200
SNC4		10	0.2	9000	980
SNC5		10	0.2	1500	200
SNC6		6	R. D.	5.4×10^5	9800
SNC7		6	0.2	1700	310
SNC8		5	0.5	933	155
SNC9		5	0.5	600	100

¹ Unit for flow rate: standard cubic centimetres (cm^3) per minute (sccm).

The tables show that the values for 4-point resistance are considerably lower than the 2-point values. The differences between the two sets of values represent the effective contact resistance which is eliminated in the 4-point probe method. The film thicknesses were measured in some samples but not from all of the samples, as this requires laborious SEM cross-sectional analysis. However the thicknesses have all been estimated to be $\sim 3.5 \mu\text{m}$ based upon previous results from films grown under similar conditions. Also, there may be some variations in thickness across the whole film. Therefore, the resistance values were not converted into resistivity.

To obtain a precise measurement of the B-content within the films secondary ion mass spectrometry (SIMS) analysis could have been employed but for a question of availability this technique was not used. However, considering the work published by May *et al.* ^[3] from samples grown in the same HFCVD reactor, the B-contents may be roughly estimated in the range of $10^{19} - 10^{20} \text{ cm}^{-3}$.

3.3.1.1. Comparison between resistance values

Considering the variation of 2-point and 4-point resistance, from the plot in figure 3.1, it is clear that the 4-point resistance values are considerably lower than the 2-point resistance, presenting a roughly linear dependence.

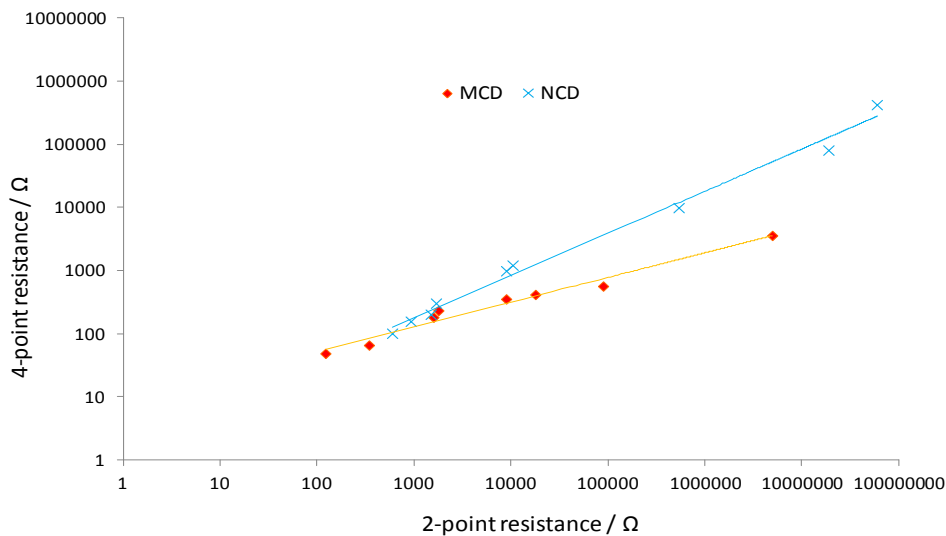


Figure 3.1- Plot of the variation of 4-point resistance against 2-point resistance for MCD and NCD films (logarithmic plot), and linear best fits showing the increase in the gradient as crystallite size decreases.

In accordance with previous studies^[3], for the same B level, the resistance of the MCD films was considerably smaller than for the NCD films. In other words, the MCD films were more conductive than NCD films for the same B addition to the CVD gas mixture, denoting a lower doping efficiency in the latter.

Some approximations can be considered in estimation of the B incorporation into the diamond lattice according to the process gas mixture. In general, the B/C ratios in the films are one order of magnitude smaller than the B/C ratios in the gas-phase mixture.^[2] It is expected that the conductivity is approximately linear as a function of B content in the interval of approximately $5 \times 10^{20} \text{ cm}^{-3}$ to $6 \times 10^{21} \text{ cm}^{-3}$, changing to near metallic for greater values.^[4]

3.3.1.2. Microstructure Characterization

The morphologies of the samples are presented in figure 3.2. As expected from previous experiments, the crystallites were predominantly randomly-oriented with grain sizes in the range of 0.5 - 1 μm . To clarify the predictions about the growth rate for a deposition run with the duration of 7 hours, a selection of samples were cleaved and the cross-sections analysed via SEM. Figure 3.3 shows an image taken from one of the cross-sections, proving the predicted growth rate for the HFCVD reactor of $\sim 3.5 \mu\text{m}$ per hour for diamond films grown under typical MCD conditions.

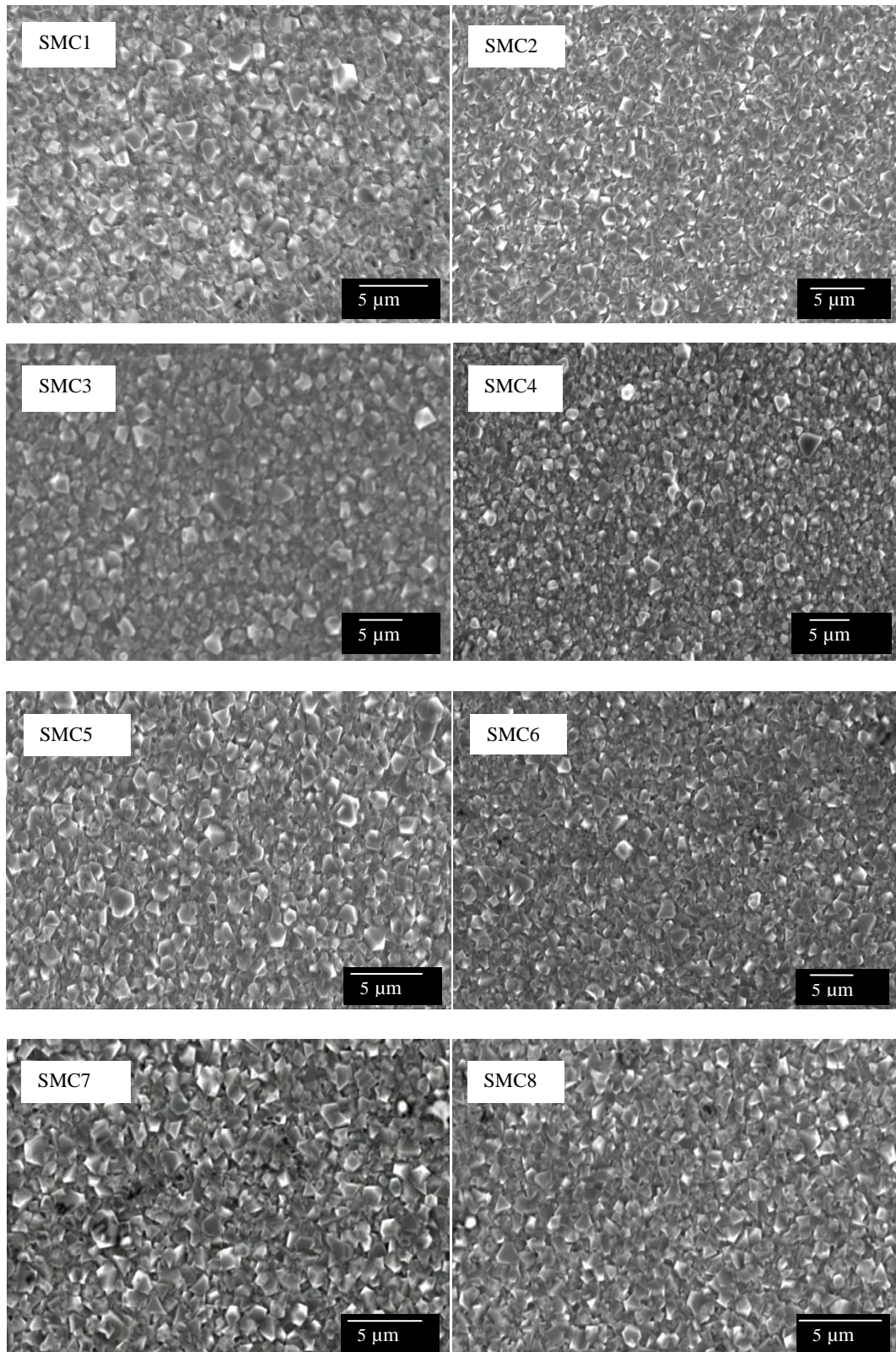


Figure 3.2- SEM images of the surfaces of the MCD films (see Table 3.1) with thickness $\sim 3.5 \mu\text{m}$, showing predominantly randomly-oriented crystallites with grain sizes around $0.5 - 1 \mu\text{m}$. The increasing B content has not has a significant effect upon the film morphology.

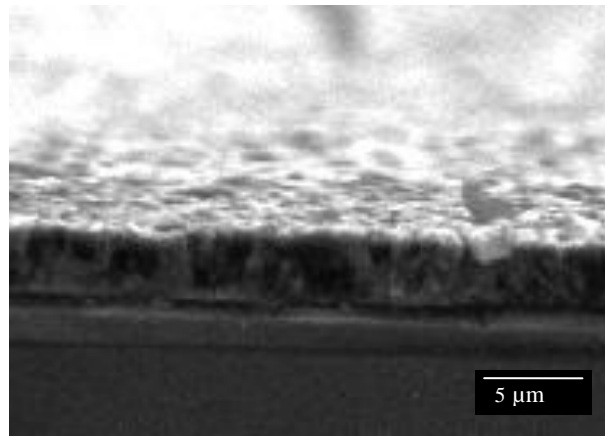
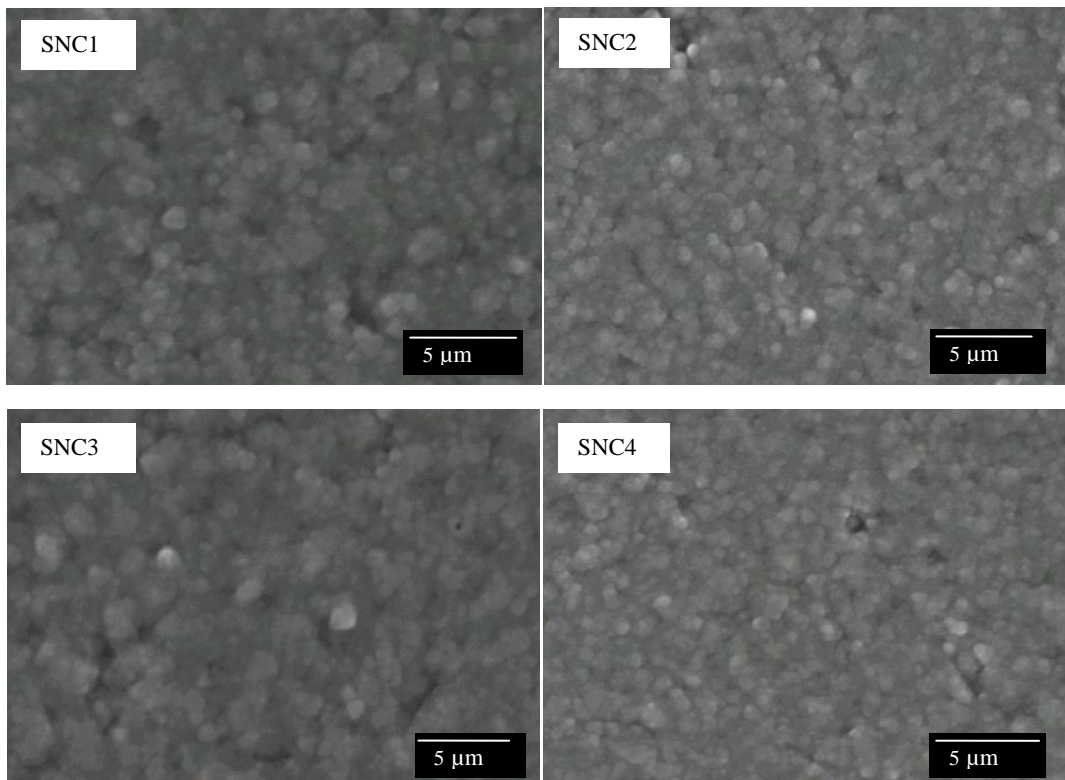


Figure 3.3- SEM images of the cross-section of sample SMC5, showing a thickness $\sim 3.5 \mu\text{m}$ as predicted for a 7 hour deposition run with 1% CH_4/H_2 . This shows that the growth rate was also not significantly affected by B content.

Figure 3.4 shows the SEM images for the NCD films (see Table 3.2). With the increase in CH_4 concentration the grain size has been reduced in comparison to the MCD films. The crystal size decreased for ratios $\text{CH}_4/\text{H}_2 > 3\%$ and the crystalline morphology tended to completely disappear giving rise to an aggregate of diamond nanocrystallites and disordered graphite (so-called ‘cauliflower’ diamond).^[5]



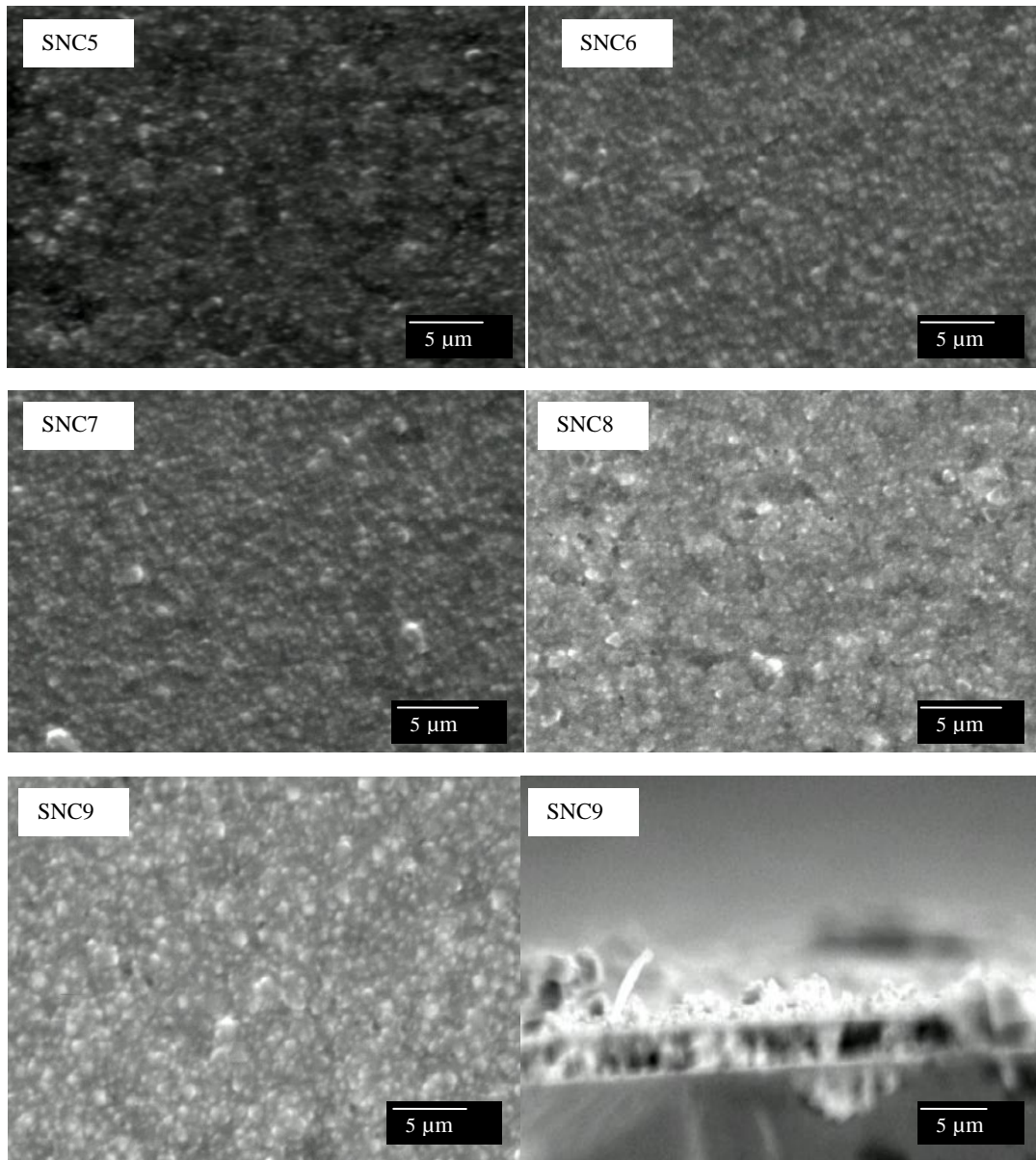


Figure 3.4- SEM images of the surface of the NCD films, showing a decrease in crystallite size with increasing methane concentration (samples SNC1 - SNC7), and a cauliflower or amorphous appearance for the highest methane concentrations (SNC8 and SNC9).

The morphology of the films created in NCD diamond films is smoother than in the MC films, even if in some of the samples the grains are still faceted. The film thickness (see last picture of figure 3.4) for the sample SNC9 is $\sim 4 \mu\text{m}$ which may be related with the high CH_4 content in the gas mixture. The growth rate was not significantly affected by B content.

3.3.1.3. Raman spectra and B-doping level

Usually, UV light does not make evident the characteristic features of B-doped diamond films, such as the Fano effect and the peaks at 500 and 1225 cm^{-1} .^[8,9] Although those features were not detectable in the spectras taken from these samples.

The resonant enhancement of the sp^2 and sp^3 bonding of the films is very dependent on the excitation wavelength. The sensitivity to the diamond component is maximised with UV excitation.^[6] Higher wavelengths reveal more clearly the non-diamond species, while shorter wavelengths produce Raman spectra with lower background, with a diamond peak relatively more intense, but the non-carbon phases are not revealed.

In this section, data are presented showing the variation of electrical resistance and Raman spectra as a function of B addition during the growth of the B-doped diamond films, comparing the effect observed for films with different crystallinities. Figures 3.5 and 3.6 show the Raman spectra acquired from the MCD and NCD films, respectively. In each graph the spectra have been organized in order of decreasing resistance.

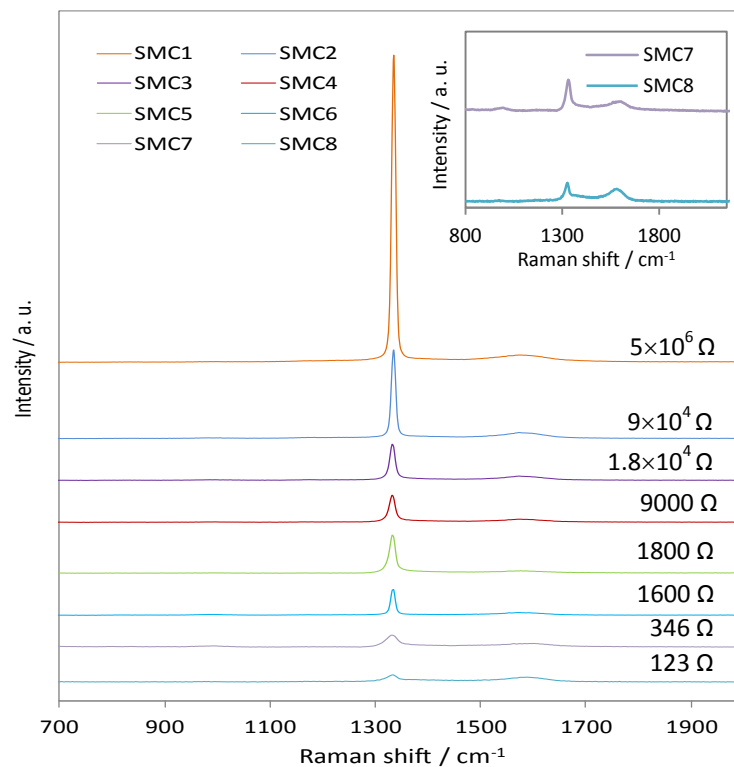


Figure 3.5- Raman spectra obtained with UV (325 nm) excitation wavelength from MCD films with different B-doping levels and thickness $\sim 3.5\text{ }\mu\text{m}$ (Table 3.1). The films decrease

in resistance from the top to the bottom. The spectra of samples SMC7 and SMC8 are inset for better detail.

The effects of addition of boron to diamond films can be visualised through the Raman spectra. With the increasing addition of B the *Fano* effect becomes visible with the intensity of the diamond peak at 1332 cm^{-1} decreasing greatly in intensity and downshifting in wavenumber. In the spectra of figure 3.5, the intensity of the diamond peak decreases and broadens when the resistance decreases, especially for the three spectra at the bottom of the graph, which have the highest B-content.

Such effects can be described as the quantum interference between the zone-centre optical phonon and a continuum of electronic transitions around the same energy.^[6] This effect happens above a critical percolation threshold corresponding to the onset of the metallic conductivity on the boron impurity band. Its parameters can be deduced by fitting the Raman shifts of heavily boron-doped diamond films.^[7]

In the graph, a small G band ($\sim 1580\text{ cm}^{-1}$) can also be detected indicating the presence of crystalline graphite impurities which are possibly created by the B impurities perturbing the lattice symmetry, especially at high B contents. A broad feature at $\sim 1000\text{ cm}^{-1}$ is also visible. Figure 3.6 shows the Raman spectra obtained from the NCD films (Table 3.2). A similar effect in the diamond peak can be observed with the increase in the B content in these films. There is a visible decrease of its intensity, plus a pronounced broadening accompanied with a shift to lower wavenumbers.

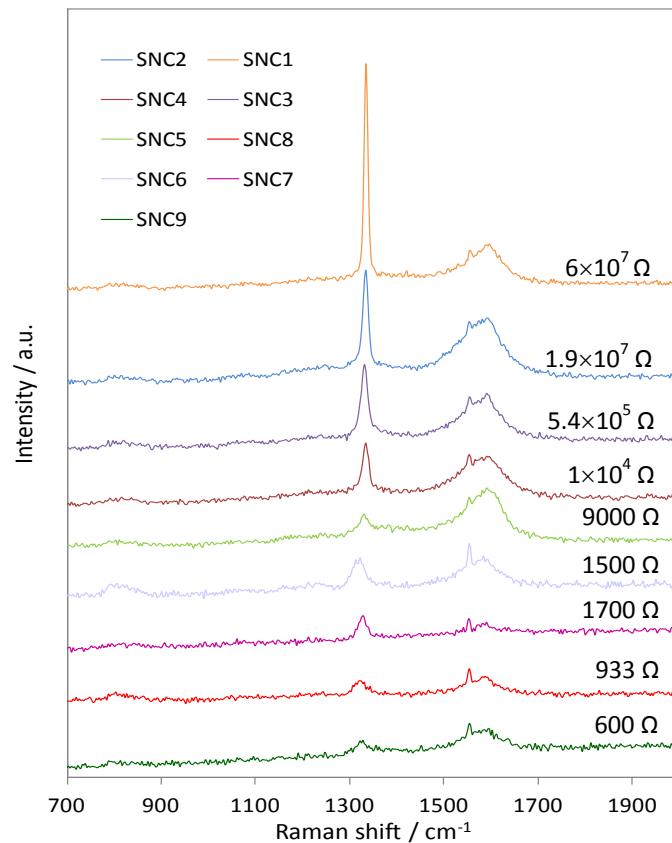


Figure 3.6 - Raman spectra obtained with UV (325 nm) excitation from NCD films with different B-doping levels and thickness $\sim 3.5 \mu\text{m}$. The B content increases from the top to the bottom of the graph.

Actually, the UV Raman spectra from the NCD films are similar in appearance and show trends similar to those from the MCD films, except for the intensity of the G band ($\sim 1580 \text{ cm}^{-1}$) that is more prominent in the case of NCD films. This fact is related with an increase in the sp^2 carbon content at the increased number of grain boundaries.

3.4. Conclusions

In this study the growth of diamond films with different crystallinities and B-levels has been explored using a HFCVD reactor. Parameters such as the growth rate of the diamond films, and the influence of the increase in the CH_4 concentration on the crystal morphology were investigated. Moreover, the addition of B to the CVD gas phase and the effectiveness of the B incorporation into the carbon lattice were assessed by means of the measurement of the electrical properties of both MCD and NCD films.

The B-doping of MCD films has shown to be more effective. This fact has been associated to the preferential location of B at the grain boundaries associated to the higher contents of graphitic carbon and the increased number of defects in NCD films. In addition, the effect of the B content was observed through the modifications in the Raman spectra taken from the films, where some of the characteristic features of the Fano effect have been observed. The decrease in the intensity of the diamond peak at 1332.5 cm^{-1} together with its broadening and shift to lower wavelengths was clearly observed from the UV spectra of both types of diamond film. The absence of other features has been attributed to the excitation wavelength in use which masks some of those features.

As a summary, from these experiments was established the fundamental parameters to produce B-doped HFCVD diamond films according to the specifications required.

3.5. References

1. R. Kalish, Doping of Diamond, *Carbon* **37** (1999) 781.
2. P.W. May, W.J. Ludlow, M. Hannaway, P.J. Heard, J.A. Smith, and K.N. Rosser, Raman and conductivity studies of boron-doped microcrystalline diamond, faceted nanocrystalline diamond and cauliflower diamond films, *Diamond and Related Materials* **17** (2008) 105-117.
3. P.W. May, W.J. Ludlow, M. Hannaway, P.J. Heard, J.A. Smith, and K.N. Rosser, Raman and conductivity studies of boron-doped microcrystalline diamond, faceted nanocrystalline diamond and cauliflower diamond films, *Chemical Physics Letters* **446** (2007) 103-108.
4. P.W. May, P. Overton, J.A. Smith and K.N. Rosser, Boron doping of microcrystalline and nanocrystalline diamond films. Where is the Boron going?, *Materials Research Symposium Proceedings* **1039** (2008) 17-03.
5. P.W. May, Diamond thin films a 21st-century material, *Philosophical Transactions of the Research Society of London A* **358** (2000) 474-494.
6. J.W. Ager III, W. Walukiewicz, M.D. McCluskey, M.A. Plano, and M.I. Landstrass, Fano interference of the Raman phonon in heavily boron-doped diamond films grown by chemical vapor deposition, *Applied Physics Letters* **66** (1995) 616-618.

7. F. Pruvost and A. Deneuve, Characterization of homoepitaxial heavily boron-doped diamond films from their Raman spectra, *Diamond and Related Materials* **10** (2001) 531-535.
8. S. Praver and R.J. Nemanich, Raman spectroscopy of diamond and doped diamond, *Philosophical Transactions of the Research Society of London A* **362** (2004) 2537–2565.
9. M. Bernard, A. Deneuve and P. Muret, Non-destructive determination of the boron concentration of heavily doped metallic diamond thin films from Raman spectroscopy, *Diamond and Related Materials* **13** (2004) 282-286.

Chapter 4.

Development of a new apparatus for secondary electron emission measurements

This section describes the process of developing a entirely new home-built apparatus for the acquisition of the secondary electron emission coefficients from diamond CVD films, detailing the design criteria, the preliminary testing, the definition of components and finally the procedures undertaken for the calibration of the new system.

4.1. Initial assumptions and testing

Electron multiplication dynodes can operate in reflection or transmission, as presented in figure 4.1. In reflection configuration, a primary electron beam strikes a surface and secondary electrons are reflected. In transmission mode, primaries strike a surface and secondaries are emitted at the opposite surface of a thin diamond film.

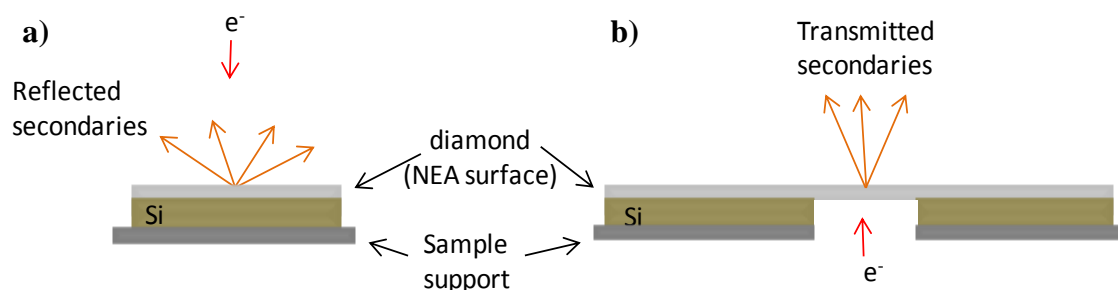


Figure 4.1- Sketch of the configuration for measurements in reflection (a), and transmission (b) configurations, respectively.

Theoretically, a transmission configuration is superior since it avoids electron-beam contamination effects, such as H-desorption at the NEA surface. Moreover, in actual detectors a transmission arrangement creates a linear propagation of signal through the detector, with a guaranteed primary electron collision at the first dynode.^[1] Despite the difficulty of producing sustainable diamond thin membranes or the application of strong fields for the extraction of the electrons, a transmission configuration would still be preferable.

The objective at this stage was to build a setup capable of measuring both the reflection and transmission of secondary electrons from CVD diamond films. Therefore, prior to building the system adequate for this purpose, a few preliminary experiments were performed to test the working principles. Experiments in transmission configuration had never been performed by the Diamond group, and so it was necessary to get an idea of the operating parameters, such as beam energy and film thickness, that would yield results.

The project partners in the original grant proposed to measure SEE yields from diamond. Thus, the University of Leicester had designed and built a traditional system for measuring yields based on a Faraday cup (FC) acting as a collector. Rather than replicate their system, it was decided to build a SEE system that operated using a different measurement paradigm. This way, it would be possible to compare and contrast the results from the two systems and determine the advantages or disadvantages of either approach.

In the new system, the secondary electrons would be accelerated onto a phosphor screen (PS) and the light emitted by the PS, whose intensity is directly related to the number of electrons that struck the phosphor, is collected by a photomultiplier tube (PMT). However, the intensity is also a function of the energy of the electrons, the type of phosphor used, and these have to be accounted for by prior calibration. Also, since the phosphor only captures a fraction of the electrons that are in its solid angle, a further correction needs to be applied in order to convert the measured value into the SEE yield.

Figure 4.2 presents a scheme of the initial setup that was used, which consisted of a high vacuum chamber (10^{-7} Torr) with an electron gun pointing towards a glass viewport. The samples were mounted on a metal holder in front of the viewport and a low-voltage PS P22R was placed behind it.

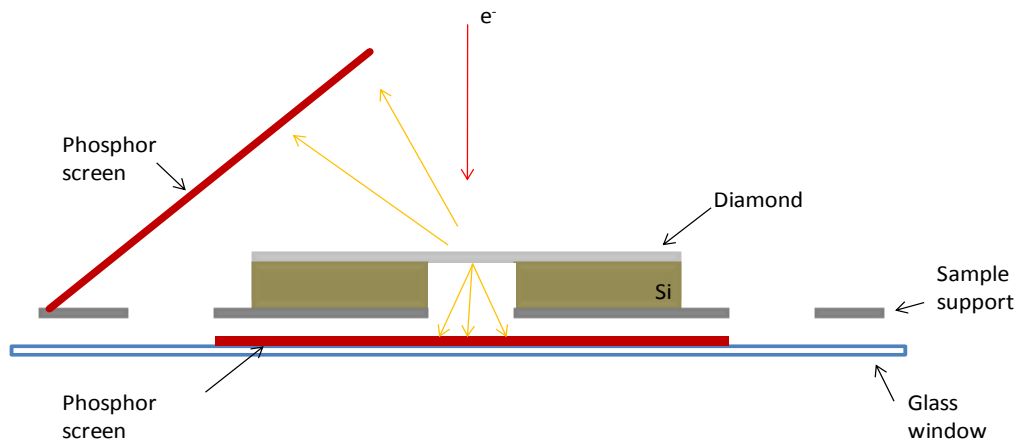


Figure 4.2- Schematic diagram of the electron transmission and reflection testing rig used for preliminary tests.

The electron beam struck the top surface of the diamond and the secondaries exited through the opposite surface, striking the PS placed right behind. Another PS was added at 45° to capture some of the reflected secondaries.

The rear PS allows visual observation of the spot, by the emission of light (photons) when impinged by electrons with a typical threshold of a few hundred eV. More importantly, it allows verification of whether there is any transmission of electrons through the diamond film. In the case of reflection, the electrons reaching the front PS are a mixture of primaries, backscattered electrons and secondaries. In these experiments the positioning of the PS was optimised in order to maximize the signal obtained from the reflection of electrons, which was chosen to be close to 45° to the sample surface. A monochromator was used to disperse the light and measure the wavelength output of the PS.

When a substance absorbs energy, a fraction of that energy may be emitted again from the solid in the form of electromagnetic radiation (photons) in the near-visible or visible region. Materials showing this characteristic are called luminescent, and are generally referred as phosphors.^[2] When the source of excitation are electrons the phenomenon is identified as cathodoluminescence.

The colour of the light emitted by the PS depends on the phosphor material. There is a wide range of phosphor powders available in the market, depending on the application and wavelength required. In the present case, the PS detector requires the use of a low-threshold-energy phosphor. At this stage, a yttrium oxide-sulfide phosphor activated with europium ($\text{Y}_2\text{O}_2\text{S}:\text{Eu} + \text{Fe}_2\text{O}_3$) was used (P22R). This phosphor emits in the red with an emission peak at 611 nm. Another phosphor (P15) was also used. This is a self-activated oxide phosphor

made of zinc oxide (ZnO.Zn), which has a blue-green emittance at 504 nm in wavelength. The phosphor is prepared in a suspension by mixing a solution of potassium silicate (K_2SiO_3) in D.I. water at 10% cc with ~ 1 g of the required phosphor powder.

The phosphor suspension was then applied on top of a square piece of glass and left to dry resulting in a thin coverage with a few nanometres. Normally, in order to avoid charging effects a thin metal layer is applied on the glass surface before depositing the phosphor.

Having all the components placed together, a series of diamond membranes with thicknesses between 3 - 15 μm were tested. These films were excessively thick and did not allow any transmission and therefore no signal was detected. Therefore, while deposition protocols for making thin ($< 0.5 \mu m$) and continuous diamond films were being developed in the Diamond group in Bristol, a 140 nm diamond membrane kindly supplied by Dr. Oliver Williams (Fraunhofer Institute) was tested instead. Figure 4.3 shows the schematic diagram of the setup that was used for mounting the samples and the positioning of the PS. Figure 4.4 presents the images taken during one experiment with the beam energy at 5 keV.

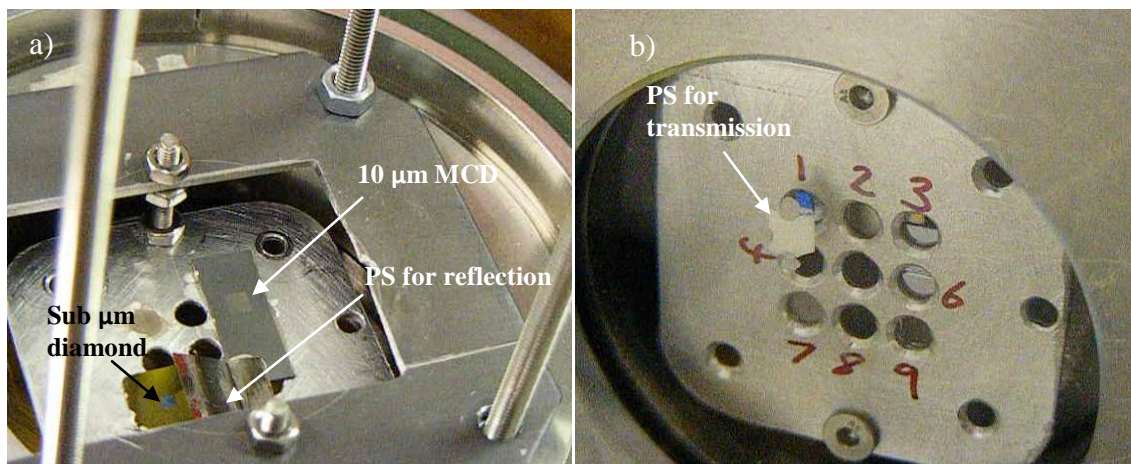


Figure 4.3- Pictures of the sample holder with nine apertures to allow evaluation of the transmission of electrons through the diamond membranes, showing the PS positioned at 45° to the sample surface for reflection (in a) and the PS fixed on the glass window by means of silver tag, placed behind the thin diamond membrane (in b).

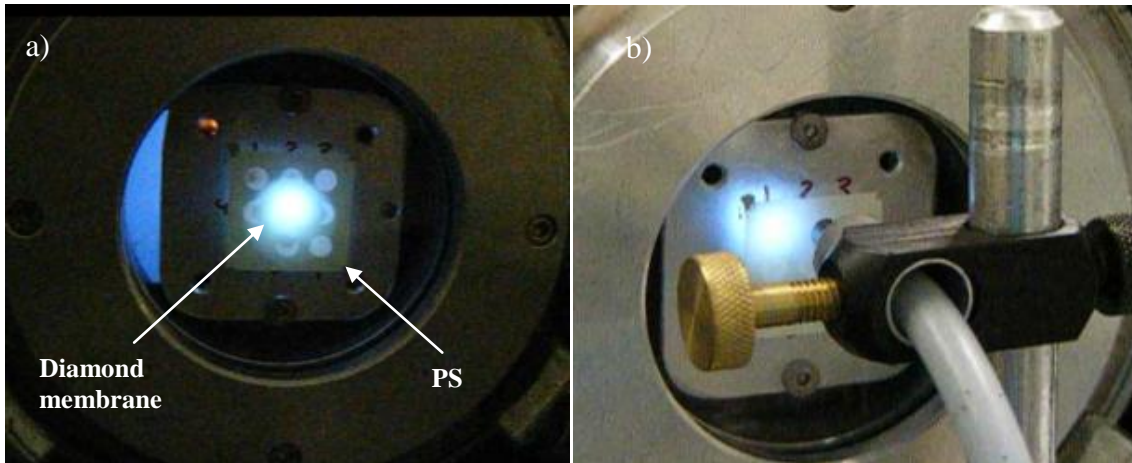


Figure 4.4- Pictures taken during one of the experiments made at 5 keV, using a P15 PS facing the emitting surface of a 140 nm thick diamond membrane, showing a strong transmission through the diamond film with the electron gun pointing toward the observer (in a). In b) a fibre-optic cable takes the light to a monochromator in order to quantify the transmitted signal through the diamond membrane in comparison with a the primary signal detected by the PS in the absence of the membrane.

The graphs from figure 4.5 show a comparison between the signals acquired at different beam energies (3 - 5 keV). Specifically, the measurements made with and without a membrane placed normal to the electron beam taken at 5 keV are presented in figure 4.5b. From the graph it was possible to estimate a total transmission of about 37% for this diamond thickness.

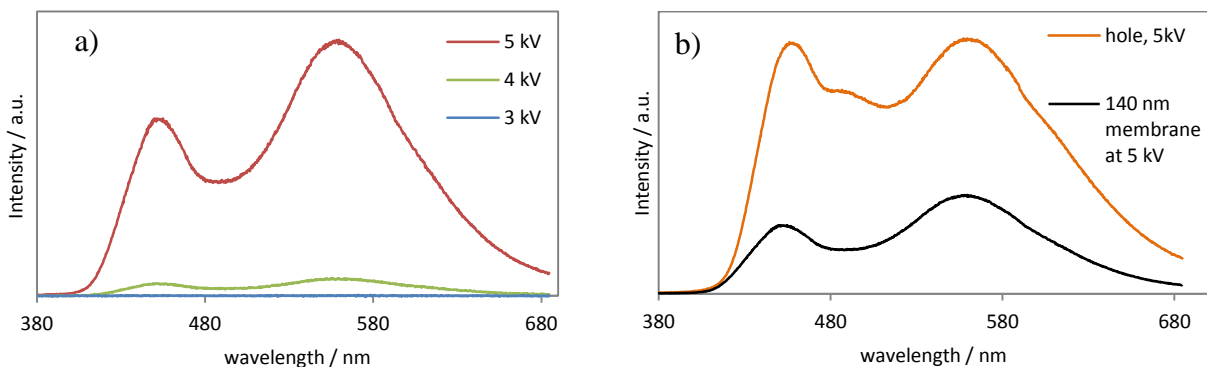


Figure 4.5- Graphs showing the emission spectrum obtained from the PS at different primary electron energies impinging a 140 nm diamond membrane (a), and the emission curves with and without the diamond membrane acquired at 5 keV (b).

The ultimate goal would be having a membrane sufficiently thin to produce a gain larger than unity, representing electron multiplication. Nevertheless, from these measurements the principle of obtaining electron emission measurements based on a system of PS seemed viable. This was the starting point for the design and construction of the new equipment. After a series of trials the configuration for the new setup resulted as presented in figures 4.6 and 4.7.

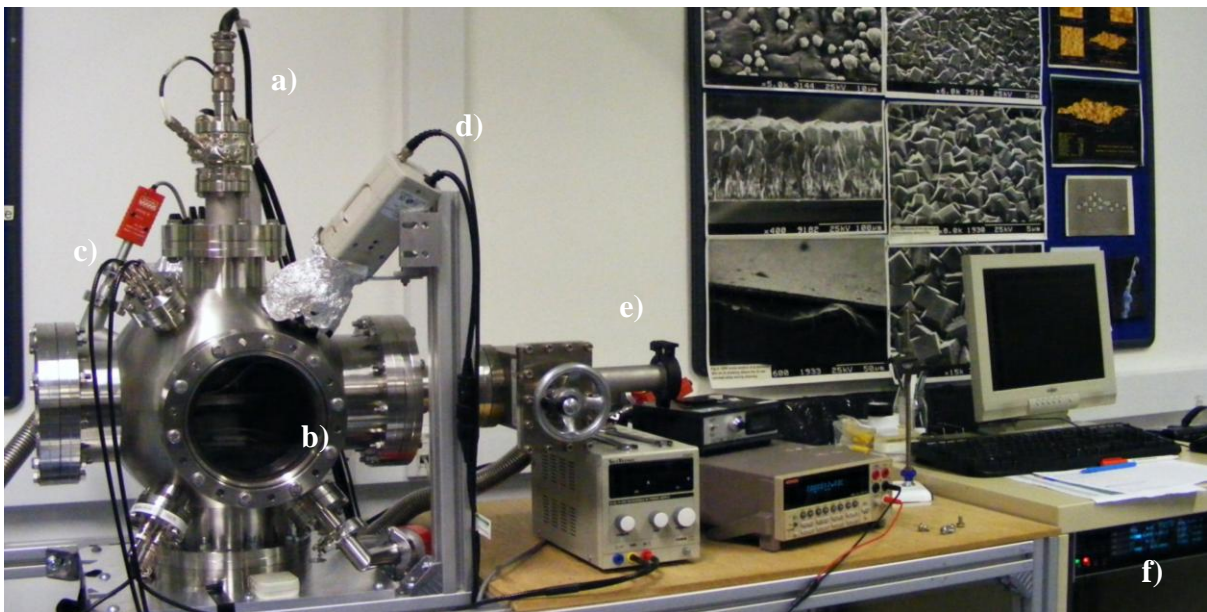


Figure 4.6- Picture of the setup developed for the acquisition of SEE yields, prepared to work in both reflection and transmission configurations (front view). From the image are identifiable the main components which compose the external parts of the equipment: (a) electron gun, (b) view port for visual control (fully covered during the measurements), (c) feedthroughs for biasing and current reading, (d) camera for beam observation under calibration, (e) loading port and (f) electron gun control box.



Figure 4.7- Picture of the setup developed for the acquisition of SEE yields (side views), showing: (a) electron gun, (b) support arm for the PMT during reflection measurements, and associated view-port (c) (covered during the measurements, except for the PMT area), (d) support arm for the PMT for transmission measurements, (e) front view port for visual control and (f) turbo pump connected to the back of the vacuum chamber.

In figure 4.8 are presented the schematic diagrams of the setup mounted inside the vacuum chamber.

For the measurements in transmission, a couple of PS were placed underneath the emission surface of a transmissive membrane. A P22 PS (in red) was placed parallel to the sample to compare the signal intensity equivalent to the incident primary electron beam with the signal measured in transmission from a diamond membrane.

A grounded P15 PS (in blue) has been placed at an adjustable angle around 30° relative to the first one, as schematically presented in the figure below. It is expected that the primaries move in their trajectory directly towards P22 PS. By means of an applied bias to the mesh, the secondaries are accelerated towards and collected at the P15 PS.

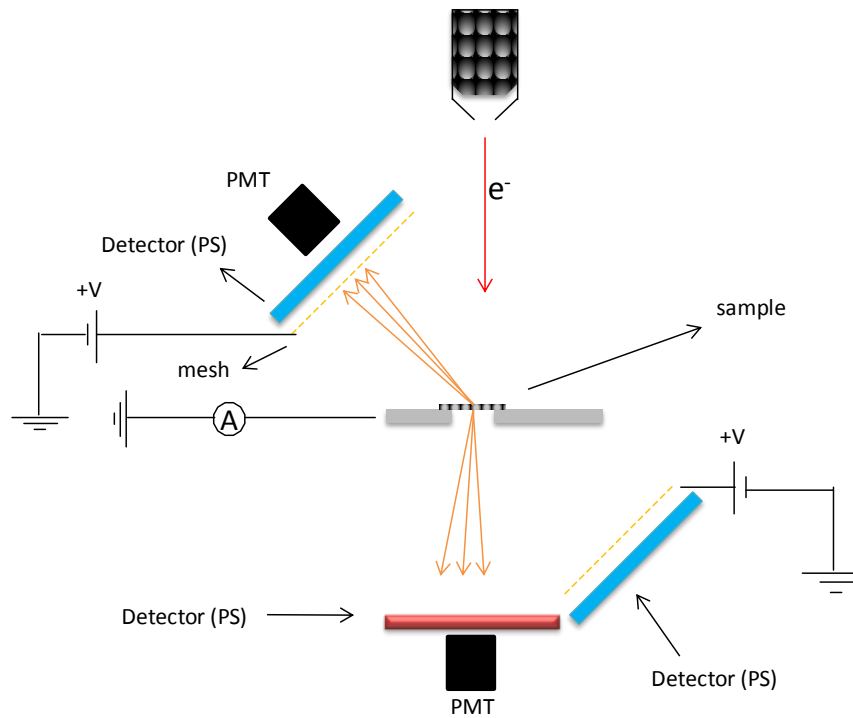


Figure 4.8- Schematic diagram of the setup adopted for reflection and transmission measurements, using a system with PSs and PMTs.

For measurements taken in reflection, the secondary electrons emitted from a sample surface normal to a primary electron beam are collected by a P15 PS positioned at an angle of 45° relative to the emission surface. Both sample stage and PS are electrically insulated allowing for biasing, and the collected currents can be measured by a precision ammeter. During the first stages of development, the signal was acquired by a 9128B PMT with a spectral range of 280 - 630 nm and transferred to an oscilloscope. Later on, a Labview program was written allowing acquisition of the data directly from the measurements, and partial operation of the electron gun, although many of its functions were kept in manual control as described below. To verify the accuracy of the readings acquired by the software, the values detected by the PMT and acquired by the Labview program were checked periodically by means of an oscilloscope and compared.

4.1.1. System calibration

The equipment uses a Kimball Physics EGL-2022 electron gun with a matching EGL-2022 power supply, with beam energy capability from 50 eV to 5 keV and beam current from 1 nA

to 500 μA . The gun uses a Ta disc cathode and is suitable to run at pressures from 10^{-11} up to 10^{-5} torr, although the cathode lifetime may be reduced in poor vacuum conditions or for high beam currents.

The electron gun and power supply are a complete subsystem which was purchased and attached to the vacuum system. The power supply has a modular design with small power supply clusters necessary to generate the voltages to run the electron gun: energy, source voltage, source current, control-grid voltage, first anode voltage, first anode current, focusing lens voltage, emission current and X and Y deflection voltages. The electron beam is first accelerated in the grid and first anode and then focused and accelerated or decelerated in the extraction segment of the gun. The electron gun schematics are presented in figure 4.9.

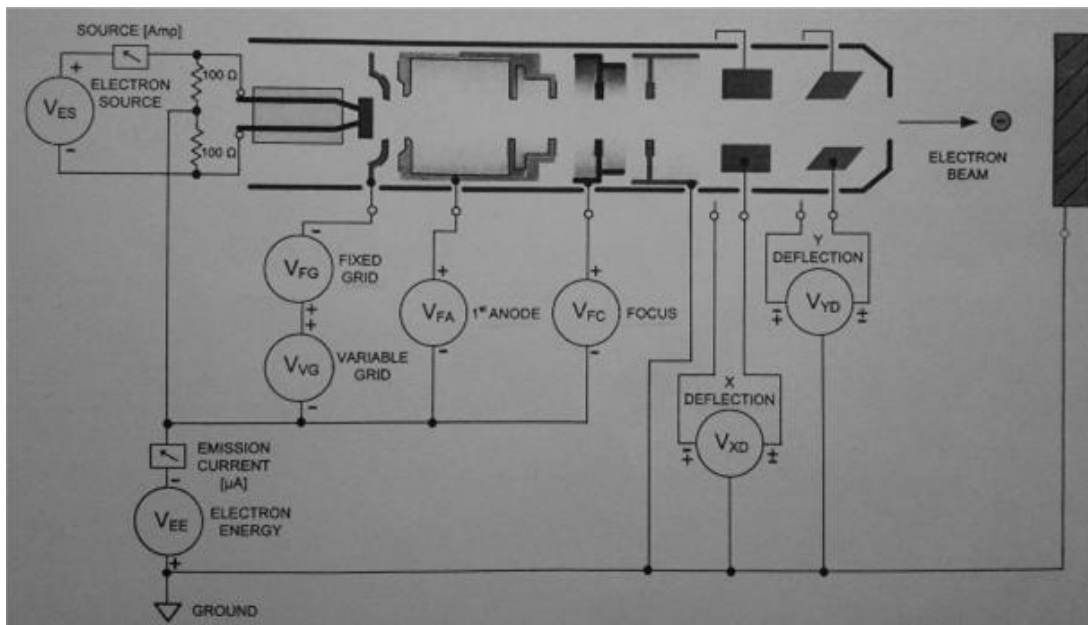


Figure 4.9- Standard EGL-2022 electron gun block diagram (from Kimball Physics EGL-2022 electron gun manual).

The power supply was provided with a Kimball Physics FlexPanel digital interface controller. An additional external connector on the panel adds the option of remote computer control and metering of all voltage supplies by means of analog input-output systems at ground potential. Remote computer control was carried out by rear panel National Instruments connectors and a home-developed computer program using Labview software. The program provides a virtual panel of controls and meters for the electron gun voltages on a computer screen.

4.1.1.1. Electron Beam output monitoring

For the initial gun operation it was essential to align the electron gun and optimize the size, focus and position of the beam spot for established power supply settings. Although being a highly time-consuming procedure it was found to be crucial for the success and reproducibility of any further testing.

Ideally, the beam calibration should be done both by visual control and current monitoring simultaneously. Hence, a small Faraday cup (SFC) and a grounded PS were mounted side-by-side on the sample holder, as shown in figure 4.10.

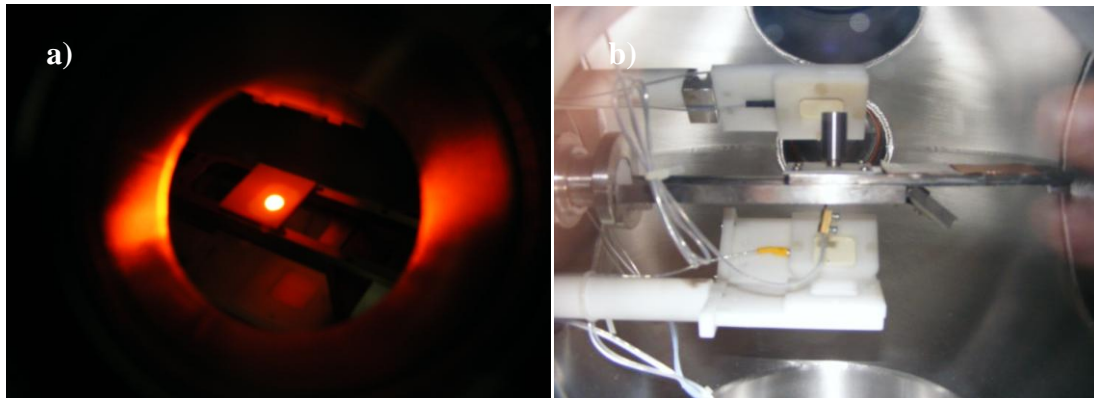


Figure 4.10- Images showing the method adopted for the electron beam calibration, with visual control of the spot by means of a phosphor screen (a) and control of the beam current using a SFC placed side-by-side with the phosphor screen on the sample holder.

The SFC was connected to a multimeter working as an ammeter to measure the beam current. The procedure consisted of running the electron gun manually, adjusting the beam energy in increments of 50 eV, for a constant emission current. Then, for each one of the beam energies, the voltages of the remaining adjustable components were manually ramped within the range allowed (see table 4.1). The conditions which corresponded to the smallest spot size with optimum focus were then selected as the optimum values. An electron filter was applied to the view-port for better observation of the spot.

Table 4.1 - Power supply controllable outputs.

Energy (eV)	0 to 5 k
Grid (V)	0 to +100
First anode (V)	0 to +1000
Focus (V)	0 to +5000
X deflection (V)	-150 to +150
Y deflection (V)	-150 to +150

After completing the experiments for all the beam energies (50eV - 5 keV), the sample holder was moved and the SFC placed facing the electron gun. The process was repeated again for all the beam energies but this time, using the optimal voltages obtained from the previous observations with the phosphor and varying only the X and Y deflections within the allowed range in order to obtain the maximum current output acquired by a multimeter. The highest current was an indication that the electron beam was fully centred with the SFC. Again, the same testing was repeated for different emission currents. The beam calibration conditions thereby determined were verified periodically because any involuntary small twist in the sample holder or even any changes in the gun filament would affect the calibration of the system.

The calibration data were curve-fitted and the corresponding equations loaded into the software to allow the remote running of the electron gun, although after the first experiments the values were converted into a look-up table for easy processing.

Besides the beam calibration, a few other important conclusions were taken from these experiments, namely the variation of the emission current with respect to the beam current measured at the target. Figures 4.11 and 4.12 show the relations detected between the beam current at the target and the emission current E_c from the electron gun, at different beam energies.

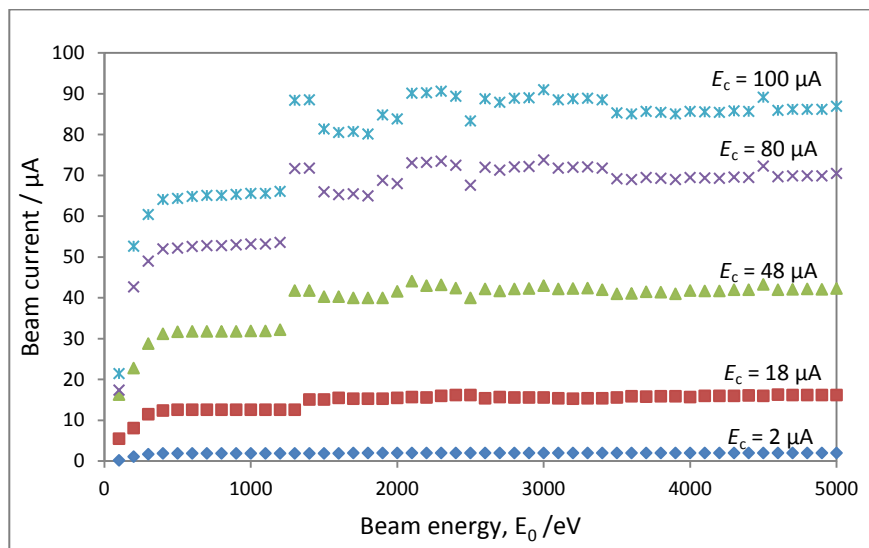


Figure 4.11- Graph with the variation of the beam current with the emission current E_c for beam energies up to 5 keV, showing an increased reduction of the beam current with increasing E_c . For $E_0 < 1.3$ keV the difference between both values is even more remarkable, possibly because a percentage of the electrons do not have enough energy to reach the SFC.

The emission current is the sum of the beam current plus all the current that goes to ground through the grounded elements within the gun, which is consistent with the variations observed.

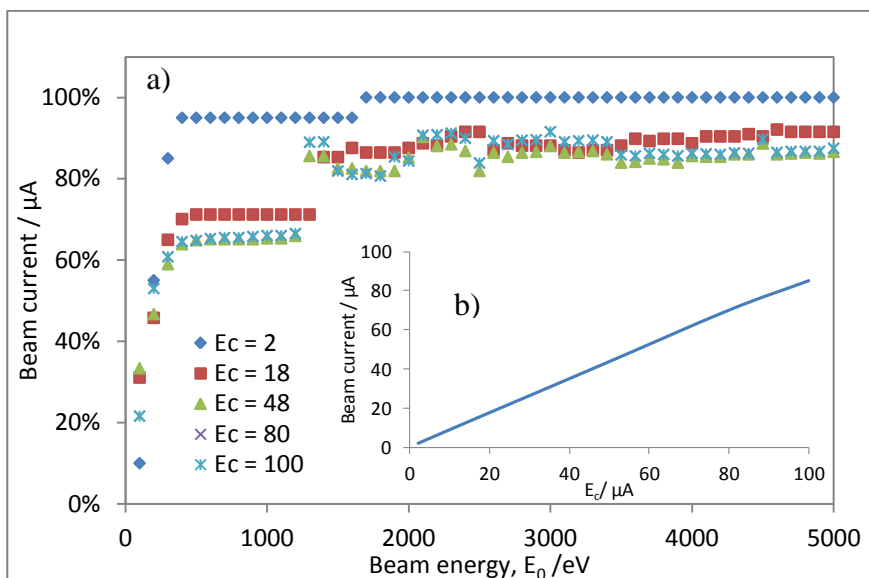


Figure 4.12- Graph of the variation of the beam current with the beam energy for five different values of emission current E_c (μA), showing a decrease in the ratio of the beam current to E_c (a) and the linearity between E_c and the beam current (b).

From the graphs it is possible to visualize the increase of the beam current with E_c , although for higher E_c there is a reduction in the ratio between beam current and E_c . In addition, for low beam energies the number of electrons reaching the target in a well defined high energy spot is considerably smaller increasing substantially for $E_0 > 500$ eV.

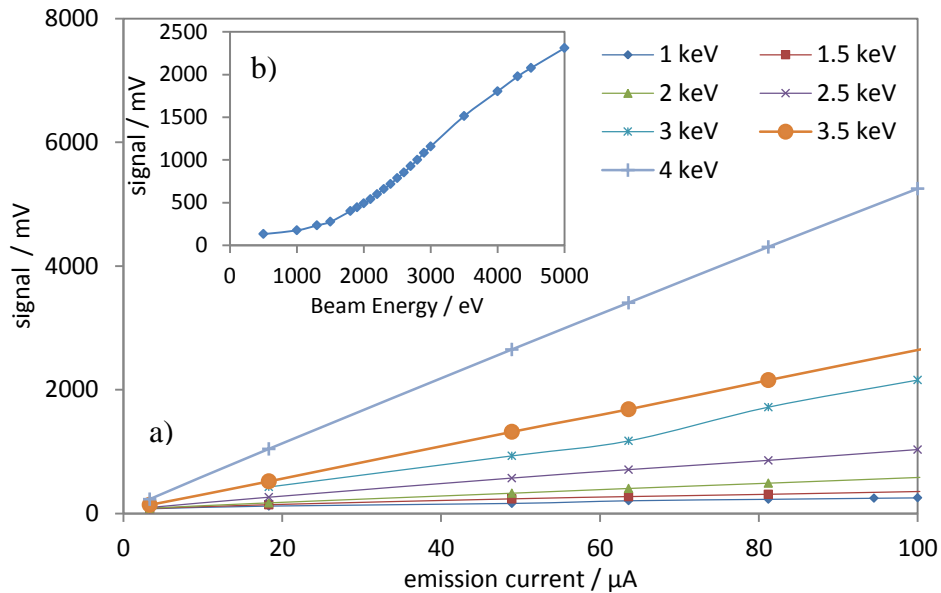


Figure 4.13- Graphs representing the variation of the signal acquired by the PMT, showing a linear relation and the increase of gradient with beam energy.

Another characteristic that was observed was the variation of phosphor response with the beam energy. For any type of detector it is very important that the detection efficiency is a well determined function of the incident electron beam energy. The absolute detection efficiency of an electron multiplier is dependent upon the ratio of the number of received electrons to that of the true signals generated. Figure 4.13 shows one experiment taken of this variation for different emission currents where the PMT response curve shows linearity with E_c . Figure 4.13b shows that the PMT response curve is approximately linear with the beam energy. Moreover, a constant beam current could be maintained over a range of beam energies for approximately the same spot size (~ 2 mm). Generally, at beam energies below 500 eV the detector efficiency is relatively insensitive to energy, which may be associated with the shape of the curve at low beam energies.

The power supply also had the option to feedback stabilized Emission Current Control (ECC) adjusting the source voltage and providing a stable and constant emission current from the cathode. All the calibration studies in the aim of this research were carried out using the ECC option for increased stability.

Having acquired all the data suitable for the electron gun calibration the following stage was to test actual samples and define a measurement method.

4.1.1.2. Measurement method

The samples were mounted by means of conducting silver dag on a copper plate coated with graphite to allow good back contact. The graphite coating was prepared from ground graphite powder in aqueous solution which was applied to the surface and left to dry for a couple of hours before attaching the samples. Graphite was chosen to coat the copper plate because this avoids any additional source of reflected electrons, without compromising the back contact of the samples. Graphite is often used as a plasma limiter at the walls of reactors, to control the impurity flux^[3], since it is one of the poorest secondary electron emitters, having maximum yield coefficients of 1.0 and 0.45 for soot.^[4]

Different approaches were attempted for the calibration of the detectors. In the case of the transmission configuration the process was relatively simple and did not require the use of a reference system for calibration. From the preliminary experiments described above, it seemed reasonable to adopt a comparison between the signal measured by the detector with the electron beam impinging directly on the detector, and the signal measured with a thin diamond film placed in between. The SEE yield would correspond to the ratio of those values. The preparation of the samples and the results from a series of experiments undertaken in transmission configuration are included in chapter 7.

Calibration for the measurements in reflection configuration was more complicated. Alongside the samples to test were placed a graphite sample and a previously measured reference sample with known yield. The sample holder was then loaded into the vacuum chamber and left to pump down until reaching a pressure in the order of $\sim 10^{-7}$ Torr. The reference samples which have been used in the calibration of the system have been tested at the SRC at the University of Leicester, using the apparatus described in section 2.7.2. The samples were diamond CVD films with hydrogen termination, which means that after each

measurement they had to be cleaned and re-hydrogenated again. This process was repeated using the exact same conditions after each set of measurements.

The measurement method consisted of, first measuring the signal response of the graphite sample over all the range of primary energies. These data are designated as S_0 , which corresponds to:

$$S_0 = S_{\text{graphite}} + S_{\text{background}} \quad (4.1)$$

where $S_{\text{background}}$ is the signal obtained from backscattered electrons that have been emitted from the substrate holder, mount and surroundings.

Then, moving the sample holder to centre the beam on the diamond sample to measure, the data acquired is designated S_{sec} according to the expression:

$$S_{\text{sec}} = S_{\text{diamond}} + S_{\text{background}} \quad (4.2)$$

The approximate SEE yield is calculated by the ratio of the signals,

$$Yield = \frac{S_{\text{sec}}}{S_0} \quad (4.3)$$

although a few approximations have to be considered. For instance, a correction factor for the graphite has to be taken in account as described below.

The relation in equation 4.3 is valid considering that the background signal is much smaller than the signal emitted by the diamond sample ($S_{\text{background}} \ll S_{\text{diamond}}$) and including in the expression $\delta_{\text{graphite}}(E_0)$ which corresponds to the yield measured for the graphite sample at each primary energy, then a more accurate expression is:

$$Yield = \frac{S_{\text{sample}}}{S_{\text{graphite}}} \cdot \delta_{\text{graphite}}(E_0) \quad (4.4)$$

Neither the maximum yield value nor the primary energy at which it occurs is affected by this correction, only the yield curves after correction are slightly narrowed. The correction factor

$\delta_{\text{graphite}}(E_0)$ is a factor of the primary energy and can be taken from the literature yield curves for graphite^[3-7], considering a fitting for each value of E_0 in a theoretical yield curve from graphite. Again, these considerations are reasonable due to the very small yield of graphite, equalling unity at most.^[4]

In addition, in order to validate the assumption that $S_{\text{background}} \ll S_{\text{diamond}}$, the background was measured using a metal plate with a 1 cm square hole. The hole represents the area that would normally be occupied by a sample. Both current and signal were measured, running the setup with the electron beam centred on the hole. The current was measured through a metal grid positioned in front of the view-port where the PMT was positioned, and was connected to an ammeter. The results are presented in figure 4.14.

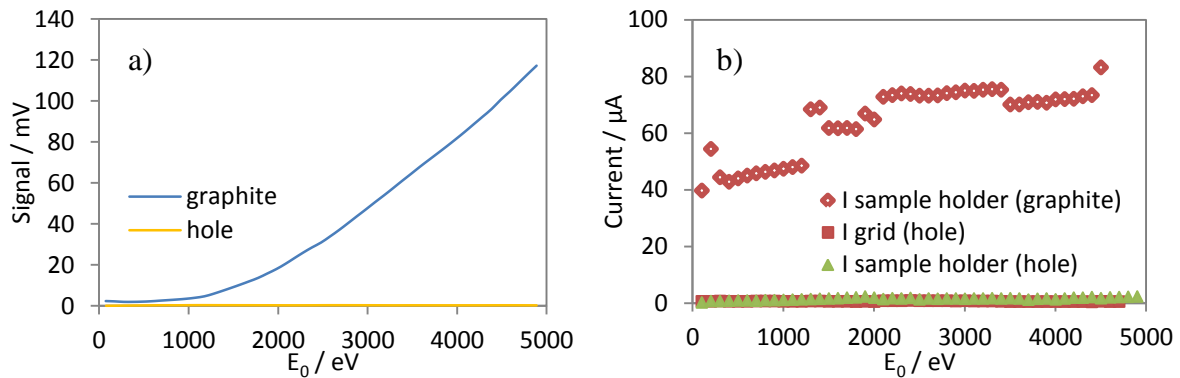


Figure 4.14- Measurement of $S_{\text{background}}$ taken with the electron beam centred with a 1 cm square hole made on a metal plate similar to the ones used for the measurements mounted in the sample holder (a). The graph in (b) shows the measurement of the background current by comparing the currents measured with the grid placed in front of the view-port where the PMT is associated, the current at the sample holder and the current generated in the sample holder with the beam facing a graphite sample.

$S_{\text{background}}$ corresponds to the signal that originated from the electron cloud around the hole with energies $\ll E_0$.

From the graphs in figure 4.14 it is possible to verify that the background signal and current were very small when compared to the actual signal to measure. This shows that the approximations considered for the measurement method seem reasonable. Therefore, the relative maximum yields acquired from different samples after measurement under the same conditions should be correct and reliable.

Another approach to verify the measurements is by comparing the values of yield measured in specific conditions with the yields measured in other equipment and using the latter as a reference. After acquiring S_0 and S_{sec} and the yield calculated using the expression in equation 4.4, the results were related to the reference sample which was measured using the same procedure. Thus, the known yield from the reference sample is compared with the one thereby calculated and the same relation is established for all of the diamond samples measured.

The measurement setup allowed biasing of both sample and detector. Therefore, experiments were undertaken to optimize the biasing conditions in order to obtain a good equivalence between the values acquired with this (reference sample and others) setup and the ones obtained at SRC in Leicester. For this purpose, a series of experiments were done by measuring S_{sec} at constant E_0 , applying a range of conditions: (a) biasing the sample alone, (b) biasing the detector alone and (c) biasing sample and detector together.

As mentioned above, the first samples measured had been previously measured with the equipment described in chapter 2. Differences might be expected, since a yield determined by current measurements is more absolute, since is expected that all the electrons in an enclosed FC are expected to be detected. In an emission process like the one presented, only a fraction of the electrons will be detected by the phosphor detector. This fact is related to the cosine distribution expected for the reflected electrons.^[8]

The graphs in figure 4.15 show some of the experiments done with diamond films grown by HFCVD and tested in both equipments. The samples were $\sim 2.3 \mu\text{m}$ medium B-doped diamond films on Si with resistances of 5 and 170 k Ω , respectively.

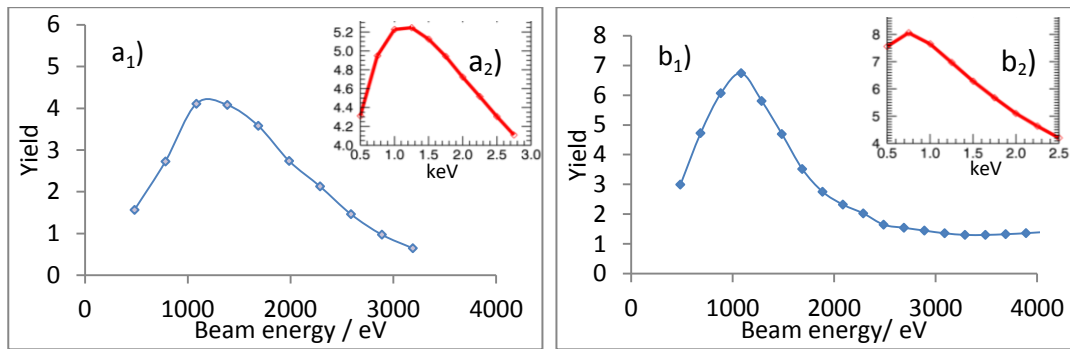


Figure 4.15 - Graphs showing the SEE yields measured from two different samples in both setups. The graphs in blue (a_1 and b_1) were obtained from the new setup and the ones in red (a_2 and b_2) at SRC. The samples were $\sim 2.3 \mu\text{m}$ medium B-doped diamond films on Si (5 and 170 $\text{k}\Omega$, respectively, in a) and b)).

The results show a difference of around 13% in the samples measured using both sets of equipment. This represents the correction factor to apply to the measurements taken with the system of PS acting as detectors.

Some of these results have been published by Lapington *et al.*^[9] but only relative to the measurements done at the SRC. The corresponding samples were prepared in the HFCVD systems in the Diamond group as part of the collaboration amongst the project partners.

4.2. Conclusions

A new piece of equipment has been developed for the acquisition of SEE yield data from diamond films. The setup consists of a system of PS acting as detectors, associated to a PMT for the acquisition of signals which are transferred to a computer with a Labview interface. The reflection yields are calculated by the ratio of the signal measured from a specific sample by the signal corresponding to the primaries, after subtracting the background signal. A graphite sample has been used to calibrate the background associated to the measurements and the respective yield is applied as a correction factor. The values measured in the new apparatus presented a difference of around 13% in relation to those measured at the SRC, which uses the traditional method of acquisition of the currents at the target and a LFC used as detector. The yield values are then corrected in relation to a reference sample with known yield.

In the case of measurements in transmission configuration, the signal acquired in the presence of a diamond membrane is divided by the signal from the one resulting from the direct incidence of the electron beam on the PS, without the need of a reference sample.

Although some improvements can be done, the new equipment is ready to perform measurements.

4.3. References

1. J.S. Lapington, P.W. May, N.A. Fox, J. Howorth and J.A. Milnes, Investigation of the secondary emission characteristics of CVD diamond films for electron amplification, *Nuclear Instruments and Methods in Physics Research A* **610** (2009) 253-257.
2. J.H. De Boer, in *Electron Emission and Adsorption Phenomena*, Cambridge University Press, chapter 16, 17 (1935)399-445.
3. H. Farhang, E. Napchan and B.H. Blott, Electron backscattering and secondary electron emission from carbon targets: comparison of experimental results with Monte Carlo simulations, *Journal of Physics D: Applied Physics* **26** (1993) 2266-2271.
4. H. Bruining, in *Physics and Applications of Secondary electron Emission*, Pergamon Press, McGraw-Hill, New York (1954).
5. J. Cazaux, Charging in Scanning Electron Microscopy “from Inside and Outside”, *Scanning* **26** (2004) 181–203.
6. M.E. Woods, B.J. Hopkins, G.F. Matthews, G.M. McCracken, P.M. Sewell and H. Fahrang, An investigation of the secondary-electron emission of carbon samples exposed to a hydrogen plasma, *Journal of Physics D: Applied Physics* **20** (1987) 1136-1142.
7. C.G.H. Walker, M.M. El Gomati, A. Assa'd, M. Zadrazil, The secondary electron emission yield for 24 solid elements excited by primary electrons in the range 250-5000eV: a theory / experiment comparison, *Scanning* **30** (2008) 365-380.
8. J.H. Jonker, On the theory of secondary electron emission, *Philips Research Reports*, **7** (1952) 1-20.
9. J.S. Lapington, V. Taillandier, B.L. Cann, J. Howorth, J. Milnes, R. Vaz, P.W. May, N.A. Fox, R. Stevens and L. Wang, Investigation of the secondary electron emission characteristics of alternative dynode materials for imaging photomultipliers, *Journal of Instrumentation* **7** (2012) E04002.

Chapter 5.

Studies of the SEE from HFCVD diamond films

5.1. Introduction

As detailed previously in section 1.8.1, the emission of secondary electrons from a solid is the result of a combination of three processes: the generation of internal secondaries, their diffusion through the material and, finally, their emission into the vacuum. These processes depend on the emitter properties and determine the yield values that can be measured.

This chapter contains a comprehensive study of the electron emission from a diversity of HFCVD diamond films designed to have specific characteristics in terms of the B content, morphology, thickness, substrate material and surface termination. The yields from MCD and NCD films which were grown to a range of conductivity levels on both Si and Mo substrates were compared. These experiments were conducted in diamond films with thicknesses of $\sim 3.5 \mu\text{m}$. In addition, a set of B-doped MCD films with thicknesses ranging $0.5 - 4 \mu\text{m}$ on Si were tested and the values compared with the previous ones. A selection of samples has undergone subsequent surface treatments of hydrogenation, oxygenation, caesiation and lithiation. The yields from the C/H, C/O/Li and C/O/Cs were evaluated considering the variations across the surfaces and under prolonged electron beam exposition.

5.2. Experimental

The diamond films were grown on $1 \times 1 \text{ cm}^2$ substrates of both p-doped Si (100) and Mo. The substrates were cut using a commercial laser milling machine from Oxford Laser micromachining systems as described in section 2.3. After being cut the samples were immersed in methanol and cleaned in an ultrasonic bath for 30 minutes, before rising with D.I. water. Before deposition, the substrates were cleaned with methanol followed by seeding with ESD using a 5 nm diamond colloidal suspension in methanol to ensure a high nucleation density. All the diamond films were deposited in the HFCVD reactors in the Diamond CVD Group at the University of Bristol using Re filaments. The growth process occurred at a pressure of 20 Torr and using different process gas concentrations, as described in table 5.1. The gas source of boron was 5% B_2H_6 diluted in H_2 . The B contents have been inferred from resistivity measurements.

The samples have been grouped into different sets according to the specific characteristics. For instance, set 1 and 3 correspond to diamond films grown to a thickness of $\sim 3.5 \text{ }\mu\text{m}$, using standard MCD deposition conditions in a gas mixing ratio of 1% CH_4/H_2 with different B_2H_6 additions and using both Si and Mo substrates, respectively. Set 2 includes MCD films grown for different thicknesses on Si, but with constant B_2H_6 additions. Finally, sets 4 and 5 contain NCD films $\sim 3.5 \text{ }\mu\text{m}$ thick, produced using a mixing ratio of 3% CH_4/H_2 with different B_2H_6 additions and using both Si and Mo substrates.

To ensure hydrogen termination, the CVD depositions were finalized by switching off the CH_4 and B_2H_6 flows for the last 5 min of each cycle, while maintaining the H_2 flow and keeping the temperature constant for that period of time, before turning off the filament. This process was performed for all the samples. In the cases where the diamond surfaces suffered further hydrogenation, the treatments were carried out under MW PCVD conditions for 5 minutes in 500 sccm of H_2 , at a pressure of 80 Torr and a power of 1 kW, creating a substrate temperature of below $600 \text{ }^\circ\text{C}$, followed by cooling down in hydrogen for 5 minutes.

Table 5.1 - HFCVD diamond deposition conditions for the samples used in the present study, divided into different sets according to the substrate material (Si *versus* Mo), crystallinity (MCD *versus* NCD), thickness (constant or variable) and resistance (in decreasing order for each set).

Sample	Substrate	Crystal	H ₂ (sccm)	CH ₄ (sccm)	B ₂ H ₆ (sccm)	Thickness (μm)	2-point resistance (Ω)
Set 1	Si	MCD	200	2	0	3.5	5 M
					R.D.		102 k
					0.2		13 k
					0.5		320
					0.7		40
Set 2	Si	MCD	200	2	0.2	0.5	2.3 k
						1.15	1.9 k
						2	1.8 k
						4	2.5 k
Set 3	Mo	MCD	200	2	R.D.	3.5	15 k
					0.2		10 k
					0.2		1.1 k
					0.5		659
					0.7		23
Set 4	Si	NCD	200	6	R.D.	3.5	133 k
					R.D.		15 k
					0.2		4.5 k
					0.2		1.7 k
					0.5		600
					0.7		47
Set 5	Mo	NCD	200	6	R.D.	3.5	1.6 k
					R.D.		4.1 k
					0.7		245

For the oxygenation treatments, the diamond films were submitted to ozone treatment in a Jelight UVO Ozone cleaner for 30 minutes, to ensure an even oxygen termination. In the case of caesiated and lithiated surfaces, Cs and Li were deposited on previously oxidized surfaces, by thermal evaporation of the respective metal dispensers from SAES Getters.

The evaporation process was conducted in a Balzer 510 coater working at a pressure of 2×10^{-3} Torr, where a quartz crystal served to monitor the thickness of the coatings.

For caesiation, the conditions were regulated to deposit a Cs monolayer on the sample surfaces, whereas for Li approximately 50 nm thick coatings were obtained. After caesiation the samples were annealed for 5 - 10 minutes at 200 °C. Such annealing treatment was done immediately after caesiation without exposing the samples to the atmosphere, since it is believed that the Cs oxidises if exposed to air before annealing. The lithiated samples were washed in D.I. water to remove the excess of Li, followed by isopropanol (IPA) and drying. Prior to the measurements the LiO terminated samples were annealed at 150 °C for 30 minutes.

All the samples were analysed using a JEOL 5600 SEM and the Raman spectra were obtained at room temperature using a Renishaw 2000 spectrometer, using UV 325 nm (HeCd laser) and green 514 nm (Ar⁺ laser) excitation wavelengths. The resistance measurements were made using a digital voltmeter.

The SEE experiments were conducted in a high vacuum chamber ($\sim 10^{-7}$ Torr) as described in section 4.1. A schematic diagram of the setup for measurements in reflection is displayed in figure 5.1. The yield values as a function of the primary beam energy were measured using the same conditions for all the diamond samples. The samples were mounted on the sample holder using primarily silver dag to position them and to ensure a good back contact, after which they were firmly clamped with a metal plate on top. Together with the samples to be measured were mounted a reference sample and a graphite sample. The reference sample has a known yield value measured previously and serves to calibrate the values obtained from the samples under measurement. The graphite sample has been previously tested, and serves to measure the background signal, as detailed in section 4.1.1.2.

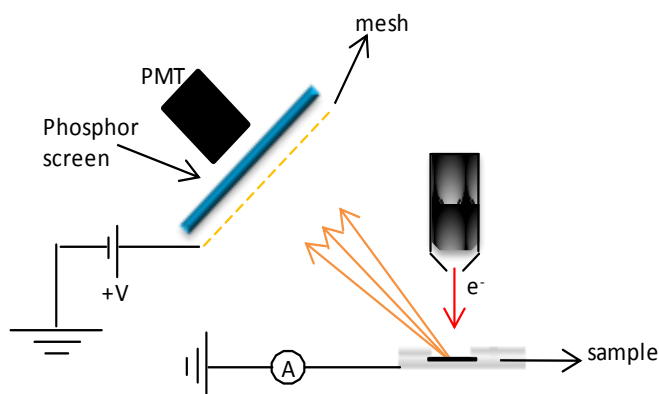


Figure 5.1- Schematic diagram of the setup used for measurements in a reflection configuration.

The measurements were acquired for beam energies up to 4.5 keV, $\sim 100 \mu\text{A}$ for the emission current, 500 V for the mesh bias and 10 V for the sample bias. For higher precision the signals were acquired from three different beam exposure areas ($\sim 2 \text{ mm}$) of the surface and an average taken of those values. The yield values were obtained by the ratio of the signal measured from the sample S_{sample} to the signal measured from graphite S_{graphite} , and the result multiplied by a correction factor $\delta_{\text{graphite}}(E_0)$ corresponding to the known yield of graphite at that primary energy, as detailed in section 4.1.1.2.

5.3. Results and discussion

After deposition, the quality of the diamond films was assessed by Raman spectroscopy and the crystal morphologies assessed using SEM imaging. The B-content was estimated by 2-point resistance measurements (see table 5.1). Following characterization, SEE yield measurements were performed before and after surface functionalization with H, CsO and LiO layers of selected samples. The effect of a prolonged primary beam exposure on the yield was investigated for the different diamond surface terminations.

5.3.1. Measurement of the SEE yield from MCD films on Si and Mo

A comparison between the SEE yields measured from ten different samples has been done. The samples belong to the sets 1 and 3 (table 5.1), corresponding to MCD films with the same thickness ($\sim 3.5 \mu\text{m}$), with a range of B concentrations using Si and Mo substrates, respectively. As presented in figure 5.2, the SEE yield values obtained are between 6 and 14, which is lower than many of the values reported in the literature. However, Bekker *et al.*^[1] and Mearini *et al.*^[2] have reported similar values (6-14) obtained for H-terminated diamond on Mo. In addition, Ascarelli *et al.*^[3], Dvorkin *et al.*^[4], Trucchi *et al.*^[5] and TERNYAK *et al.*^[6] reported yield values of 5.8-18 for H-terminated diamond on Si. The results are also consistent with some previous measurements from HFCVD diamond films performed by J. Lapington *et al.*^[7] The yields are generally higher for Mo than for Si, probably as a result of the increased conductivity of the substrate allowing easier electron flow through the back contact to the diamond surface. The general trend with B-doping is that the SEE yield increase with film resistivity to a maximum value and then decreases again. The maximum value occurs for lightly doped samples.

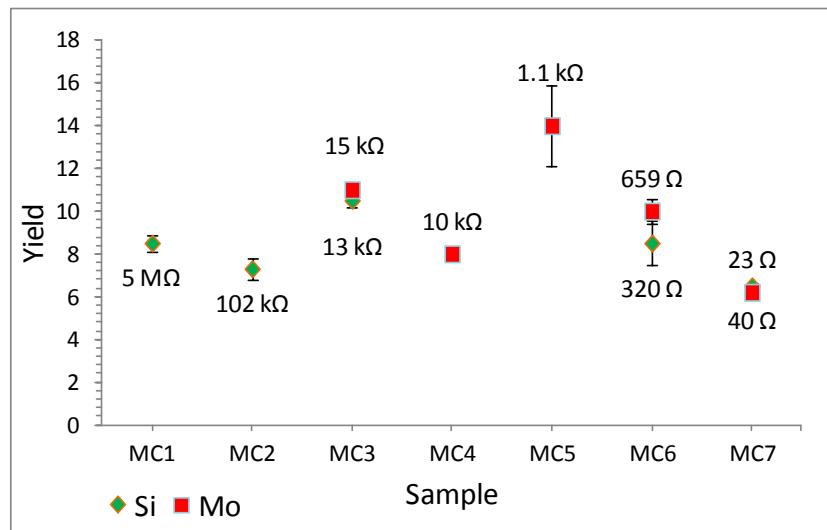


Figure 5.2- Relative SEE yields measured from the samples belonging to the sets 1 and 3 (table 5.1), corresponding to $\sim 3.5 \mu\text{m}$ thick MCD films, grown with different B_2H_6 additions to the gas phase. The substrate materials were Si (green) and Mo (red). The 2-point resistances of the diamond films are shown for each sample.

For a better visualization of the trends, the same results are presented in figure 5.3 with the yield displayed as a function of the resistance. A maximum yield value of 14 was obtained for a 1.1 k Ω diamond film on Mo.

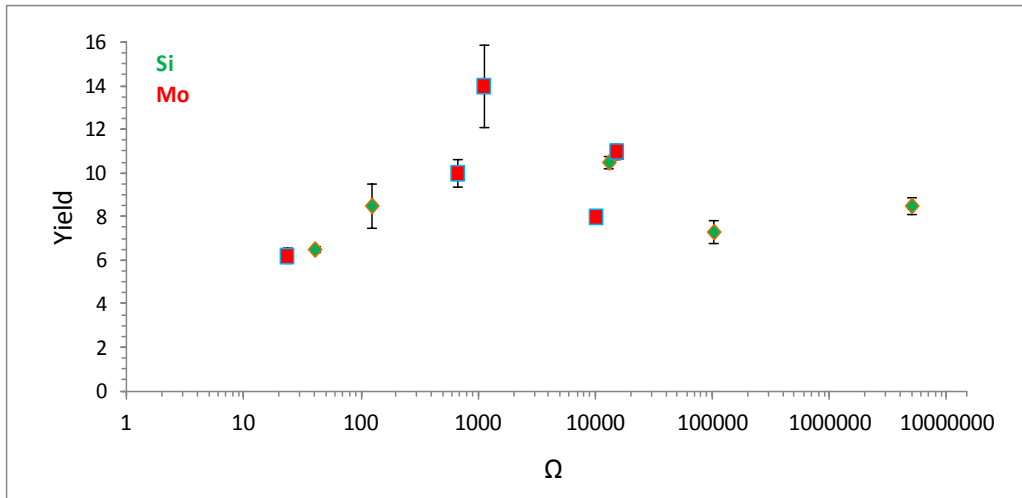


Figure 5.3- SEE yields measured from the samples from sets 1 and 3 (table 5.1) *versus* the resistance measured from the different $\sim 3.5\text{-}\mu\text{m}$ -thick MCD films, grown with different B contents. The substrate materials were Si (green) and Mo (red).

The variation of yield with film thickness was assessed using samples from set 2 (plus S3 from set 1), which consists of MCD films which were grown on Si substrates with thicknesses of 0.5; 1.15; 2; 3.5 and 4 μm . The results are displayed in figure 5.4, with reference to the resistivity values measured from each sample.

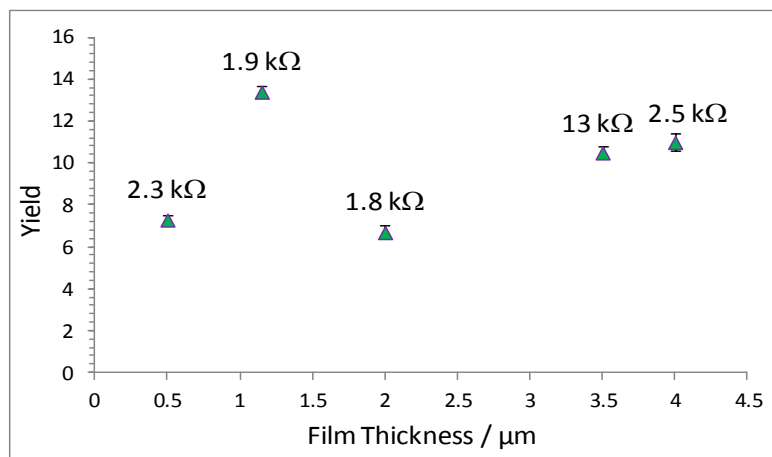


Figure 5.4- Variation of the SEE yield with the film thickness measured from the samples S6-S9 from set 2 (table 5.1), corresponding to MCD films grown on Si with similar B contents. The thicknesses vary from 0.5 μm - 4 μm . Sample S3 with 13 k Ω cm (from set 1) was included as a matter of comparison.

Figure 5.4 shows that within the range of thicknesses used SEE yield is roughly independent of film thickness. The slight variation in yield measurements with film thickness can be attributed to the increasing average crystallite size in the diamond film with thickness resulting from the columnar growth process, but this appears to be a minor effect.

5.3.2. Measurement of the SEE yield from NC diamond on Si and Mo

A similar study was made considering NCD instead of MCD films. Nine samples from sets 4 and 5 were considered, all with thicknesses of $\sim 3.5 \mu\text{m}$ with a range of conductivities and with Si and Mo as substrate materials. Figure 5.5 shows the yields measured from those samples.

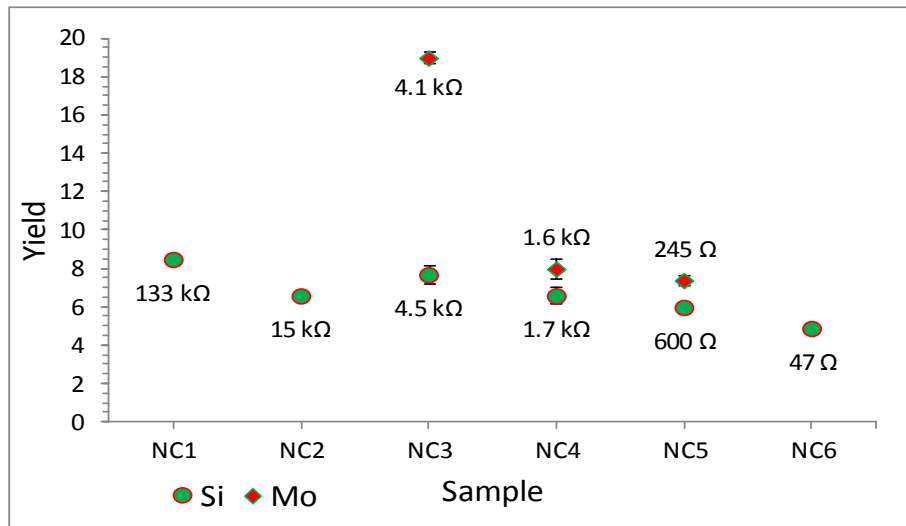


Figure 5.5- Comparison of the SEE yields measured from the samples S15 – S23 belonging to the sets 4 and 5 (table 5.1), corresponding to $\sim 3.5 \mu\text{m}$ thick NCD films, grown with different B contents. Substrate materials were Si (green) and Mo (red).

For the samples with a Si substrate, the trend is not so clear as it was for the MCD samples (figure 5.2), with there being a gradual increase in SEE with increasing resistance, and no obvious maximum value. This could be due to scatter in the points, or because the peak occurs at resistance values greater than the maximum measured (133 kΩ) and so lies off the graph. Again, the highest SEE yield values were measured from the films grown on Mo substrates. The values for these NCD films were generally smaller than for MCD films, except for a yield of 18 measured for a 4.1 kΩ diamond film on Mo which stands out from all

the samples tested in these experiments. For a clearer visualization of the results, figure 5.6 presents the yield variation as a function of the resistivity for the same samples.

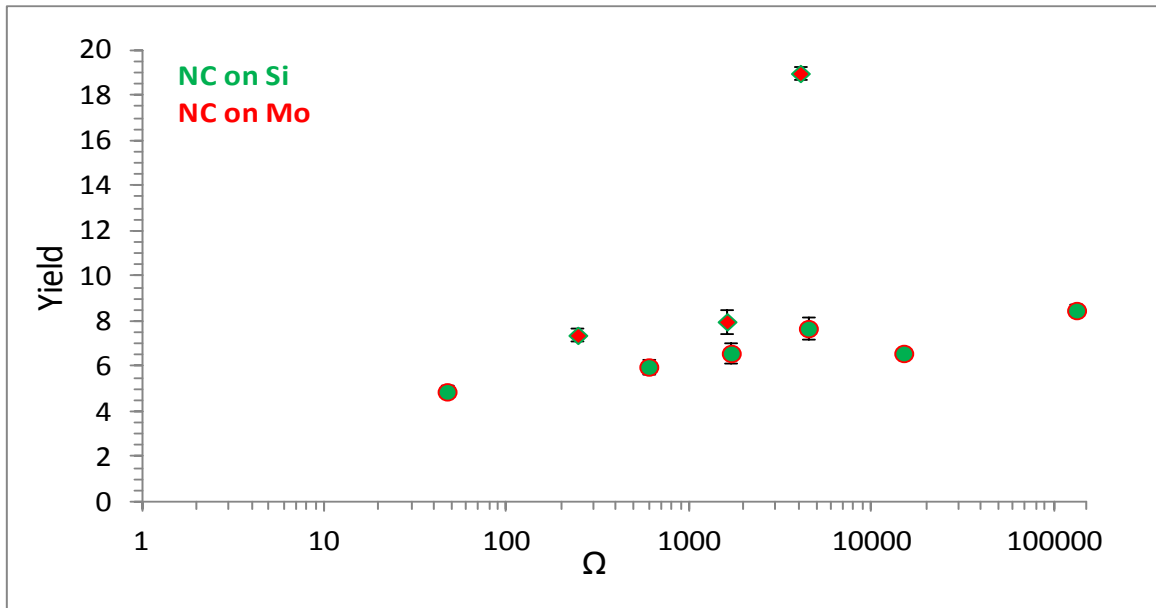


Figure 5.6- SEE yields measured from the samples S15 – S23 from sets 4 and 5 (table 5.1), corresponding to different ~ 3.5- μ m-thick NCD films, grown with different B contents *versus* the resistance values. As substrate materials were used Si (in green) and Mo (in red).

Figure 5.7 and 5.8 show a comparison between the yields measured from the MCD and NCD films grown on Si in relation to their resistance.

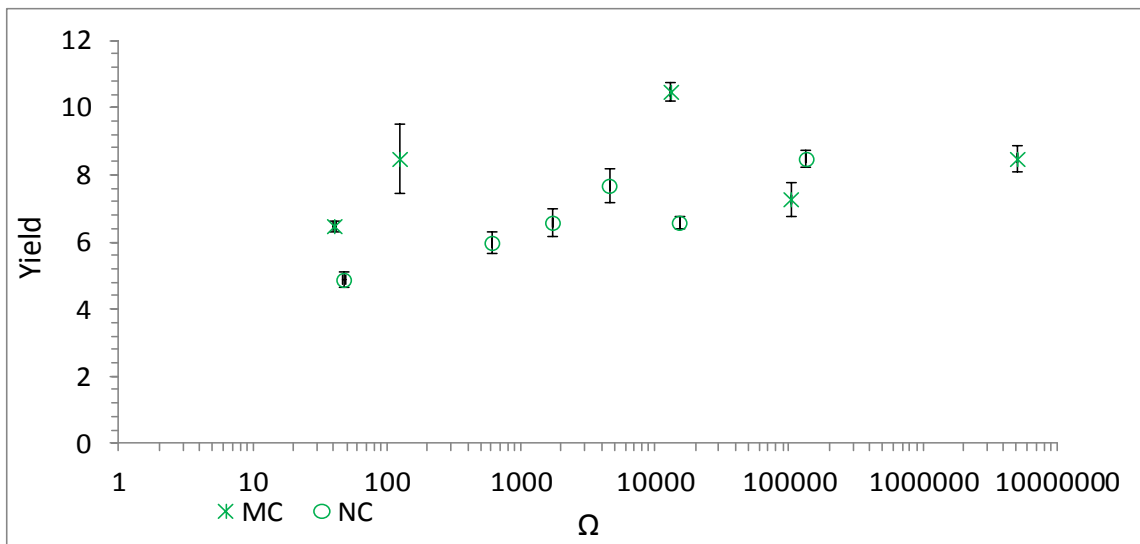


Figure 5.7- Comparison of the SEE yields measured from the MCD samples (S1-S5) from set 1 and the NCD samples (S15 –S20) from set 4 in relation to the resistance.

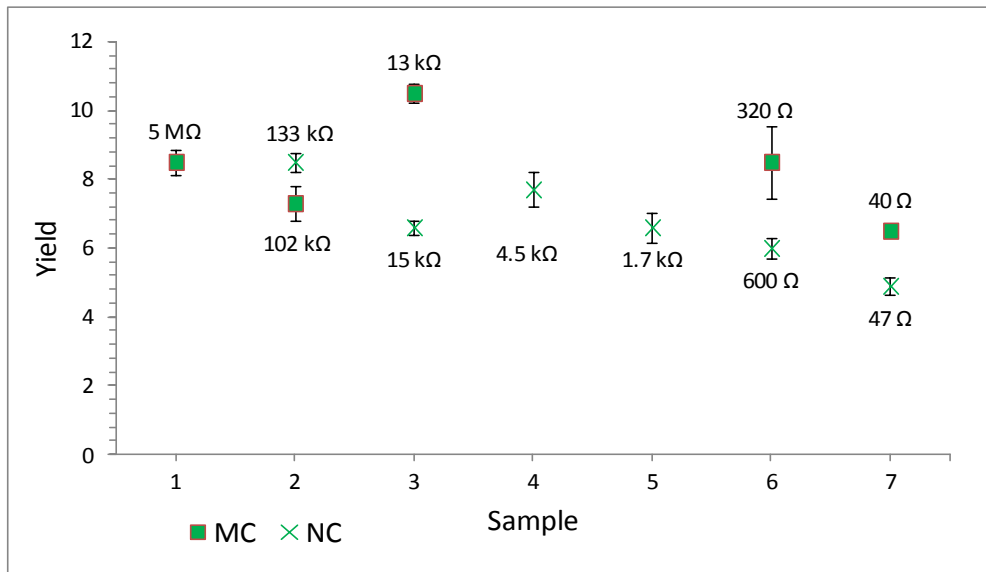


Figure 5.8- Comparison of the SEE yields measured from the MCD samples (S1-S5) from set 1 and the NCD samples (S15 –S20) from set 4, all corresponding to Si substrates.

From figure 5.8 can be seen a similar trend for both types of films with the exception for the resistivity at which the yield tends to have a peak, which appeared around 13 kΩ in the case of MCD films.

In a similar analysis, figure 5.9 shows a comparison between the yields measured from the MCD and NCD films grown on Mo in relation to their resistance where a larger disparity in terms of the values obtained from the NCD films is apparent.

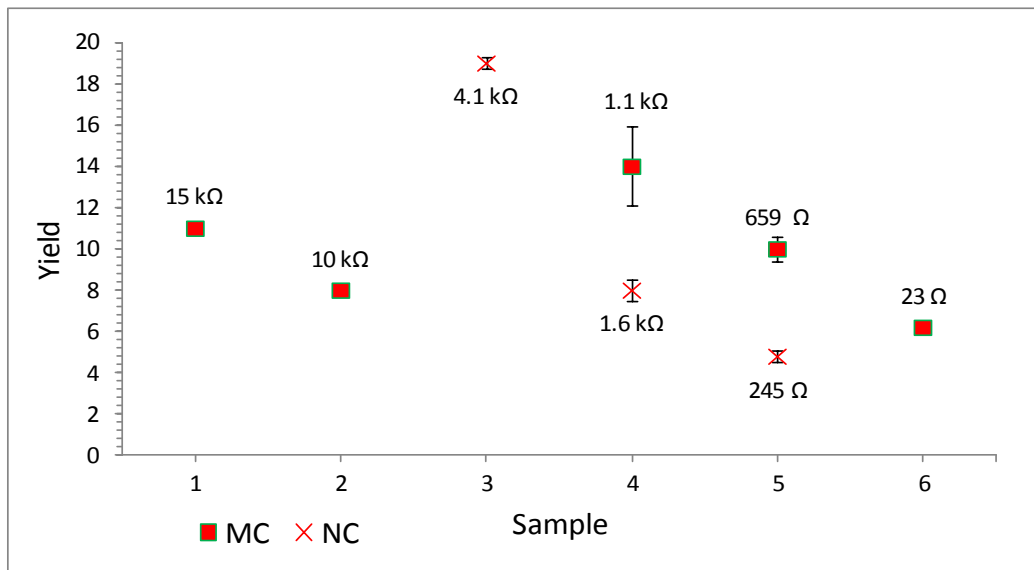


Figure 5.9- Comparison of the SEE yields measured from the MCD samples (S10-S14) from set3 and the NCD samples (S21 –S23) from set 5, all corresponding to ~ 3.5 μm-thick films on Mo substrates.

The yields obtained in the case of MCD are higher than those of NCD films for a constant thickness when comparing similar degrees of B-doping. As a conclusion of this section, in figure 5.10 are summarized all the measurements taken from the samples from sets 1, 3, 4 and 5 which represent all the $\sim 3.5 \mu\text{m}$ thick diamond films.

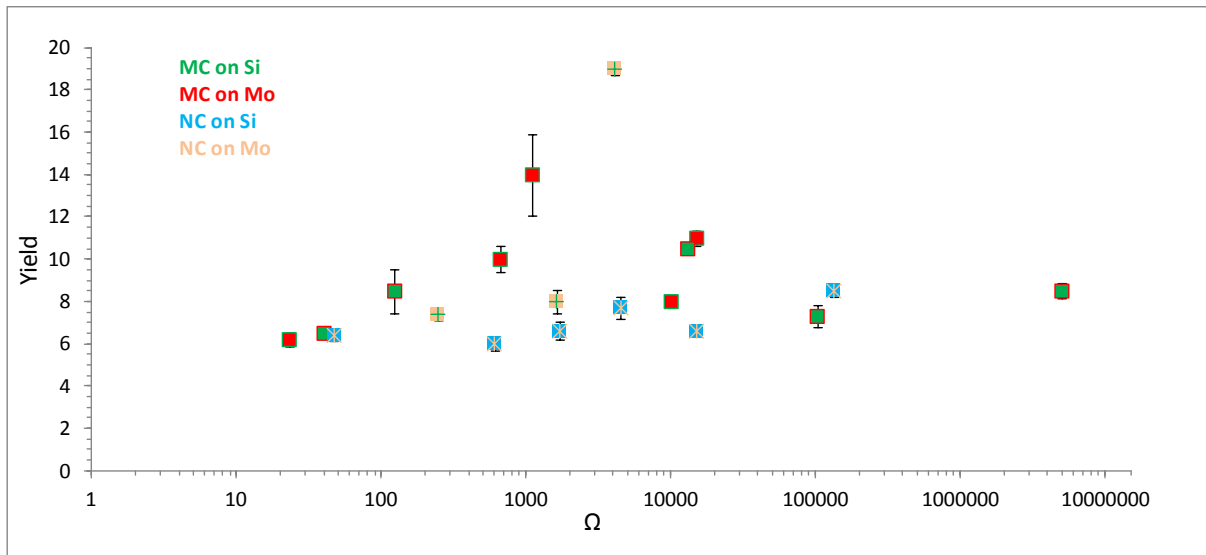


Figure 5.10- Comparison of the of all the SEE yields measured from the samples with $\sim 3.5 \mu\text{m}$ thickness, both MCD and NCD on Si and Mo, according to the colours displayed in the legend.

The measurements presented so far were performed on the as grown films without further surface treatments. The as-grown surfaces are H-terminated by default, but might have associated impurities at the grain boundaries, such as graphite, which may hinder the SEE yields.

From figure 5.10, can be observed that there is a concentration of maximum yield values between 6 and 11, with only two out of twenty three samples presented yield out of this range. In addition, the majority of NCD films have yields of 6-8, except for one sample with no clear justification.

5.3.3. Variation of yield with surface termination

A selection of samples was evaluated in terms of the influence of different surface treatments on the yield values obtained. The samples selected were labelled as S10 - S13 (according to table 5.1) and represent four MCD films with the same thickness and a variation in the B contents. The substrates were made of Mo.

Samples S11 and S12 have been measured after having undergone a process of hydrogenation. Samples S10 and S13 have been oxygenated followed by lithiation. Figure 5.11 presents the yield variations measured from those samples as a function of the beam energy.

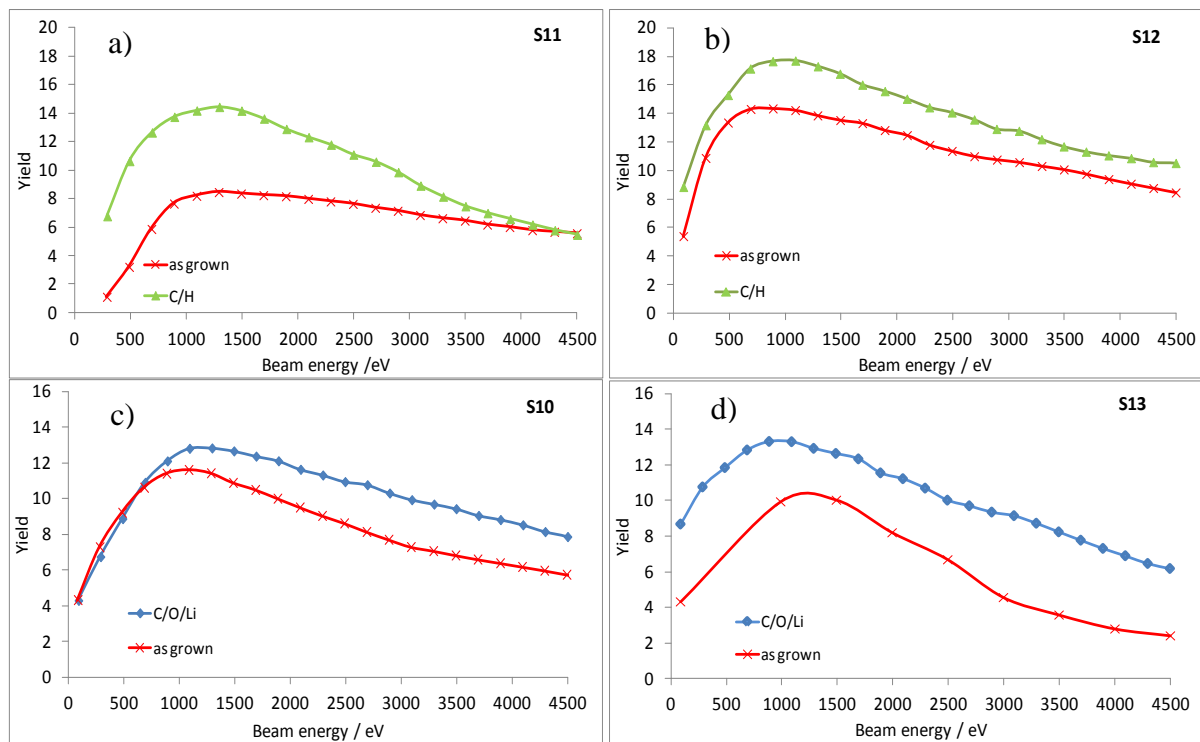


Figure 5.11- The graphs represent the SEE yields as a function of the primary beam energy measured from as-grown surfaces by comparison with further surface treatments of hydrogenation (in a) and b) for samples S11 and S12) and oxygenation plus lithiation (in c) and d) samples S10 and S13).

The graphs show a shift to higher SEE values in the four samples, with a considerable increase in the case of sample S11 (figure 5.11 b) where the yield changed from 8 to 14 for the same beam energy ~ 1.2 keV.

Following these measurements, samples S10 and S11 were cleaned before being submitted to further oxygenation and then caesiation. The highest yields values were measured from the C/H surfaces and the results are presented in figure 5.12 and the values are summarized in table 5.2.

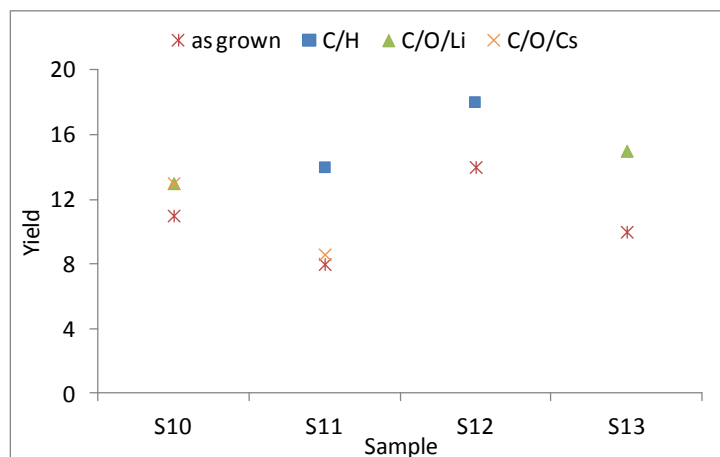


Figure 5.12- Comparison of the maximum SEE yields measured from samples S10 - S13 with distinct surface treatments: as grown, H-, LiO- and CsO- terminated.

As seen from the graph in figure 5.12 the H-termination has shown to promote the increase of the values measured in both samples. The LiO treatment seems to have been more effective on sample S13 than on sample S10. The C/O/Cs surfaces have had a rather insignificant effect on sample S11 and roughly the same impact on sample S10 as the LiO treatment.

Table 5.2 - Summary of the maximum yield values from samples S10 to S13 (3.5 μm -thick MCD films on Mo substrates), with different surface terminations.

Sample	k Ω	as grown	C/H	C/O/Li	C/O/Cs
S10	15	11 \pm 0.34	-	13 \pm 0.30	13 \pm 0.24
S11	10	8 \pm 0.21	14 \pm 0.17	-	8.6 \pm 0.36
S12	1.1	14 \pm 1.91	18 \pm 2.08	-	-
S13	659	10 \pm 0.59	-	15 \pm 0.61	-

The effect of the impurity concentration is not evident which may be perhaps associated with the narrow range considered in these experiments. Moreover, the uniformity of the diamond surfaces in terms of their coverage by adsorbed chemical species may be important for the success of a certain surface treatment and consequently, the yield values measured from the samples.

5.3.4. Variation of the SEE yield across the hydrogenated surfaces

As mention previously the measurement method consisted of acquiring the signals from three different areas on the sample surfaces and averaging them. It was possible to identify a significant variation of yield in different areas by moving the electron beam along the surface. Such variation can be associated to non-uniform NEA, and also with a microstructure effect, such as roughness scattering effects. The graphs in figures 5.13-5.14 show the variation of yield across the samples S11 and S12 after H-treatment.

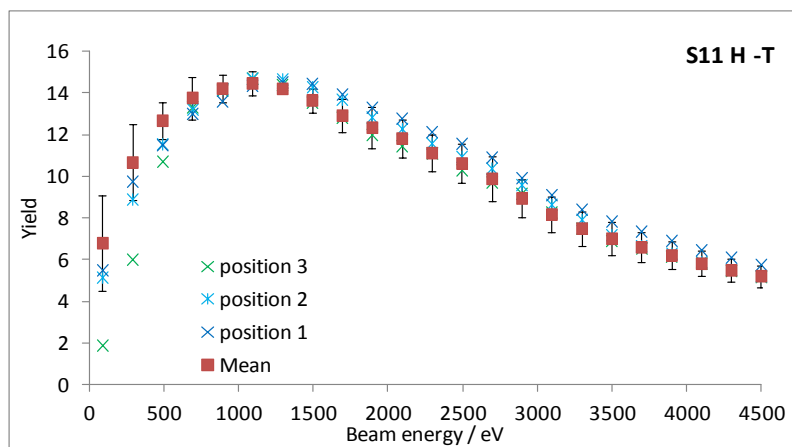


Figure 5.13- Variation of yield across the surface of sample S11 measured after hydrogenation treatment.

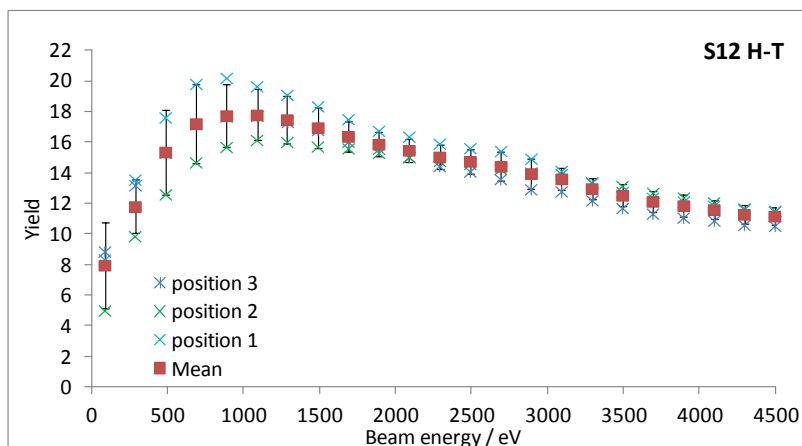


Figure 5.14- Variation of yield across the surface of sample S12 measured after hydrogenation treatment.

5.3.5. Variation of the yield with beam exposure

The effects of a prolonged beam exposure on the yield values were measured for two different samples after their surfaces had been hydrogenated and lithiated, respectively. Figure 5.15 presents a comparison of the yield variation for the C/H surface of sample S12 and the C/O/Li surface of sample S13 under continuous exposure of the same area in the sample surfaces to a 1.5 keV electron beam. The data were collected every 5 s during the first min and every 15 min afterwards while the beam energy was held constant at 1.5 keV. The current density was held constant during each experiment, with a beam diameter of roughly 2 mm.

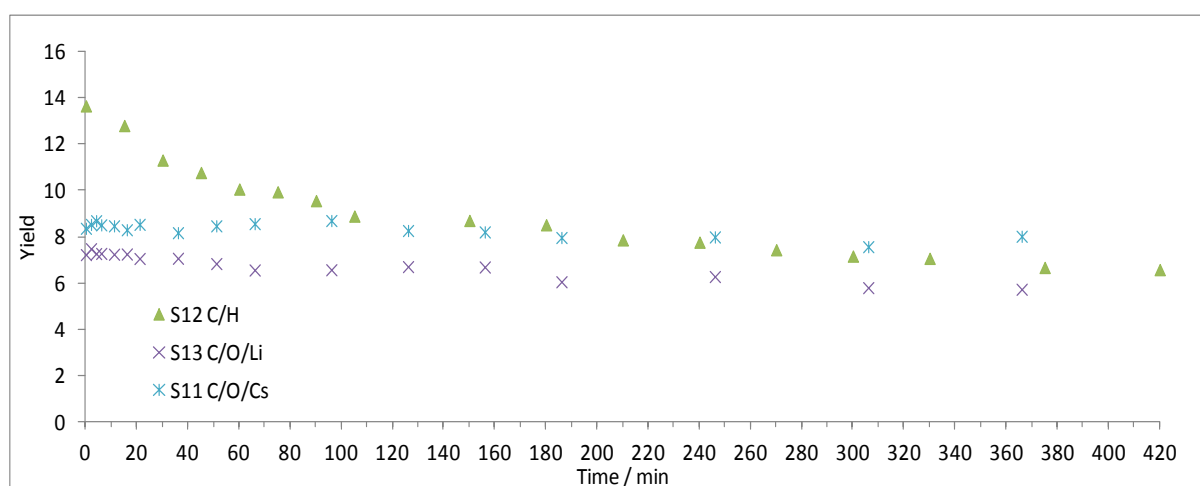


Figure 5.15- Comparison of the yield variation under continuous exposure of the same area in the sample surfaces to a 1.5 keV electron beam. The measurements correspond to the C/H, C/O/Li and C/O/Cs surfaces of sample S12, S13 and S11, respectively.

The H/C surface of sample S12 has shown a rapid decrease of the values measured indicating a decrease in the emission characteristics. This fact may be associated with a process of H desorption under electron bombardment.

Mearini *et al.*^[8] showed that the yield under continuous electron bombardment may be stabilized upon operation in a molecular hydrogen environment. Caesiated surfaces present relative stability when exposed to air or heated in vacuum to temperatures below 120°C. In addition they would be relatively stable under continuous electron beam exposure.^[2] However, the electron-stimulated desorption from caesiated diamond surfaces proved to be extended across the whole surface whereas in hydrogenated samples this phenomena is localised to the areas irradiated by the electron spot.^[9]

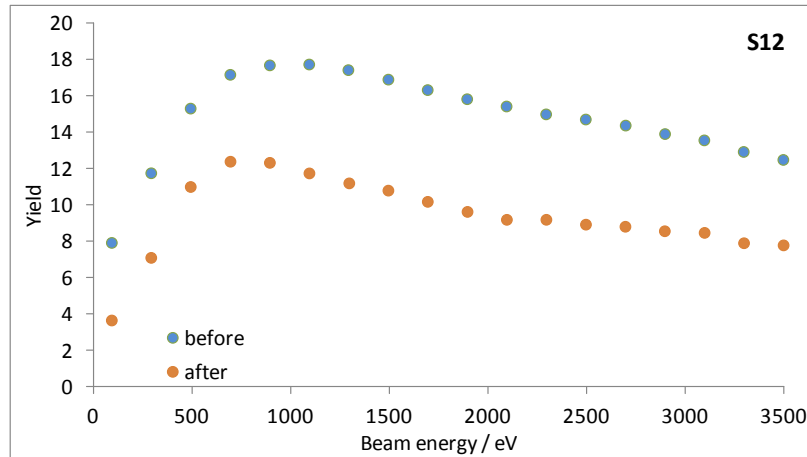


Figure 5.16 - Comparison of the yield variation as a function of the beam energy for the C/H surface of sample S12, in measurements performed before and after continuous exposure to a 1.5 keV electron beam. This is an indication of a variation in the emission properties, which may be associated with H-desorption.

In contrast, the remaining two surfaces have approximately constant values with time. After such prolonged surface exposure the yield measured from sample S12 suffered a reduction of $\sim 30\%$ (figure 5.16). This is a clear indication of the existence of beam induced surface modifications which alter the emissive properties of the samples under yield measurement. The Li or Cs coatings appear to be more robust and do not desorb as easily as the hydrogenated surfaces, at these beam energies. Fortunately, this process is reversible since the surfaces can be retreated recovering their initial characteristics.^[10]

5.4. Conclusions

A comparison between the SEE yields measured from different diamond samples was carried out. MCD films with thicknesses of $\sim 3.5 \mu\text{m}$ ($5 \text{ M}\Omega - 40 \Omega$) grown on Si and on Mo ($15 \text{ k}\Omega - 23 \Omega$) showed generally higher yields for a similar range of resistances, when Mo substrates were used. This is probably a result of the increased conductivity of the substrate allowing easier electron flow through the back contact to the diamond surface. A maximum yield value of 14 was obtained for a $1.1 \text{ k}\Omega$ diamond film on Mo, which is in accordance with the values found in the literature for H-terminated diamond CVD films grown on Mo. Nevertheless, much higher values have also been published (yield of 80, for example), but the key to obtain such high SEE is still not fully understood. This could be attributed to measurement

deficiency in the new setup, but in fact, the project counterparts at SRC have the same question. A possible justification could be the way of handling the samples and the atmospheres at which they are stored before measurements, although these reasons are unlikely in the samples used for these experiments.

Other experiments were performed on H-terminated 0.5- 4 μm -thick MCD films (2.3 k Ω - 1.8 k Ω) grown on Si, for which a maximum yield of 13 was measured for a 1.25 μm -thick film with resistance of 1.9 k Ω . The slight variation in yield measurements with film thickness can be attributed to the increasing average crystallite size in the diamond film with thickness resulting from the columnar growth process, but this appears to be a minor effect.

Surprisingly, the highest yield value obtained in these experiments which was of 18, was measured from a 3.5 μm NCD film (4.1 k Ω) grown on Mo, whereas for the remaining NCD films the yields were below 8. The resistance of the samples ranged between 133 k Ω -47 Ω for the films grown on Si substrates, and 4.1 k Ω - 245 Ω for the films coated on Mo. All the samples had H-terminated surfaces produced under the same conditions.

Further measurements were done on the 3.5- μm -thick MCD films after surface functionalization with LiO and CsO ad-layers. The highest increases in the yields were obtained after hydrogenation and after lithiation of as-grown surfaces, with values varying from 8 to 14 and 10 to 15, respectively. Interestingly, the highest SEE yield was measured after hydrogenation of a bare surface of a sample with resistance of 1.1 k Ω . The reason for this might be a non-effective preparation or contamination of the LiO and CsO functionalized surfaces, during the cleaning or baking processes. The fact is that SEE yield values for lithiated surfaces were not found in the literature. But for the case of caesiation, there are various reports of yields in the range of 25 – 132, from which higher yields were expected. Nevertheless, the details related to the measurement conditions are not always reported, which makes those experiments difficult to replicate. However, under prolonged beam exposure, H-terminated surfaces showed faster deterioration than LiO- and CsO- terminated ones.

Summarising, MCD films grown on Mo have shown higher values than NCD films grown in the same conditions which is associated with the increased content of amorphous carbon for the NCD films.^[8] In addition, the yields are generally higher for Mo than for Si, probably as a result of the increased conductivity of the substrate allowing easier electron flow through the back contact to the diamond surface. The yield values measured for H-terminated diamond on Mo were of the same magnitude (6-14) than other values published in the literature.^[1-2]

The same applies for H-terminated diamond on Si, with values previously published of 5.8 - 18.^[3-7]

The general trend with B-doping is that the SEE yield increase with film resistivity to a maximum value and then decreases again. The maximum value occurs for lightly doped samples.

5.5. References

1. T.L. Bekker, J.A. Dayton, Jr., A. S. Gilmour, Jr., I.L. Krainsky, M.F. Rose, R. Rameshan, D. File and G. Mearini, Observations of secondary electron emission from diamond films, *Physical Review* **92** (1992) 949-952.
2. G.T. Mearini, I.L. Krainsky, J.A. Dayton, Y. Wang, C.A. Zorman, J.C. Angus, R.W. Hoffman and D.F. Anderson, Stable secondary electron emission from chemical vapor deposited diamond films coated with alkali-halides, *Applied Physics Letters* **66** 2 (1995) 242-244.
3. P. Ascarelli, E. Cappelli, F. Pinzari, M. C. Rossi, S. Salvatori, P. G. Merli and A. Migliori, Secondary electron emission from diamond: Physical modelling and application to scanning electron microscopy, *Journal of Applied Physics* **89** (2001) 689.
4. V.V. Dvorkin, N.N. Dzbanovsky, N.V. Suetina, E.A. Poltoratsky, G.S. Rychkov, E.A. Il'ichev and S.A. Gavrilov, Secondary electron emission from CVD diamond films, *Diamond and Related Materials* **12** (2003) 2208–2218.
5. D.M. Trucchi, C. Scilletta, E. Cappelli, P.G. Merli, S. Zoffoli, G. Mattei and P. Ascarelli, Optimization of the performance of CVD diamond electron multipliers, *Diamond and Related Materials* **15** (2006) 827-832.
6. O. Ternyak, Sh. Michaelson, R. Akhvlediani, A. Hoffman, Enhancement of electron emission from near-coalescent nanometer thick continuous diamond films, *Diamond and Related Materials* **15** (2006) 850.
7. J.S. Lapington, V. Taillandier, B.L. Cann, J. Howorth, J. Milnes, R. Vaz, P.W. May, N.A. Fox, R. Stevens and L. Wang, Investigation of the secondary electron emission characteristics of alternative dynode materials for imaging photomultipliers, *Journal of Instrumentation* **7** (2012) E04002.

8. G.T. Mearini, I.L. Krainsky, Y.X. Wang, J.A. Dayton, Jr., R. Ramesham and M.F. Rose, Fabrication of an electron multiplier utilizing diamond films, *Thin Solid Films*, **253** (1994) 151.
9. H.J. Hopman, J. Verhoeven and P.K. Bachmann, Electron stimulated desorption from oxygenated and hydrogenated synthetic diamond films, *Diamond and Related Materials* **9** (2000) 1238.
10. B.B. Pate, The diamond surface atomic and electronic structure, *Surface Science* **165** (1986) 83-142.

Chapter 6.

Study of the influence of the surface termination in the yield of commercial PCCVD diamond

6.1. Introduction

The yield curves as a function of the primary beam energy can provide information on the electron transport characteristics of the material under measurement. The number of impact ionization events by which the internal secondaries are generated increases with increasing beam energy and therefore the internal gain increases. At the same time the electrons are generated deeper inside the sample, thereby increasing the transport distance through which the secondaries have to travel before reaching the surface. Therefore, a comparison between the transport efficiency amongst different samples becomes possible when conducting an analysis under the incidence of a primary beam with the same characteristics.

Alternatively, the emission probability and therefore the SEE yield are influenced by the magnitude of the surface barrier which the secondary electrons have to overcome before being emitted into the vacuum. When the surfaces are functionalized by means of an electropositive ad-layer, for instance, H, Cs or Li, then the secondary electrons that travel through the material and reach the surface are easily emitted.

The study of the electron transport and emission properties of HFCVD diamond films with NCD and MCD morphologies after hydrogenation, caesiation and lithiation has already been described in section 5.3.3. The SEE yields for the various surface compositions have been used to examine the effect of the electronic properties of such surfaces on the emission

characteristics. The maximum yield values measured from those samples were 18, 15 and 13 obtained from MCD with hydrogenated, lithiated and caesiated surfaces, respectively.

The morphology of MCD films produced via HFCVD is predominantly randomly orientated with surface roughness rather small when compared to the standard unpolished PC CVD diamond films available commercially. This rough surface may condition the process of electron emission since when the secondary electrons are emitted from a rough surface they are likely to be intercepted by neighbour crystals or other surface irregularities, which may deflect them back to the surface. Electrons emitted from a smooth surface face no further obstacles in their trajectory, being therefore favourable to the increase of the SEE yield.^[1]

In this chapter the electron emission properties of commercial p-doped (111) PC CVD diamond samples with distinct surface functionalization are investigated. In addition, a (100) SC CVD diamond with H-termination is examined.

6.2. Experimental

The samples tested in this study were PC CVD diamond samples of dimensions (10×10×0.6) mm of unpolished B-doped ($> 10^{20} \text{ cm}^{-3}$) diamond, predominantly (111) oriented acquired from Element Six Ltd. A CVD (100) single-crystal diamond sample of dimensions (2.6×2.6×0.3) mm from the same supplier was also part of this study. The PC samples were supplied without any polishing treatment, thus the surface finish was as-grown. The SCD sample had a polished surface to a roughness of around 10 nm.

The first preparation stage consisted of cleaning the samples to remove any surface contamination from the polishing process. Three different cleaning procedures were attempted. In the first one, the samples were simply immersed into fuming nitric acid (HNO_3) for 30 minutes and then rinsed with D.I. water. The second method consisted of cleaning the samples in hot HNO_3 for 30 min, followed by ultrasonic agitation for 30 min in acetone and then in methanol for extra 30 min. Yet, another cleaning method consisted of dipping the samples in a mixture of concentrated sulphuric acid (H_2SO_4) and KNO_3 at 200°C for 30 minutes before rising with water and drying. This last method was adopted for the preparation of the samples included in the present study, since it proved to be more effective. After cleaning, the diamond films were submitted to ozone treatment in a Jelight UVO Ozone

cleaner under an oxygen gas flow for 30 minutes, thought to be enough to ensure an even oxygen termination. The oxygen layer is necessary for the effectiveness of NEA in CsO and LiO terminated surfaces. In the presence of an incomplete layer the maximum expected for the NEA surface is not achieved.^[2] The surfaces then underwent different functionalization according to table 6.1.

Table 6.1- Different surface treatments applied to the CVD samples before SEE measurements.

Sample	Surface termination			
E6 BD unpolished (top side)	H	O	CsO	LiO
E6 BD polished (back side)	LiO			
E6 SC CVD	H			

The hydrogenation treatments were carried out in a microwave plasma system for 5 minutes at a pressure of 80 Torr, with 500 sccm of H₂ and a microwave power of 1 kW, creating a substrate temperature of below 600°C. The process was followed by cooling down in hydrogen for 5 minutes.

To overcome any charging effects, prior to H-termination the SCD sample was coated with a 0.5 µm layer of residual B-doped diamond which had been grown using a HFCVD reactor. In the case of caesiated and lithiated surfaces, Cs and Li were deposited on previously oxidized surfaces, by thermal evaporation of the respective metal dispensers supplied by SAES Getters. The evaporation process was conducted in a Balzer 510 coater working at $\sim 10^{-3}$ Torr, where a crystal of quartz has been used to monitor the thickness of the coatings.

In the process of caesiation, the conditions were regulated for the deposition of a Cs monolayer on the surfaces, whereas in the case of lithiated surfaces, approximately 50-nm thick coatings were obtained. Immediately after caesiation and without exposing the samples to the atmosphere to avoid Cs oxidation, the samples were annealed for 5 - 10 minutes at 200°C. The lithiated samples were washed in D.I. water to remove the excess of Li leaving only a monolayer, and then dried. Prior to the measurements the LiO-terminated samples were annealing at 150°C. In order to avoid any oxidation of the adsorbed layers, after the surface treatments and before measurements the samples were kept in a oxygen-free argon atmosphere.

To control the graphitic carbon content on the top and back side of the PC samples after the different cleaning stages, Raman spectra were taken at room temperature using a Renishaw 2000 spectrometer, at UV 325 nm (HeCd laser) excitation wavelength. A JEOL 5600 SEM equipment was used to analyse the samples after the surface functionalization treatments.

The SEE experiments were conducted in a high vacuum chamber ($\sim 10^{-7}$ Torr) as described in section 4.1. As for all the reflection mode experiments, together with the samples to be measured a reference sample and a graphite sample were also mounted in the sample holder. The reference sample has a known yield value which works as a calibration for the measured yield values from the diamond samples. The graphite sample has also been previously tested, and serves to subtract the background signal from the measurements. The samples were glued to the sample holder with conducting silver dag, left to dry, and then clamped to the base of the sample holder by means of a metal plate placed on top. The measurements were acquired for beam energies up to 4.5 keV at ~ 100 μ A for the emission current, 500 V for the mesh bias and 10 V for the sample bias. For higher precision, the signals were acquired from different beam exposed areas (~ 2 mm square) of the surface and those values averaged.

6.3. Results and discussion

6.3.1. Yield measurements from oxygenated-caesiated surfaces: (C/O/Cs)

The differences in the electron emission obtained from the oxygenated surfaces in comparison with the ones which have been caesiated were assessed first of all using SEM analysis. Figure 6.1 shows one example of the experiments to qualitatively predict the SEE from both O-terminated and CsO-terminated surfaces. After oxygenation half of the sample was masked by means of a piece of aluminium foil before Cs evaporation.

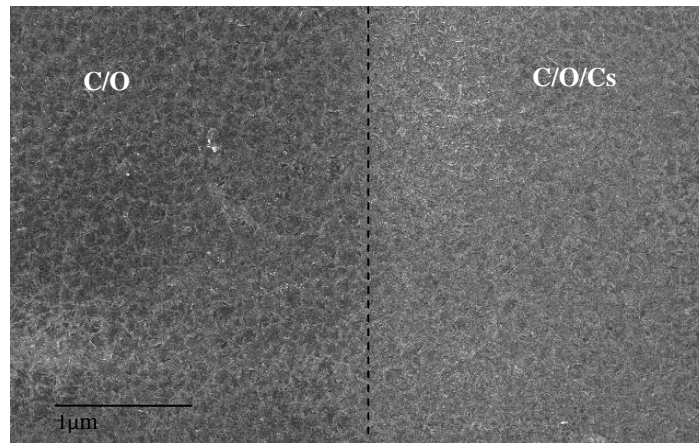


Figure 6.1- SEM image taken from a PC sample where the left side has a CsO-termination and the right side only an O- termination. The CsO-terminated side appears brighter, indicating a larger intensity of secondary electron emission.

Even though a difference in terms of SEM brightness is apparent, the differences between both sides were not remarkable, which could be verified by the measurement of the respective SEE yields. For these measurements, a series of signal acquisitions were taken following an imaginary line across the surface. The results are summarized in figure 6.2, from where it is possible to observe the variation of the values measured from the different areas, with the lowest corresponding to the area at the right side in figure 6.1 and the highest corresponding to the left side.

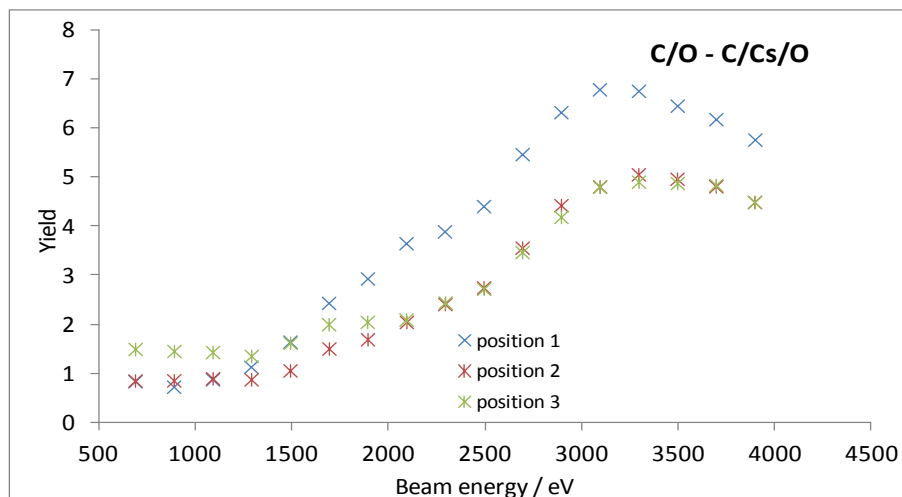


Figure 6.2- Graph showing the SEE yield values corresponding to the surface displayed in the SEM picture in figure 6.1. Position 1 is on the right-hand half of the film (CsO-terminated), Position 3 is on the left-hand side of the sample (O-terminated), and Position 2 is between those.

The maximum yield value obtained was around 6.7 at 3.1 keV, which is considerably lower when compared with the yields measured previously for the MCD HFCVD films (~13 at 2.9 keV) presented in chapter 5. One of the explanations may be related with an incorrect storage or handling of the sample, with accidental exposure to the atmosphere and surface contamination. To confirm if this was the case or if there is any trend for the PCD films under investigation, further experiments were done, repeating the entire process from the surface treatment to the yield measurements.

Figure 6.3 presents the results obtained from two other measurements, showing an increase to a maximum yield value of 9 at 2.9 keV despite the fluctuation that can be observed across the surface. Moreover, figure 6.3 c) shows a graph taken from the literature for comparison.

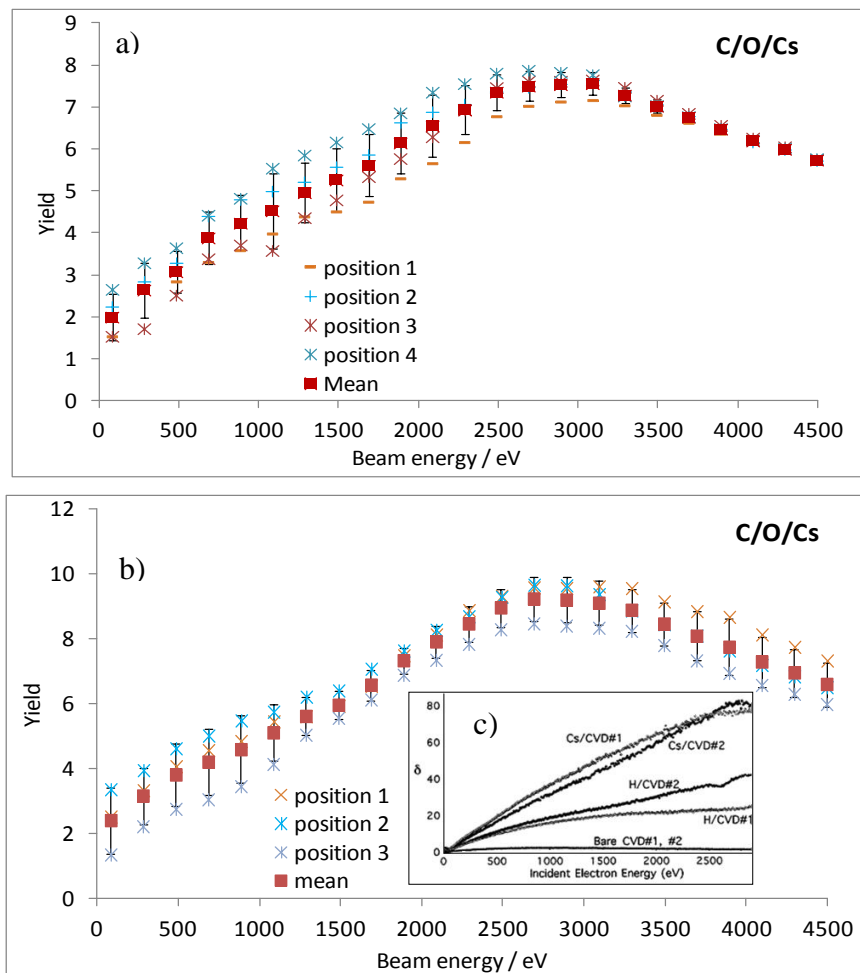


Figure 6.3- Graph presenting the SEE yield values measured from two PCD unpolished surfaces, showing a maximum yield value of 9 at 2.9 keV (in b), despite the fluctuation that can be observed across the surface in both samples which may be related with a non-uniform surface termination. The measurements were performed with the beam impinging on three different areas (positions 1-4). In figure c), a graph taken from the literature ^[3] shows a similar shape up to 3 keV but with much higher yield coefficients.

The primary beam energy of 2.9 keV corresponding to the maximum yield is in accordance with the values for the beam energy obtained previously for Cs/C terminated surfaces on p-type MCD CVD films and on p-type (100) SCD samples, although in the current experiments the highest yield values (~ 9) are much smaller than the ones published in the first case (80 and 130, respectively) most of them referring to evaporation of Cs directly onto the diamond surface without prior oxygenation^[3]. This is despite the fact that in most of the cases the conditions under which the surfaces were treated are not fully detailed.^[4-8] This fact may be controversial since the Cs is expected to stick more easily to a previously oxygenated surface than to a bare or hydrogenated one^[9], leading to the conclusion that other factors could be related with the discrepancy in the yield values. Actually, all the results known from the literature for caesiated diamond surfaces present a similar trend in terms of the beam energy necessary to promote a yield maximum (one example is presented in figure 6.3c). The differences observed may be related with the transport properties of the bulk or perhaps with the surface coverage uniformity of the PCD rough surface.

6.3.2. Lithiated surfaces (LiO/C)

A monolayer of Li on previously oxygenated C(100) and C(111) surfaces has been demonstrated to exhibit NEA surfaces comparable to caesiated ones but with improved stability.^[10, 11] Therefore, similarly to the last section, the SEE yields from PCD surfaces after lithiation have been investigated to evaluate the effects upon the yield coefficients. Figure 6.4 and 6.5a show the results obtained from the measurements of two lithiated samples prepared using similar conditions at three different positions on the sample.

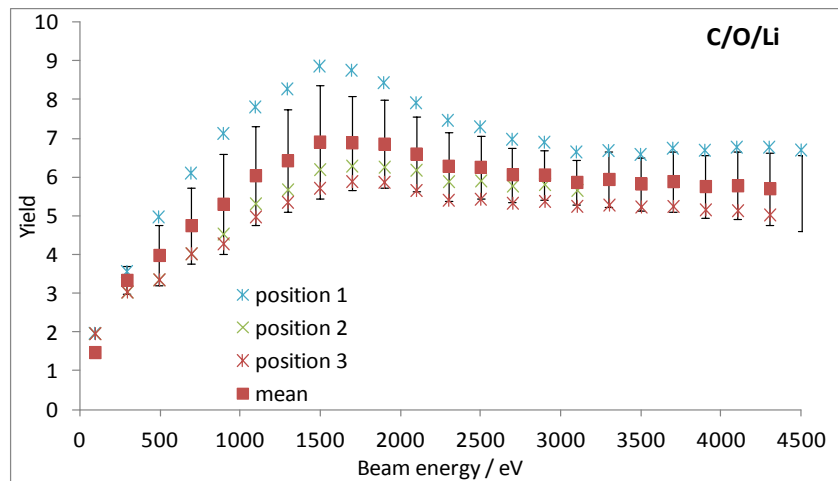


Figure 6.4- SEE yield values measured from a Li-O terminated PCD unpolished surface, showing a maximum yield value of 8.9 at 1.5 keV but a maximum of ~ 7 if averaged across the surface. The variation of SEE values across the surface may be related with a non-uniform termination.

In addition to the growth surface some experiments have been done on the back-side (nucleation) surface to investigate whether the surface roughness was playing an active role. This nucleation surface is much flatter than the growth surface, but contains much smaller grains and hence a much higher number of grain boundaries. As displayed in figure 6.5 b) the variation across the surface is maintained, although the maximum values suffered a decrease by about 50% in relation to the growth surface. This decrease is probably due to scattering of electrons from the grain boundaries.

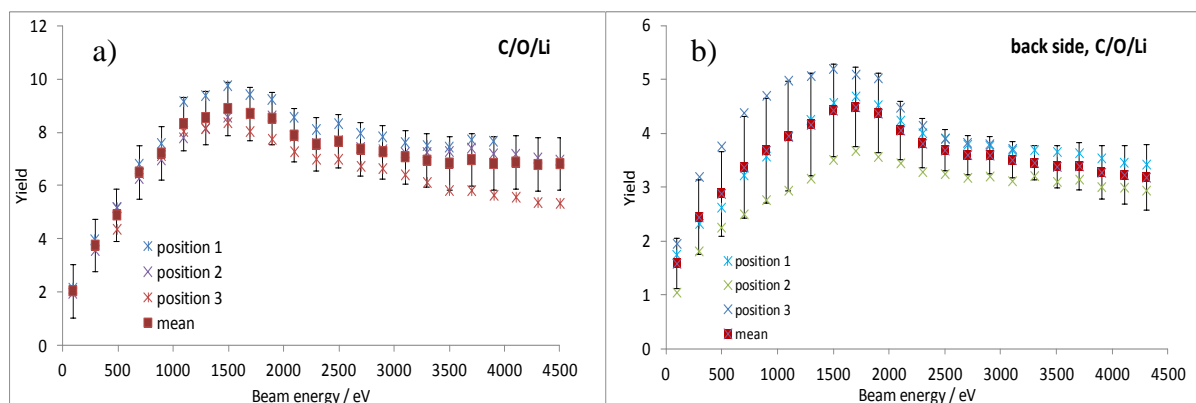


Figure 6.5- The SEE yield values measured from the front (growth) surface of a PCD sample (in a) and from the back side (nucleation surface) of the sample (in b) after lithiation of one side at a time. As observable from the graphs, the back surface displayed a reduction in the yield of about 50% in relation to the top surface.

Raman spectroscopy analysis gave evidence of the presence of sp^2 on the back side of the sample even after acid cleaning for 3 hours, from the increased density of grain boundaries (see figure 6.6).

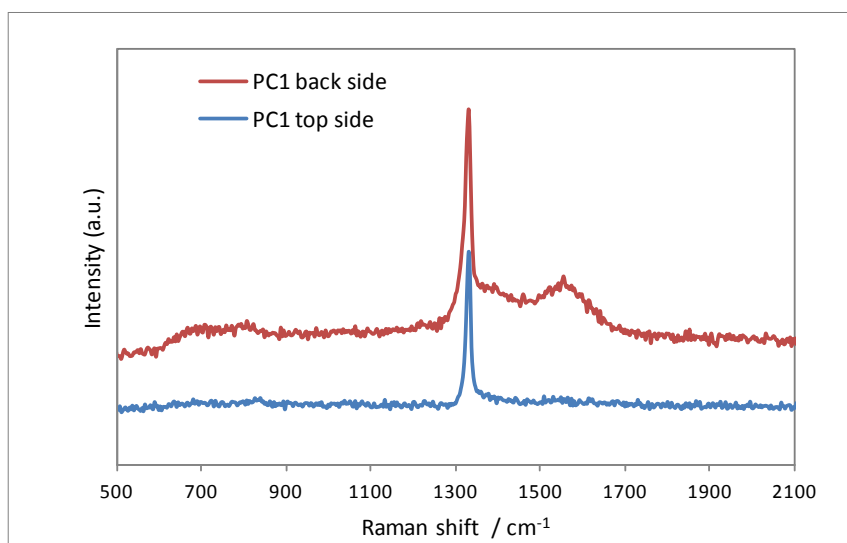


Figure 6.6- UV-Raman spectra taken from both sides of one of the Element Six samples after cleaning for 3 hours, showing that besides the sharp diamond peak at 1332 cm^{-1} the back side of the sample still contains a small amount of sp^2 carbon (G-band at 1550 cm^{-1}) probably present at the grain boundaries.

Furthermore, the differences in the electron emission obtained from the oxygenated surfaces in comparison with the Li-terminated samples were observed under SEM, as presented in figure 6.7. The image at right corresponds to the results presented in figure 6.5a, with some areas reaching a maximum yield of 10.

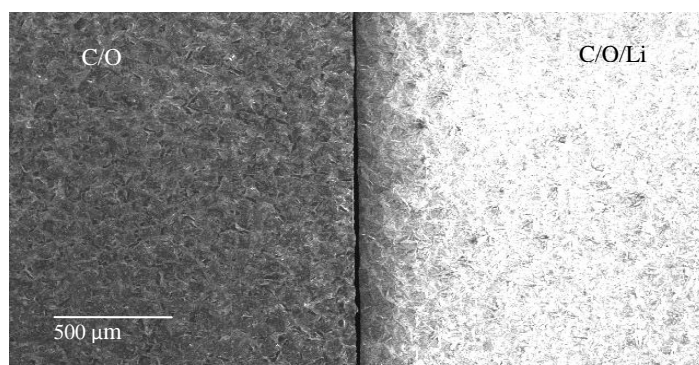


Figure 6.7- SEM image comparing two identical PCD samples, one with oxygen termination (left) and the other with Li-O termination (right), showing a considerably larger intensity of secondary electron emission from the lithiated surface.

A CVD (100) SCD sample was also tested, although only for a H-terminated surface. To overcome any charging effects, prior to H-termination the sample was coated with a 0.5 μm layer of residual B-doped diamond grown using a HFCVD reactor. Figure 6.8 shows a yield coefficient of ~ 10 after measuring two distinct areas of the sample, which is slightly higher than the maximum values of 8.9 measured from PCD samples with Cs and Li functionalization.

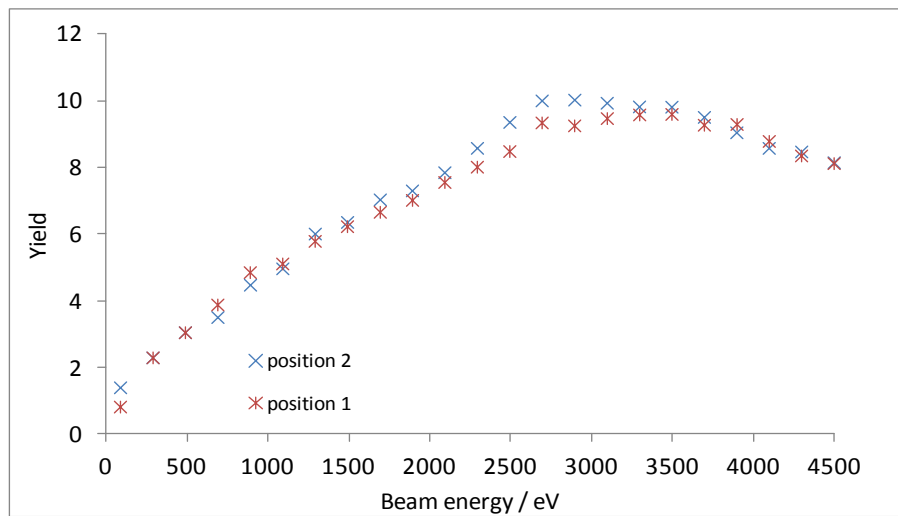


Figure 6.8- The SEE yield values measured from a SCD sample prepared with H-termination after being coated with a 500 nm residual B-doped layer, showing a maximum yield value of ~ 10 at 2.6 keV.

These ad-layers are expected to promote a lower onset for the emission energy, thus the transport properties of the bulk may be responsible for the results. Table 6.2 contains a summary of all the experiments performed in the present chapter.

Table 6.2 - Summary of the SEE yield values measured for the PCD CVD and SCD CVD samples with different surface functionalization.

Sample	Surface	Yield
B-doped PCD (BDPC) (unpolished)	C/O/Li	8.9 ± 0.75
	C/O/Cs	7.5 ± 0.29
	C/O/Li	6.9 ± 1.46
	C/O/Cs	9 ± 0.67
	C/O	4.3 ± 0.30
	C/H	4.3 ± 0.25
	C/O/Li, C/O	$5.4 \pm 0.53,$ 4 ± 0.34
	C/O/Cs, C/O	$4.4 \pm 0.20,$ 2.7 ± 0.29
BDPC (back side)	C/O/Li	4.5 ± 0.85
SCD	C/H	9.7 ± 0.41

Surprisingly, the measurements from both hydrogenated and oxygenated PC surfaces originated similar yield values. The explanation may be related to some sort of contamination of the H-terminated surface.

6.4. Conclusions

PC CVD diamond samples of unpolished B-doped ($> 10^{20} \text{ cm}^{-3}$) diamond, acquired from Element Six Ltd were functionalized with CsO and LiO adsorbed layers. The maximum yield value obtained for the caesiated surfaces was around 9 at 2.9 keV, which was considerably lower when compared with the yields measured previously for the MCD HFCVD films (~ 13 at 2.9 keV).

The primary beam energy of 2.9 keV corresponding to the maximum yield is in accordance with the values for the beam energy obtained previously for Cs/C terminated surfaces on p-type MCD CVD films and on p-type (100) SCD samples, although in the current experiments the highest yield values (~ 9) are much smaller than the ones published in the first case (80 and 130, respectively) most of them referring to evaporation of Cs directly onto the diamond surface without prior oxygenation, although Cs is expected to stick more easily to a previously oxygenated surface than to a bare or hydrogenated one.

Actually, all the results known from the literature for caesiated diamond surfaces present a similar trend for the beam energy necessary for maximum yield. The differences observed may be related with the transport properties of the bulk or perhaps with the surface coverage uniformity of the PC rough surface.

SEE yield values measured from a LiO terminated surfaces, had maximum yield of 8.9 at 1.5 keV, although presented a larger variation in the values acquired from different surface areas. In addition, the H-terminated SCD sample showed a yield of ~ 10 presenting small variance across the surface. The smoother surface in the case of SCD is expected to allow a more uniform NEA surface and in addition, the electron emission at the surface should not be hindered by neighbour crystals interfering.

The process of secondary electron emission is dependent on the generation, transport and emission characteristics of the sample under consideration, such as the type of surface adsorbed layers and degree of coverage. It is also dependant on the experimental conditions such as the primary beam energy, since it establishes the number of electrons generated in the sample and the distance from the surface at which they are generated.

Among several others, two factors are of high importance: first the percentage of surface coverage by oxygen, and second, the percentage of Cs adsorbed. Therefore, all the results can be related with differences at this level. According to the experiments, the Li-O surface coverage reaches normally a maximum of 60%^[12], the best achieved so far for this type of surface termination, and much less than for a hydrogen termination which is close to 100%.

Another important factor to be taken in consideration is the diamond surface roughness and its effect on the NEA effectiveness and on the electron emission process. Previous studies on (100) and (111) SCD have shown remarkable transport properties, contributing to the high yields obtained and the crystallography was observed to play a role in the surface adsorption properties with implication in the emission properties of the samples.^[5]

A B concentration of about 10^{18} cm^{-3} is expected to be sufficient to avoid the sample charging; therefore in the measurements presented the samples were unlikely to suffer from charging effects altering the values measured.

Certainly, a combination of all these variables conditioned the values measured in these experiments.

6.5. References

1. H. Bruining, in *Physics and Applications of Secondary electron Emission*, McGraw-Hill, New York (1954) 1.
2. T.L. Martin, Lithium oxygen termination as a negative electron affinity surface on diamond: a computational and photoemission study, PhD thesis, School of Chemistry, University of Bristol (2011).
3. J.E. Yater, A. Shih and R. Abrams, Electron transport and emission properties of diamond, *Journal of Vacuum Science and Technology A* **16** 3 (1998) 913-918.
4. G.T. Mearini, I.L. Krainsky, J.A. Dayton, Y. Wang, C.A. Zorman, J.C. Angus, R.W. Hoffman and D.F. Anderson, Stable secondary electron emission from chemical vapor deposited diamond films coated with alkali-halides, *Applied Physics Letters* **66** 2 (1995) 242-244.
5. J.E. Yater and A. Shih, Secondary electron emission characteristics of single-crystal and polycrystalline diamond, *Journal of Applied Physics* **87** (2000) 8103-8112.
6. H.J. Hopman, J. Verhoeven and P.K. Bachmann, Electron stimulated desorption from oxygenated and hydrogenated synthetic diamond films, *Diamond and Related Materials* **9** (2000) 1238.
7. V.V. Dvorkin, N.N. Dzbanovsky, N.V. Suetina, E.A. Poltoratsky, G.S. Rychkov, E.A. Il'ichev and S.A. Gavrilov, Secondary electron emission from CVD diamond films, *Diamond and Related Materials* **12** (2003) 2208–2218.
8. J.E. Yater, A. Shih, J.E. Butler and P.E. Pehrsson, Electron transport mechanisms in thin boron-doped diamond films, *Journal of Applied Physics* **96** 1 (2004) 446-453.
9. K.P. Loh, J.S. Foord, R.G. Egde and R.B. Jackman, Tuning the electron affinity of CVD diamond with adsorbed caesium and oxygen layers, *Diamond and Related Materials* **6** (1997) 874-878.
10. K.M. O'Donnell, T.L. Martin, N.A. Fox and D. Cherns, *Ab initio* investigation of lithium on the diamond C(100) surface, *Physical Review B* **82** (2010) 115-303.
11. K.P. Loh, X.N. Xie, S.W. Yang, J.S. Pan and P. Wu, A spectroscopic study of the negative electron affinity of caesium oxide-coated diamond (111) and theoretical calculation of the surface density-of-states on oxygenated diamond (111), *Diamond and Related Materials* **11** (2002) 1379-1384.
12. N.A. Fox, private communication (2012).

Chapter 7.

Growth and characterisation of thin diamond membranes

7.1. Introduction

Growing diamond films with thicknesses greater than 0.5 μm is relatively straightforward, but for thinner films the issue is poor seeding density leading to non-continuous films. The importance of seeding in the nucleation of diamond for heteroepitaxial growth was discussed in section 1.6.2. Besides the different methods for the application of a seeding layer, there are a variety of seeding powders and dispersions available on the market. The dimension and properties of synthetic nanodiamond powders (NDs) depend on the production method such as HPHT, CVD, shock wave compression of carbon materials in the presence of catalysts, explosion or detonation.^[1] First studied in Russia in 1960s, the use of NDs has been extended to a variety of applications due to their large-scale and low-cost production based on the detonation of carbon-containing explosives.^[2] Also, compared to their counterparts, detonation NDs have the advantage of presenting a narrow particle-size distribution in the region of 4 to 5 nm.^[3, 4] This material is ideal for the seeding of thin diamond films but some difficulties may be encountered in obtaining effective dispersions. Most commercial detonation nanodiamond suspensions are usually aggregated into 100 nm clusters, constituted by a strong sp^2 -bonded matrix binding the core sp^3 particles together.^[5] Such large, tightly-bound aggregates were formed during the cooling down of the detonation process by which they are produced.^[6] Previous studies demonstrate that the reduction of such aggregates into the primary core particles is not possible with sonication alone.^[5] Therefore, two main difficulties are encountered: breaking up the aggregates to the primary 5 nm particles, and

dispersing them efficiently. In addition to wet-stirred-media-milling with zirconia beads, high power ultrasonication was found to be an efficient method to break up aggregates dispersing them in water and highly polar solvents, such as methanol and dimethyl sulfoxide.^[6,7] Subsequent agglomeration between primary particles takes place due to the contribution of surface forces and additionally due to chemical bonding mediating the aggregation.^[8] Hydrogenation of detonation diamond, with annealing in hydrogen gas was presented as an alternative effective method to achieve stable cluster-free colloids.^[5] H-terminated surfaces are expected to be highly hydrophobic due to the polarity of the C-H bond, whereas C-O is hydrophilic.^[9,10]

In this section an extensive experimental study is presented, on the growth of thin NCD films exploring various seeding methods considering some of the aspects mentioned above and the effect of the nucleation layer on the quality of the resulting diamond membranes.

The measurement of the electron emission from diamond films in a transmission configuration requires the preparation of free-standing pinhole-free NCD films with thicknesses ideally on the order of a few hundred nanometres, for measurements under field free conditions. Such diamond membranes are ideally sustained by a solid material frame for easy handling and mounting.

The techniques developed for the preparation of the free-standing films are also described, and the preliminary transmission yields obtained are discussed, together with the predictions from Monte Carlo simulations. Finally, a few modifications are proposed for the improvement of the measurement setup.

7.2. Experimental

The silicon substrates were cut to $1 \times 1 \text{ cm}^2$ using a commercial laser milling machine from Oxford Laser micromachining system. Then, the samples were carefully washed individually in an ultrasonic bath, first with acetone for 30 minutes, then with methanol for another 30 minutes and finally with D.I. water. Several seeding methods were attempted: manual abrasion, electrospray deposition (ESD), ultrasonic seeding, and a layer-by-layer (LBL) method, as described in table 7.1. The manual abrasion was performed with 1-3 μm diamond powder for 3 to 5 minutes, after which the substrate surfaces were cleaned with a cotton pad

soaked in methanol to remove the excess of nanoparticles from the surface. For the remaining methods a 5 nm nanodiamond suspension supplied by Japan New Metal Corp. was tested using methanol as the liquid medium, except for the case of LBL where the liquid used was D.I. water. Prior to ESD the suspensions were ultrasonicated between 5 - 30 minutes. Different suspension quantities were tested in the attempt to optimize the seeding layer uniformity. The dispersions were analyzed by Dynamic Light Scattering (DLS) with an (Malvern Zetasizer Nano) apparatus before and after ultrasonication or centrifugation, as described in table 7.2. The LBL seeding was prepared by means of a polyethyleneimine (PEI) solution in D.I., where the substrates were immersed for around 5 min, followed by immersion in the diamond suspension for up to 1 hour and then rinsing with D.I. before drying.

The diamond films were grown in the HFCVD reactor using 1 - 2.5 % CH_4/H_2 for periods from 90 min to 30 min, given an expected mean growth rate of $\sim 0.5 \mu\text{m/h}$ determined previously. A collection of samples was made, according to table 7.1 and 7.3. In this process, a few samples were carefully analysed by AFM before and after CVD in an attempt to identify trends and correct the causes behind heterogeneities. In addition, the thicknesses were also measured via SEM. All the samples were analysed by SEM and the higher quality surfaces were selected as samples from which to fabricate framed diamond membranes.

The process to do this was optimised after many experiments. It consisted of a laser machining method to mill out a $\sim 2 \text{ mm}^2$ area from the back of the silicon substrates to a depth of around 80% of the thickness of the substrate, followed by chemical etching in a saturated KOH solution at $100 \text{ }^\circ\text{C}$ to remove the remaining Si. It was found that if the laser was used to remove all of the Si, the diamond film would be greatly damaged, as described in the following sections. Conversely, if KOH were used to etch the whole thickness, this would take several days. The optimal process involved using the laser to etch most of the Si away in a few minutes, and then the slower, gentler KOH etch to remove the last of the Si without damaging the diamond film.

7.3. Results and discussion

7.3.1. HFCVD diamond deposition and seeding methods

A summary of the diamond films prepared is compiled in table 7.1, listing the experimental parameters taken in consideration in the present study both for seeding and CVD growing conditions. The samples are organized in order of decreasing CVD process duration (*i.e.* film thickness). For each cycle, the seeding method and the CH₄ were varied. The table aims to give a representative sample of the experiments and the main issues related with the quality of the films, but include only some of the samples prepared.

Table 7.1 - Parameters used in the preparation of a series of thin NCD films. The diamond films were grown in a B-free undoped atmosphere, varying the cycle duration, C content and seeding methods. The samples are presented in order of decreasing deposition time.

Sample	H ₂ (sccm)	CH ₄ (sccm)	Dep. Time (min)	Seeding
M1	200	2	90	ESD, 0.5 ml
M2	200	2	90	ESD, 1 ml
M3	200	2	75	ESD, 1 ml
M4	200	2	60	ESD, 0.5 ml
M5	200	2	60	ESD, 1 ml
M6	200	2	60	ESD, 0.5 ml
M7	200	2	60	M.A.
M8	200	10	60	Ultrasonic
M9	200	2	45	ESD, 1 ml
M10	200	2	45	ESD, 0.5 ml
M11	200	2	45	M.A.
M12	200	2	45	Ultrasonic
M13	200	3	45	M.A.
M14	200	3	45	ESD, 0.5 ml
M15	200	5	45	M.A.
M16	200	10	45	M.A.
M17	200	5	40	M.A.
M18	200	2.5	30	M.A.
M19	200	3	30	M.A.
M20	200	5	30	M.A.
M21	200	5	25	ESD, 0.8 ml
M22	200	5	25	Ultrasonic

The SEM images taken from a collection of sample are displayed in figure 7.1.

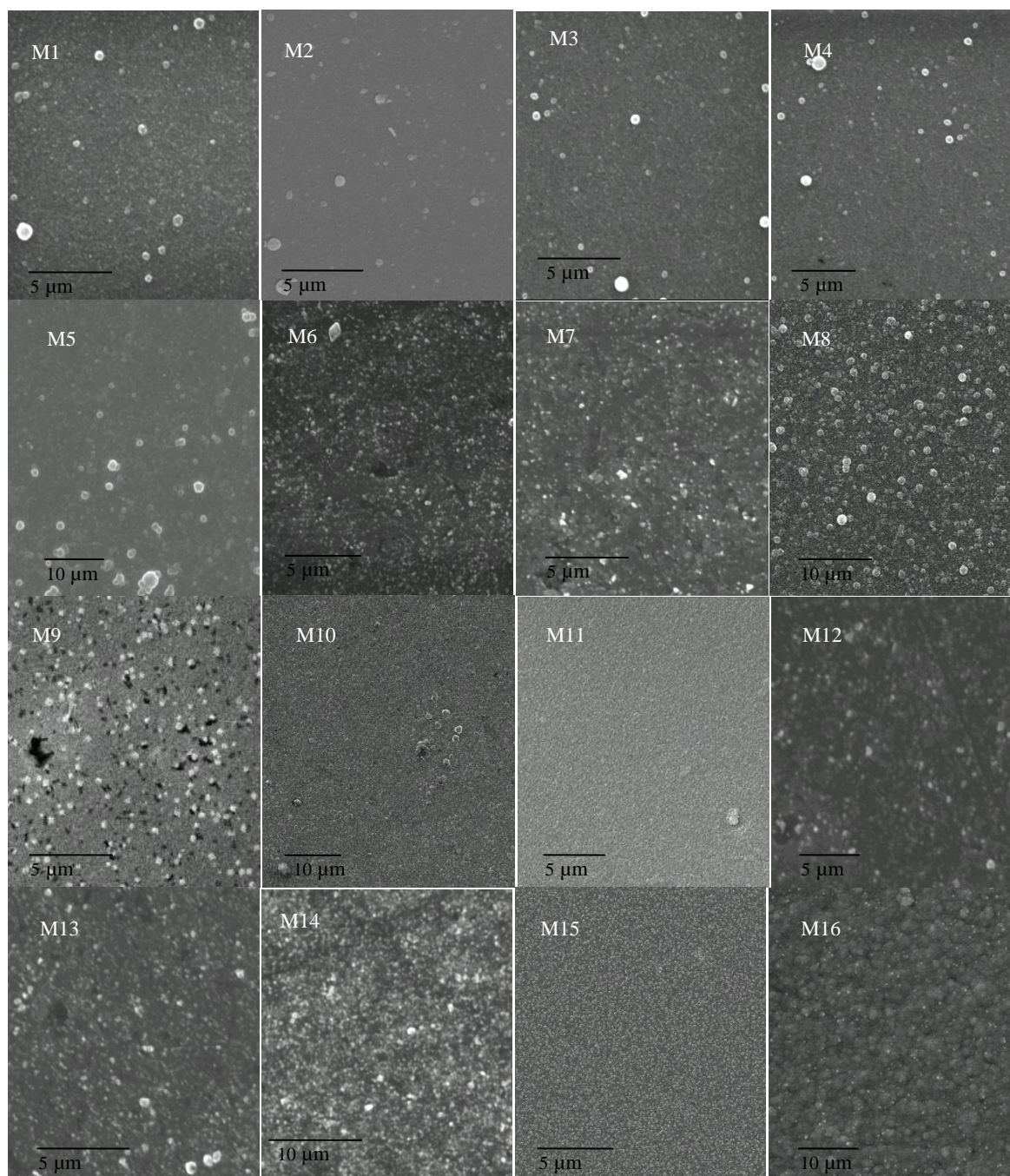


Figure 7.1- SEM images of the NCD films grown under the conditions described in table 7.1.

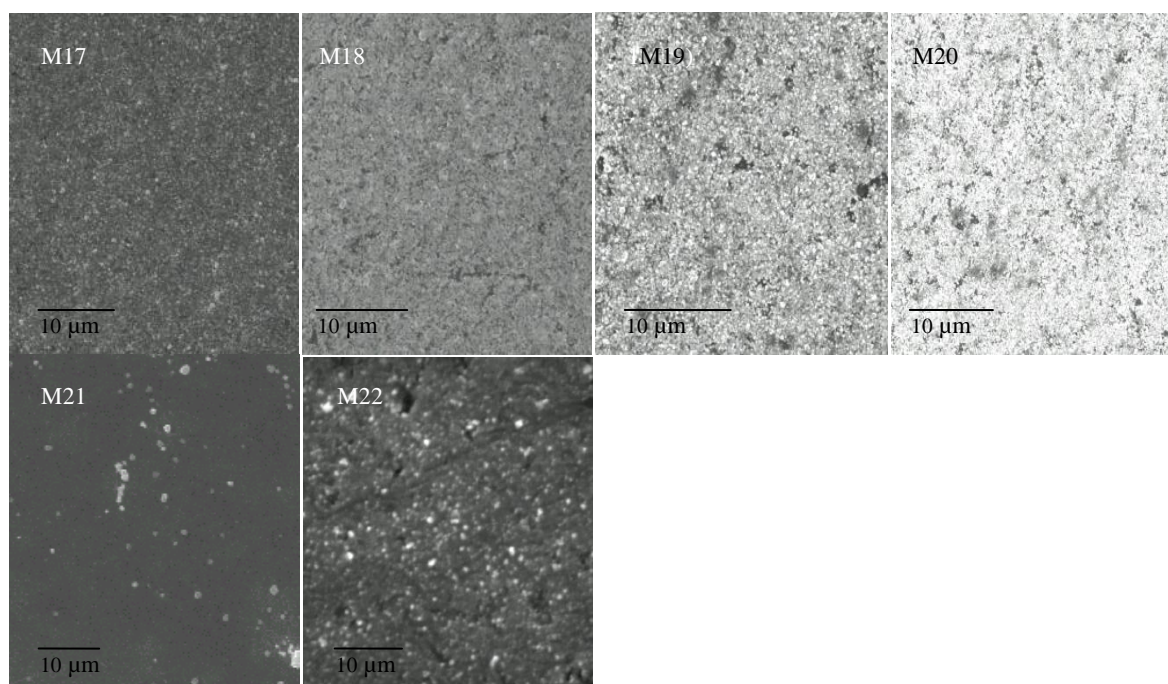


Figure 7.1 (cont.)- SEM images of the NCD films grown under the conditions described in table 7.1.

The images indicate that in most cases the seeding layers were considerably uneven. A few potential causes acting alone or in combination were suggested to account for these results. In all the processes, but especially for the substrates nucleated by ESD, a spotless surface was essential for a successful seeding. It was found that any minor defect or impurity on the surface compromised greatly the uniformity of the seeding layer. Hence, the cleaning method was continuously under improvement until achieving the optimal conditions described in the experimental section above, which have proven to give rise to better results. In addition, the SEM images reflect the difficulty in obtaining an ideal monolayer of uniformly dispersed diamond nanoparticles. Furthermore, AFM profiles were taken from two samples, grown for 30 min using 1.25% and 1.5% CH_4/H_2 gas phase concentrations, respectively, as displayed in figure 7.2. The samples were analysed using AFM to allow a clear view of their surfaces before and after the CVD process. Figure 7.2a shows the particle distribution after seeding by EDS using 1 ml of suspension. The image shows that more than one layer has been deposited where the nanoparticles sit on top of each other making it impossible to evaluate the nucleation density.

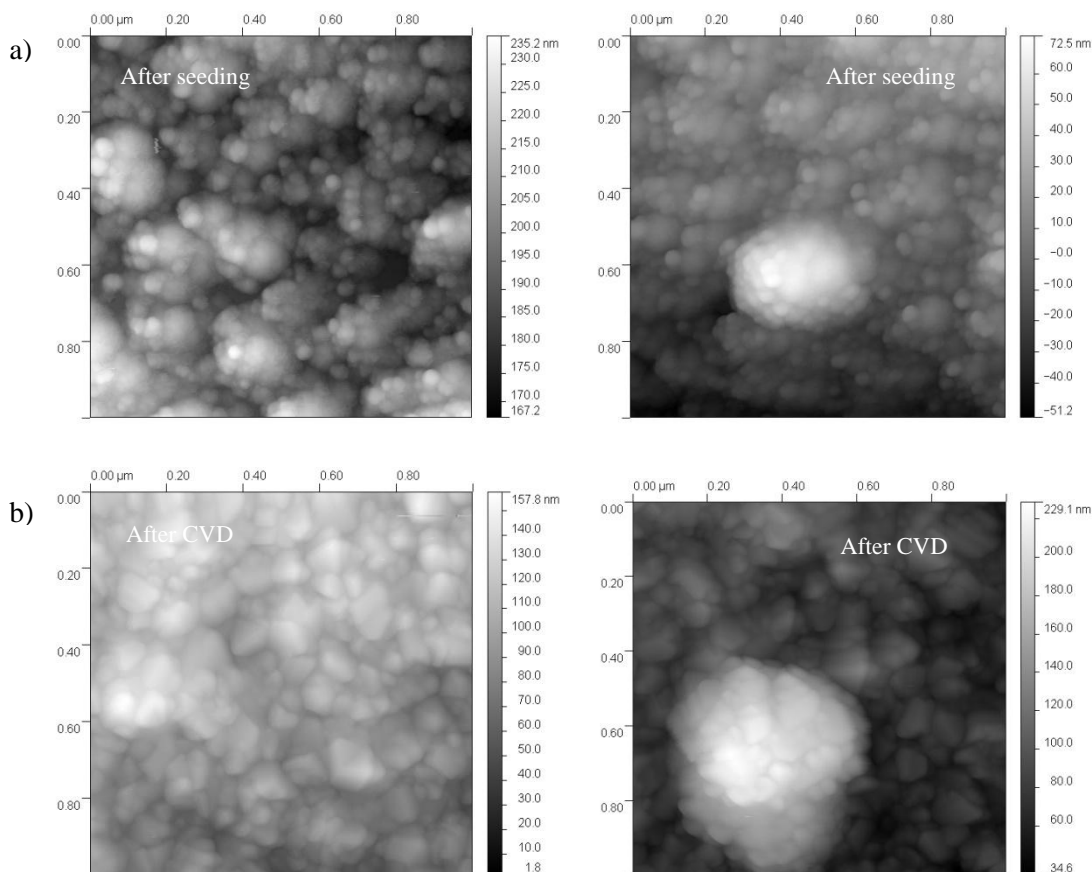


Figure 7.2- AFM images of two different samples showing the surfaces after seeding by ESD using 1ml of colloidal suspension (a), and (b) after undergoing 30 min of CVD diamond growth at 1.25% and 1.5% CH_4/H_2 , respectively. The grey scale relates to a depth profile, measured from the deeper areas (in black) to the highest level at the top of the surface (in white).

This fact was related with an excessive amount of colloidal suspension sprayed onto the surface. Therefore, a reduction from 1 ml to 0.5 ml of sprayed suspension proved to be favourable. However, the main issue was the presence of particle agglomerates on the surface as a result of a heterogeneous colloidal suspension. The particle size distributions obtained by DLS confirmed an average ~ 59 nm sized particles even after centrifuging, which is indicative of particle aggregation in the suspension which were originally sized to 4 - 5 nm (table 7.2). Then, it was found that by agitating the nanodiamond suspensions immediately before the seeding process, the number and size of these aggregates was significantly reduced. When the NDs are dispersed in D.I. water or methanol, they become negatively charged by the dissociated acidic groups on their surfaces repelling each other. Hence the suspensions are expected to be relatively stable.

Table 7.2 - Particle sizing with DLS of 5 nm diamond suspension in methanol, prepared in equivalent conditions to the seeding suspension. The values indicate that the average diameter of the diamond particles in the suspension varied from ~ 78 nm to ~ 59 nm, before and after centrifugation. The difference between ultrasonication and centrifugation was found to be insignificant.

Treatment \ Mean values	Particle size (nm)	Peak intensity (%)	Peak width (nm)
No treatment	77.88	99.20	25.33
10 min in ultrasound	60.74	100	23.12
20 min in ultrasound	58.15	100	21.13
30 min in centrifuge	59.28	100	22.04

In some samples, the lack of uniformity may also be related to the incorrect performance of the ESD setup, due to a partial blockage of the syringe needle, an incorrect needle angle or simply the incorrect positioning of the sample holder towards the nozzle.

On the other hand, the manually abraded samples displayed a common issue related with the scratches left by the abrasion process (figures 7.1 and 7.2). The size of the diamond particles (1 – 3 μm) used for abrasion was considerably larger in relation to the film thicknesses grown. This meant that some of the scratches were found to be too deep to grow a uniform film. Conversely, the nucleation density appeared to be insufficient for the growth of fully continuous diamond films. The AFM profiles taken from a manually abraded sample after a CVD diamond cycle of 45 min using a 2.5% CH_4/H_2 are displayed in figure 7.3. When compared with the AFM profiles from figure 7.2 from samples that were grown for a shorter period and with less C concentration, the growth rate was considerable smaller.

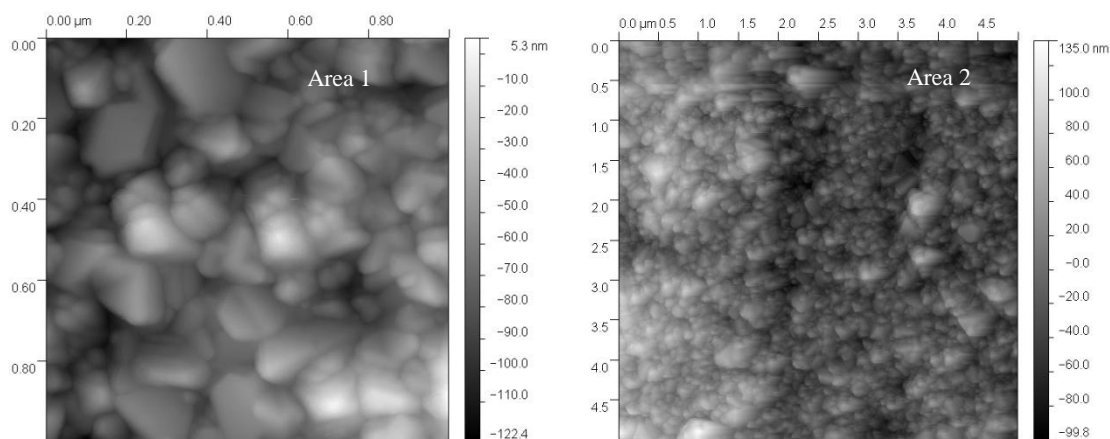


Figure 7.3- AFM images of two different surface areas of a manually abraded sample after a CVD diamond cycle of 45 min using 2.5% CH_4/H_2 , showing areas of reduced growth after a reasonably long cycle.

Returning to the ultrasonically seeded samples, the seeding particles were observed to stick one on top of another, forming not aggregates, but an overlap of partial layers, leading to a highly dense but not very uniform surface coverage (figure 7.4).

In the sequence of the experiments, a group of diamond films was prepared using the B-doping reactor, for which the growing conditions are summarized in table 7.3. The samples were produced by varying the deposition time, the atmosphere carbon content and the seeding methods. No B was added to the gas mixture; therefore any B incorporation into the diamond films was a result from the contamination of the reaction chamber (residual doping).

Table 7.3 - Parameters used in the preparation of a series of thin NCD films, varying the deposition time, C content and seeding methods. The samples are presented in order of decreasing deposition time. The diamond films were grown using a B-doping chamber although no B was added to the gas phase.

Sample	H ₂ (sccm)	CH ₄ (sccm)	Dep. Time (min)	Seeding
N1	200	2	60	Ultrasonic
N2	200	2	45	ESD, 1 ml
N3	200	2	45	M.A.
N4	200	2.5	45	ESD, 1 ml
N5	200	3	45	ESD, 1 ml
N6	200	3.5	45	M.A.
N7	200	5	45	M.A.
N8	200	2	30	ESD, 0.5 ml
N9	200	2.5	30	ESD, 1 ml
N10	200	3	30	ESD, 1 ml
N11	200	3	30	ESD, 0.5 ml
N12	200	3.5	30	ESD, 0.5 ml
N13	200	4	30	ESD, 0.5 ml

To illustrate the problems faced during the perfection of the seeding methods, the SEM images from a collection of films are shown in figure 7.4. In general, the surface images denote the same type of effects resulting from seeding process imperfections.

The films with the most homogeneous surfaces and which appeared to be virtually pinhole-free, were cleaved in half and the cross-sections analysed via SEM in order to evaluate the thicknesses of the diamond films. Though, as this was a destructive technique, it was limited to a few control samples and the film thicknesses of the remaining were simply estimated.

This is justified by the fact that cutting the samples in half gives a more precise measurement in terms of thickness, because it is expected that the area immediately beneath the filament to have a relative higher growth rate comparatively to the edges of the sample. But due to the necessity to keep the surface areas as large as possible to facilitate the preparation of framed membranes, such procedure was avoided.

Figure 7.5 presents the SEM images of a number of good quality films obtained and the corresponding film thicknesses. These films are considerably thicker than would be optimal for transmission SEE measurements. This is because most of the seeding techniques were being tested for the first time so it was decided to start with reasonably long CVD deposition

times, and once the seeding was optimised, reduce the deposition time to give the required film thicknesses in later experiments. In addition, it was thought that thicker films would be easier to manage in terms of testing the membrane preparation process, which proved to be true as demonstrated in the next sections.

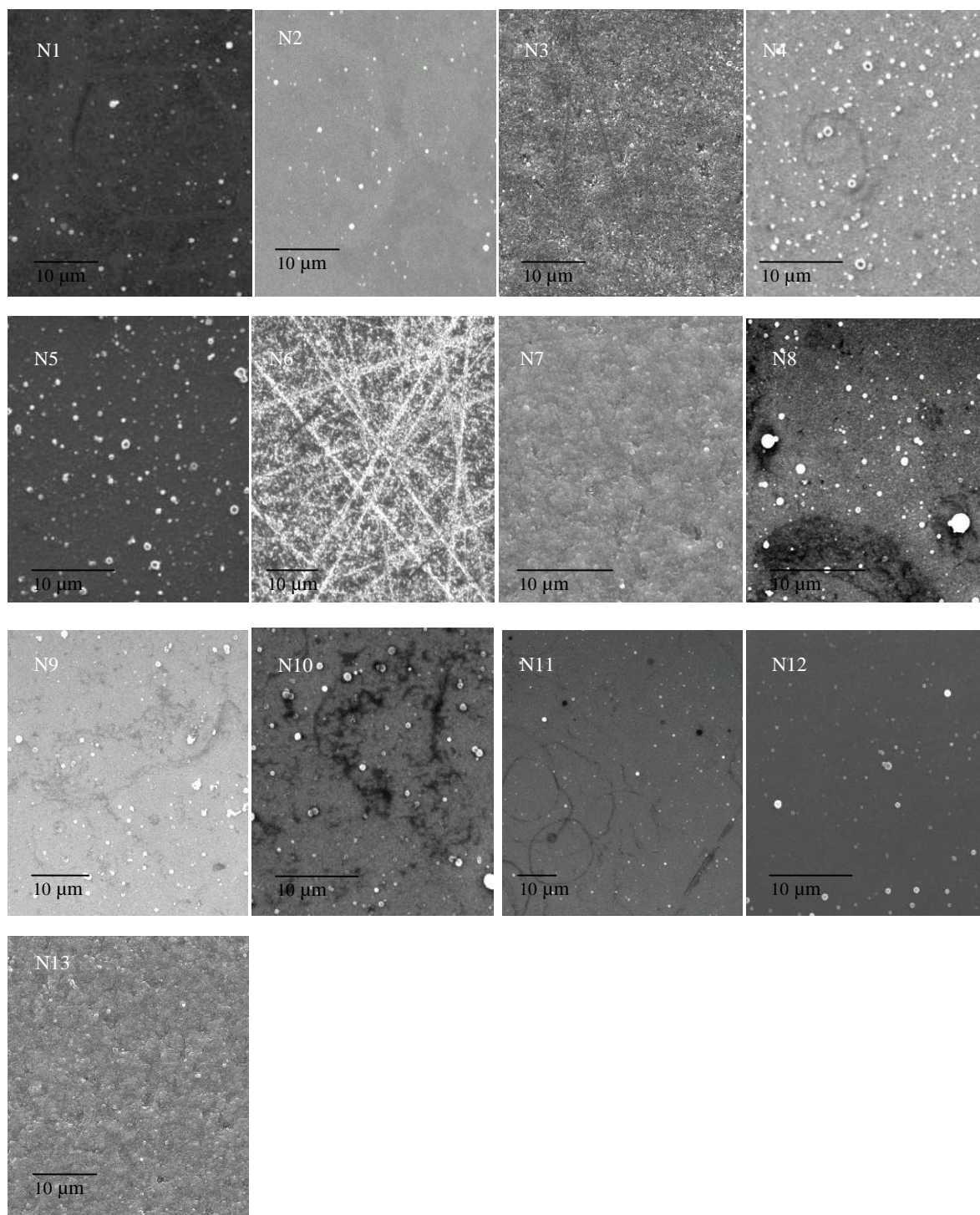


Figure 7.4- SEM images of the NC diamond films grown under the conditions described in table 7.3.

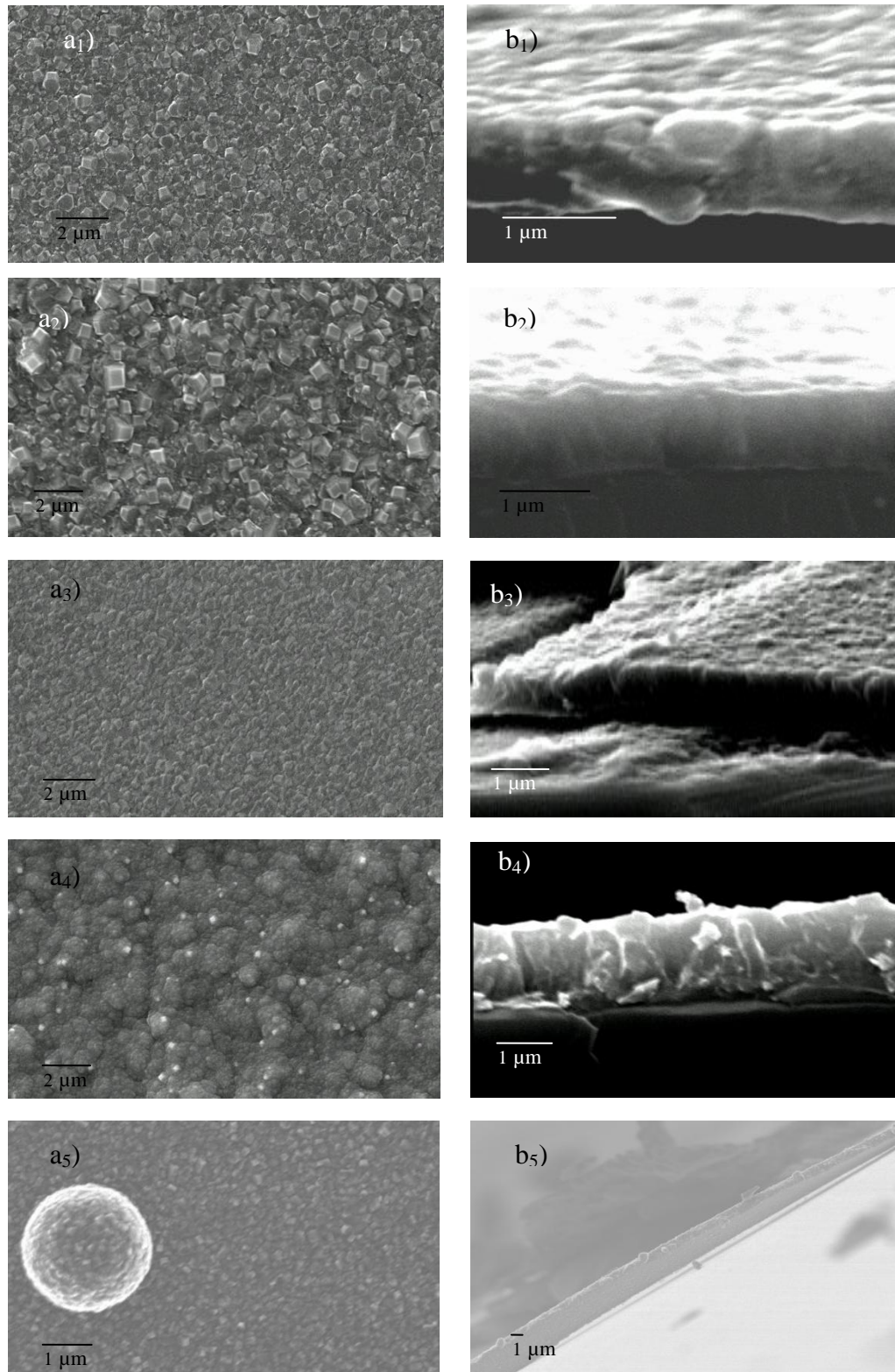


Figure 7.5- SEM images of five diamond films seeded by ESD with 0.8 ml of seeding suspension immediately after ultrasonication for 20 min. All the films were grown for 50 min at 1.25% CH_4/H_2 except the sample in for a_4) at 2.5%. The films presented good uniformity and the cross-section images show a similar thickness of $\sim 1 \mu\text{m}$ and $\sim 1.3 \mu\text{m}$ for the sample in b_4).

Despite the presence of agglomerates in the films, continuous diamond films with thickness of a few hundred nanometres were obtained, as presented in figure 7.6.

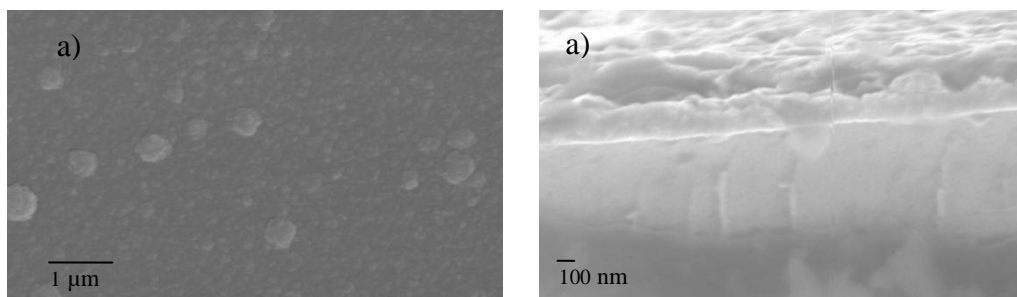


Figure 7.6- SEM images from a continuous thin diamond film (a), and b) a cross-section image where a film thickness under 220 nm can be measured. The seeding method was ESD with ~ 0.6 ml of diamond suspension and it was grown at 1% CH₄/H₂ for 40 min.

To finalize the experiments on seeding for Si for heteroepitaxial diamond growth, a LBL method was tested. The results have shown a tendency for the appearance of cracked diamond films due to the polymer drying and cracking (figure 7.7). Although there is certainly room for improvement, no further experiments were done using this technique.

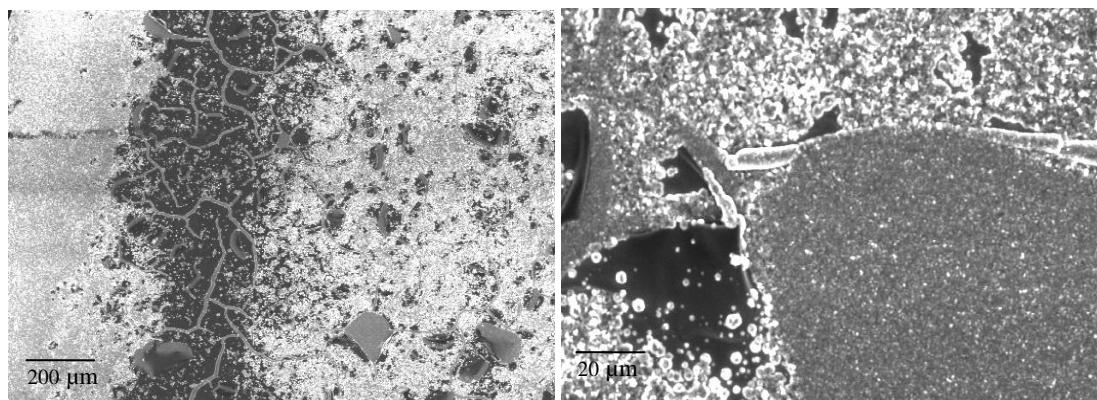


Figure 7.7- SEM images of Si seeded via the LBL process, showing evidence of the polymer layer drying and cracking.

At the end of this cycle of growth and morphology observations, the higher quality films were selected to undergo the following step which consisted in the preparation of free-standing membranes. Unfortunately, due to the severity of the processes involved in the substrate removal a considerable number of samples were lost, as detailed throughout the next section.

7.3.2. Preparation of free standing diamond membranes

To fabricate supported diamond membranes, laser machining has been used to mill out an area of approximately 2 mm² on the silicon substrates to a depth of around 80% of the Si thickness. Then, the remaining Si has been removed by chemical etching with concentrated KOH solution at 100 °C. The process is illustrated in figure 7.8.

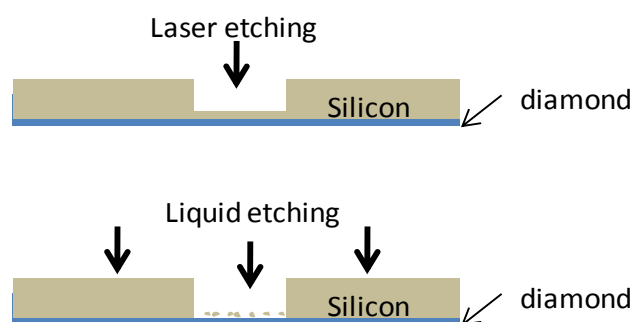


Figure 7.8- Sketch of the method that has been used in the production of free-standing diamond membranes.

Before proceeding to the removal of the Si substrates from diamond-coated samples, a series of tests were performed using pieces of uncoated Si wafer in an attempt to understand the method and optimize the etching parameters.

7.3.2.1. Laser machining

According to the equipment specifications, the laser machine system that has been used is capable of machining most types of common materials, although it is necessary to adjust the laser parameters for each specific case. Different milling conditions were tested varying the laser parameters such as, the cutting velocity, pulse distance, frequency, laser attenuation, number of scans and laser power. In this manner, the effectiveness in milling the 0.54-mm-thick Si pieces, normally used as substrates could be determined.

Figure 7.9 presents the results obtained using the conditions summarized in table 7.4. The milling conditions have been chosen based on the machine specifications.

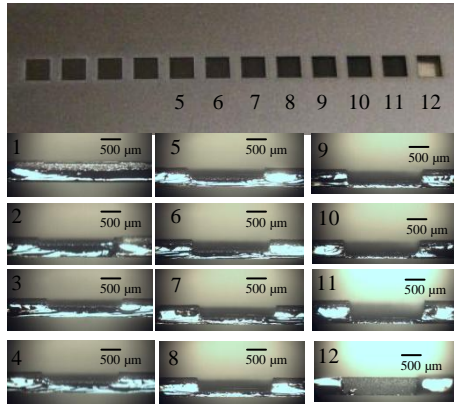


Table 7.4 -Experimental parameters for the laser milling shown in figure 7.9.
Laser power: 0.130 W
Cutting velocity: 1 mm/s
PSO pulse distance: 0.01
Number of scans: 8
Hatch pitch: 0.01
Distance z in depth: 0.01
Laser frequency: 1000 Hz
$I = 90 \%$
Attenuators at 100 %

Figure 7.9- Optical microscope pictures of the milling experiments performed on Si samples, showing the removal of material in depth with increasing the number of scans, in the conditions summarized in table 7.4.

Following the above experiments, diamond-coated Si substrates were then used. Milling deeper than 80% was found to easily damage the diamond film with holes created by the laser beam (figure 7.10).

An SEM image taken from a cross-section after this process is shown in Figure 7.11. This etching method proved to be very efficient since most of the substrate material is removed in one step without special preparation requirements.

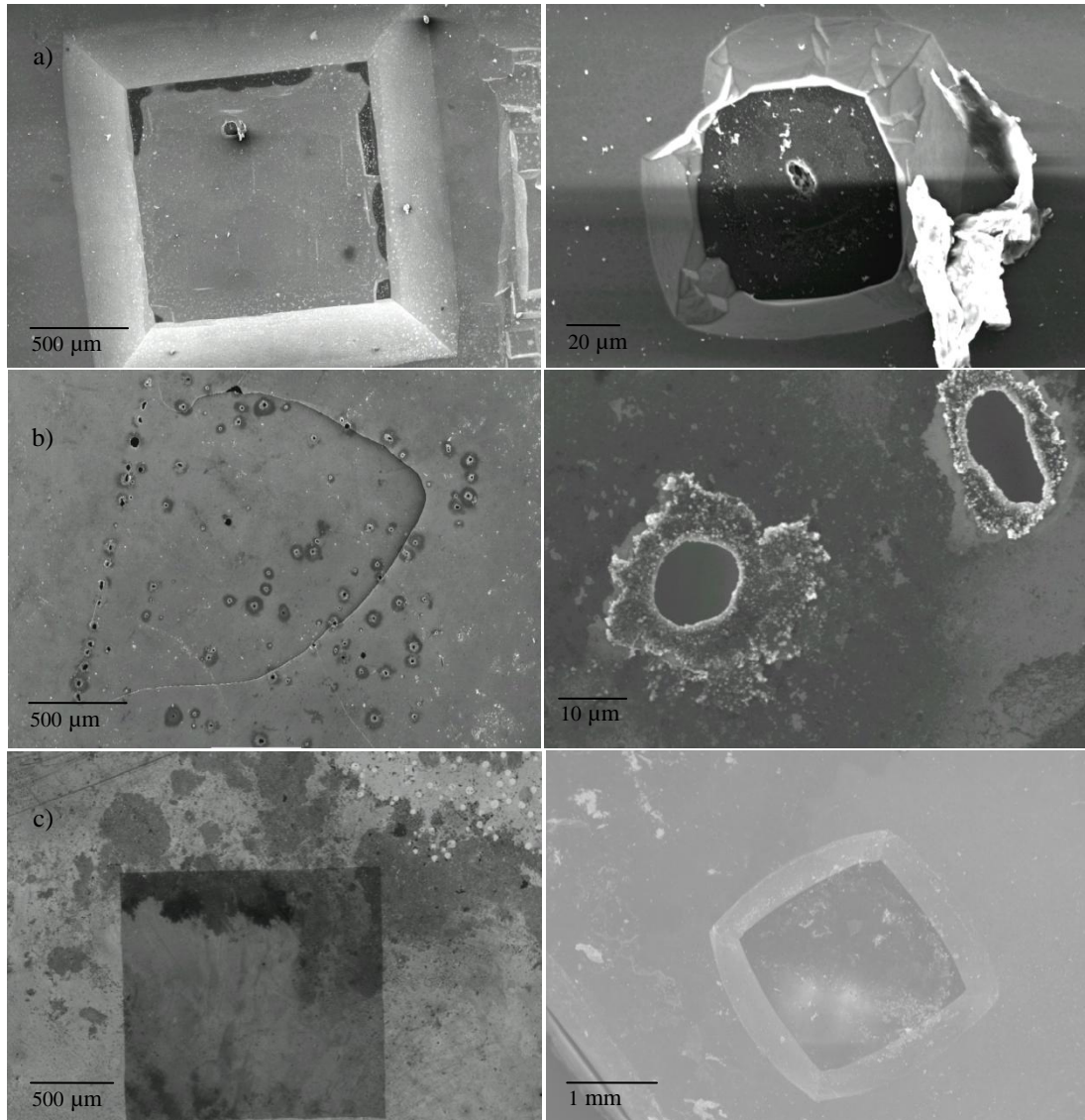


Figure 7.10- SEM image taken from the back side of a diamond film ($\sim 10 \mu\text{m}$ thick) undergoing the etching process. In a) can be seen a diamond surface with clear evidence of the holes created during the laser milling. Image b) has been taken from the top side, showing evidence of diamond film cracking during the chemical etching (left), induced by the presence of holes and the stresses created in the film during the chemical etching. Image c) (sample front and back side, respectively), shows a successfully fabricated membrane using a $\sim 140\text{-nm}$ -thick diamond film, kindly supplied by Dr. Oliver Williams (Fraunhofer Institute).

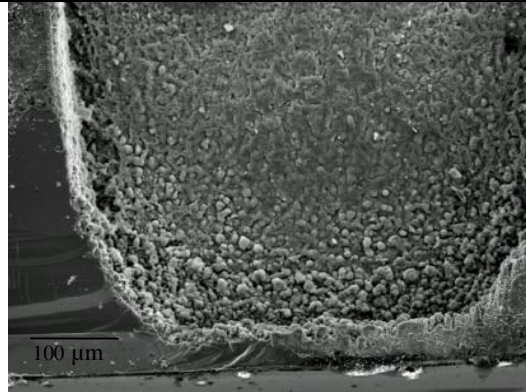


Figure 7.11- SEM image taken from a cross-section after undergoing the milling process. The picture illustrates the feasible limit of ~ 80% for the milled depth without compromising the diamond film integrity.

The method was designed to guarantee that a silicon frame is kept as a membrane support for ease of handling of the sample. Despite the need of using some kind of chemical etching to finalize the samples, overall the processing time is shortened and a good finishing could be obtained (figure 7.12).

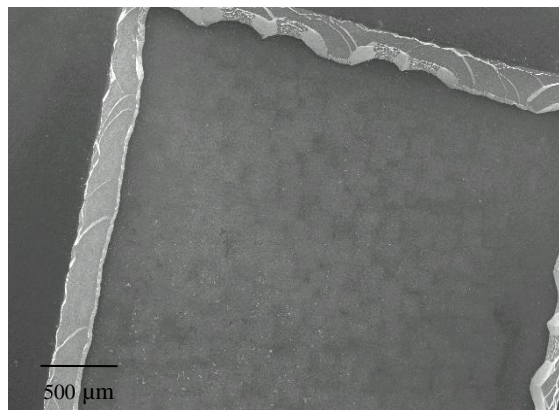


Figure 7.12- SEM image taken from the back side of a diamond membrane (~ 10 μm thick) after completing the etching process with success.

As mentioned previously, the remaining layer of Si has been removed by immersing the samples in a hot concentrated KOH solution. The method was improved from completely dipping the samples into the solution, to a process of suspending them with a metal clamp leaving approximately half of the samples outside the etching bath. For the thinner diamond films a different procedure was adopted, since the milled area cracked easily under etching, possibly as a result of non-uniform etching of the film leading to asymmetric stresses.

Figure 7.13 illustrates a small piece of equipment mounted for chemical etching. The sample to etch is placed on top of a metal plate with the diamond facing down. This method exposed only the area of Si that was to be removed, leaving the diamond film protected from the etchant.

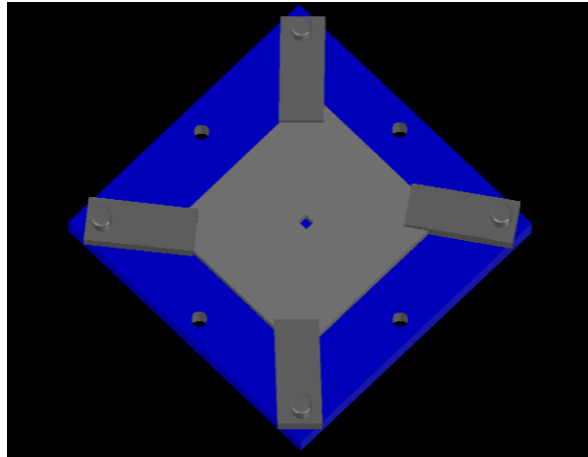


Figure 7.13- Schematic diagrams of the setup mounted for the chemical etching of thin diamond films, consisting of two metal plates firmly clamped together and sandwiching the sample to etch. The top metal plate has an aperture that exposes the substrate and defines the area to etch. Small drops of etchant are poured into the hole and left to react.

A metal plate with a $\sim 2 \text{ mm}^2$ orifice was then placed on top of the substrate making the orifice coincident with the area previously milled in the laser machining equipment. The parts were then firmly clamped together. Small drops of a hot KOH solution were dropped into the hole leaving it to react. Periodically the system was unclamped to determine how the reaction was proceeding, and the process was repeated until all the Si was removed from the design area.

In general, a complete removal was observed after up to 10 hours of chemical etching, depending on the temperature of the solution. When the temperature higher than $100 \text{ }^\circ\text{C}$, the process was considerably accelerated but the thinner films had a tendency to crack with the film ending up been removed altogether. Therefore, there was a need to keep the temperature to an acceptable level to avoid the KOH recrystallization but without being excessively harsh for the films.

To summarise, a series of diamond membranes with thicknesses ranging from 14 μm to 140 nm have been produced successfully. One of the issues about the preparation of such delicate membranes for measurements under vacuum is related to their ability to hold considerable pressure differentials. Due to their extreme fragility, some of them were broken during the SEM characterization or in the process of assembling for electron emission measurement. The SEE measurements of the surviving membranes are described in the following section.

7.3.3. Transmission yield measurements

The experiments were performed under high vacuum ($\sim 10^{-7}$ Torr) using the home-build setup described in chapter 3. Figure 7.14 shows the schematics of the apparatus for the transmission measurements. The measurement method adopted consisted of mounting the membranes with the nucleation side facing the electron gun, so that the electrons were emitted by the growth surface. This positioning was chosen because this surface is expected to have higher quality. The samples were carefully attached to the sample holder by means of a metal plate which was clamped together (figure 7.15).

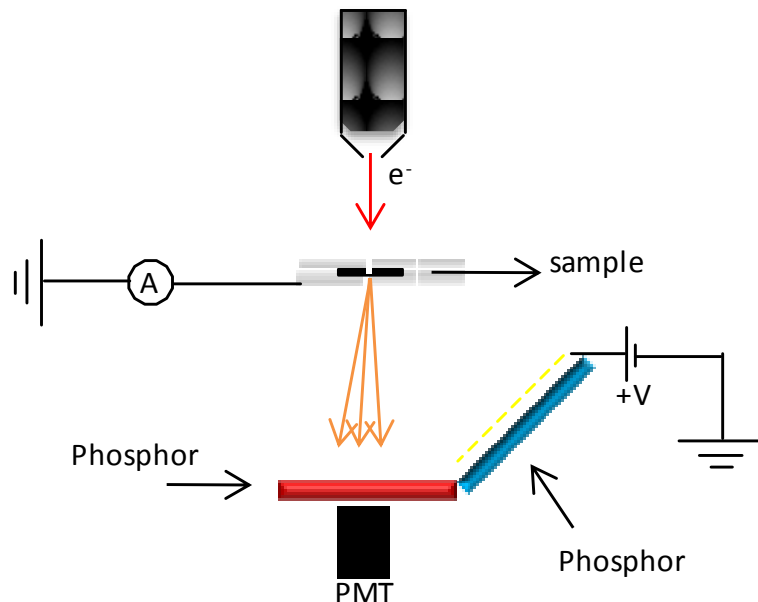


Figure 7.14- Schematic diagrams of the apparatus for the transmission measurements, detailed in chapter 3.

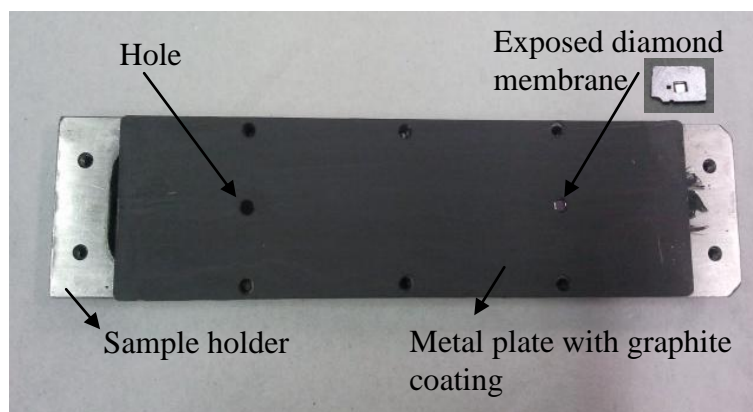


Figure 7.15- Photograph of the sample holder illustrating the method of mounting the samples for transmission measurements.

The metal plate has several full-width holes with diameters ~ 2 mm to ensure a constant emissive area and also for beam calibration. The measurements were made by centring the electron beam with the hole and measuring the signal obtained from the red PS detector positioned directly underneath. The signal acquired corresponds to the primary transmitted signal resulting from the electron beam (S_0). Then, the same procedure was completed with the diamond sample facing the electron beam, with the signal acquired being the total transmitted signal through the diamond membrane (S_{trans}).

The transmission yield was measured from three MCD diamond membranes with thicknesses of ~ 0.4 , 3.5 and 10 μm , labelled as samples 1 - 3, respectively. The yield values determined by the ratio S_{trans}/S_0 are presented in figure 7.16.

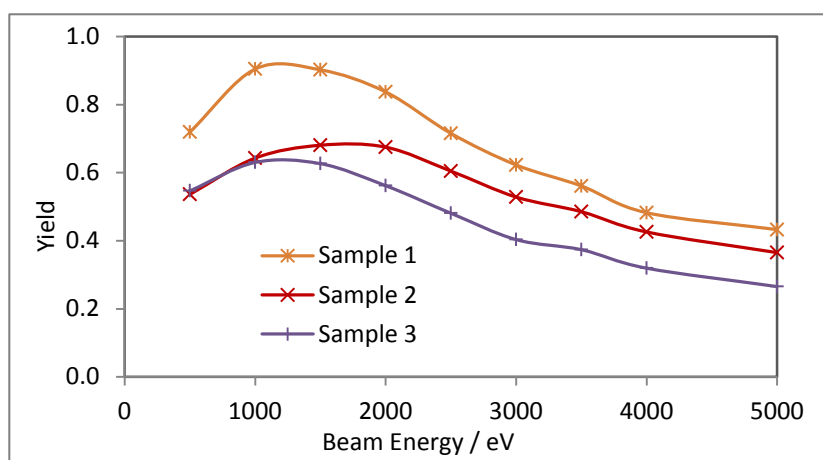


Figure 7.16- SEE yields measured from samples 1 - 3. The value increases from ~ 0.6 for the diamond films with 3.5 μm and 10 μm , to ~ 0.9 for 0.4 μm thick diamond.

Moreover, the surface termination has been taken into consideration, given the importance of a NEA emissive surface. Sample 2 was subsequently exposed to atomic H for a period of 5 min, and the yield measurements were repeated. The results obtained from the H-terminated film are shown in figure 7.17, by comparison with the acid cleaned O-terminated surface, where an insignificant increase of the values can be observed.

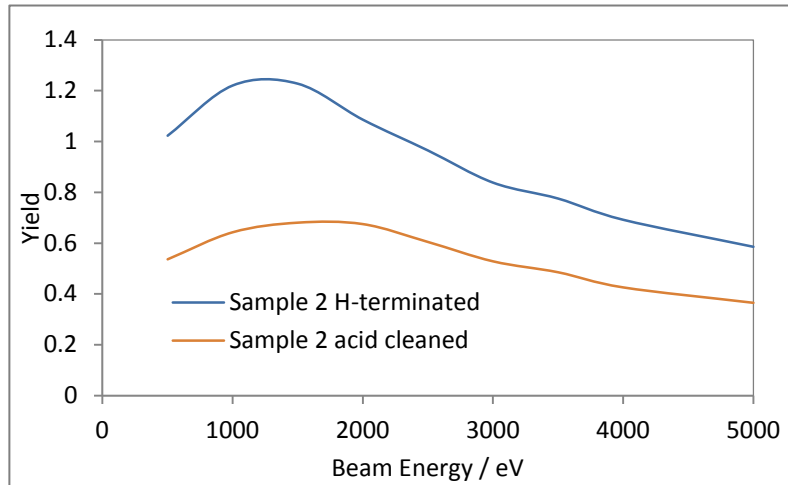


Figure 7.17- Yield curves obtained for sample 2 with H-terminated surface by comparison with the acid cleaned O-terminated surface.

The values were overall considerably low but not completely surprising, given the diamond thicknesses involved and the field free conditions in which the measurements were performed, as predicted by Monte Carlo simulations.

7.3.4. Monte Carlo simulation

As discussed in chapter 1, the electron transport from their point of generation within the diamond to the sample surface depends on the electron-solid interactions. The transmission of electrons through the diamond depends on its characteristics and thickness. The penetration depth and hence the distance at which the secondaries are generated are determined by the value of the primary beam energy. Thus, knowing the film thickness it is possible to simulate the transport distance of the secondaries towards the surface, which is frequently done by using Monte Carlo simulation codes.^[11-13]

The idea behind the Monte Carlo model of secondary electron emission is to simulate the trajectories of primary and secondary electrons within the solid at given cross-sections for active scattering processes. In such calculations it is generally assumed that the secondaries are being generated by 10^5 - 10^6 primary electrons.^[14]

In the present study, the electron transmission was simulated using a free Monte Carlo CASINO code to determine a model for the transmission of electrons through the diamond. This is obviously an approximation, as it regards the target as being amorphous although with the same density and composition of diamond. Nevertheless, it can be used as a useful guidance towards the threshold thickness in the transmission of electrons through a diamond membrane. Figure 7.18 shows the results obtained from one of the simulations at 5 keV, predicting a film thickness in the order of 215 nm for a positive gain in the absence of any drift field.

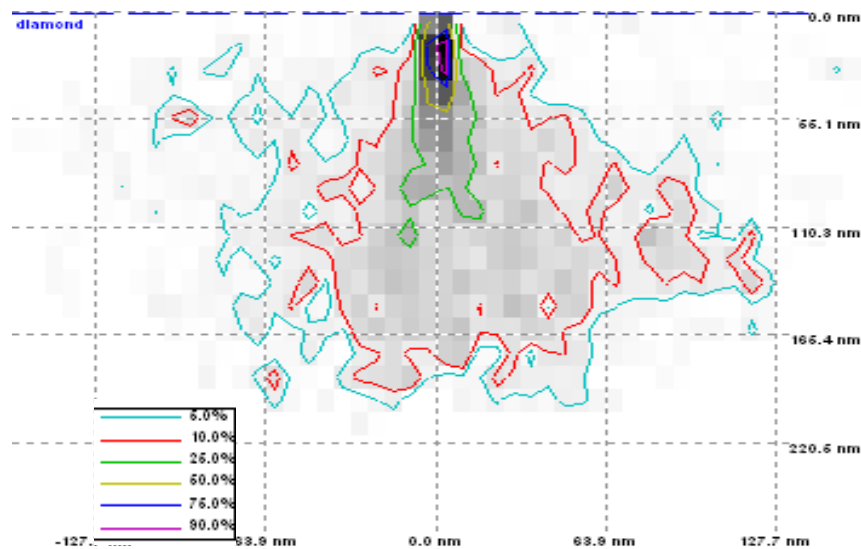


Figure 7.18 - Monte Carlo simulation for the distribution of backscattered electrons in diamond at $E_0 = 5$ keV. The colours represent the electron energy.

Furthermore, in the current study there was a limitation in terms of the beam energy (5 keV), whereas in the literature relatively high yields measured in transmission have been acquired with beam energies up to 20 keV.^[15]

Despite the fact that a bias was not applied in these first measurements, the experiments are valid in terms of giving an indication of the limit for the electron transport length in the samples.

7.4. Conclusions

The present study allowed an improvement in the growth of thin NCD films, essentially through the optimization of the seeding processes. This is crucial to obtain uniform nucleation layers, therefore resulting in high uniformity diamond films. The results obtained from all the seeding methods depend highly on the primary particle size. ESD with colloidal suspensions of 5 nm diamond powders gave good results after ultrasonication and centrifugation immediately before seeding. Thin diamond films were grown successfully with thicknesses of ~ 200 nm.

A new method of partial dry etching was developed, using a laser milling process to remove selected areas from the Si substrates of diamond-coated samples and using a hot KOH solution to remove the remaining substrate. Using this method Si framed diamond membranes of various thicknesses from 14 μm to 140 nm were successfully fabricated. The membranes were difficult to handle without compromising their integrity. A process for mounting the samples and handling them while avoiding damage needs to be developed.

Transmission yields were measured from three MCD diamond membranes with thicknesses of ~ 0.4 , 3.5 and 10 μm , giving values from ~ 0.6 for the diamond films with 3.5 μm and 10 μm and ~ 0.9 for the 0.4 μm thick diamond for bare surfaces under field free conditions. After hydrogenation SEE yields increased by a factor of ~ 2 . The results were in accordance with Monte Carlo simulations predicting a film thickness in the order of 215 nm for a positive gain at 5 keV in the absence of any drift field. Hence, the measurement method needs further improvements to permit a maximization of the yield values taken from the samples.

7.5. References

1. A.M. Schrand, S.A. Ciftan Hens and O.A. Shenderova, Nanodiamond Particles: Properties and Perspectives for Bioapplications, *Critical Reviews in Solid State and Materials Sciences*, **34** (2009) 18–74.
2. V.V. Danilenko, On the History of the Discovery of Nanodiamond Synthesis, *Physics of the Solid State* **46** 4 (2004) 595–599.

3. V.Y. Dolmatov, Detonation-synthesis nanodiamonds: synthesis, structure, properties and applications, *Russian Chemical Reviews* **76** (4) (2007) 339-360.
4. C. Mangeney, Z. Qin, S. A. Dahoumane, A. Adenier, F. Herbst, J.P. Boudou, J. Pinson and M.M. Chehimi, Electroless ultrasonic functionalization of diamond nanoparticles using aryl diazonium salts, *Diamond and Related Materials* **17** (2008) 1881-1887.
5. O.A. Williams, J. Hees, C. Dieker, W. Jäger, L. Kirste and C.E. Nebel, Size-Dependent Reactivity of Diamond Nanoparticles, *ACS Nano* **4** 8 (2010) 4824–4830.
6. A. Krüger, F. Kataoka, M. Ozawa, T. Fujino, Y. Suzuki, A.E. Aleksenskii, A.Y. Vul' and E. Osawa, Unusually tight aggregation in detonation nanodiamond: Identification and disintegration, *Carbon* **43** (2005) 1722–1730.
7. M. Ozawa, M. Inaguma, M. Takahashi, F. Kataoka, A. Krüger and E. Ōsawa, Preparation and Behavior of Brownish, Clear Nanodiamond Colloids, *Advanced Materials* **19** (2007) 1201-1206.
8. A.E. Aleksenskii, M.V. Baidakova, A.Y. Vul' and V.I. Siklitskii, The structure of diamond nanoclusters, *Physics of the Solid State* **41** (1999) 668–671.
9. L. Ostrovskaya, V. Perevertailo, V. Ralchenko, A. Dementjev and O. Loginova, Wettability and surface energy of oxidized and hydrogen plasma-treated diamond films, *Diamond and Related Materials* **11** (2002) 845–850.
10. R. Hoffmann, A. Kriele, H. Obloh, J. Hees, M. Wolfer, W. Smirnov, N. Yang and C.E. Nebel, Electrochemical hydrogen termination of boron-doped diamond, *Applied Physics Letters* **97** (2010) 052103-3.
11. Z.J. Ding and R. Shimizu, A Monte Carlo modeling of electron interaction with solids including cascade secondary electron production, *Scanning* **18** (1996) 92–113.
12. K.L. Jensen, J.E. Yater, J.L. Shaw, B.B. Pate and J.J. Petillo, Modeling the performance of a diamond current amplifier for FELs, *Proceedings of 2011 Particle Accelerator Conference*, THP205 2507-2509.
13. D.C. Joy, A Database on Electron-Solid Interactions, *Scanning* **17** (1995) 270–275.
14. J. Kawata, K. Ohya and K. Nishimura, Simulation of secondary electron emission from rough surfaces, *Journal of Nuclear Materials* **220-222** (1995) 997-1000.
15. J.E. Yater, J.L. Shaw, K.L. Jensen, T. Feygelson, R.E. Myers, B.B. Pate and J.E. Butler, Secondary electron amplification using single crystal CVD diamond film, *Diamond and Related Materials* **20** (2011) 798-802.

Chapter 8. Conclusions

This thesis aimed to investigate the secondary electron emission (SEE) properties of diamond films as a potential material to use in dynode devices. Chemical vapour deposition (CVD) diamond films were prepared with a range of B-doping levels, crystallinities, thicknesses and surface terminations on both Mo and Si substrates.

MCD films demonstrated a lower doping efficiency than NCD films. These results were in accordance with the preferential B incorporation at the grain boundaries rather than in substitutional sites in the carbon matrix. With the increase in CH_4 concentration the grain size was reduced in comparison to the MCD films, and for increased ratios of CH_4/H_2 ($> 3\%$) the crystalline morphology tended to give rise to an aggregate of diamond nanocrystallites and disordered graphite. Then, due to the smaller grain size and consequent higher amount of grain boundaries, NCD films present normally higher resistivities than MCD films.

In addition, the effect of the B content was observed through the modifications in the Raman spectra taken from the films. The decrease in the intensity of the diamond peak at 1332.5 cm^{-1} together with its broadening and shift to lower wavelengths, characteristic features of the Fano effect, were clearly observed from the UV spectra of the diamond films. In addition, the growth rate was not significantly affected by B content.

A new home-built equipment for acquisition of SEE yields in reflection and transmission configurations was developed. The setup consists of a system of phosphor screens (PSs) acting as electron detectors, which are then associated to a photomultiplier tube (PMT) for the acquisition of signals. The reflection yields are calculated by the ratio of the signal acquired from the sample to measure to the signal corresponding to the primary electrons. The values measured in the new apparatus presented a difference of around 13% in relation to those measured using a Faraday cup (FC) for the collection of the electrons.

Chapter 8 Conclusion

A comprehensive study of the reflection yields from CVD diamond films was carried out, evaluating the effects of the variation of parameters such as B concentration, crystal size, film thickness and substrate material on gain, and gain degradation under beam exposure.

MCD films (~3.5 μm thick) grown on Mo showed generally higher yields than when grown on Si for a similar range of resistances. This may be related with the increased conductivity of the substrate allowing easier electron flow through the back contact of the diamond film. A maximum yield value of 14 was obtained for a 1.1 k Ω diamond film on Mo, similarly to the values found in the literature for H-terminated CVD diamond films grown on Mo substrates.

Nevertheless, yields ~80 have also been published but the key to obtain such high values is still to understand. Results in the same order of magnitude (~14) were measured by the project counterparts in the Space Research Centre (SRC) at the University of Leicester, which in many ways reassured the measurements obtained from these experiments.

Experiments performed on H-terminated 0.5-4 μm -thick MCD films grown on Si for the same level of resistance, showed a maximum yield of 13 determined for a 1.25 μm -thick film with resistance of 1.9 k Ω . The slight variation in yield measurements with film thickness was attributed to the increasing average crystallite size with the film thickness resulting from the columnar growth process, even though this appeared to be a minor effect. The highest yield value (~18) was obtained from a 3.5 μm H-terminated NCD film grown on Mo with a resistance of 4.1 k Ω , whereas for the remaining NCD films the yields were below 8.

Furthermore, a comparison between the yields obtained after surface functionalization with LiO or CsO ad-layers and hydrogenated diamond surfaces, showed the highest increase in yield corresponding to the hydrogenated and lithiated surfaces, with values varying from 8 to 14 and 10 to 15, respectively. Interestingly, the highest SEE yield was measured after hydrogenation of a bare surface of a sample with resistance of 1.1 k Ω . These modest results might be due to a non-effective preparation or contamination of the LiO and CsO functionalized surfaces, during the cleaning or baking processes.

Unpolished B-doped ($> 10^{20} \text{ cm}^{-3}$) PC CVD diamond samples, acquired from Element Six Ltd presented a maximum yield of 9 obtained for CsO surfaces, considerably lower than compared with the yields measured previously for the MCD HFCVD films (~13) for the same surface functionalization. The differences observed may be related with the transport properties of the bulk or perhaps with the surface coverage uniformity of the PC rough surface.

SEE yield values measured from a LiO terminated surfaces, had maximum yield of 8.9, although presenting a larger variation in the values acquired from different surface areas. In addition, the H-terminated SCD sample showed a yield of ~ 10 presenting small variance across the surface, since its smoother surface is expected to allow a more uniform NEA and in addition, the electron emission at the surface should not be hindered by neighbour crystals interfering.

The processes of growing sub- μm pin-hole free diamond films were studied and the methods for the production of diamond membranes by Si etching optimized. The improvement in the growth of sub- μm NCD films was successfully achieved by the optimization of the seeding processes, crucial to obtain uniform nucleation layers. All the seeding methods tested proved to be highly dependent on the size of the seeds. Electrospray deposition (ESD) with 5 nm diamond colloidal suspensions showed the best results, when performed immediately after ultrasonication and centrifugation. Thin diamond films were grown successfully with thicknesses of ~ 200 nm.

A new method of partial dry etching was developed, using a laser milling process to remove selected areas from the Si substrates and using a hot high concentration KOH solution to remove the remaining substrate, whereby diamond membranes of various thicknesses from 14 μm to 140 nm were successfully fabricated.

Transmission yields of $\sim 0.6 - 0.9$ were measured from diamond membranes with thicknesses of $\sim 10 - 0.4 \mu\text{m}$, under field free conditions, which after hydrogenation were increased by a factor of ~ 2 . Those results were in accordance with Monte Carlo simulations predicting a film thickness around 215 nm for a gain >1 at 5 keV in the absence of any drift field.

8.1. Future work

The experimental work developed in the aim of this thesis was wide and involved different interconnected areas of research. Each area may now be explored in further detail, having by base all the work presented here, considering any principle not fully understood; areas not fully explained or/and explored; correction of what went wrong, improving what went right and trying to do things differently.

8.1.1. SEE apparatus

The new apparatus for SEE measurements opens a big window for changes, since all the system is new and needs to be deeply understood. Modifications should be made at different levels, such as finding a different method to calibrate the measurements acquired; optimizing the sample loading system; reformulate the resistive baking system; insert a LEED system attached to the detector; improving the software program being used at the moment; change the shape of the detectors; fully test the transmission system and modify accordingly, apply a multimeter to allow biasing and measuring the current generated in simultaneous and any other modification which may simplify the process of calibration and measurement.

8.1.2. SEE yield measurements

The list of parameters that can be considered and combined to evaluate the SEE yields from a single sample is almost endless. Despite the reasonable number of publications on SEE yield measurements from diamond films that can be found in the literature, the area is full of uncertainties. This is clear by the disparity of values that can be found.

An important aspect to have in consideration for future measurements would be the baking of the samples before performing the actual yield measurement, which should be done in a range of temperatures, for different surface functionalization of the diamond films.

8.2. Growth and characterisation of thin diamond membranes

The field of study can be further optimized with the improvement / development of seeding methods for deposition of monolayer of diamond seeds; try different growth conditions to test the limit of minimum thickness achievable on the HFCVD reactors in the Diamond Laboratory and perhaps test other reactors.

In addition, the processing for preparing membranes from etching the Si substrate is very good but could be even further improved, for instance, by reducing the total preparation time, especially in what concerns to the liquid etching.

Appendix A. Scientific communications and collaborations

A.1. Scientific communications

1. R. Vaz, P.W. May, N.A. Fox and J. S. Lapington, Secondary electron emission studies of CVD diamond films, 2012 De Beers Diamond Conference, Warwick, U.K., 07/2012 (*poster*).
2. J.S. Lapington, V. Taillandier, B.L. Cann, J. Howorth, J. Milnes, R. Vaz, P.W. May, N.A. Fox, R. Stevens and L. Wang, Investigation of the secondary electron emission characteristics of alternative dynode materials for imaging photomultipliers, *Journal of Instrumentation* 7 (2012) E04002, (DOI: 10.1088/1748-0221/7/04/E04002) (*paper*).
3. R. Vaz, P.W. May, N.A. Fox and J. S. Lapington, Secondary electron emission studies of CVD diamond films, XX International Materials Research Congress - IMRC 2011, Cancun, Mexico, 08/2011 (*poster*).
4. R. Vaz, P.W. May, N.A. Fox, J. S. Lapington, J. Howorth, J. Milnes and C.J. Horsfield, Secondary electron emission from CVD diamond films, AWE Management Board Meeting, Merchant Venture Building, University of Bristol, U.K. 09/2011 (*poster*).
5. R. Vaz, P.W. May and N.A. Fox, Secondary electron emission studies of CVD diamond films, Diamond Group, School of Chemistry, ONYX Graduate Training Alliance Workshop, University of Bristol, U.K. 09/2011 (*poster*).
6. R. Vaz, P.W. May, J. Lapington, V. Taillandier, Secondary electron emission measurements from B-doped CVD diamond, Hasselt Diamond Workshop 2010 – SBDD XV, Hasselt, Belgium, 02/2010 (*poster*).

A.2. Collaborations / Links to other researchers

- Development of techniques for seeding and diamond coating of complex shape ‘Venetian-blind type’ transmissive reflection dynodes, Photek, UK, (Dr James Milnes) (Dynode project industrial partner, continuous collaboration).
- Diamond coating of quartz, fused silica and aluminum nitride (AlN), University of Leicester, UK, (Dr Jon Lapington) (Dynode project university partner, continuous collaboration).
- Quarterly meetings with the ‘Dynode project’ partners: University of Leicester Photek and AWE (industrial sponsor).
- Cutting and surface structuring of silicon carbide samples to use as inserts in moulds for polymers injection moulding using a Oxford lasers Alpha 532 micromachining system, University of Aveiro, (Dr. Victor Neto) (sporadic collaboration).
- Deposition of graphene using electrostatic spray processes, NUS in Singapore, (Dr Loh Kian Ping) (sporadic collaboration).

A.3. Attendance at conferences

- Hasselt Diamond Workshop 2010 SBDD XV, 22nd - 24th February 2010, Hasselt, Belgium.
- Technological Plasma Workshop 2011, 6th - 7th January 2011, Bristol.
- XX International Materials Research Congress, 14th - 19th August 2011, Mexico.
- 2012 De Beers Diamond Conference, 9th - 11th July 2012, Warwick, U.K.